Simulation and Reconstruction of Muon Tracks with the "multi-PMT Digital Optical Module" in Comparison to the "PINGU Digital Optical Module" for the IceCube-Gen2 High-Energy Array

Simulation und Rekonstruktion von Myonenspuren mit dem "multi-PMT Digital Optical Module" im Vergleich zum "PINGU Digital Optical Module" für das IceCube-Gen2 High-Energy Array

Der naturwissenschaftlichen Fakultät der Friedrich-Alexander-Universität Erlangen-Nürnberg zur Erlangung des Doktorgrades Dr. rer. nat.

vorgelegt von
Thomas Kittler
aus Fürth

Als Dissertation genehmigt von der naturwissenschaftlichen Fakultät der Friedrich-Alexander-Universität Erlangen-Nürnberg

Tag der mündlichen Prüfung:	14.07.2020
Vorsitzender des Promotionsorgans:	Prof. Dr. Georg Kreimer
Gutachter/in:	Prof. Dr. Gisela Anton Prof. Dr. Alexander Kappes

Abstract

The IceCube neutrino observatory is the largest operating neutrino telescope at the moment. It consists of 5160 Digital Optical Modules (DOMs) on 86 vertical strings buried in a depth of 1.5 km to 2.5 km within the Antartic ice instrumenting a volume of approximately 1 km^3. An upgrade of the in-ice array to a volume of almost 10 km^3, called IceCube Gen2 high-energy array, is the subject of current research. The multi photomultiplier (PMT) Digital Optical Module (mDOM), which consists of 24 symmetrically distributed 3-inch PMTs, is considered as detection unit for the Gen2 high-energy array. Alternatively, an upgraded version of the IceCube DOM, called PINGU Digital Optical Module (PDOM), containing only one 10-inch PMT facing downwards, is also considered as detection unit. This work analyzes the effect of the sensor segmentation of the mDOM on the angular resolution of through-going muon tracks in comparison to the angular resolution obtained with the PDOM within the context of a Gen2 high-energy array geometry.

In order to eliminate the effect of different photon detection efficiencies of the two sensor designs, the quantum efficiencies of the respective PMTs are scaled in the simulation to ensure an equalized effective photocathode area per module. For down-going and horizontal through-going muons with an energy between 3 TeV and 70 PeV a detector equipped with mDOMs yields between 10 % and 40 % better angular resolution in almost all energy regimes after sensor-independent quality cuts (based on Monte Carlo information) have been applied. For up-going muons with energies below 1 PeV the upscaled PDOM yields between 7 % and 13 % lower angular errors.

Finally, estimations of the 90 % exclusion limits and the 5σ discovery fluxes of neutrino point sources are conducted for both sensors in a Gen2 high-energy array. For sources with a declination below 5° the upper limits and discovery fluxes obtained with the mDOM are 8 – 11 % lower. The upscaled PDOM leads to 4 – 12 % lower exclusion limits and discovery fluxes for sources with a declination above 33°.

Table of Contents

List of Tables

Table **Page**

List of Figures

Figure **Page**

CHAPTER 1

INTRODUCTION

Astronomy is one of the oldest natural sciences of mankind. Already in ancient Greece people were fascinated by celestial phenomena and tried to come up with rational explanations for their observations. At these times data acquisition was done by the naked eye.

Centuries later, the fascination of astronomy as vivid as ever, the invention of the first telescopes in the early 17th century enabled the astronomers to gain much more insight into the cosmos. Since a human was still required to actually look through the telescopes, the observable energy range of astronomical objects was still limited to the optical spectrum.

The advancement in physics during the following centuries, especially the continuously evolving theory of light, the deeper understanding of the structure of matter including the discovery of atoms and subatomic particles, eventually affected astronomy as well. But it was not until a certain degree of technological progress was available, that physicists could actually start to build instruments, that could observe astronomical objects outside of the visible spectrum.

From the 20th century on telescopes have been built to explore a larger part of the electromagnetic spectrum. Nowadays, telescopes are available, which are sensitive from radio waves (with wavelengths up to tens of meters) to gamma rays (wavelengths down to 10^{-18} m and below). The accessibility of these new channels have led to ground braking new discoveries, like the cosmic microwave background or active galactic nuclei.

The discovery of particles from outer space bombarding the Earth, called cosmic rays, in the beginning of the 20th century marks another milestone in the history of astronomy, which eventually led to the formation of a new branch of physics, namely astroparticle physics. Countless experiments, since then, have measured the composition and the energy distribution of cosmic rays, but until today it is still unclear what the sources of high energetic cosmic rays actually are.

While astronomy was, and still is, largely dominated by the detection of photons as messenger particles, we are on the verge of a new era with telescopes designed to detect other particles from astronomical sources. One of these alternatives are neutrinos. Neutrinos can propagate through dense regions and cover large distances to a potential observer without being affected by electromagnetic fields since they are nearly massless and interact only via the weak force in the standard model. Especially concerning the question of the origin of high energetic cosmic rays, the identification of sources of high-energy neutrinos is of great interest, since these are likely to be sources of high-energy cosmic rays as well.
The cubic kilometer Cherenkov telescope IceCube [69] has been built inside the deep ice at the South Pole with the goal of measuring these particles. IceCube is an array of 5160 "Digital Optical Modules" (DOMs) with an instrumented volume of about $1\,\mathrm{km}^3$. Being operational in its current form since 2010, IceCube successfully discovered the existence of a diffuse cosmic neutrino flux in 2013 [63]. Unfortunately, until today it was not possible to actually detect a point source of high energetic neutrinos. The so-called "golden channel" for point source searches are neutrino induced muon tracks, since these yield the best angular resolution. In order to increase the sensitivity to potential point sources, angular resolution and the amount of detected neutrinos are crucial. To increase both, the IceCube Collaboration has been working on the next generation extension of the IceCube detector, called IceCube-Gen2, which will consist of approximately 9000 additional optical modules, increasing the instrumented volume almost by a factor of ten. In addition to the increased volume, new optical sensor designs are being developed, which, amongst other possible advantages, are designed to provide more information about events within the telescope.
In this thesis the impact of one of the new sensor designs for IceCube-Gen2, namely the "multi PMT Digital Optical Module" (mDOM), on angular resolution and on the sensitivity to point sources has been studied in detail. All results are presented in comparison with equivalently obtained results by using the "PINGU Digital Optical Module" (PDOM), an upgraded version of the DOM used in the IceCube detector, which represents the baseline option for IceCube-Gen2.
Chapter 2 presents the scientific motivation and chapter 3 describes the detection principle of a neutrino detector and a detailed description of the IceCube detector including the most recent results of neutrino point source searches obtained with IceCube. Additionally, the planned upgrade IceCube-Gen2 and the properties of the mDOM and the PDOM are presented. In chapter 4 all steps of the simulation process are described and properties of the used simulated data sets are discussed. The applied muon-track reconstruction algorithms and event selections are described and the angular resolutions obtained with the mDOM and the PDOM are presented in chapter 5. In chapter 6 these angular resolutions and event selections are used to estimate the neutrino point source sensitivity of IceCube-Gen2 equipped with either mDOMs or PDOMs. A detailed discussion of the obtained results is presented in chapter 7, while chapter 8 completes this thesis with a summary, conclusion and a short outlook.

CHAPTER 2

SCIENTIFIC BACKGROUND

In this chapter the scientific background and motivation for neutrino astronomy will be outlined. Section 2.1 introduces cosmic rays and explains what is known so far and what are the topics of current research. A breif summary why neutrinos make excellent messenger particles for astrophysics is presented in section 2.2. It is assumed, that so-called cosmic accelerators are the source of high energetic cosmic rays, therefore, section 2.3 outlines a simple acceleration model yielding a power law spectrum for the cosmic ray flux and section 2.4 explains why neutrinos are expected to be created at these sources. Section 2.5 completes this chapter by listing some promising candidates of neutrino point sources.

2.1 Cosmic Rays

Cosmic rays are charged particles with extraterrestrial origin bombarding the Earths atmosphere. Since the first discovery in 1912 [103], numerous experiments have measured the composition and the energy spectrum of cosmic rays, see figure 2.1. Approximately 90% of cosmic rays are protons, about 9% alpha particles, roughly 1% heavier nuclei and only a very small fraction are electrons. The spectrum of cosmic rays can be expressed as a broken power law $E^{-\gamma}$ with different regimes. Up to approximately 4×10^{15} eV the spectrum can be described with a spectral index of 2.6. It is assumed, that mainly galactic sources are responsible for this part of the spectrum, while Super Nova Remnants (SNR) seem to be the most promising candidates for galactic sources. At higher energies the spectrum softens to approximately $E^{-3.1}$. This steepening of the spectrum is called "the knee" and could indicate the transition from galactic to extragalactic sources. The last feature, called "the ankle" at 4×10^{18} eV, marks a hardening of the spectrum to approximately $E^{-2.6}$. The sources for this part of the cosmic ray spectrum are believed to be exclusively extra galactic, since galactic sources are probably not powerful enough to accelerate particles to these

energies. Main candidates for these extremely high energies are Active Galactic Nuclei (AGNs), Gamma Ray Bursts (GRBs) and starburst galaxies (see section 2.5). At energies above 10^{19} eV a cut-off in the spectrum is visible. At these energies cosmic ray particles start to interact with the cosmic microwave background (CMB) and therefore are not present in the spectrum measured on Earth anymore. This effect is called the Greisen-Zatsepin-Kuzmin limit (GZK-limit) [54][29].
Even a hundred years after the discovery of cosmic rays it is still unknown where the high energetic part of the cosmic rays is originated. Although, various promising candidates for galactic as well as for extragalactic sources exist, it has not been proven which of these actually contribute to the spectrum and it is not clear what the acceleration mechanisms are. The main reason for this is the loss of directional information of cosmic rays while propagating through the universe due to galactic magnetic fields changing the direction of the traversing charged particles. Therefore, the only way to actually locate sources is to use electrically neutral messenger particles, like photons or neutrinos.
As soon as the cosmic rays reach Earth, they start to interact with particles in the atmosphere producing so-called air showers. A schematic of a proton induced air shower is displayed in figure 2.2. While the electromagnetic component of an air shower is quickly attenuated once it reaches the surface, muons can penetrate the Earths crust for a few kilometers and produced neutrinos are likely to propagate through the whole planet without any further interaction. These components are the main background for any search for astrophysical neutrinos and will be discussed in more detail in chapter 6.

2.2 Neutrinos as Messenger Particles

Neutrinos are electrically neutral, nearly massless, leptonic elementary particles, which interact only via the weak force in the standard model. No electrical charge means no diffusion of the directional information through galactic magnetic fields, neutrinos therefore point back to their sources. Interacting only via the weak force enables neutrinos to propagate through dense regions, like galaxies, molecular clouds or dense regions at or near the source itself. Photons, in contrast, have a much higher probability of interaction with matter while propagating through denser regions of the universe ($\alpha_{em}/\alpha_w \approx 10^4$ [51]) and they can interact with the so-called extragalactic background light (EBL) via

$$\gamma + \gamma(\text{EBL}) \rightarrow e^+ + e^-, \tag{2.1}$$

as soon as the necessary energy is available [34]. Figure 2.3 shows the so-called "gamma-ray horizon" of the universe as a function of redshift and photon energy. The gray area in this figure is opaque to photons. It can be seen, that the universe with a redshift of $z > 1$ becomes opaque for photons at energies above 100 GeV. For photon energies above 100 TeV the nearby blazar Mrk 501

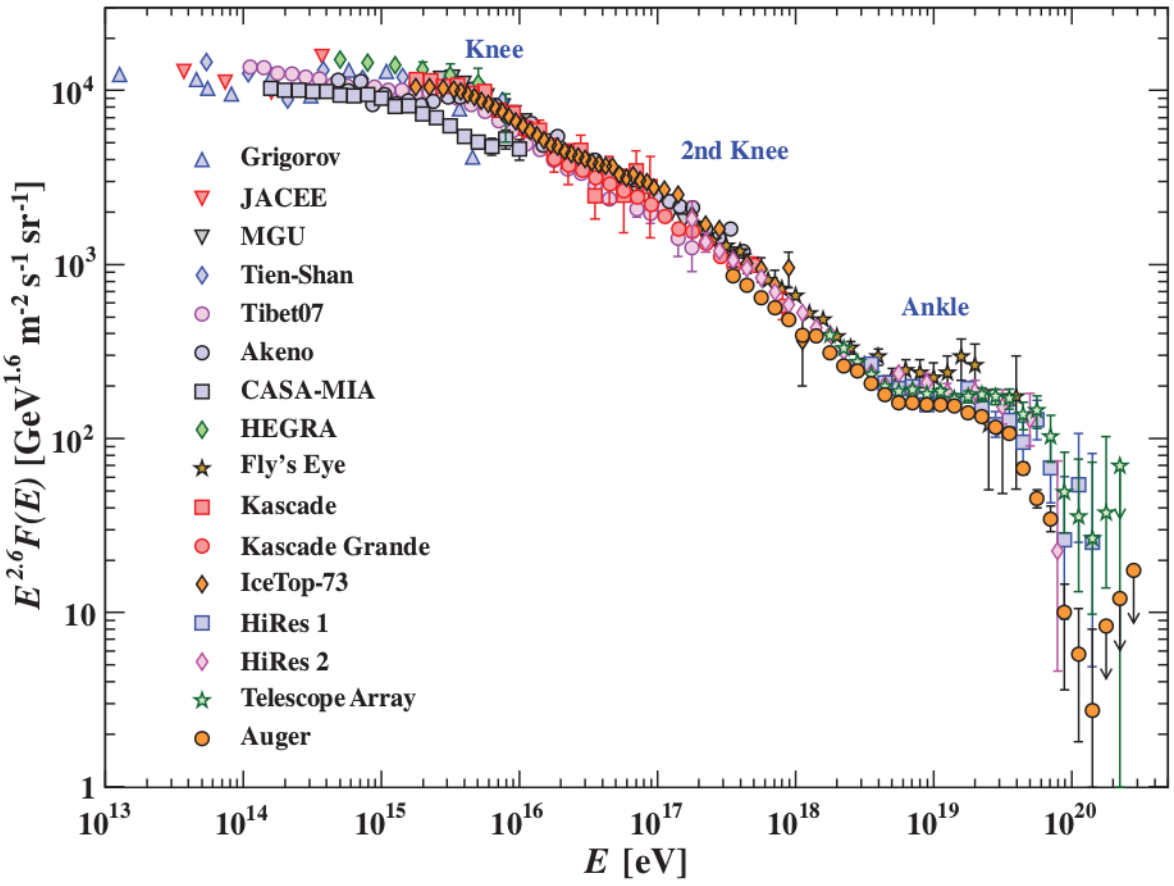

Figure 2.1: Cosmic ray spectrum multiplied by $E^{2.6}$ to emphasize the changes of the spectral index. Taken from [53].

becomes invisible for gamma-ray astronomy, while at energies above 1 PeV photons from our own galactic center don't reach Earth anymore.

Neutrinos, however, do not interact with photons, which makes it possible to explore areas of the universe that would be concealed otherwise. On top of that, identifying a gamma ray source as a neutrinos source would add complementary valuable information about that source, which could be used to further test theoretical models. All of these properties make neutrinos extremely interesting messenger particles for astronomy, opening a whole new window to the universe.

2.3 Particle Acceleration

It is widely believed, that the mechanisms accelerating particles to high energies are variations of the so-called "Fermi acceleration". The main idea behind this mechanism is, that particles gain energy by traversing a shock front. Due to magnetic inhomogeneities the same particle can then be scattered upstream again and then cross the shock front again, thus the energy of the particle

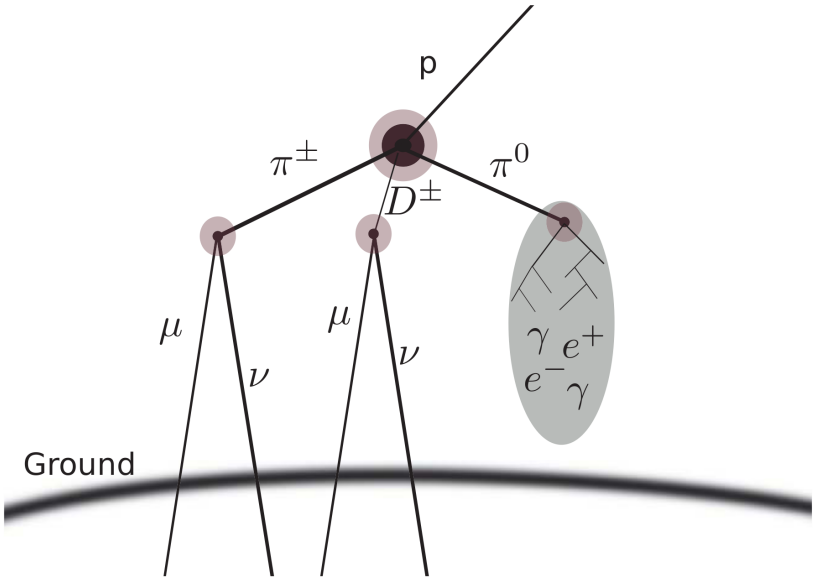

Figure 2.2: Schematic of a proton induced air shower. Only produced ν and μ can penetrate underground instruments. Taken from [98].

is further increased. This cycle can repeat itself multiple times until the particle escapes the shock front region.
A simplified calculation to clarify the mechanism and the resulting energy spectrum can be made as follows (from [30]): On average, for each crossing of the shock front the particle energy increased by a relative amount $\Delta E = \xi \cdot E$, with E being the current particle energy. After n cycles the particle energy can be expressed as

$$E_n = E_0(1+\xi)^n \tag{2.2}$$

where E_0 denotes the initial particle energy. Hence, for a particle to reach an Energy E'

$$n = \ln \frac{E'}{E_0} / \ln(1+\xi) \tag{2.3}$$

cycles are needed. After each cycle the particle has a certain probability to escape the shock region P_{esc}. Therefore, the probability of a particle to be still within the shock region after n cycles is $(1-P_{esc})^n$. The number of particles with an energy larger than E' is proportional to

$$N(\geq E') \propto \sum_{m=n}^{\infty} (1-P_{esc})^m = \frac{(1-P_{esc})^n}{P_{esc}}. \tag{2.4}$$

Substituting equation 2.3 into equation 2.4 one obtains

$$N(\geq E') \propto \frac{1}{P_{esc}} \left(\frac{E'}{E_0}\right)^{-\gamma} \tag{2.5}$$

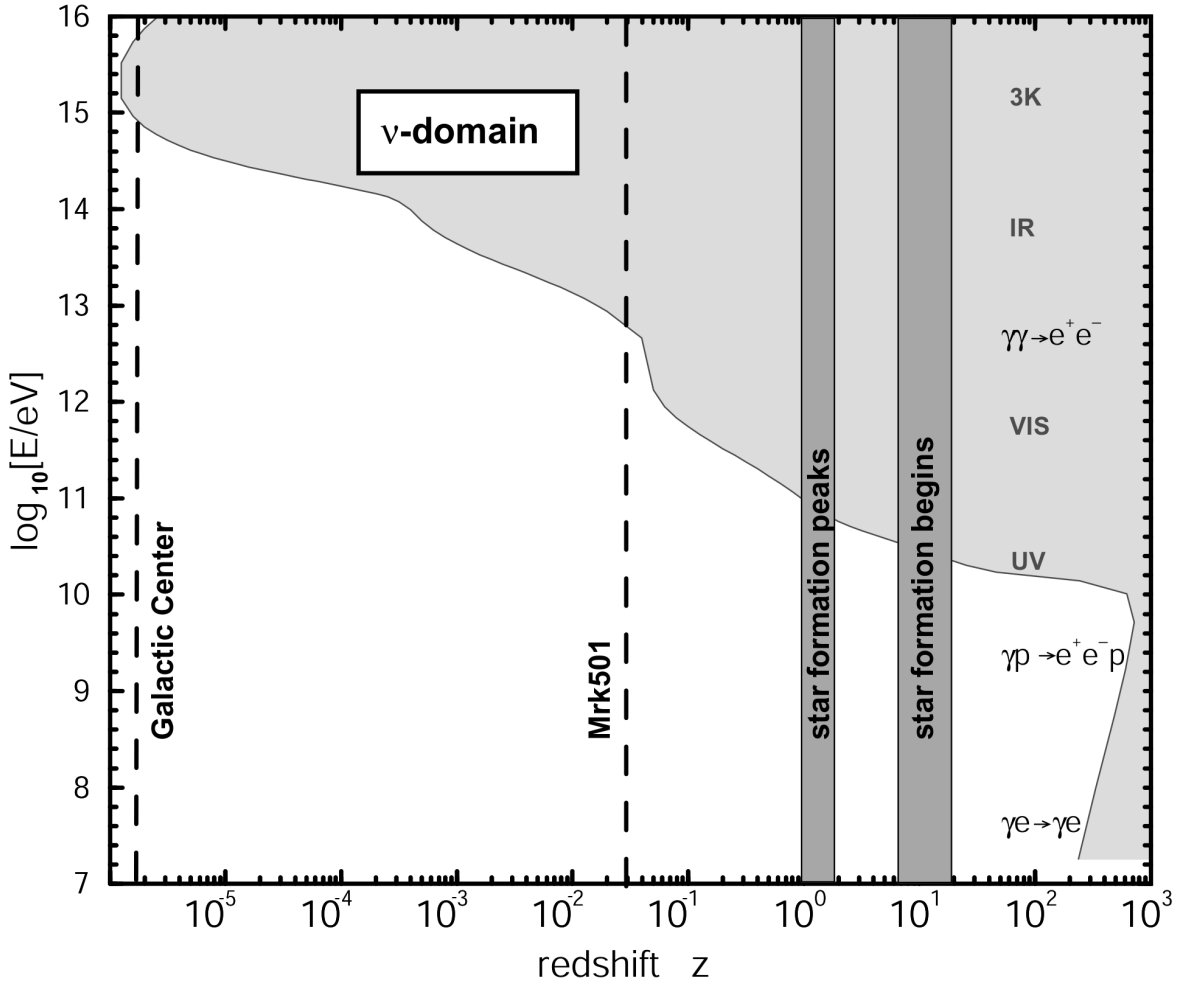

Figure 2.3: Universe visible in gamma-rays. The grey shaded area indicates the region from which photons do not reach the Earth. Taken from [5] (adapted from [58]).

with

$$\gamma = \frac{\ln(\frac{1}{1-P_{esc}})}{\ln(1+\xi)}$$

which can be approximated to $\gamma \approx P_{esc}/\xi$ for small values of P_{esc} and ξ. This simple approximation shows that an acceleration mechanism based on shock fronts yields an energy spectrum which follows a power law, as is observed for cosmic rays.

2.4 High Energetic Neutrinos from Cosmic Sources

As stated in section 2.1, cosmic rays consist mainly of protons, therefore it is justified to assume, that at a possible source of cosmic rays protons are accelerated to extremely high energies. These

ultra relativistic protons can then interact with other surrounding protons or photons creating pions:

$$p + p/\gamma \rightarrow \pi^+ + \pi^- + \pi^0 + X \tag{2.6}$$

where X are other components created in these types of reactions. Pions are unstable particles with lifetimes of 2.6×10^{-8} s for $\pi^\pm$ and 8.5×10^{-15} s for π^0. The dominating decay channels are (from [53]):

$$\pi^+ \rightarrow \mu^+ + \nu_\mu \qquad (\text{BR} \approx 99.99\%) \tag{2.7}$$

$$\pi^- \rightarrow \mu^- + \bar{\nu_\mu} \qquad (\text{BR} \approx 99.99\%) \tag{2.8}$$

$$\pi^0 \rightarrow 2\gamma \qquad (\text{BR} \approx 98.82\%) \tag{2.9}$$

Muons are also unstable with a lifetime of $\tau \approx 2.2 \times 10^{-6}$ s and will decay into electrons and neutrinos (BR$\approx$ 100%) via

$$\mu^+ \rightarrow e^+ + \nu_e + \bar{\nu_\mu} \tag{2.10}$$

$$\mu^- \rightarrow e^- + \bar{\nu_e} + \nu_\mu. \tag{2.11}$$

These particle reactions yield a neutrino flux with a flavor composition of $\nu_e : \nu_\mu : \nu_\tau = 1 : 2 : 0$ (same for neutrinos and anti neutrinos). Due to neutrino oscillation and the assumption, that the extends of possible production sites are greater then the oscillation lengths the flavor composition changes to $1 : 1 : 1$ at a possible observer on Earth [8].
If a source of high energetic neutrinos would be identified it seems likely, that these were produced due to the decay of pions, which themselves were created in reactions of high energetic protons. Hence, the detection of a high energetic neutrino point source is a so-called "smoking gun" evidence for a hadronic accelerator and therefore an extremely likely source of high energetic cosmic rays. One could make the argument, that γ-ray sources follow the same logic due to π^0 decay, but γ-rays are also produced via inverse compton scattering

$$e^\pm + \gamma(\text{low energetic}) \rightarrow e^\pm + \gamma(\text{high energetic}). \tag{2.12}$$

Thus, γ-ray sources are not necessarily hadronic accelerators, but could also be leptonic accelerators and therefore not sources of cosmic rays (which are mainly hadrons).

2.5 Candidates of Neutrino Point Sources

In the last sections a summary of what is known about cosmic rays was given and a possible acceleration mechanism yielding an energy spectrum which follows a power law was outlined. Additionally, the connection of sources of high energetic neutrinos and high energetic cosmic rays was described. Within the last section of this chapter a short list and brief description of the most promising candidates for high-energy neutrino sources is presented.

2.5.1 Galactic Sources

As mentioned in section 2.1, the cosmic ray spectrum follows a broken power law $E^{-\gamma}$ with various values of γ for different energy regimes. It is believed, that the dominant contributors below an energy of $\approx 10^{15}$ eV (e.g. below the "knee") are galactic sources [102]. In the following three types of promising galactic sources are briefly introduced.

2.5.1.1 Pulsars

Pulsars are spinning magnetized neutron stars which are possible remnants of supernova explosions. In the process of the supernova explosion, the stars which have typical radii in the order of 10^6 km, shrinks down to a size of 10 to 20 km due to gravitation. Densities of neutron stars are in the order of 10^{13} g/cm^3, so comparable to nuclear densities. In this process and due to the high density neutrons are formed via:

$$p + e^- \rightarrow n + \nu_e \tag{2.13}$$

These neutrons cannot decay since all energy levels reachable for electrons out of a neutron decay are occupied.
During the gravitational collapse the angular momentum is conserved, which causes a tremendous decrease of the rotation period. While a regular star with a radius of 10^6 km could have a rotation period in the order of a month, the resulting neutron star with a radius of 20 km has then a rotation period of about 1 ms.
Neutron stars also have extraordinary strong magnetic fields which are usually not aligned with the rotational axis of the star. The rotation of such strong magnetic fields around the rotation axis will create strong electric fields, which can accelerate charged particles, like electrons or protons to energies up to 1 PeV[35]. The exact details of these processes, however, are still unknown and topic of research.
The presence of high energetic protons could then trigger processes like those described in section 2.4, therefore one might argue, that pulsars are possible sources of high energetic neutrinos.

2.5.1.2 Binaries

Binaries consisting of a neutron star and a normal star could also lead to high energetic neutrinos. The enormous gravitational forces of the neutron star constantly attracts plasma from the normal star, thus forming an accretion disk (see fig. 2.4). Due to the acceleration of the plasma around the neutron star, enormous electromagnetic fields appear, which could reach particle energies up to 10^{19} eV [35]. These energies can increase even further if, instead of a neutron star a black hole is present.
A common feature of such system are highly relativistic particle jets perpendicular to the accretion disk. Such jets seem a likely surrounding for shock acceleration, thus a possible source of high energetic particles.

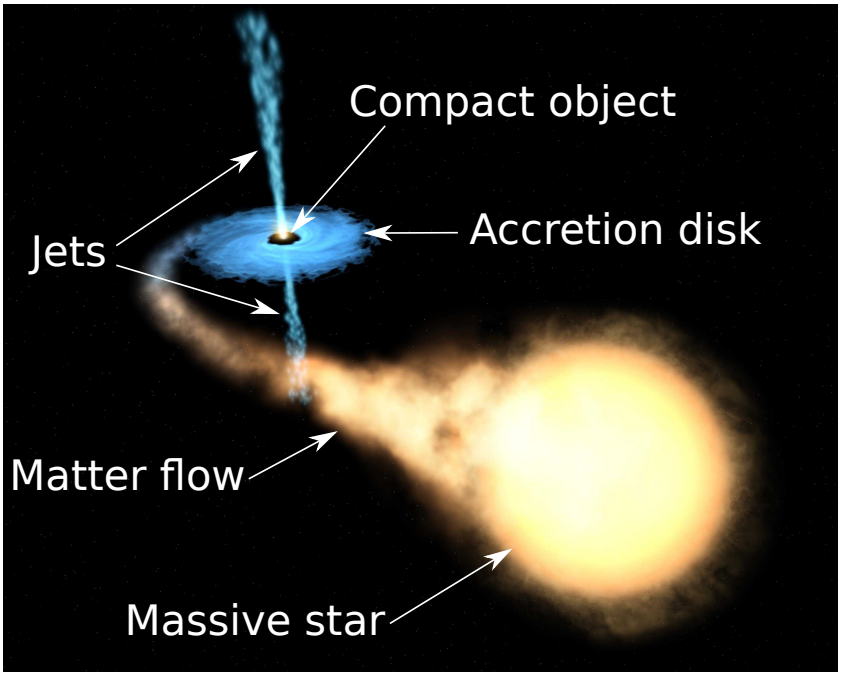

Figure 2.4: Artistic view of a binary system with a neutron star or black hole as one partner and a normal start as the other partner. Adapted from [27].

2.5.1.3 Supernova Remnants

The ensemble of expanding shells, swept up surrounding medium, shock fronts and turbulent magnetic fields are called supernova remnants (SNRs), see fig. 2.5. These environments seem to be ideal for shock acceleration, which makes SNRs a very likely source candidate for high energetic cosmic rays, and therefore also neutrinos. The observation of TeV gamma rays from the SNR RX J1713.7-3946 led to the conclusion, that protons with energies up to 100 TeV are present at the source [7].
A simple approximation, which takes the amount of SNRs in the Milky Way into account and assumes, that about 10% of the available energy is used for the acceleration of cosmic rays, shows that SNRs could be the dominant galactic source of cosmic rays, e.g. with energies up to 10^{15} eV [102]. This makes SNRs as a possible source for neutrinos even more interesting.

2.5.2 Extragalactic Sources

It is assumed, that most cosmic ray particles with energies above $10^{18.5}$ eV are of extragalactic origin [102]. One argument for this assumption is that galactic sources are not powerful enough to accelerate particles to these energy regimes. Another argument is, that even if galactic source could accelerate particles to such high energies, these particle would leave the galaxy, since their gyroradius is larger then the Galaxy. In the following some promising extra galactic sources are

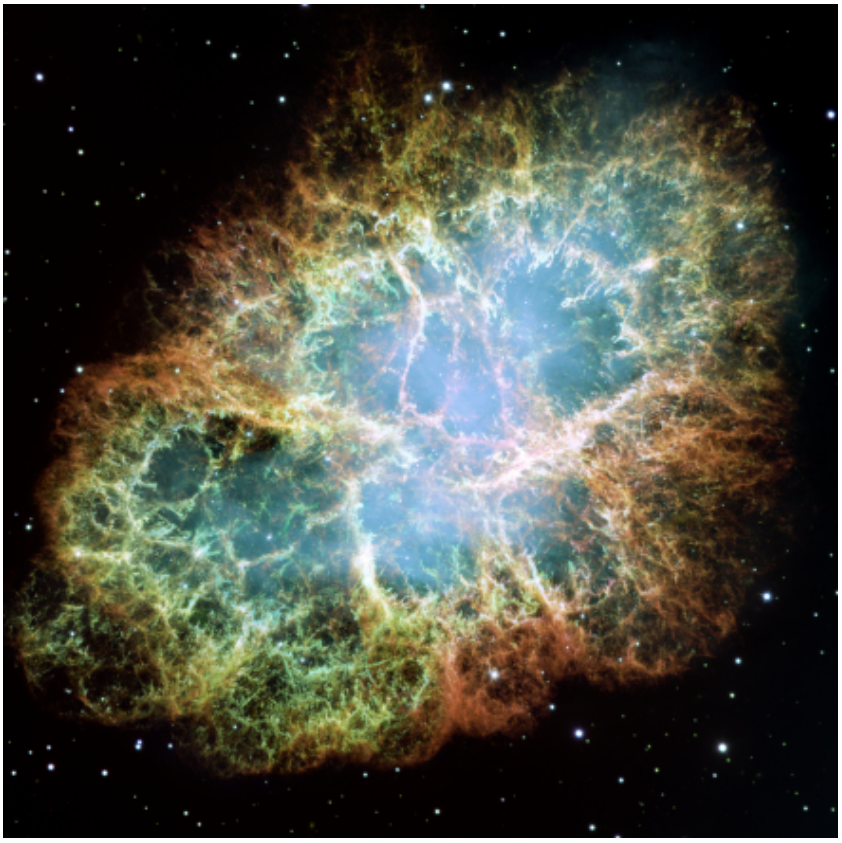

Figure 2.5: Mosaic picture of the Crab Nebular, the remnant of the supernova SN1057, taken by the Hubble space telescope in visible light. Taken from [37].

briefly outlined.

2.5.2.1 Active Galactic Nuclei

An Active Galactic Nucleus (AGN) is the center region of a galaxy with a super massive black hole with a mass of $10^6 - 10^9$ solar masses in its center. The black hole attracts matter and transforms gravitational energy into radiation and kinetic energy. Similar to binaries, an accretion disk can be formed with two perpendicular jets. If these jets point towards Earth the AGN is called a blazar, a particular class of AGNs. Blazars have already been identified as strong gamma-ray emitters (e.g. [56]), with up to TeV energies, and are therefore likely candidates for neutrino sources.

In September 2017 IceCube detected a high energetic muon neutrino event (290 TeV) from the direction of the known blazar TXS 0506+056 [72]. Follow-up observations with the Major Atmospheric Gamma Imaging Cherenkov Telescopes (MAGIC) [10] led to the detection of gamma rays with energies up to 400 GeV [91]. The spatial and temporal coincidences of the high-energy neutrino and the blazar flare were estimated in the 3σ range. Prompted by this event, IceCube

analyzed 9.5 years of data at the position of the blazar and found 3.5σ evidence for neutrino emission from this direction. Although in both cases the significance is below the 5σ threshold, these results are a strong hint, that blazars are indeed neutrino sources (see 3.2.7 for further details).

2.5.2.2 Gamma Ray Bursts

Gamma Ray Bursts (GRBs) are the most energetic transient events known in the universe. A total energy of up to 10^{53} erg is emitted in extremely short time windows [30]. A GRB with a time above 2 s is already considered a long burst. GRBs can have various origins, but the death of a massive star collapsing into a black hole, or the merger of two compact objects in a binary system, i.e. two neutron stars, are likely candidates. Whatever the exact scenarios causing GRBs are, a source of gamma rays, is also a possible source for high energetic neutrinos.

2.5.2.3 Starburst Galaxies

Galaxies with an exceptionally high rate of star formation are called Starburst Galaxies. Such galaxies require a huge amount of molecular gas, which causes the high star formation rate, as well as the formation of large stars. Large stars burn bright and fast and are likely to result in a supernova. The ejecta of supernovae interacting with the surrounding medium are possible sources of particle acceleration, which makes Starburst Galaxies a possible source for cosmic rays and therefore neutrinos. The detection of gamma rays with energies of several hundred GeV ([101], [78]) from known Starburst Galaxies also qualifies them as potential neutrino sources.

CHAPTER 3

ICECUBE & ICECUBE-GEN2

The following chapter is dedicated to the description of the IceCube neutrino detector and the next generation upgrade IceCube-Gen2. In order to understand why the detector is designed the way it is, the detection principle is explained in section 3.1. A detailed description of the IceCube neutrino detector, including the detector medium and event topologies can be found in 3.2. The signal processing chain is also part of this section, up to the point which is necessary to understand the rest of this thesis. An overview of the most important discoveries and limitations of IceCube is given at the end of this section. In section 3.3 motivation and plans for the next generation upgrade IceCube-Gen2 are presented, as well as a descriptions of two possible new concepts for the central detection unit.

3.1 Detection Principle

3.1.1 Neutrino Interactions with Matter

"Detection" most of the times means translation of a physical phenomenon into an electric signal, which can then be processed further, like the force experienced by a mass in a gravitational field via digital scales or the intensity of a light beam with the help of a photoelectric cell. As mentioned in section 2.2, neutrinos are nearly massless and only interact via the weak force. In consequence, neutrinos cannot be detected directly but need to undergo an interaction which produces secondary particles with different properties which then in turn can be detected. For an interaction to happen a reaction partner is necessary. In the case of IceCube, the relevant reaction partner is a nucleus of the detection medium, the Antarctic ice.

One has to distinguish between two types of reactions [1]: First, the charged current (CC) interaction via the exchange of an electrically charged $W^{\pm}$ boson,

$$\nu_l + X \xrightarrow{W^{\pm}} l + Y \tag{3.1}$$

where ν is the neutrino, $l \in \{e, \mu, \tau\}$ is the appearing lepton (of the same family as the neutrino), X is the nucleus and Y are other hadronic reaction results (e.g. pions and kaons). In the relevant energy ranges for IceCube ($E(\nu) \gtrsim 10\,\text{GeV}$), Y basically represent a hadronic particle shower.
The second interaction is the neutral current (NC) interaction via the exchange of an electrically neutral Z^0 boson:

$$\nu_l + X \xrightarrow{Z^0} \nu_l + Y. \tag{3.2}$$

The major difference between a CC and an NC interaction is the appearance of a charged lepton l of the same flavor as the primary neutrino ν_l. If the energy of the produced charged particles (leptons and hadrons) is large enough, they will propagate through the detector medium faster than light and emit radiation called "Cherenkov light" [16], which can then be detected.
Another important fact to keep in mind throughout this chapter is the extremely low cross section of neutrinos interacting with nucleons, which directly influences the amount of neutrino interactions within the vicinity of the detector (e.g. [20]). Figure 3.1 shows the neutrino cross section for inelastic scattering of neutrinos with nucleons for both interaction channels. A clear positive correlation between neutrino energy and the cross section is visible over the whole displayed energy range. While $\frac{d\sigma}{dE_\nu}$ is close to one at energies below 1 GeV, it decreases with increasing energy to below 0.5 above 1 PeV. It can also be seen, that the cross section of a CC interaction is about a factor of 2.5 to 3 larger than the cross section of a NC interaction over the whole shown energy range. For energies below 10 PeV a clear distinction between neutrinos and antineutrinos is visible which vanishes for energies above.

3.1.2 Cherenkov Light

Charged particles propagating through an optical transparent dielectric medium faster than the speed of light in this medium emit "Cherenkov light" [16]. Cherenkov light is emitted at a characteristic angle θ_c, the Cherenkov angle, with respect to the propagating particle. This angle depends on the spectral index of the medium n and the velocity of the particle $\beta = v/c_0$:

$$\cos(\theta_c) = \frac{1}{n \cdot \beta} \tag{3.3}$$

[1] Since IceCube is currently not capable of separating particles and the respective antiparticles and the processes are essentially identical, for the rest of the thesis particles and antiparticles will not be distinguished and it can be assumed, unless explicitly stated otherwise, that the differences are irrelevant.

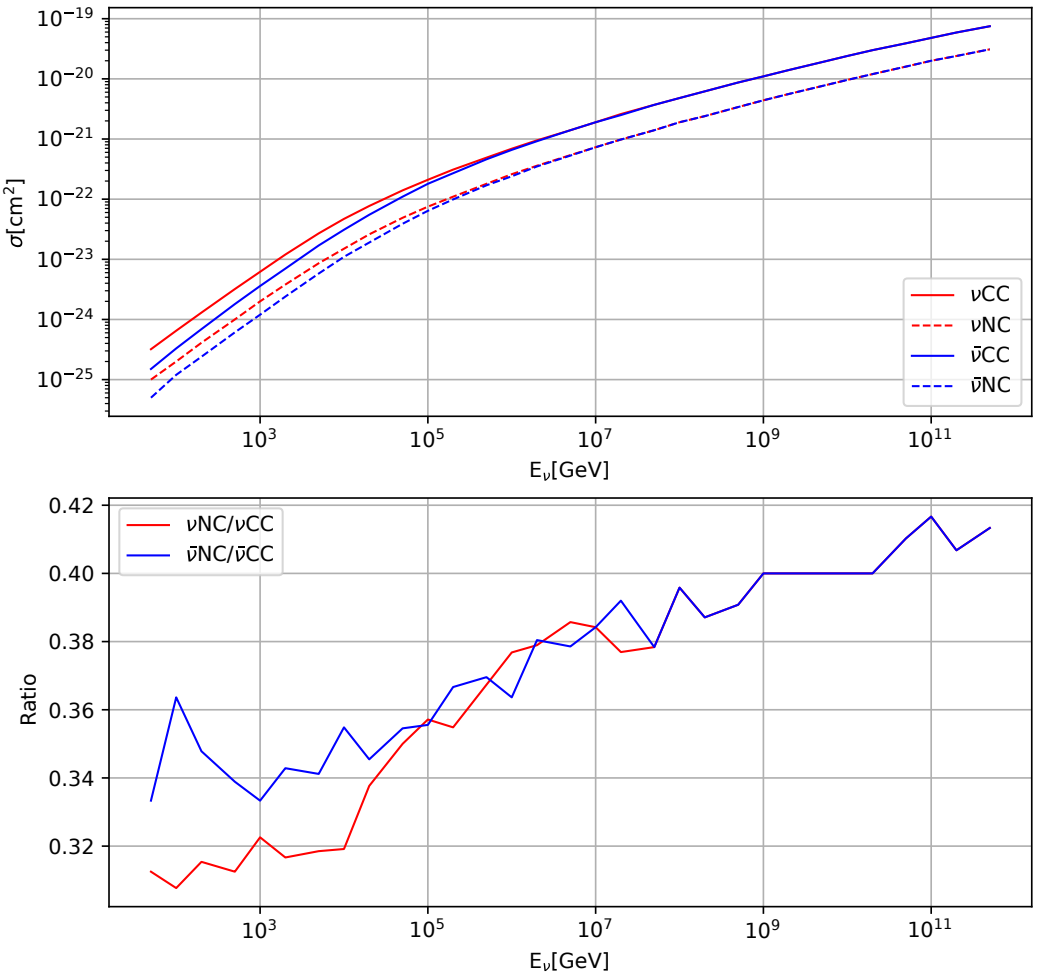

Figure 3.1: *Top*: Cross sections of neutrinos and antineutrios for inelastic neutrino-nucleon scattering (CC and NC) as a function of neutrino energy. *Bottom*: Ratio of NC over CC cross sections. Data taken from [20].

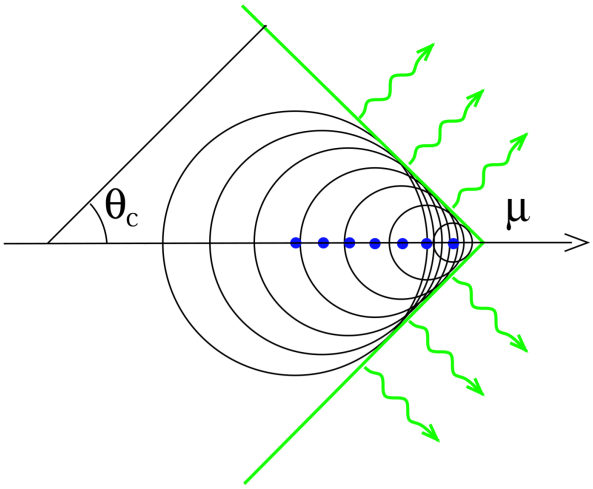

Figure 3.2: Schematic illustration of Cherenkov radiation. Each blue dot is the center of an elemental wave (black circles). If the particle μ propagates faster then the speed of light in this medium a coherent light wavefront forms (green). Adapted from [5].

One can compare the phenomenon of Cherenkov radiation to the sonic boom caused by a supersonic aircraft. The fact, that the aircraft travels faster through the air then the sound waves it produces leads to an appearance of a shock front. Similarly, charged particles propagating through a medium cause the appearance of elemental waves, which form a light front once the particles moves with relativistic speeds (see figure 3.2).

The number of emitted Cherenkov photons per length x and wavelength λ can be described as [53]

$$\frac{d^2N}{dxd\lambda} = \frac{2\pi\alpha z^2}{\lambda^2}\left(1 - \frac{1}{\beta^2 n^2(\lambda)}\right), \tag{3.4}$$

where α is the fine-structure constant and z is the charge of the particle. For ice the Cherenkov spectrum peaks between 350 nm and 400 nm and rapidly decreases for longer wavelengths. The Cherenkov radiation is the most important process in terms of detection, but it only plays a minor role concerning energy loss of particles inside the detector.

3.1.3 Secondary Interactions

As described in equations 3.1 and 3.2, the secondary particles of neutrino interactions are either charged leptons, in the case of a CC interaction, or neutral leptons and in both cases a hadronic part. Depending on the nature of the secondary particles the subsequent processes and therefore the detectable signal can be very different. This section briefly describe the most important processes for these particles (ignoring the neutrino from an NC interaction, since it either leaves the detector without any further interactions or interacts again via CC or NC).

3.1.3.1 Electrons

With a mass of $\approx 511\,\mathrm{keV}$ electrons are the lightest particles among the charged leptons and in this context can be viewed as stable (mean life time $> 6.6 \times 10^{28}\,\mathrm{yr}$, CL=90%) [53]. Ionization and bremsstrahlung are the main processes causing energy losses for electrons propagating through matter. While energy loss through bremsstrahlung rises almost linearly with energy and energy loss through ionization only logarithmically, bremsstrahlung becomes the dominant process at energies above a few tens of MeV. The via bremsstrahlung produced photons can then interact with the surrounding matter and produce electron positron pairs or free electrons via Compton scattering. These particles in turn undergo ionization and bremsstrahlung, as long as the energy is high enough, yielding a so-called electromagnetic cascade or shower. All particles within the shower emit Cherenkov radiation given that their respective energy is above the Cherekov threshold. The longitudinal energy profile can be characterized by the material dependent radiation length X_0, which determines the distance after which the shower energy is reduced to $1/e$. For ice, the characteristic radiation length is $\approx 36\,\mathrm{cm}$ [53], which means, that electromagnetic showers with energies up to serveral TeVs have a typical extension of a few meters. For extremely high-energy electromagnetic showers with primary energies of multiple PeV up to several EeV the extension can grow as large as 100 m due to a decrease of the cross section for bremsstrahlung [60].

3.1.3.2 Muons

Muons are the second lightest charged leptons with a mass of $\approx 106\,\mathrm{MeV}$ and can therefore decay to electrons via,

$$\mu^- \rightarrow e^- + \overline{\nu}_e + \nu_\mu \tag{3.5}$$

with a branching ratio of $\approx 100\%$ and a mean life time of $2.2 \times 10^{-6}\,\mathrm{s}$ [53]. Four different processes are relevant for energy loss of muons propagating through matter, namely ionization, bremsstrahlung, pair production and photonuclear processes [100]. Below muon energies of 1 TeV ionization is the dominant process and although some δ-electrons can be relativistic this process can be seen as quasi-continuous leading to an almost constant radiation of Cherenkov photons along the muon track. With increasing energies the other processes become more and more dominant, meaning that with increasing energy the continuous light from the muon and δ-electrons becomes less important (see figure 3.3). Bremsstrahlung and pair production due to the interaction of the muon with a nucleus cause electromagnetic cascades along the muon track while photonuclear processes yield hadronic cascades. All of these processes have a heavily stochastic nature concerning the location of a process as well as the deposited energy. Two muons with the same energy following the same route through the detector can have very different energy loss patterns.

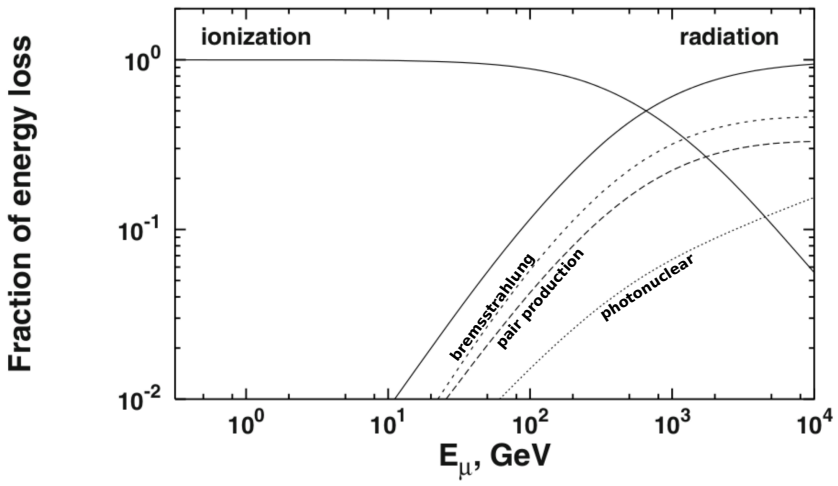

Figure 3.3: Fraction of energy loss for muons propagating through matter as a function of muon energy. Adapted from [100].

High energetic ($E_\mu \gtrapprox 1\,\text{TeV}$) muons can propagate several kilometers before decaying due to time dilatation.

3.1.3.3 Tau Leptons

Tau leptons are the heaviest leptons with a mass of $\approx 1.8\,\text{GeV}$ and the most short-lived with a mean life time of $\approx 290 \times 10^{-15}\,\text{s}$ [53]. Due to their short life times, tau leptons decay almost immediately after they are produced, either yielding hadrons (K's and π's) and a $\overline{\nu}_\tau$ (BR $\approx 65\%$), causing the appearance of a hadronic cascade, or to leptons via

$$\tau^- \rightarrow e^- + \nu_\tau + \overline{\nu}_e \qquad (\text{BR} \approx 17\%), \text{ or} \tag{3.6}$$

$$\tau^- \rightarrow \mu^- + \nu_\tau + \overline{\nu}_\mu \qquad (\text{BR} \approx 17\%). \tag{3.7}$$

The emerged leptons then undergo the processes as described above.
The distance between appearance of a tau lepton and its decay strongly depends on the tau leptons energy with around 50 m at 1 PeV and increasing linearly up to the EeV regime [17]. In between appearance and decay the tau lepton produces an almost continues signature inside the instrumented volume.

3.1.3.4 Hadrons

The radiation length of hadrons in ice is about 91 cm [76]. The dominant process is the interaction with other hadronic particles, e.g. nucleons of the surrounding material, yielding additional hadrons (mostly pions). This leads to the appearance of a hadronic cascade. Compared to an electromagnetic cascade less Cherenkov light is emitted, which is caused by the larger masses of

the created particles ($m(\pi^{\pm}) \approx 140\,\mathrm{MeV}$ [76]) and the possible appearance of neutrons, which don't cause Cherenkov radiation. Furthermore, the elongation of a hadronic cascade is larger than that of an electromagnetic cascade as a consequence of the longer radiation length. In general the stochasticity of hadronic cascades is much larger compared to electromagnetic cascades, due to a bigger variety of possible particles, like π^0, which subsequently lead to an electromagnetic sub-cascade, heavier hadrons or neutrons.

3.2 The IceCube Neutrino Observatory

The IceCube neutrino observatory is a cubic-kilometer scale detector located at the Amundsen Scott South Pole station close to the geographic South Pole [1]. The detector itself consists of an array of photosensors (Digital Optical Modules) buried within the antartic ice, the "In-Ice Detector", and of an array of photosensors at the surface, called "IceTop" [87]. Its construction was finished in 2010 with the deployment of the last photosensors within the ice, making it the largest neutrino detector on Earth. IceCube's primary objective is the detection of astrophysical neutrinos which heavily influenced the detector layout leading to a detector with approximately $1\,\mathrm{km}^3$ of instrumented volume that starts to be sensitive at neutrino energies above 10 GeV [86].

3.2.1 The Digital Optical Module

The central detection unit of IceCube is the so-called Digital Optical Module (DOM). A photograph of an IceCube DOM can be seen in figure 3.4 and a schematic overview is given in figure 3.5. The main part of a DOM is a photomultiplier tube (PMT). In the case of the IceCube DOM this is a Hamamatsu R7081-02 with a photocathode diameter of 25 cm [85]. The PMT is surrounded by a metal grid to shield it from the Earths magnetic field. In order to improve the optical coupling of the PMT to the pressure resistant glass sphere optical gel is poured in between. The high-voltage divider provides the necessary voltages for the dynodes of the PMT and the DOM mainboard and the delay board are responsible for the digitization of the signal and communication with the surface station (for further information see [84]). An LED Flasher Board is included for in-situ calibration and studies of the optical properties of the ice. The penetrator enables the voltage supply and the transmission of data to the surface. In [85] a detailed description of the PMT characteristics and the calibration process before deployment can be found.

3.2.2 The In-Ice Array

The in-ice array of IceCube consists of 5160 DOMs buried in the ice between a depth of 1450 m, and 2450 m instrumenting a volume of approximately $1\,\mathrm{km}^3$ (see figure 3.6) [69]. The DOMs are attached to 86 vertical so-called strings, 60 DOMs per string, including a mechanical support structure and twisted copper-wire pairs. 78 out of 86 strings form a hexagonal footprint on a triangular grid with a horizontal distance of $\approx 125\,\mathrm{m}$ and a vertical spacing of 17 m. The primary

Figure 3.4: Photograph of the last deployed IceCube DOM. Taken from [45].

goal of this part of the detector is the detection of astrophysical neutrinos with energies above 1 TeV.

The remaining 8 strings were deployed in the central region of the in-ice array surrounding string 36. This sub-array, called "DeepCore" (see [86]), was designed to lower the neutrino energy threshold to approximately 10 GeV enabling IceCube to test various models and constrain parameters of particle physics (e.g. [97]) and theories beyond the Standard Model (e.g. [71]). In addition to the smaller horizontal distances the vertical spacing was adjusted for DeepCore and PMTs with a 35 % higher quantum efficiency were used.

3.2.3 The Surface Array IceTop

An extensive air shower array on the surface, directly above the in-ice array, called "IceTop", represents the last part of the IceCube neutrino observatory. IceTop consists of 162 tanks filled with clear ice with two DOMs frozen inside [87]. The tanks are mainly placed on top of the strings of the in-ice array (see fig. 3.6), leading to the same triangular grid with an intermediate distance of 125 m. The central region of IceTop is instrumented slightly denser lowering the

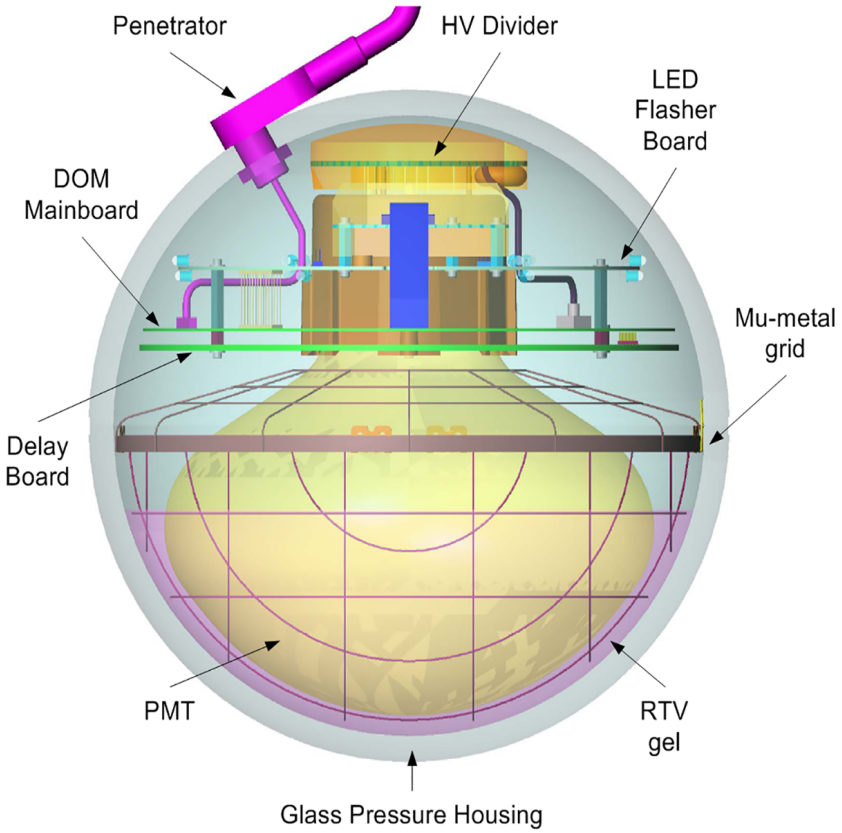

Figure 3.5: Schematic view of the IceCube DOM. Taken from [84].

energy threshold for air showers.
While the surface array was mainly constructed to explore the mass composition of primary cosmic rays, it has been partly used as a veto in order to identify atmospheric background during the search for astrophysical neutrinos.

3.2.4 The Antarctic Ice

A deep understanding of the Antarctic ice is crucial in order to reconstruct any physical parameters of the primary neutrinos given the raw data of the detector. The ice of the South Pole in the depths relevant for IceCube has been formed from compressed snow, which fell tens of thousands of years ago [80]. Air bubbles, which have been trapped in the ice disappeared due to the consistent influence of high pressure, but dust particles carried to the pole by wind are still present in the ice. These impurities mainly determine the strength of scattering and absorption of photons propagating through the ice [61]. The concentration of dust in the ice is strongly correlated to the global climate at that time [80], therefore it is justified to assume, that ice, which has been formed at the same time also has similar optical properties.

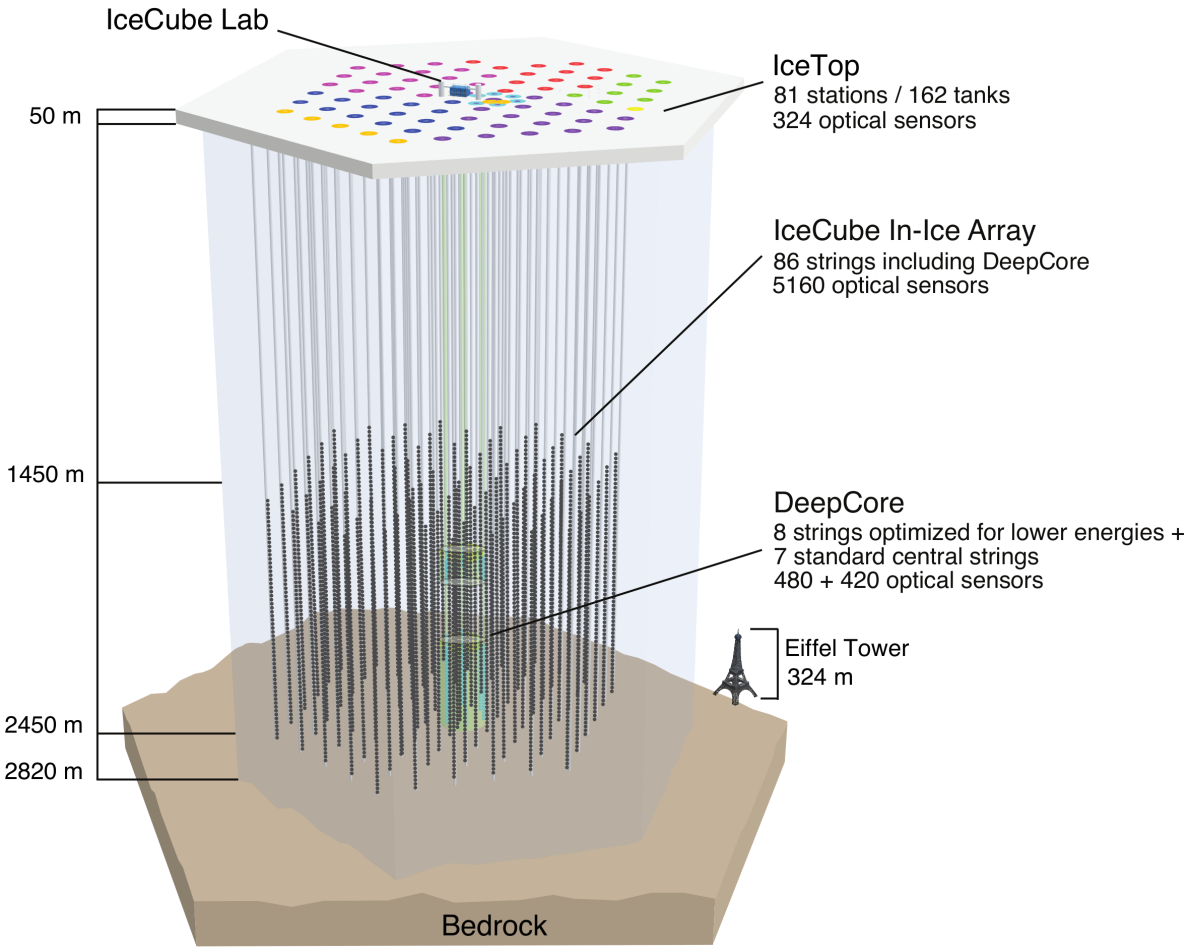

Figure 3.6: Schematic view of the IceCube Neutrino Obeservatory. Taken from [69].

The models used in IceCube parameterize the ice in parallel layers with a width of 10 m [64], including a tilt and an anisotropy [18]. Each layer has its own depth dependent scattering and absorption parameters (see fig. 3.7). In order to determine these parameters the LED flashers inside the DOMs were used to emit photons that neighboring DOMs can detect. Afterwards, simulations are used to simulate the exact same scenarios with different ice parameters until the agreement between detector data and simulations reaches its maximum [61] [64].

3.2.5 Data Acquisition

Once a photon hits a PMT and causes the emission of a photoelectron from the photocathode an amplified electric pulse with amplitudes from mV to V can be measured at the anode. This initial waveform is then digitized using two Analog Digital Waveform Digitization (ATWD) chips running in "ping-pong" mode to reduce dead time and one fast Analog to Digital Converted (fADC) chip. The combination of digitized waveforms of the ATWD and the fADC, called a "DOM launch"

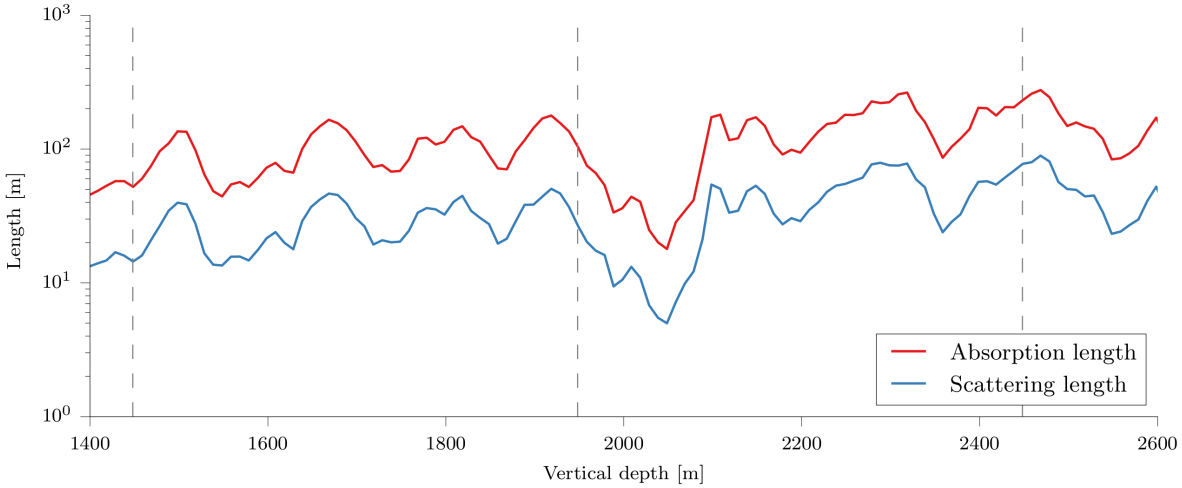

Figure 3.7: Absorption length and effective scattering length as a function of depth. The dashed lines represent the top, center and bottom of the IceCube in-ice array. Figure taken from [105].

[98], is sent to the IceCube Lab on the surface for further processing and represents the "raw" data of the detector.
DOM launches that occur within 1 μs and are not further apart then two DOMs on the same string are called Hard Local Coincident (HLC) launches, while single DOM launches are called Soft Local Coincident (SLC) launches. Most trigger algorithms work on HLC launches motivated by the fact, that interesting events inside the detector produce multiple photons within a confined space. One of these trigger algorithms is the so-called "SMT-8" (Simple Multiplicity Trigger), which fires if 8 HLC launches occur within a 5 μs time window. Once a trigger fires, all recorded waveforms that lie within the trigger time window minus 4 μs and plus 6 μs are calibrated, taking DOM dependent characteristics into account. After calibration single photo electron (SPE) templates are used in order to extract the exact time of arrival of individual photons from the waveforms [66].
All of the information from one event is then stored within one data frame, which is a collection of key-value pairs. Since the amount of data that can be transmitted via satellite to the data warehouse in Madison, WI, is limited, further filtering is done at the pole with various algorithms (see [69] for more details on data acquisition and online filtering) and the files are compressed before transmission.

3.2.6 Event Topologies

In the previous sections an overview of the IceCube neutrino detector was presented including the central detection unit, the DOM, the Antarctic ice and the signal processing chain from detector photons to accessible data in a data warehouse. The next section outlines the most important

event topologies of the IceCube in-ice array and the resolution of the most essential reconstructed physical quantities of these event types.

3.2.6.1 Track-like Events

For a search of neutrino point sources unarguably the most important events are muon induced "track-like" events. An important channel for neutrino astronomy is therefore the CC interaction of a muon neutrino:

$$\nu_\mu + X \rightarrow \mu + Y \tag{3.8}$$

There are other interactions also leading to the production of a muon, like the CC interaction of a tau neutrino with the tau decaying to a muon or the interaction of an electron anti-neutrino with electrons (Glashow resonance [92]) with the resulting W^- boson decaying into a muon and an muon anti-neutrino (branching ratio $\approx 11\,\%$) [95]. In figure 3.8 an event display of a simulated 700 TeV muon propagating through the detector is shown.
Since high-energy muons can propagate through the whole instrumented volume and continuously cause light emission, track-like events yield the best angular resolution of all event types in IceCube. One has to distinguish between starting track events, which have their primary neutrino interaction within the instrumented volume, and through-going events where the primary interaction is outside the detector. The latter naturally leads to better angular resolution, simply because the muon track within the detector is longer which leads to a larger lever arm. The angular resolution for both types of track-like events is displayed in figure 3.9 along with the kinematic angle (the angle between the direction of the primary neutrino and the secondary muon) which marks a natural lower boundary.
Reconstructing the energy of track-like events is only possible to a certain limit once the energy of the particle exceeds 100 GeV, since most of its energy will be deposited outside the vicinity of the detector [66]. One strategy is to reconstruct the deposited energy inside the instrumented volume, which results in a lower bound of the true energy. Above a muon energy of 1 TeV however, the average energy loss rate of muons, dE/dx increases approximately linearly with the muon energy[76]. Nevertheless, the increasing fraction of energy loss due to bremsstrahlung, pair production and photonuclear processes (see sec. 3.1.3.2) and the high stochasticity of these processes cause large fluctuations of the actual deposited energy within IceCube of muons with the same energy [66]. The achievable resolution for reconstructed muon energy for through-going events is shown in figure 3.10.

3.2.6.2 Cascade-like Events

The second event class of IceCube are so-called "cascade-like" or "shower-like" events. This event topology is caused by electron neutrino CC interactions, causing an electromagnetic cascade (see sec. 3.1.3.1) or neutrino NC interaction leading to a hadronic cascade (see sec. 3.1.3.4). In both

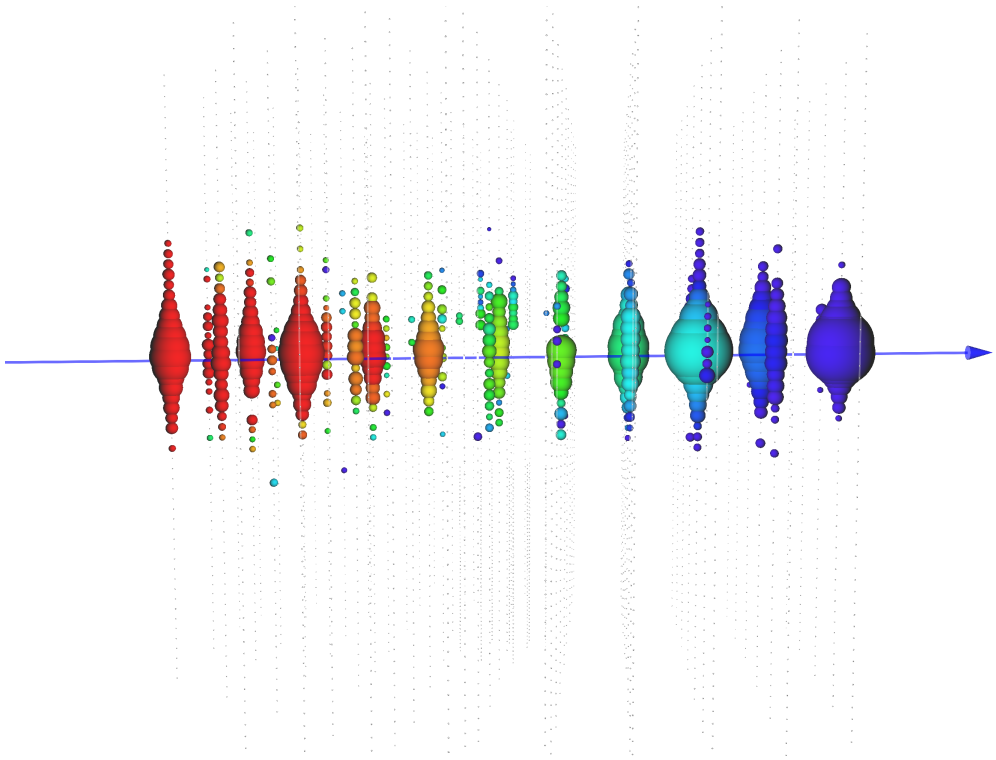

Figure 3.8: Event display of a simulated muon track with an energy of approximately 700 TeV. Each "bubble" represents a DOM, the size of a bubble encodes the collected charge while the color code illustrates the time (red: early hits, blue: late hits). The track of the muon is displayed as blue solid line.

cases these event types are characterized by their strong spatial confinement compared to track-like events (see figure 3.11), which also leads to very different results concerning reconstruction. The appearance of lots of light emitting paricles in a particle shower and their short interaction lengths (see section 3.1.3.1 and section 3.1.3.4) makes it extremely difficult for the reconstruction algorithms to map the detected light to a specific particle with a certain direction, thus leading to a reduced angular resolution. Figure 3.12 displays the angle between reconstructed direction and true direction as a function of energy for cascade-like events in IceCube. While at energies above 1 TeV the median angular error goes below 1° for track-like events it is only just below 10° at 100 TeV for cascade-like events. Even at extremely high energies above 1 PeV and more, the angular resolution for cascades does not go into the sub degree regime, making this event type effectively unusable for point source searches.

The spatial confinement is disadvantageous for directional reconstruction but helps to reconstruct the deposited energy since the whole event takes place within the vicinity of the instrumented volume (given that the primary interaction is not too close to the edge of the detector). Figure 3.13 shows the resolution of the reconstructed energy of cascade-like events in IceCube. It can

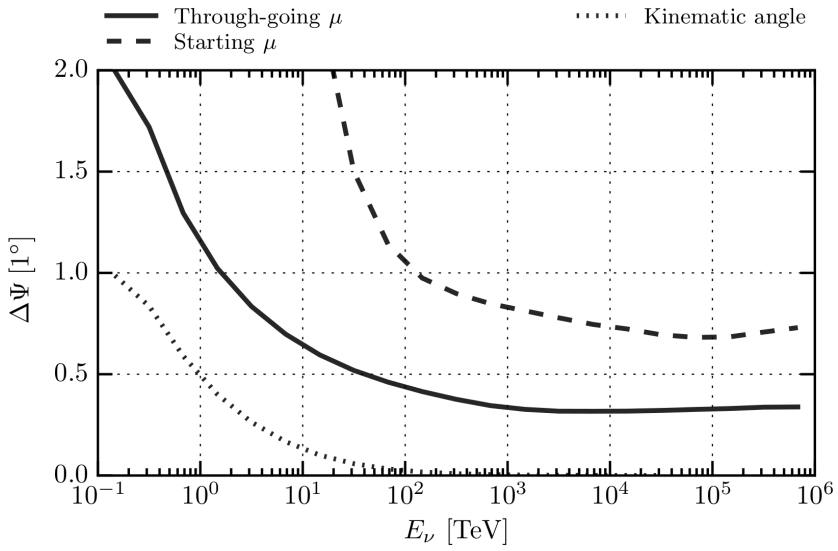

Figure 3.9: Median angular resolution of IceCube versus neutrino energy calculated with Monte Carlo simulations. The dashed line shows the resolution for starting tracks, the solid line for through-going muons and the dotted line shows the kinematic angle. Taken from [68].

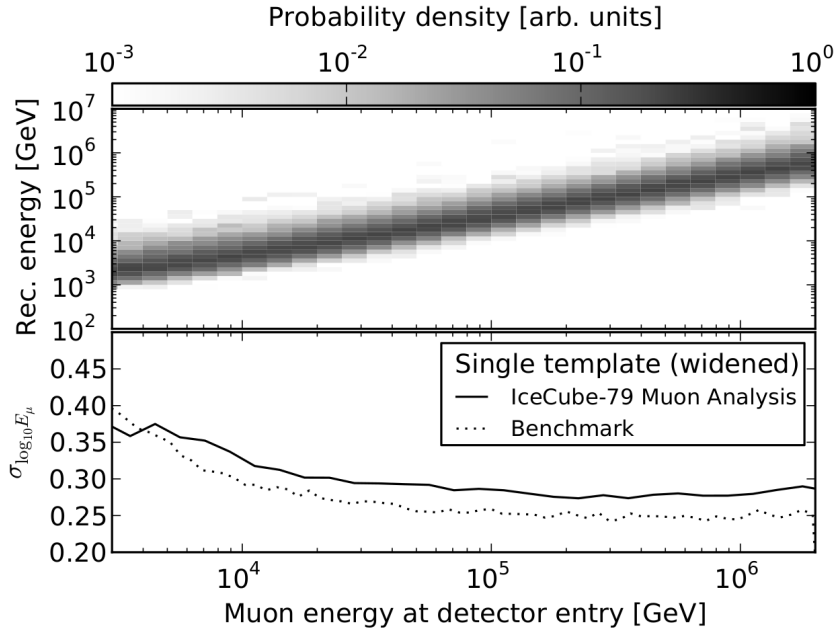

Figure 3.10: *Top*: Resolution of the reconstructed muon energy at the detector entry of IceCube. *Bottom*: Standard deviation for each bin. Taken from [66].

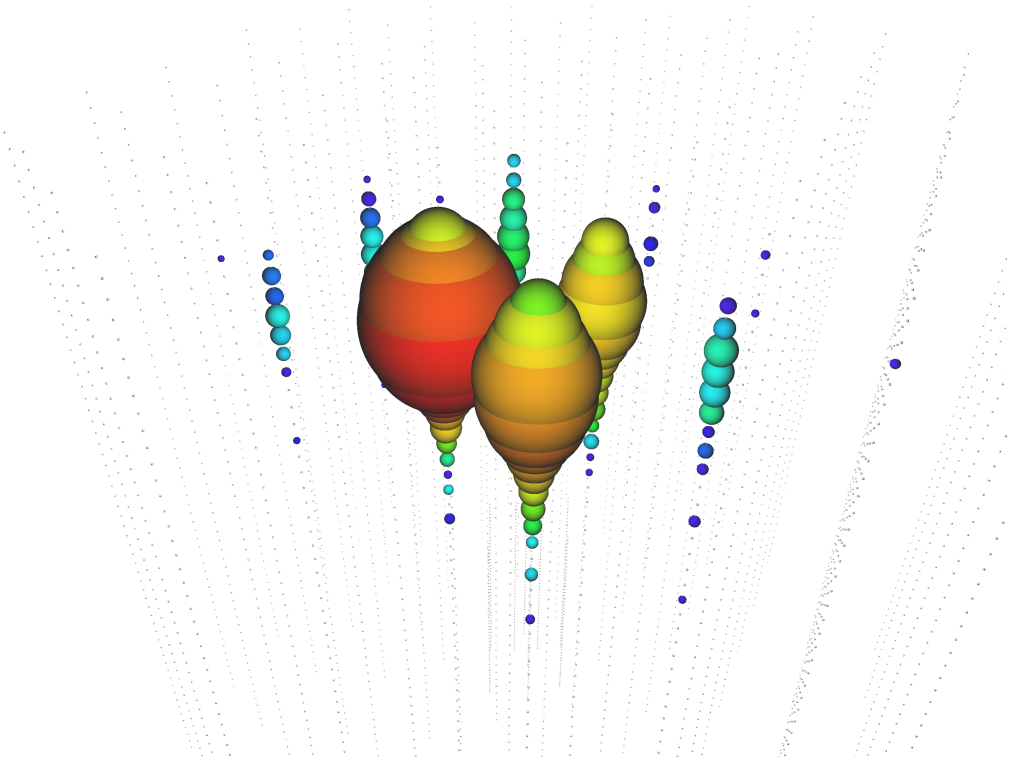

Figure 3.11: Event display of a simulated ν_e interaction causing a 900 TeV electromagnetic cascade in IceCube.

be seen, that the mean energy resolution is below 10 % over the whole displayed energy range, except for the very first bin.
These properties make cascade-like events valuable event types for analyses of the diffuse neutrino flux. The good energy resolution helps reducing the number of low energetic background events from the data sample, while the larger amount of cascade-like neutrino events increases the signal to background ratio even further.

3.2.6.3 Double Bang

The event topology named "Double Bang" (see the event display in figure 3.14) represents another neutrino induced event topology. Such an event has not been identified yet, since it is only caused by ν_τ CC interactions and in order to clearly separate the two cascades primary energies of ≈ 10 PeV and above are required [17]. At lower energies ν_τ CC interactions become more and more similar to cascade-like events, which increases the difficulty of identifying such an event. The first cascade is caused by the hadronic byproduct of the initial neutrino interaction and the second cascade is caused by the decay of the tau lepton into an electron (plus neutrinos) which produces an electromagnetic shower. This event type does neither play an important role for point source searches nor for the analysis of the diffuse neutrino flux mainly due to its rarity.

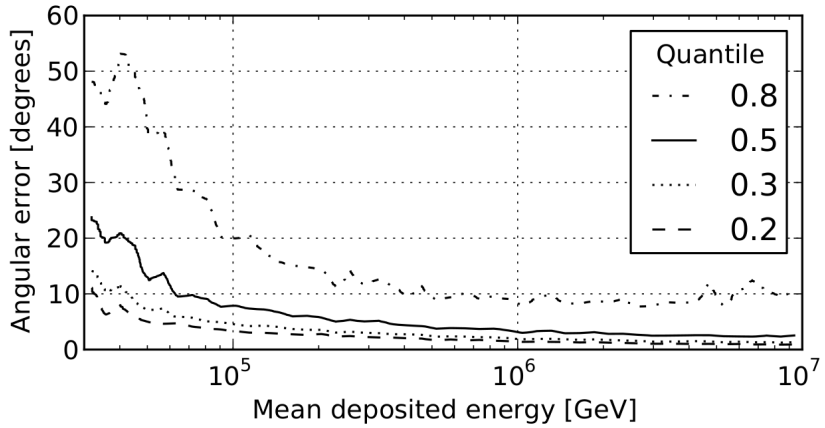

Figure 3.12: Angular resolution for electromagnetic cascades as a function of energy in IceCube. Taken from [66].

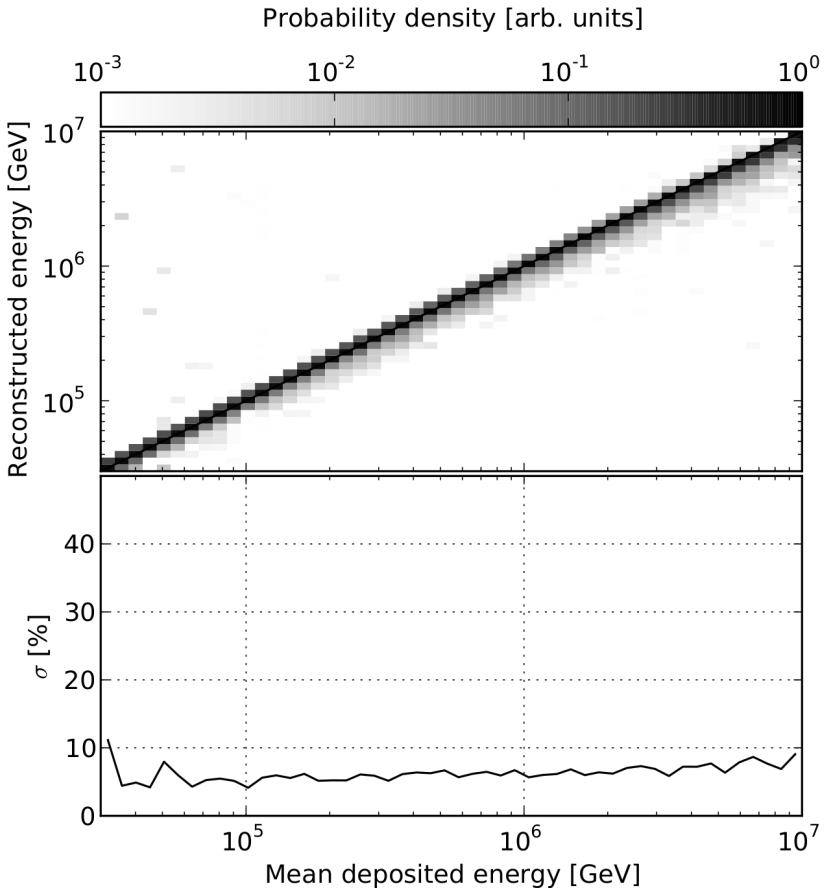

Figure 3.13: Reconstructed energy versus the mean deposited energy of electromagnetic cascades in IceCube. Taken from [66].

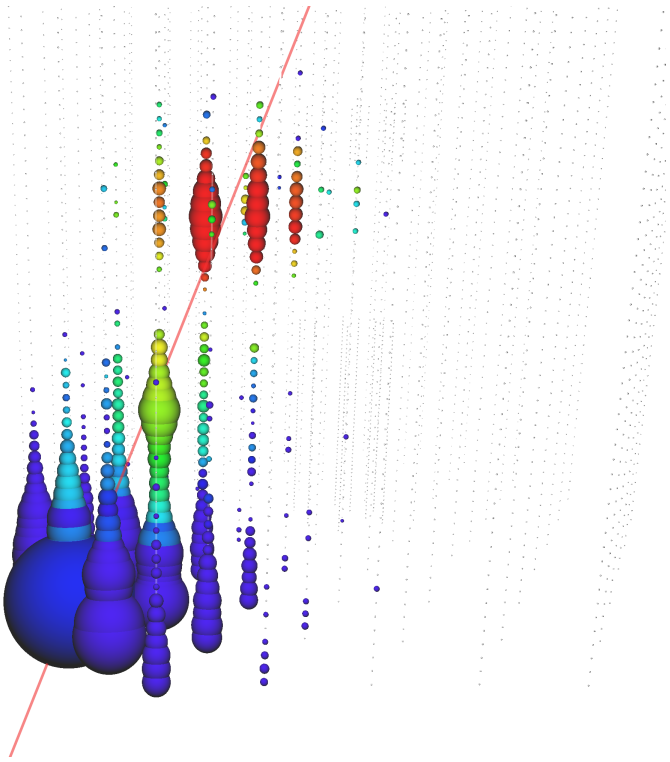

Figure 3.14: Event display of a simulated so-called "double bang" event in IceCube. The first cascade is caused by the primary neutrino CC interaction and the second cascade by the decay of the tau lepton. The original neutrino direction is indicated by the solid red line (from top to bottom).

3.2.7 Discoveries & Upper Limits

The first major discovery of IceCube was the detection of a high-energy extraterrestrial diffuse neutrino flux in 2013 [63]. For this analysis only high-energy starting events (HESE) were taken into account, so events with the primary interaction within the instrumented volume, away from the outer layers of the detector and with at least 6000 detected photoelectrons, thus reducing atmospheric background significantly. The final data sample contained 28 events, 21 cascade-like events and 7 track-like events, and was inconsistent with an atmospheric background at the 4σ level. This analysis has been updated in the meanwhile, including 2078 days of detector lifetime, which increased the final data sample to 80 events leading to a significance of more then 6σ [14][23]. Figure 3.15 shows the events from this analysis as well as expected background events. Assuming an unbroken power-law spectrum, $E^{-\gamma}$ of the astrophysical neutrino flux, the best fit yields a spectral index of $-2.92^{+0.33}_{-0.29}$.
A different approach was used in [19] where through-going and starting muons from charged-current muon neutrino interactions have been used. The advantage of this approach is a much larger effective area compared to the HESE analysis which leads to a larger final data sample.

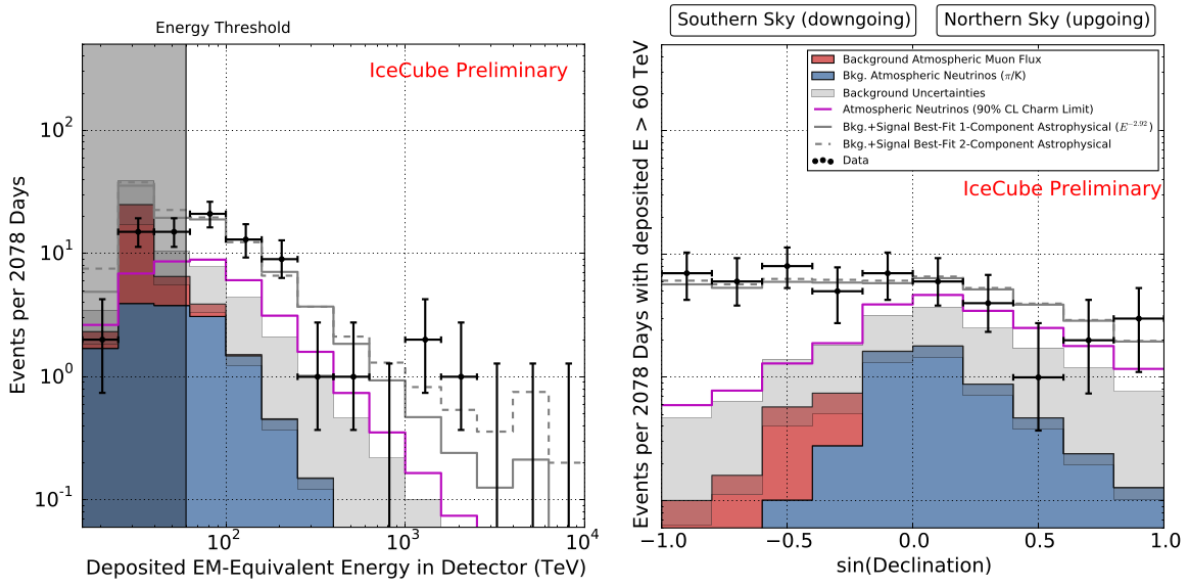

Figure 3.15: Deposited energy (left) and arrival direction (right) vs. observed and expected events. Background contribution from atmospheric muons is shown in red, background contribution from atmospheric neutrinos is shown in blue with an 1σ uncertainty displayed as the gray band. The magenta line is the 90% CL upper limit of the charm component of atmospheric neutrinos (prompt neutrinos). The gray lines show the best-fit astrophysical spectra assuming an unbroken power-law model, where the solid line assumes a single power-law model and the dashed line assumes a two-power-law model. Taken from [14].

The best-fit spectral index of this study assuming an unbroken power law is $-2.19^{+0.26}_{-0.23}$, indicating a much harder spectrum compared to the HESE analysis, although both results are within a 2σ range. A comparison of the best-fit results obtained by these two studies can be seen in figure 3.16. The seemingly large differences of the two best-fit spectral indices give reason to assume a break in the power-law spectrum. A statistical test probing a two power-law spectrum conducted in [14] yielded a p-value of 37%. If the the astrophysical neutrino flux follows indeed a more complex model then an unbroken power-law, much more data is needed to prove this with a high significance.

A recent breakthrough was the identification of the first possible neutrino point source, the blazar TXS 0506+056, at the 3σ level in 2018 [72]. This analysis was prompted by the detection of a high-energy neutrino event detected by IceCube in September 2017, whose reconstructed direction and time are coincident with a gamma ray flare of the blazar. Analyzing the IceCube data from the previous 9.5 years, an excess with respect to the atmospheric background at that position was found between 2014 and 2015. Under the assumption of a time-variable flux this yields to an independent significance of 3.5σ.

A different study investigating eight years of IceCube data conducting a time independent search

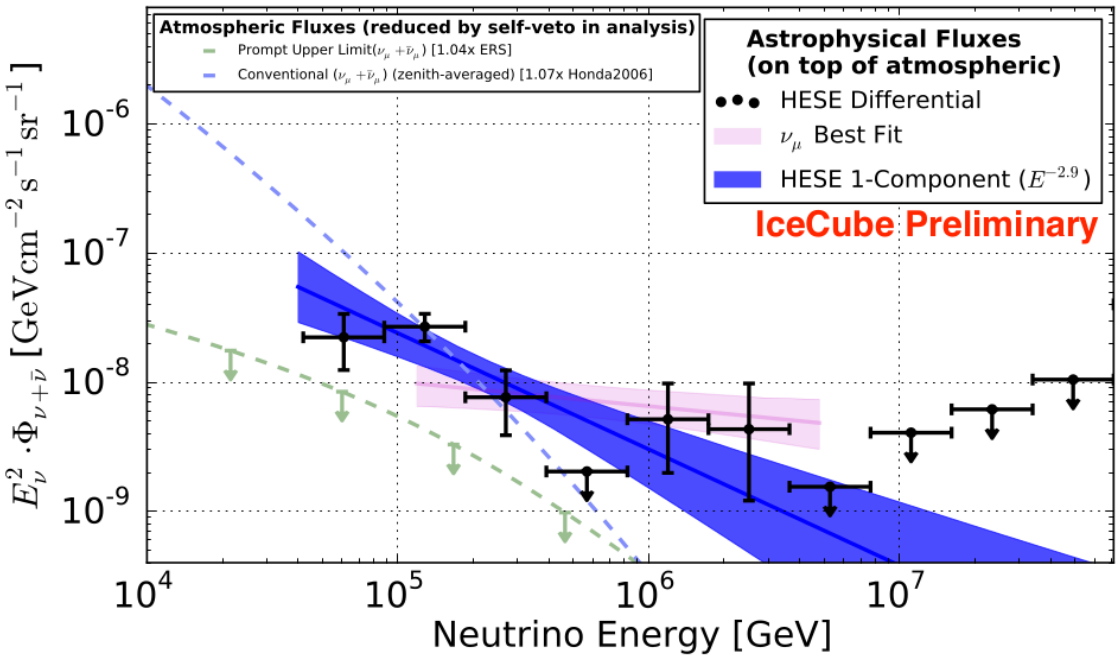

Figure 3.16: Best-fit per-flavour (neutrino and anti-neutrino combined) neutrino flux results vs. neutrino energy. The black points are obtained with a combined likelihood fit to all background components and an astrophysical flux using the events from the 6 year HESE analysis ([14]). For each energy band a normalization has been fit independently assuming an E^{-2} spectrum. The error bars indicate a 1σ uncertainty. The dashed blue line shows the best-fit conventional atmospheric neutrino flux and the dashed green line marks the best-fit upper limit of a prompt atmospheric neutrino flux. The pink band shows the 1σ uncertainty of the best-fit result of the through-going and starting muon neutrino analysis from [19] and the blue band shows the 1σ uncertainty of the best-fit results from the six year HESE analysis. Taken from [14].

for neutrino point sources was published later in 2018 ([73]). However, no new evidence for neutrino sources could be identified, but it was possible to increase the sensitivity and discovery potential of IceCube compared to previous studies (see figure 3.17).

With TXS 0506+056 being the only identified neutrino source up to date, the origin of more then 99 % of the observed astrophysical neutrino flux remains uncertain [73].

3.3 IceCube-Gen2

The major limitations of IceCube is its limited size of approximately $1\,\mathrm{km}^3$, which affects the number of detected events and angular resolution of track-like events (due to the maximal length of the lever arm). An improvement of both, size and angular resolution would go hand in hand in order to increase the detector's sensitivity for point sources. Therefore the IceCube Collaboration has been working on plans for the next generation upgrade of the IceCube detector

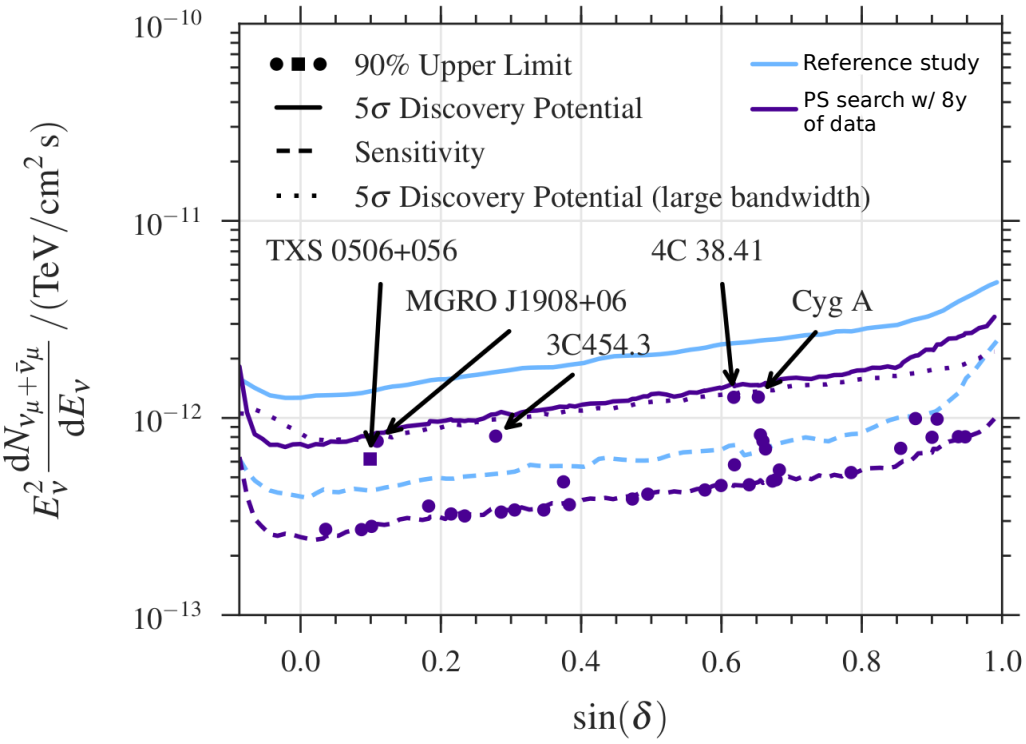

Figure 3.17: Sensitivity (dashed lines) and 5σ discovery potential (solid lines) for the neutrino flux normalization at 100 TeV assuming an E^{-2} unbroken power-law spectrum versus the sinus of the declination (δ). The magenta lines show the results from [73] and the cyan lines are from [68]. The dots and squares mark the 90 % CL upper limit on the flux normalization of various sources probed in [73] including TXS 0506+056 (square marker). Adapted from [73].

called IceCube-Gen2. IceCube-Gen2 has been the topic of active research for several years now. Keeping the obtained results from IceCube, various γ-ray telescopes and other astroparticle and particle physics experiments in mind, the current visions for IceCube-Gen2 includes not only a larger IceCube like detector, but also extensions towards the lower energies and various surface arrays [49]. For this thesis, however, only the upgrade of the in-ice array, called the IceCube-Gen2 high-energy array, and its implications towards neutrino point source sensitivity will be discussed. Other scientific goals for the upgrade are discussed in detail e.g. in [67] and [49].

In this section the motivation for the IceCube-Gen2 high-energy array concerning the identification of neutrino point sources, a potential layout as well as two possible new designs for the optical modules will be introduced.

3.3.1 Increasing the Discovery Potential for Neutrino Point Sources

The most limiting factor of IceCube, with regards to the identification of neutrino point sources, is its limited number of detected track-like events. The quantity directly connected to the number of detected track-like events is the so-called effective muon area, which is the product of an energy dependent efficiency (for more details see section 6) and the geometric area of the instrumented volume. An enlargement of the geometric area while keeping the efficiency high, therefore has a direct effect on the number of detected events.
Another important factor is the angular resolution of the detector, which is influenced on the one hand by the length of a track within the instrumented area (lever arm) and potentially the spatial distribution of the photocathode area. Several new concepts of optical modules proposed for the high-energy array incorporate this idea. Probing whether this effects the angular resolution of track-like events in a proposed detector design and therefore the sensitivity towards neutrino point source identification, is the main topic of this thesis.

3.3.2 Potential Layout

While the geometry of the high-energy array has not been finalized yet, one potential layout called "Sunflower 240 m" has been used for most studies including this thesis. The "footprint", the horizontal coordinates with respect to a coordinate system centered in the IceCube in-ice array is displayed in figure 3.18. This layout consists of 122 accessory strings arranged around the existing IceCube detector with an average horizontal spacing of 240 m. The arrangement of the Gen2 strings into a spiraled geometry prevents muons from traversing through the whole detector without getting close to any DOMs. Additionally the instrumented depth has been increased by 240 m leading to an even further enlargement of the instrumented volume (see figure 3.19). Throughout this thesis events have been simulated with 80 DOMs per Gen2 string with a vertical spacing of 17 m. This leads to a total of 9760 additional DOMs as part of the Gen2 high-energy array when this geometry layout is used.
Compared to IceCube, this geometry increases the instrumented volume by almost a factor of 10 [49]. The gain in regards to muon effective area from earlier sensitivity studies for different muon energies as a function of the zenith angle is shown in figure 3.20.

3.3.3 The "PINGU Digital Optical Module" (PDOM)

As mentioned above, apart from the extension of the instrumented volume new optical modules could have potential of further increasing the sensitivity. The baseline DOM design for the high-energy array is the PINGU DOM (PDOM), which is essentially the IceCube DOM (see 3.2.1) equipped with a high quantum efficiency PMT, and some internal hardware upgrades (for more details on the differences see [81]). The IceCube DOM design has been proven to work reliably under the extreme conditions of being frozen within the glacial ice of the South Pole for almost

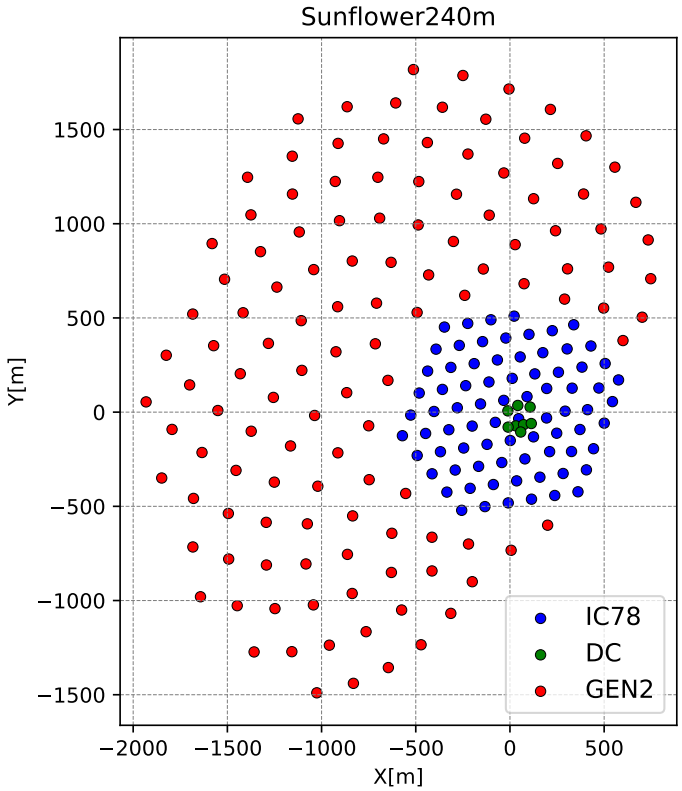

Figure 3.18: Footprint of the "Sunflower 240 m" layout, a potential geometry for the IceCube-Gen2 high-energy array. The blue dots represent the position of the existing IceCube in-ice array, the blue green dots mark the Deep Core sub array and the red dots would be the position of additional strings.

10 years with only very few technical problems, therefore the reutilization of this design seems only reasonable.

3.3.4 The "multi-PMT Digital Optical Module" (mDOM)

Inspired by the design of the KM3NeT DOM [6], a multi-PMT Digital Optical Module (mDOM) design is currently being investigated to be used in the IceCube-Gen2 high-energy array [59]. A picture of the current mDOM design is displayed in figure 3.21. The mDOM consists of 24 3" PMTs almost equally distributed within a pressure resistant glass sphere. Each PMT is surrounded by a reflector made out of a thin sheet of highly reflective material. This does not only improve the photon collection area of each PMT, but also improve the directionality of each PMT, being more sensitive to photons arriving from the front, with respect to a PMT's symmetrical axis, then from the side. The additional information provided by the fact that each PMT looks

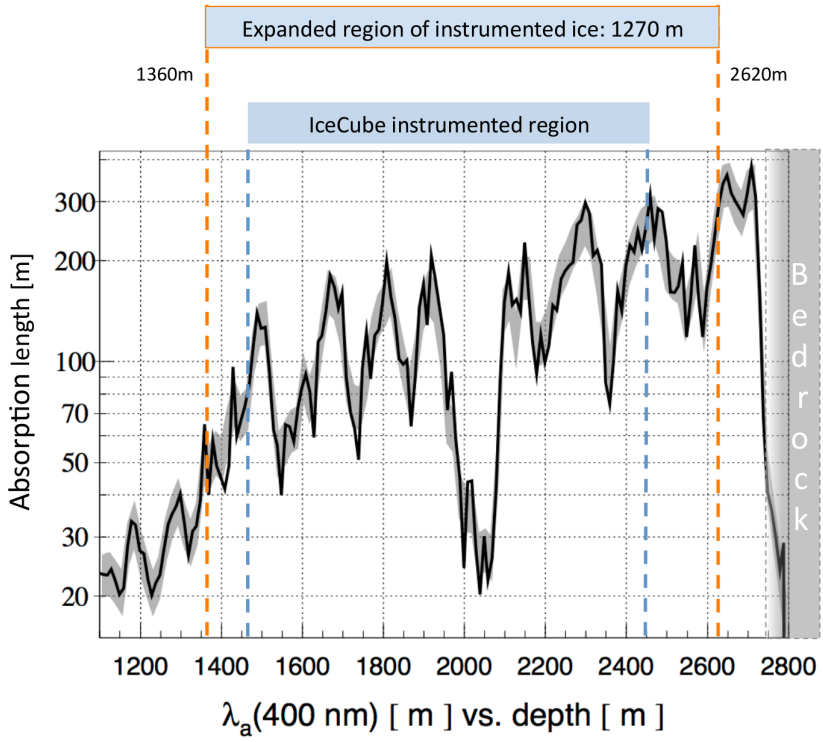

Figure 3.19: Absorption length versus depth. The instrumented string depth of IceCube and the extended string depth proposed for the IceCube-Gen2 high-energy array are indicated. This extension leads to an additional 240 m per string for Gen2. Taken from [67].

into a different direction turns out to be valuable in regards of reconstruction (see section 5). Between the pressure vessel and the PMTs a transparent gel is poured in which improves the optical coupling. A direct comparison of the mDOM and PDOM is shown in figure 3.22. In this plot the effective area, so the geometric photocathode area times the efficiency of detecting a photon was simulated with Geant4 [89] over the whole solid angle [59]. It can be seen, that the mDOM provides an almost uniform sensitivity while the PDOM is only sensitive to photons from below. Integrated over the whole solid angle, the effective area, including the quantum efficiency spectra, of one mDOM is about 2.2 times larger compared to the PDOM [59]. Naturally, these features increase the price per module significantly. At the time of this writing, the costs per mDOM are not final, since the decision on various parts has not been made yet.

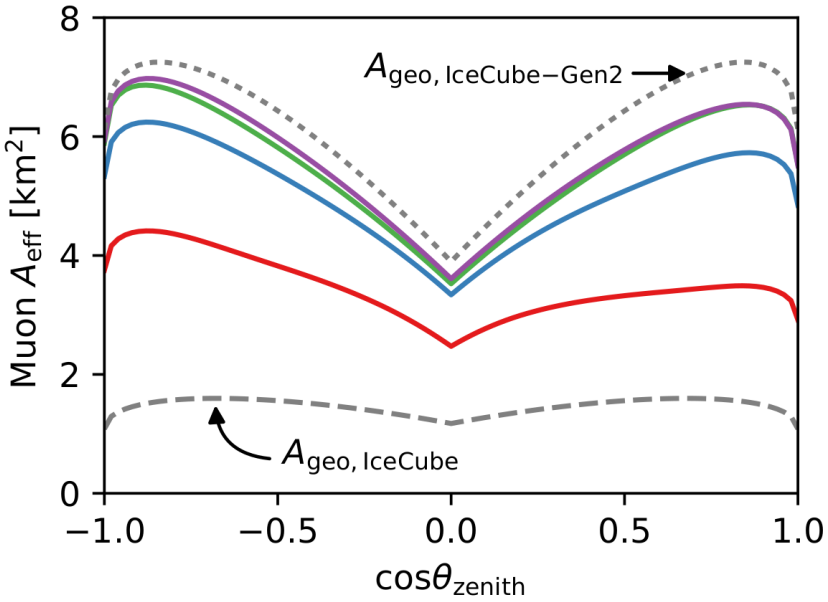

Figure 3.20: Effective muon area for different muon energies at the border of the high-energy array. Red: 10 TeV, blue: 100 TeV, green: 1 PeV and purple 10 PeV. For these results all Gen2 strings were equipped with PDOMs (see 3.3.3). For more details see [49]. Taken from [49].

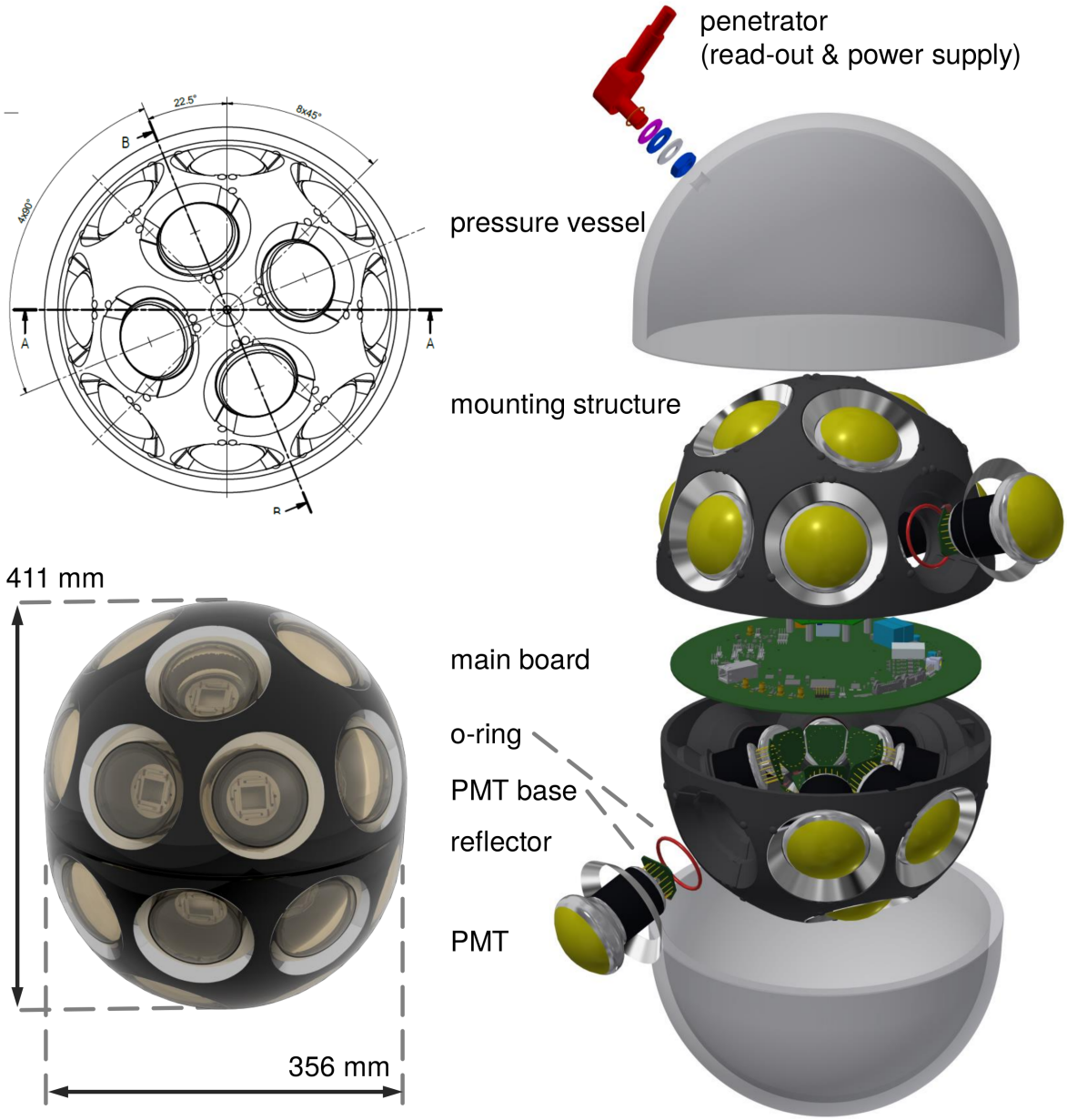

Figure 3.21: Current design of the multi PMT Digital Optical Module (mDOM). *Top left*: Top view technical drawing. *Bottom left*: artistic rendering of the closed module. *Right*: Explosion view exposing the internal design and the main components. Taken from [59].

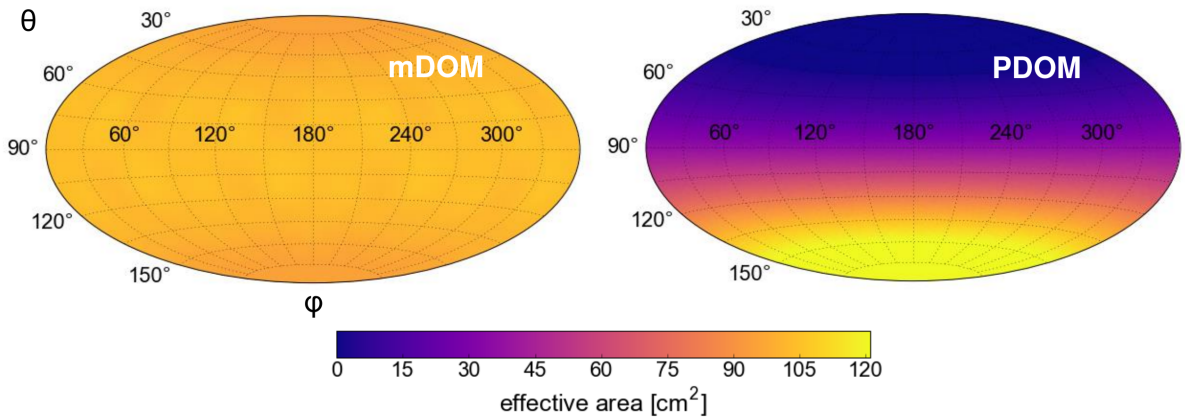

Figure 3.22: Simulation of the effective area of the mDOM (left) and the PDOM (right) with Geant4. A plane wave front of photons with 390 nm was simulated from various directions. Taken from [59].

CHAPTER 4

MUON SIMULATION

This chapter will outline the various steps of the simulation process, which was utilized to obtain the muon datasets used in this thesis. Similar to an actual experiment, it is essential to understand and verify each part of the simulation chain in order to ensure that derived results are trustworthy and not caused by any unintentional behavior. While the code necessary for simulating the detector response to various physical events was already available when this study started, most of the software that had been written for IceCube included only standard IceCube DOMs. In order to be able to reuse most of the code, adaptions to incorporate the features of the mDOM were necessary. Consequently, part of this thesis was to ensure the correct and intended behavior of every part of the simulation process and, if necessary, to correct errors or adjust parameters. The ideas and results of these sanity checks will also be presented in this chapter. The final part contains the properties of the produced datasets of through-going muons for the Gen2 high-energy array.

4.1 The Simulation Chain

This section describes the respective steps of the simulation process, also called simulation chain, in detail. In figure 4.1 a flow chart[1] summarizing the whole process is displayed. Each rectangle (green) represents a process, or in some cases a collection of processes when it makes sense to view them as one entity. Every process has an input and an output, illustrated as a blue parallelogram (omitted when the data type does not change for the sake of clarity). The red triangles do what their respective label reads: the first one splits the data into IC86 (IceCube in-ice array including DeepCore) and Gen2 (high-energy array), and the second triangle merges the data streams back

[1] This flow chart is not designed to include every technical detail of the simulation chain, therefore does not follow all rules normal data flow charts describing software would, but is just meant to provide an overseeable summary.

together. The necessity of this step will be explained below.
The simulation chain can be split into four logical parts, muon generation and propagation (orange box), photon propagation (dark blue box), detector response simulation (purple box) and base processing (red box). Each of these parts will be described in one of the following subsections.

4.1.1 Muon Generation & Propagation

The first step (orange box in figure 4.1) of the simulation is the initial generation of particles and their propagation including interactions with the surrounding material. In IceCube it is common to decouple these steps and use one tool for generation and another tool for the respective propagation. In figure 4.1 this step is represented as the first green rectangle with the label "MuonGun & PROPOSAL", where MuonGun [105] is a particle generator and PROPOSAL (Propagator with optimal precision and optimized speed for all leptons) [47] is a lepton propagator.

4.1.1.1 MuonGun

Muons created in the atmosphere are the most common event type detected by large underground neutrino detectors like IceCube, therefore, an accurate simulation of this event type is important. The full simulation of extensive cosmic ray induced air showers with tools like CORSIKA [36] is possible, but expensive with respect to computational resources and does not necessarily yield muons reaching the vicinity of the instrumented volume. Thus, the simulation of atmospheric muon background with sufficient statistics can be very time consuming.
An alternative approach for the production of muon simulations is to parameterize the muon flux at the detector and start the simulation of muons and muon bundles at that point, omitting the simulation of the whole air shower and the propagation of the muons to the detector. This idea was first realized by MUPAGE [15], a tool heavily used by the ANTARES collaboration and then adapted by the IceCube collaboration in the form of MuonGun [105].
The functionality of MuonGun is to inject muons[2] at the surface of a volume surrounding the detector (see figure 4.2). Angular and energy distributions of the injected muons are determined according to a previously defined muon flux. As indicated by the blue parallelogram in figure 4.1, MuonGun needs the parameters of the injection volume as well as the angular and energy distribution of the desired muon flux as input. MuonGun then returns a collection of corresponding muons positioned at the surface of the injection volume. This list is then passed to PROPOSAL as input (omitted in the flow chart).

[2]MuonGun is capable of injecting single muons as well as muon bundles. Since simulations needed for this work only require single muons, simulation of muon bundles will not be discussed.

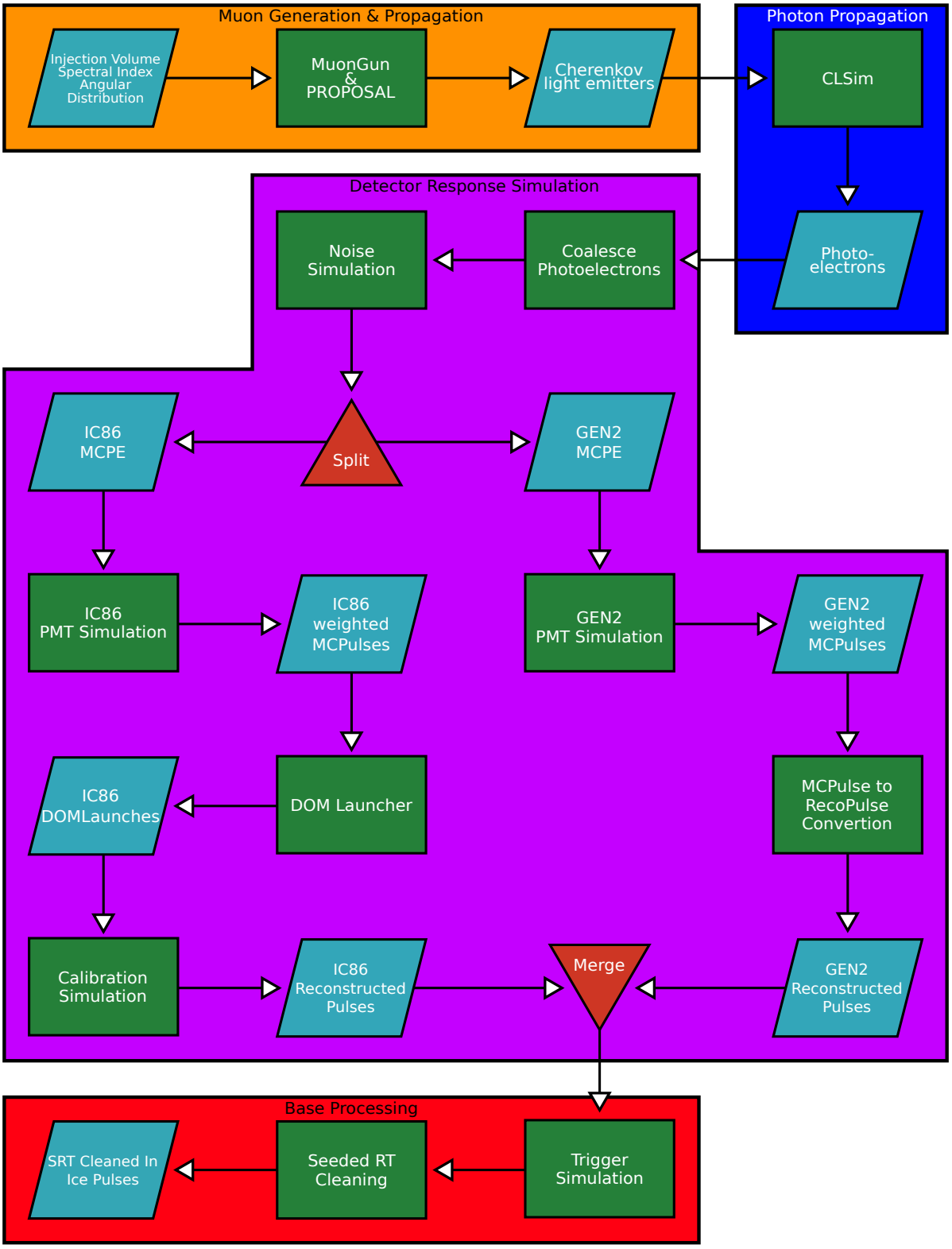

Figure 4.1: Flow chart of the whole simulation chain.

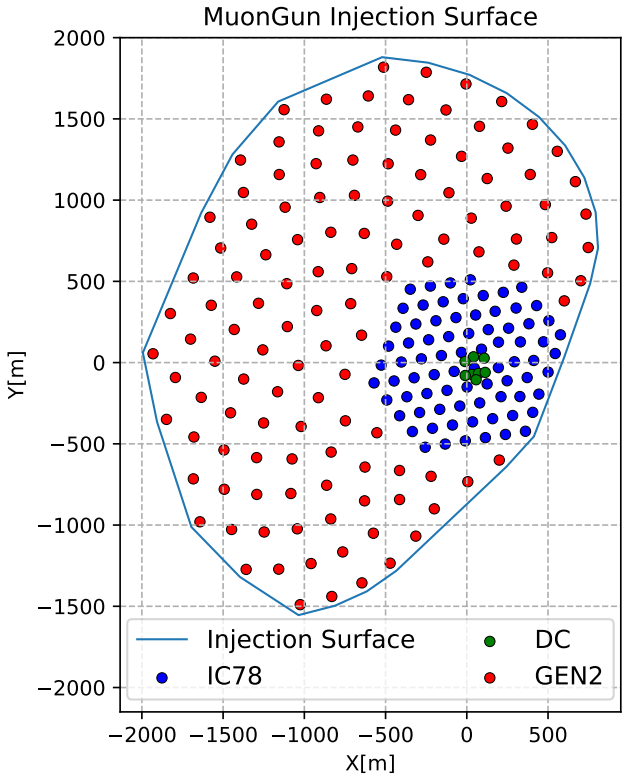

Figure 4.2: Top view of the injection surface used by MuonGun surrounding the Sunflower 240 m geometry of the Gen2 high-energy array. The blue line shows the outline of the polygon used as base area for the injection volume, which is a right prism with a vertical extension from -801 m to +664 m (in IceCube coordinates).

4.1.1.2 PROPOSAL

PROPOSAL [47] is a Monte Carlo based algorithm capable of simulating the propagation of electrons, muons and taus through transparent media like ice or water. For muon propagation PROPOSAL includes ionization, bremsstrahlung, photonuclear interactions, pair production and muon decay.

Within the context of this work, PROPOSAL takes a list of muons as input, propagates each muon through a cylindrical volume surrounding the detector, either until it leaves this volume, its energy falls below a certain limit or it decays. During this process the muon can undergo several interactions (pair production, bremsstrahlung, etc.) thus, creating new particles. Each of these secondary particles can undergo interactions by themselves, creating again new particles. For each muon propagated, PROPOSAL returns a collection of interactions including the respective type, position, time, direction and energy. This list is then passed to the next module in line,

which is responsible for simulating and propagating Cherenkov light in the ice.

4.1.2 Photon Propagation with CLSim

CLSim [13] is a simulation software tool utilizing OpenCL and capable of tracking single photons which are propagating through a transparent medium. CLSim broadly uses three different stages. The first stage is to generate the Cherenkov photons from a given source. Potential sources are electrons, muons, and tau leptons or artificial particles like a hadronic shower or an electromagnetic shower. In order to do so, CLSim is converting particles into a series of light-emitting "steps". Each of these steps is assumed to have a constant speed, Cherenkov angle and number of photons that should be emitted over the length of the step. The conversion from particles to steps can be done via Geant4, a full particle simulation, or parameterized functions. Since Geant4 gets rather slow with energies above 10 TeV, only the parameterized functions were used in this work. Once a series of steps has been generated, the amount of actually emitted photons is sampled and each photon is given a random azimuth angle (relative to the direction of the respective step).
After the photons have been generated, the next step is to propagate these photons through the surrounding medium, either until they collide with a DOM or until they are absorbed by the ice. For every photon, which has not been absorbed or collided with a DOM, the distance to the next scattering point is sampled. The range of this distance depends on the wavelength of the photon and the scattering coefficient of the surrounding material, both of which are taken into account by CLSim. The next position of the photon is set to be the next scattering point, unless a DOM is positioned in between the current position and the next. If this happens to be the case, the next position of the photon is set to be the intersection point of the photon and the DOM. DOMs are approximated as perfectly spherical, which is a good approximation for the IceCube DOM and the PDOM, both of which are simulated with a radius of $R_{\text{IceCube DOM}} = R_{\text{PDOM}} = 16.5\,\text{cm}$. It is a more coarse approximation for the mDOM, which has a cylindrical part at its horizon. For the mDOM a radius of $R_{\text{mDOM}} = 17.8\,\text{cm}$ has been used.
The next step is to decide whether the photon is absorbed before it reaches its next position. This is done by calculating the absorption probability using the material and wavelength dependent absorption coefficient. If the photon is absorbed, it is dismissed, if it reaches a DOM its current position, direction, time, wavelength and history are stored for further processing. If neither of the above is the case, position and time of the photon are updated and scattering of the photon is simulated. This is implemented by drawing a scattering angle from an internal distribution and changing the photons direction accordingly. This procedure is repeated until no photons are left to propagate.
The algorithm is capable of handling media with heterogeneous optical properties. In IceCube the parameterization of the glacial ice is usually realized in the form of tilted parallel ice layers including an anisotropy. For this work, however, a homogeneous ice model without anisotropy is used for all simulations. The necessity for this simplification will be discussed in chapter 5

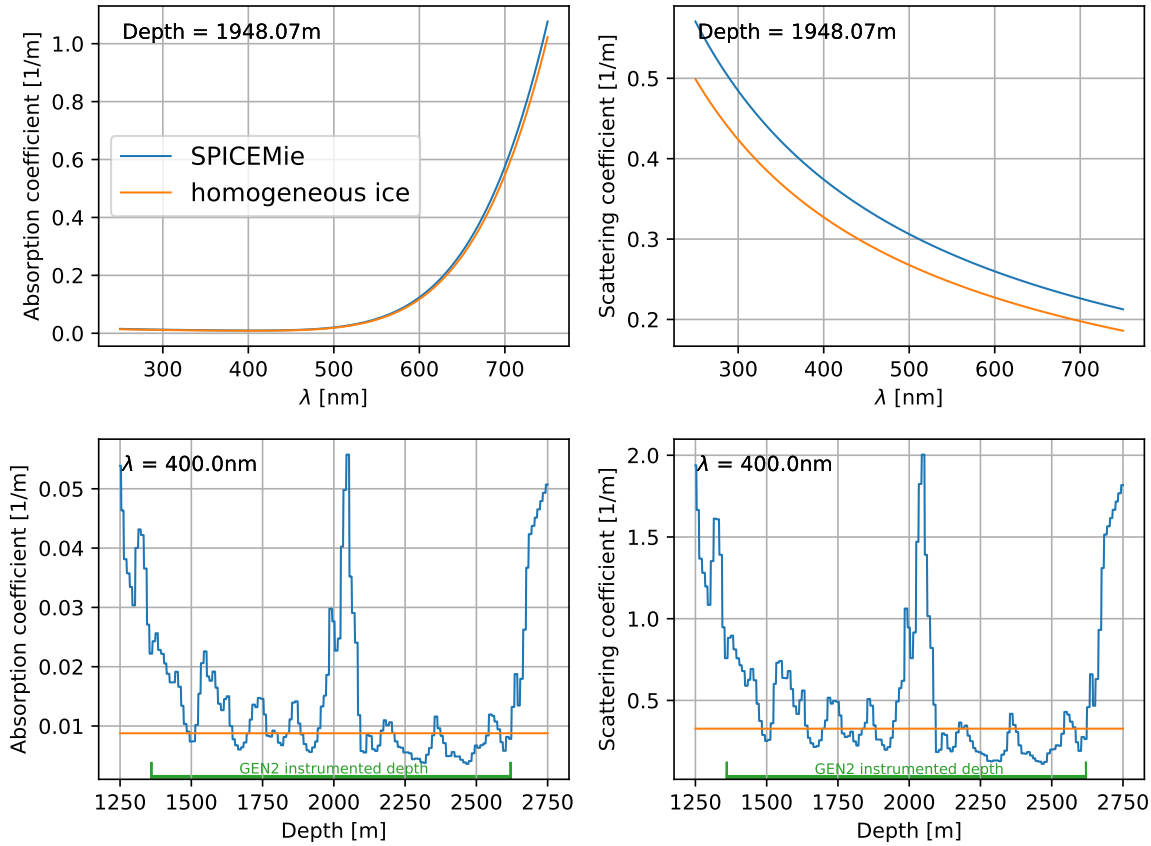

Figure 4.3: Visualization of various properties of the SPICEMie [64] versus the homogeneous ice model used in this work. *Top left*: Absorption coefficient versus wavelength at a depth of 1948 m. *Top right*: Scattering coefficient versus wavelength at a depth of 1948 m. *Bottom left*: Absorption coefficient versus depth at a wavelength of 400 nm. *Bottom right*: Scattering coefficient versus depth at a wavelength of 400 nm. The horizontal green line in the bottom plots marks the planed instrumented depth of the IceCube-Gen2 high-energy array.

and potential consequences in chapter 7. A comparison of a standard layered ice model and the homogeneous model used here can be seen in figure 4.3.

The third step of CLSim is the conversion of photons, which have hit a DOM, to photoelectrons. For every photon that hits a DOM the probability of creating a photoelectron is calculated. This is the first occurrence within the simulation chain where the same process, here the conversion from photons to photoelectrons, is done by different parts of the code depending on the module type.

In the case of the IceCube DOM and the PDOM the probability to generate a photoelectron depends on two quantities: the wavelength acceptance and the angular sensitivity. The wavelength acceptance incorporates the quantum efficiency of the PMT's photocathode as well as

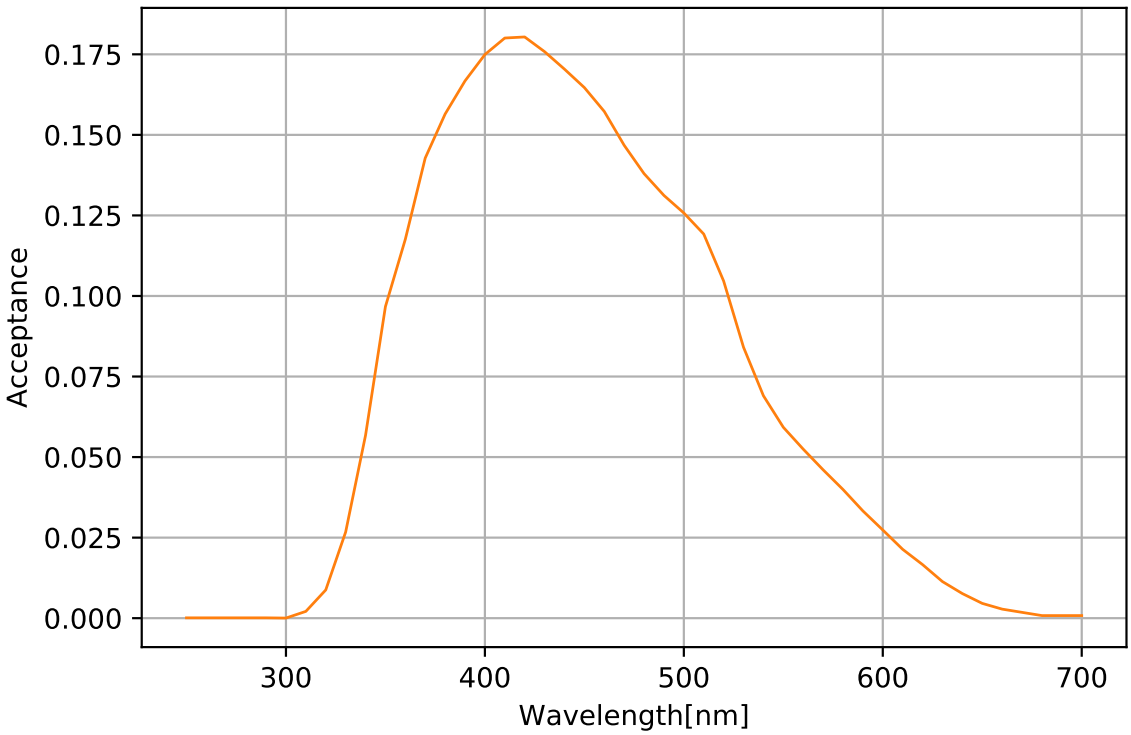

Figure 4.4: Wavelength dependent acceptance of the PDOM as implemented in CLSim. This curve includes transmittance of the glass and gel as well as the quantum efficiency of a standard IceCube DOM multiplied by 1.35 to account for the high quantum efficiency PMT of the PDOM.

the transmittance of the glass and gel and is shown in figure 4.4. As mentioned in section 3.3.3, the PDOM is an upgraded version of the IceCube DOM. At this point within the simulation, the only difference between IceCube DOM and PDOM is a higher quantum efficiency, which is implemented by using the quantum efficiency curve of the IceCube DOM and multiply it with a factor of 1.35. The angular sensitivity takes the incident angle θ of the photon into account, which is the angle between the symmetry axis of the PMT and the direction of the photon. In principle, this is a function depending on the position of the photon on the DOM's surface and its direction (two angles), but it has been averaged to depend only on θ. The implemented angular sensitivity of the PDOM is displayed in figure 4.5. The probability of actually generating a photoelectron is the product of the wavelength acceptance $W(\lambda)$ and the angular sensitivity $A(\theta)$ given the photon properties:

$$P_{\text{PDOM}}(\lambda,\theta) = W(\lambda)\cdot A(\theta) \tag{4.1}$$

Whether a photoelectron is recorded is decided by a random number generator and the probability P_{PDOM}.

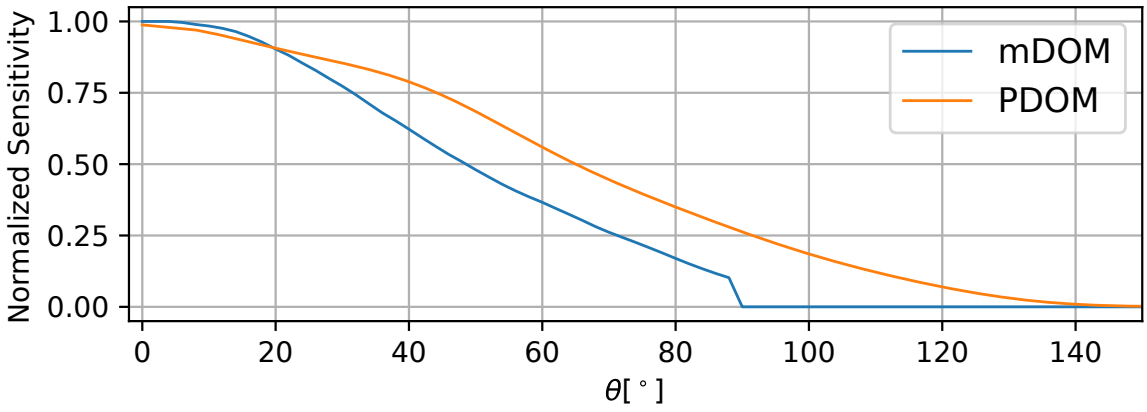

Figure 4.5: Normalized angular sensitivity of one PMT within the mDOM and the PDOM (similar to the IceCube DOM) as implemented in the simulation chain as a function of the photon impact angle θ. Values for the mDOM are adapted from a Geant4 simulation, see [59].

Since the mDOM's design is fundamentally different from the IceCube DOM, a different conversion from photon to photoelectron is used. Two major simplifications are used in the current implementation: the approximation of the whole mDOM as a sphere, and the simplification of the PMTs, including the reflector rings of each PMT, as flat disks with a radius of 5.1 cm. Each disk is positioned at the center of the respective PMT within the DOM, facing in the same direction as the PMT's symmetry axis. The extension of the flat disks is slightly reduced compared to the geometric area of PMT and reflector ring, at an impact angle of 0°, in order to take a small gap between PMT and reflector ring into account. Since one mDOM hosts multiple PMTs, it is necessary to determine if a photon, which has hit the DOM, does also hit a PMT within. This is accomplished by calculating the intersection of the elongated photon path and the flat disks within the DOM. If a PMT is hit from ahead, the identity of the hit PMT is recorded and further processing starts, if all PMTs are missed, or one is hit from behind the photon is dismissed. Once a photon hits a PMT the probability of actually generating a photoelectron is calculated in a similar way as for the PDOM. At first a wavelength dependent factor is calculated, incorporating the quantum efficiency of the PMT itself, $QE(\lambda)$, the transmittance of the glass, $T_{\text{glass}}(\lambda)$, and the transmittance of the optical gel, $T_{\text{gel}}(\lambda)$. Contrary to the simulation of the PDOM the actual path of the photon through the glass and the gel are calculated and the survival probability is derived accordingly. Figure 4.6 shows the absorption length of the optical gel, the glass and the quantum efficiency used for the simulation of the mDOM. The next step is to include the angular sensitivity of a PMT with reflector ring within the mDOM. Since every photon is checked for intersection of a PMT, simulated as a flat disk, a geometrical factor of $\cos(\theta)$ is automatically included. In order to reduce the impact of the flat disk approximation, a more realistic angular

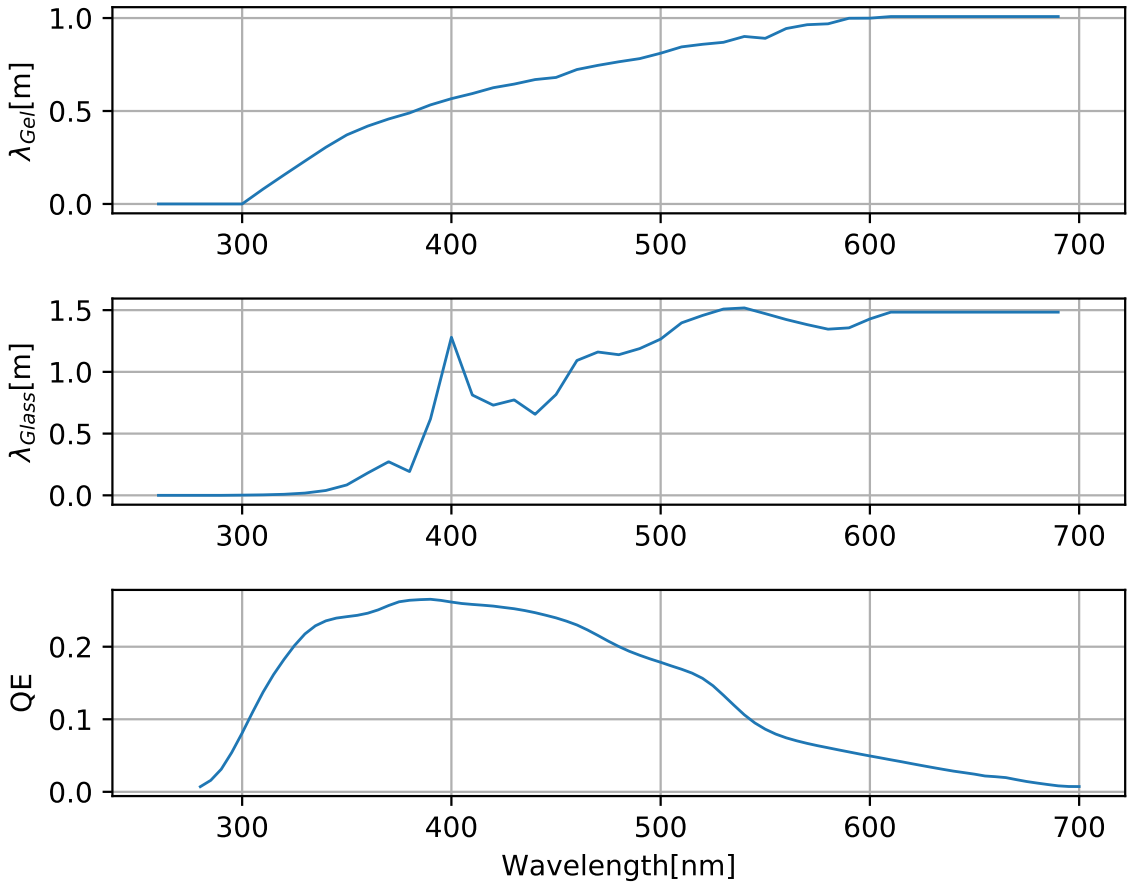

Figure 4.6: Wavelength dependent acceptance properties of the mDOM implemented within the simulation chain. *Top*: Absorption length of the optical gel (Wacker Gel, data from [48]). *Middle*: Absorption length of the glass (data from [48]). *Bottom*: Quantum efficiency of the PMT (values from measurements of the Hamamatsu R12199-02 PMT from [48])

sensitivity, from [59], has been implemented. The angular sensitivity can be seen in figure 4.5. A distinct kink right below an impact angle of 90° is noticeable. This is an irreducible consequence of the flat disk approximation caused by the fact that the geometric area of a flat disk at an impact angle of 90° is zero, whereas the sensitivity of a realistic PMT would be non zero beyond this point (as a smooth extrapolation of the curve would suggest). The angular factor of a photon which has hit a PMT is then a product of $1/\cos(\theta)$, to correct for the flat disk, times the normalized angular sensitivity, $A(\theta)$. The probability of a photoelectron generation is then the product of these factors:

$$P_{\text{mDOM}}(\lambda,\theta) = QE(\lambda)\cdot T_{\text{glass}}(\lambda)\cdot T_{\text{gel}}(\lambda)\cdot \frac{1}{\cos(\theta)}\cdot A(\theta) \tag{4.2}$$

The decision whether a photoelectron is stored is made with the help of a random number generator, similar to the PDOM scenario.

4.1.3 Detector Response Simulation

The next step of the simulation chain is the detector response simulation including PMT simulation and simulations of the electronics after the PMT. In regards of the flowchart in figure 4.1, this includes everything in the purple box.

4.1.3.1 Detector Simulation

Coalesce MCPEs The first process within the detector simulation block is to merge photoelectrons (also called MCPE[3] for Monte Carlo PhotoElectron) on the same PMT which are generated within a time window of 0.2 ns. An MCPE is defined by its generation time, equal to the arrival time of the photon at the photocathode, its charge in multiples of one photo electron, and the PMT number of the respective PMT. The time resolution achieved by IceCube is in the order of nanoseconds [69] and it can be assumed that the time resolution of new sensors are of similar magnitude. Thus, it makes sense to merge MCPEs that are close in time to each other in order to reduce the processing time of the subsequent steps and the size of the whole event. The algorithm responsible for merging the photoelectrons basically loops over a list of MCPEs for each PMT, merges all photoelectrons, which are within the defined time window by summing up the respective charge in units of PE (photoelectron). The charge is 1 for all MCPEs before merging. After merging it creates a new MCPE object with the time of the first MCPE in the current time window and the summed up charge. Finally a new list of merged MCPEs is store in the current event frame, while the old one gets deleted.

Noise Simulation: Vuvuzela The next part is the noise simulation called "Vuvuzela" [74]. This module does not include noise produced by electronics after the PMT, instead it incorporates potential noise sources of the DOM's glass sphere as well as the PMT itself. Vuvuzela simulates three different type of noise sources: thermionic emission, radioactive decays and scintillation [75].
As input, the algorithm takes the list of merged MCPEs. This list defines a certain time window, from first MCPE to last MCPE, which gets extended by ± 10 ms. For each PMT, noise-induced photoelectrons are simulated throughout this extended time window.
The thermal component, thermionic emission of electrons from the photocathode area, is simulated by drawing the actual amount of thermal noise MCPEs from a Poisson distribution with an expectation value equal to the thermal rate times the extended time window length. The time of

[3]The abbreviation "MC", for Monte Carlo, marks values that still contain so-called Monte Carlo information, so information that would not be available in a real experiment. This is done to prevent making physical statements with the usage of Monte Carlo information and is used throughout the thesis.

	mDOM	PDOM & IceCube DOM(default)
thermal rate	10 Hz	173.456 Hz
decay rate	19.5 Hz	56.942 Hz
mean cluster hits	3.91	8.072
cluster time mean	3.13	4.395
cluster time sigma	1.05	1.777

Table 4.1: Summary of the noise parameters used in "Vuvuzela".

these hits is then randomly distributed following a flat distribution.
The amount of radioactive decays, which happen mainly within the glass due to radioactive isotopes present in the glass, and their respective times are simulated in the same manner, but instead of the thermal rate, the decay rate is used. Secondaries of radioactive decays within the glass of the PMT itself are the main cause of scintillation or fluorescence and could also emit Cherenkov light, given a high enough energy. In order to take this causality into account, a second Poisson distribution is used determining the number of PEs within each cluster. The timing distribution of the cluster noise photoelectrons follows a predefined log-norm distribution. How much noise actually is generated depends on the sensor type. The most important factors are PMT type, photocathode area and glass. A detailed description of the PMT noise as well as respective measurements can be found in [59] for the mDOM and in [85] for the IceCube DOM. A summary of the parameters used for the noise simulation in this work can be found in table 4.1. The noise parameters of individual PMTs change over time due to aging effects of various parts. In order to keep the simulations as close to reality as possible, the noise parameters can also be set individually for each PMT. This is done by providing a dictionary like object to Vuvuzela which contains unique PMT keys and a set of parameters that should be used instead of the default parameters. This, of course, only applies to IC86 DOMs. For Gen2 DOMs the default parameters of the respective DOM type are always used for noise simulation.

PMT Response Simulation Once all photoelectrons have been generated, the response simulation of the PMT is started. The module simulates transition time spread, also called "time jitter", charge distribution, pre-, late- and afterpulses and saturation effects of the PMT. Within the simulation chain used here, the list of MCPEs, the output from "Vuvuzela", is split in two parts, namely an IC86 part and a Gen2 part. The reason for this is to be able to artificially increase or decrease the so-called effective photocathode area, which basically describes the photon collection efficiency of a DOM. This, in turn, is necessary to be able to compare detector performances with respect to the distribution of photocathode area rather than the total amount of photocathode area deployed (this will be explained in more detail in section 4.2).
The first effect that is simulated within this module is the transition time spread (also called "jitter"), which describes the spread of the transit time that is seen between the arrival of a photon at the photocathode and the measurement of a signal at the anode of the PMT. This

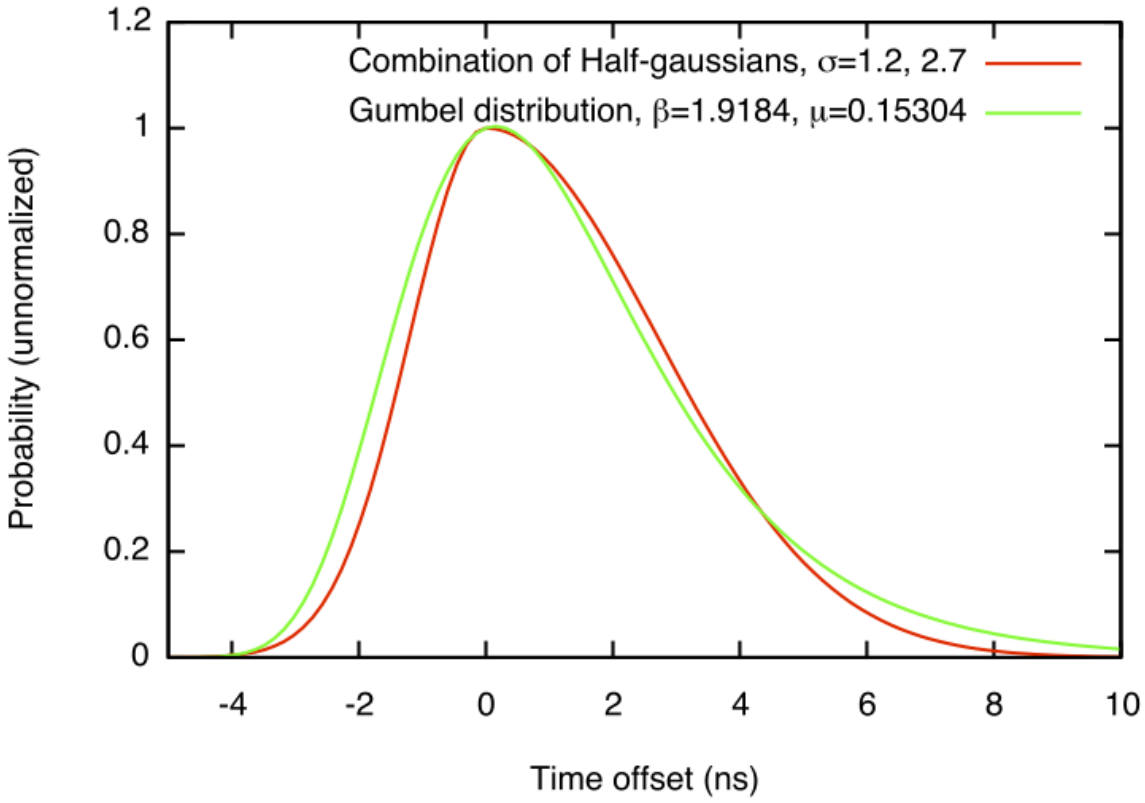

Figure 4.7: Jitter parameterization of the PMT response simulation. *Green*: Gumbel distribution (implemented). *Red*: Two half Gaussians (parametrization from [85]). Taken from [41].

spread is a consequence of the exact arrival position of the photon on the photocathode and the exact path of the photoelectron to the first dynode, and the subsequent electrons emitted by the dynodes and their respective paths through the PMT. All of these processes induce a certain stochasticity, which causes a time spread of individual output signals of the PMT. The time offset induced by these processes has been measured (e.g. in [85]) and a distribution has been fit to the measurements which is used in the simulation to draw the offset from (see figure 4.7).

The next step is to calculate the total charge of a signal caused by a single photoelectron after its transition through the PMT. This is simply done by using the distribution shown in figure 4.8.

There are three other phenomena implemented in the PMT response simulation module which influence the timing of the PMT output, namely pre-, late and afterpulses.

A pre-pulse occurs when a photon, instead of causing the emission of a photoelectron on the photocathode, hits a dynode within the PMT and knocks out an electron there. This shortens the transition of the signal through the PMT leading to an arrival time about 30 ns earlier [4], but also

[4] These times are regarding the 10 inch PMT of the standard IceCube DOM, but unless explicitly mentioned, the same parameters have been used for the simulation of the 3 inch PMTs integrated in the mDOM.

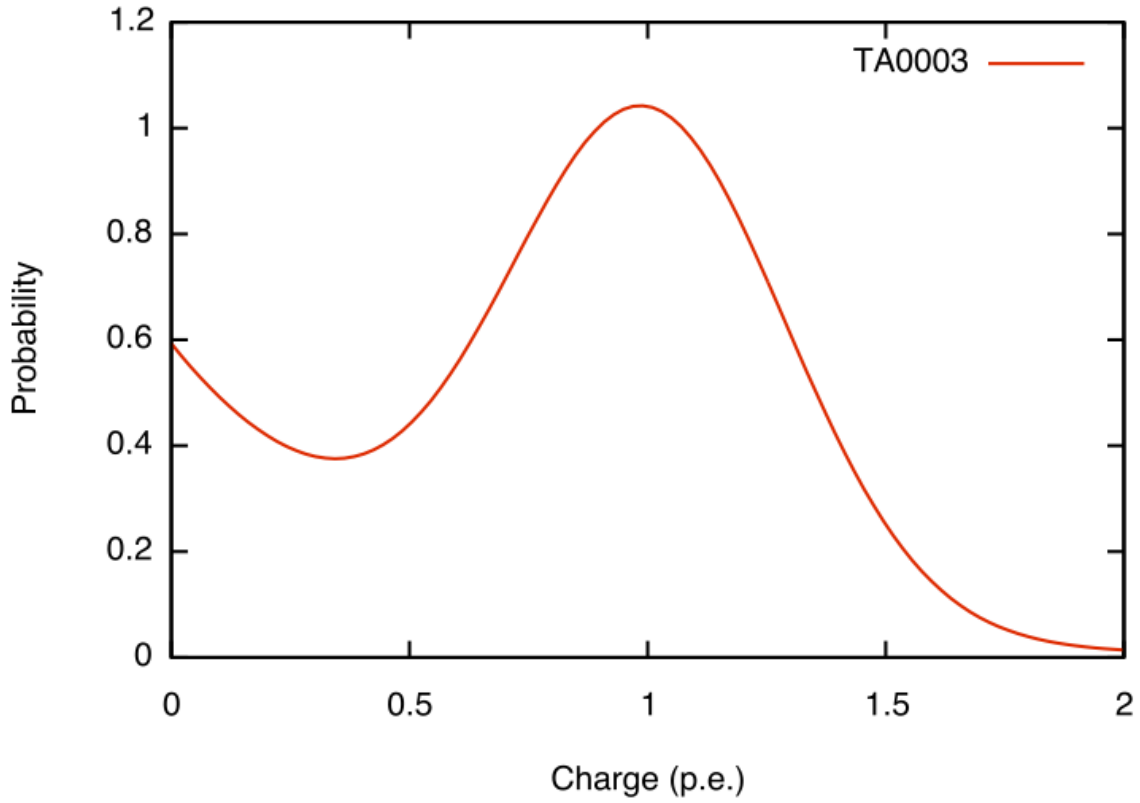

Figure 4.8: Single photoelectron (SPE) charge distribution implemented in the simulation. Taken from [41].

with a ten to twenty times smaller charge. The probability of a photon inducing a pre-pulse are implemented as 0.3 % and the charge is reduced by a factor of 20 [41].
A late pulse can happen when the photoelectron scatters back form the first dynode. The scattered electron then needs some time to turn around and hit the dynode again, which increases the total transit time. The probability of a late pulse is implemented as 3.5 %. No augmentation of the charge distribution is applied, since, apart from the delayed signal time, all other processes are similar to the normal case scenario.
The third phenomenon is the appearance of after-pulses. While photoelectrons propagate through the PMT they can ionize residual gas atoms. These positively charged ions drift back to the photocathode, where they can cause the emission of several electrons, which, in turn, will be accelerated towards the first dynode and, in the end, produce an output signal similar to the detection of a photon. Afterpulses are generated with a probability of $\approx 6\,\%$ and are subjected to a more complicated weighting of the charge.
The last effect integrated within this module is saturation. Saturation occurs since the maximal electric current available to a real PMT is limited. In order to include saturation effects in the

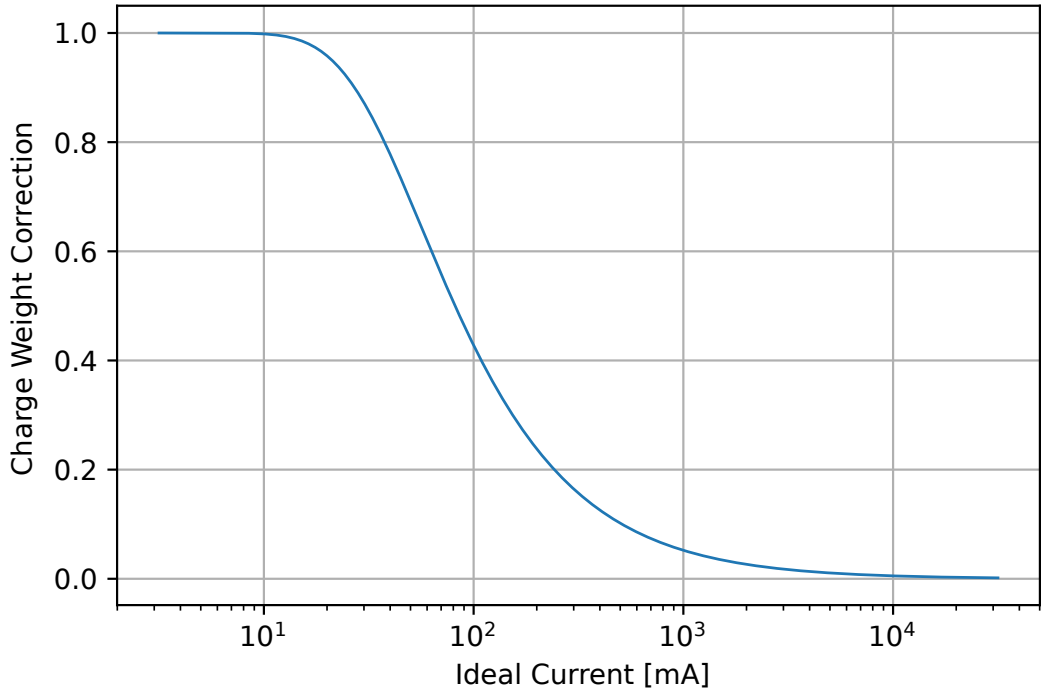

Figure 4.9: Saturation photoelectron charge weight correction factor as a function of the ideal anode current, i.e. without any saturation, as implemented in the "PMTResponseSimulator" module.

simulation one needs to calculate the ideal current , i.e. without saturation, at the anode given a series of photoelectrons. This is done by using a current template of the from

$$I(t) = w \cdot \frac{e^{|t|/\tau}}{2\tau}, \tag{4.3}$$

with $\tau = 2.2\,\text{ns}$, t is the time and w the charge of the photoelectron. The ideal current is then the convolution of these templates evaluated for each photoelectron. With the ideal current a charge weight correction for each photoelectron is calculated in order to include saturation effects. The charge weight correction as a function of the ideal current is displayed in figure 4.9.

From Monte Carlo Pulses to Reconstructed Pulses The next steps within the simulation chain can be summed up as the conversion of Monte Carlos pulses, also called "MCPulses", to reconstructed pulses, called "reco pulses" or "hits". This process includes the simulation of the DOM electronics, so the digitization of the analog signal produced by the PMT, calibration, meaning the inclusion of individual DOM properties, and the wave reconstruction. Wave reconstruction is the process of reconstructing the arrival time of photons at the photocathode of a PMT from the

digitized waveform produced by the DOMs electronics, or, in this case, the simulation of these. As indicated in the simulation flow chart (figure 4.1), this step is done in a different way for IC86 DOMs and Gen2 DOMs. The necessity of processing these two groups separately is the unavailability of respective simulations for the mDOM, due to the fact that the internal design, including the electronics, of the mDOM has not been finalized at the time of this writing. Therefore, all Gen2 DOMs are simulated with a perfect pulse reconstruction, meaning, that the times and charges of the reco pulses are equal to their respective MCPulses, neglecting any possible effects introduced by the electronics. In contrast, all IC86 DOMs undergo the normal simulation processes (processes "DOM Launcher" and "Calibration Simulation" in figure 4.1).
Theoretically, this simplification is only necessary for the simulation of detectors equipped with mDOMs while for PDOMs one could use the standard simulation tools, but this would induce a bias to a later comparison of results obtained by detectors equipped with the respective sensor types. Thus, no matter the sensor type, all DOMs on a Gen2 string are processed assuming a perfect pulse reconstruction.

4.1.4 Base Processeing

Before highly developed algorithms designed to reconstruct physical quantities are applied, the raw data needs to be preprocessed (also called base processing). This includes the application of trigger algorithms as well as some simple noise cleaning, so all processes included in the red box in figure 4.1. It might be debatable, if the steps described within this subsection can still be considered a part of the simulation process, but for the sake of simplicity and the fact that they are included in the same script that invokes the detector simulation, their description is integrated into this chapter.

4.1.4.1 Trigger Simulation

Trigger algorithms are designed to detect potentially interesting events within the constant flow of data generated by a detector like IceCube. One of the standard trigger algorithms of IceCube is the Simple Multiplicity Trigger (SMT) [69]. The SMT fires, if there are N HLC hits within a sliding time window of length w without any local conditions. It is worth noting at this point, that a hit can also be flagged as an HLC hit, if a PMT within the same module has a hit within a time window of $0.1\,\mu$s. This, of course, is only relevant for multi PMT sensors like the mDOM. The SMT for the IceCube in-ice array requires $N = 8$ hits within a time window of $w = 5\,\mu$s. The length of the time window depends on the average distance between the DOMs, therefore this time window has been extended to $10\,\mu$s in order to use the same algorithm for Gen2 simulations where the average distance between strings is about 240 m (instead of 125 m for IceCube). The trigger window of a potential event starts at the time of the first hit for which the trigger condition is met and ends when a time window with length w without any new HLC

hits is found. In order to ensure that the marked time window includes everything potentially valuable, the final readout window is the trigger window -4μs and $+6\mu$s. All data from within the readout window is collected within one event frame and gets stored on disk.
In terms of simulation, the trigger algorithms get the list of reconstructed pulses as input and return a readout time window. Similar to the real detector, everything outside of this time window is dismissed.

4.1.4.2 Hit Cleaning

The next step of the base processing is the so-called hit cleaning. Once a trigger algorithm has marked a time window as potentially interesting it is desirable to remove everything that is not correlated to the event of interest. One algorithm designed for this task is the so-called Seeded RT-cleaning (SRT) [42]. This algorithm works by iterating over all "seed" hits (defined by the user) and adds all other hits to the seed list when they are on a DOM within a radius R and within a time window T. This process is then repeated, either until no more hits are added or until the number of maximum repetitions (user defined) is reached.
Similar to the time window length of the trigger algorithm it is necessary to adapt the standard IceCube values, $R = 150\,\text{m}$ and $T = 1.0\,\mu$s, used for the SRT-cleaning in order to meet the requirements of a Gen2 high-energy array. Since these values also depend on the average spacing between strings, a factor of approximately 2 is used for the radius and time window. As seed hits the predefined method "HLCCoreHits" has been applied. This list of seed hits is then defined as all HLC hits, that have at least two other HLC hits that meet the radius and time condition.

4.2 Datasets

The main purpose of datasets produced for this work, was to compare the angular resolution of through-going muons achieved by detectors where all Gen2 strings are equipped with DOMs of a new sensor type. At first, MuonGun and PROPOSAL have been put to work in order to inject muons at the surface of the injection volume (injection surface and geometry as displayed in figure 4.2) and propagate these. Next, the photon propagation with CLSim has been done in multiple parts. Each sensor type, that should be investigated, needed its own photon propagation simulation, since the module size as well as the PMT distribution varies from sensor to sensor. For the datasets used here, two different sensor types have been used, namely the PDOM and the mDOM[5].

[5]For some datasets more sensor designs have been simulated, but this will not be mentioned any further in this work, and is therefore omitted.

module	$\overline{A}_{\text{eff}}[\text{cm}^2]$	$\overline{A}_{\text{eff}}/\overline{A}_{\text{eff}}(\text{PDOM})$
PDOM	13.6	1.00
mDOM	30.6	2.24

Table 4.2: Solid angle and wavelength averaged effective photocathode area of the nominal PDOM and the nominal mDOM. These values are used for the up- and downscaling of the datasets. Values from [59].

4.2.1 Up- and Downscaling of DOMs

As mentioned in section 3.3.4, the difference between an mDOM and a PDOM is not just the distribution of photocathode area within the module, but also the total amount of effective photocathode area per module. In order to quantify how large the differences between an mDOM and a PDOM concerning this quantity is one can calculate the solid-angle- and wavelength-averaged effective area $\overline{A}_{\text{eff}}$, defined as

$$\overline{A}_{\text{eff}} = \frac{1}{N}\int_{\theta=0}^{\pi}\int_{\phi=0}^{2\pi}\int_{\lambda=200\,\text{nm}}^{600\,\text{nm}} A_{\text{eff}}(\theta,\phi,\lambda)\cdot w_{\text{Cher}}(\lambda)\cdot\sin\theta\, d\theta\, d\phi\, d\lambda \quad , \tag{4.4}$$

with $N = 4\pi\cdot 400\,\text{nm}$, as normalization factor, $A_{\text{eff}}(\theta,\phi,\lambda)$ is the wavelength and direction dependent effective area of a DOM and $w_{\text{Cher}}(\lambda)$ as a weighting factor to fold the emission spectrum of the Cherenkov light in [59]. The wavelength and direction-dependent effective area, is obtained by simulating a disk emitting mono-energetic parallel photons from a certain direction towards the DOM whilst counting the amount of detected photons:

$$A_{\text{eff}}(\theta,\phi,\lambda) = \frac{N_{\text{det}}(\theta,\phi,\lambda)}{N_{\text{emit}}}\cdot A_{\text{rad}} \tag{4.5}$$

Within this formula N_{det} is the amount of detected photons, N_{emit} the amount of emitted photons and A_{rad} is the area of the photon emitting disk.
With these quantities and a full Geant4 simulation $\overline{A}_{\text{eff}}$ has been calculated in [59] for the mDOM and the PDOM (results are shown in table 4.2). In order to compensate for this increased collection efficiency of the mDOM an artificial efficiency scaling factor ϵ has been implemented in the simulation chain in order to either up- or downscale the effective photocathode area within the simulation. For the comparison of the mDOM to the PDOM, four versions of the same dataset were produced. Two versions where mDOMs and PDOMs were simulated in the normal way, so without any up- or downscaling, one version where all mDOMs have been downscaled by a factor of 1/2.24, in order to be comparable to the nominal PDOM, and one version where all PDOMs were upscaled by a factor of 2.24 to be comparable with the nominal mDOM. After this is done, the results obtained with two different sensors can be compared independently of the total photocathode area. In total this yields four versions per datasets, one for each sensor and efficiency scaling. In all cases, all strings which are part of IC86 have been simulated without any up- or downscaling and all sets have been simulated with the homogeneous ice model from

figure 4.3.
The final stage of the production of the datasets was the simulation of the detector response and base processing, which was done spererately for each version of a datasets since up- and downscaling of DOMs affects noise simulation and PMT simulation, more precisely, saturation of PMTs, as well. Concerning noise simulation, the scaling factor ϵ used for a specific version of a datasets was also used to scale the thermal rate and the decay rate. For the PMT simulation the threshold of the onset of saturation effects had to be scaled accordingly.

4.2.2 Properties of Dataset 20198

20198 is a set of simulations containing muons with uniform angular coverage. The simulated energy range goes from 3 TeV to 70 PeV with a spectral index of $\gamma = -1.4$. Energy and angular distribution of the four different versions of this set can be seen in figure 4.10 and figure 4.11. In these figures a slight underrepresentation of events within the fourth energy bin can be noticed. This is a consequence of crashed simulation jobs during the production of this dataset, hence does not have any physical meaning.

4.3 Sanity Checks

A goal of this thesis is to work out if the segmented photocathode area of the mDOM does increase the achievable angular resolution obtained by the Gen2 high-energy array compared to the same detector equipped with PDOMs independent of the total photocathode area. In order to ensure an unbiased comparison between the results obtained with the different sensors, it is crucial to rule out any possible biases or mistakes introduced during simulation and the up- and downscaling of the efficiencies. Therefore, within the context of this work, various sanity checks at certain steps within the simulation chain have been conducted. The results of these checks will be presented and discussed within the following section.
The version of a dataset can be identified by the sensor type that has been used for the Gen2 strings and the respective scaling factor ϵ. In order to make the plots more readable, the labels contain the name of the Gen2 sensor used, mDOM or PDOM, and its scaled effective photocathode area in units of the nominal PDOM. Thus, a nominal PDOM would have an effective photocathode area of 1.0, an upscaled PDOM an effective photocathode area of 2.24 (times the effective photocathode area of a nominal PDOM), a nominal mDOM would have an effective photocathode area of 2.24, while a downscaled mDOM would have an effective photocathode area of 1.0 (effective photocathode area of a nominal mDOM times 1/2.24).

4.3.1 Detected Photons

The first sanity check is to ensure that the equalization of the effective photocathode area worked as intended. If this is true, then the total amount of photoelectrons (MCPEs) of two versions of a

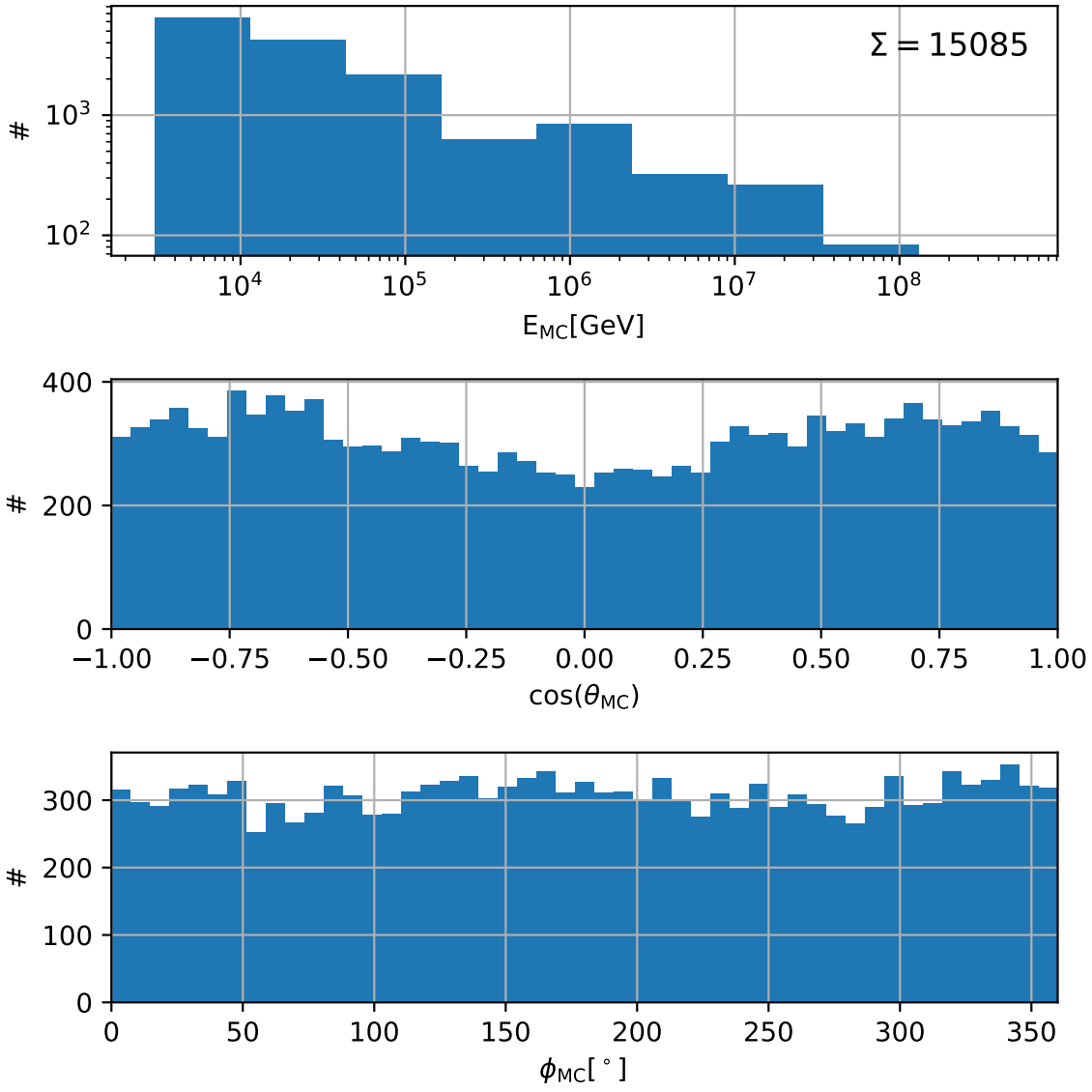

Figure 4.10: Properties of the dataset 20198 for mDOM and PDOM normalized on the PDOM (mDOM downscaled by 1/2.24). The number in the upper right corner is the total amount of triggered events (SMT8 adapted for Gen2). *Top*: Total amount of triggered events versus true initial muon energy. *Center*: Total amount of triggered events versus cosine of the true zenith angle (θ_{MC}) of the simulated muon. *Bottom*: Total amount of triggered events versus the true azimuth angle of the simulated muon.

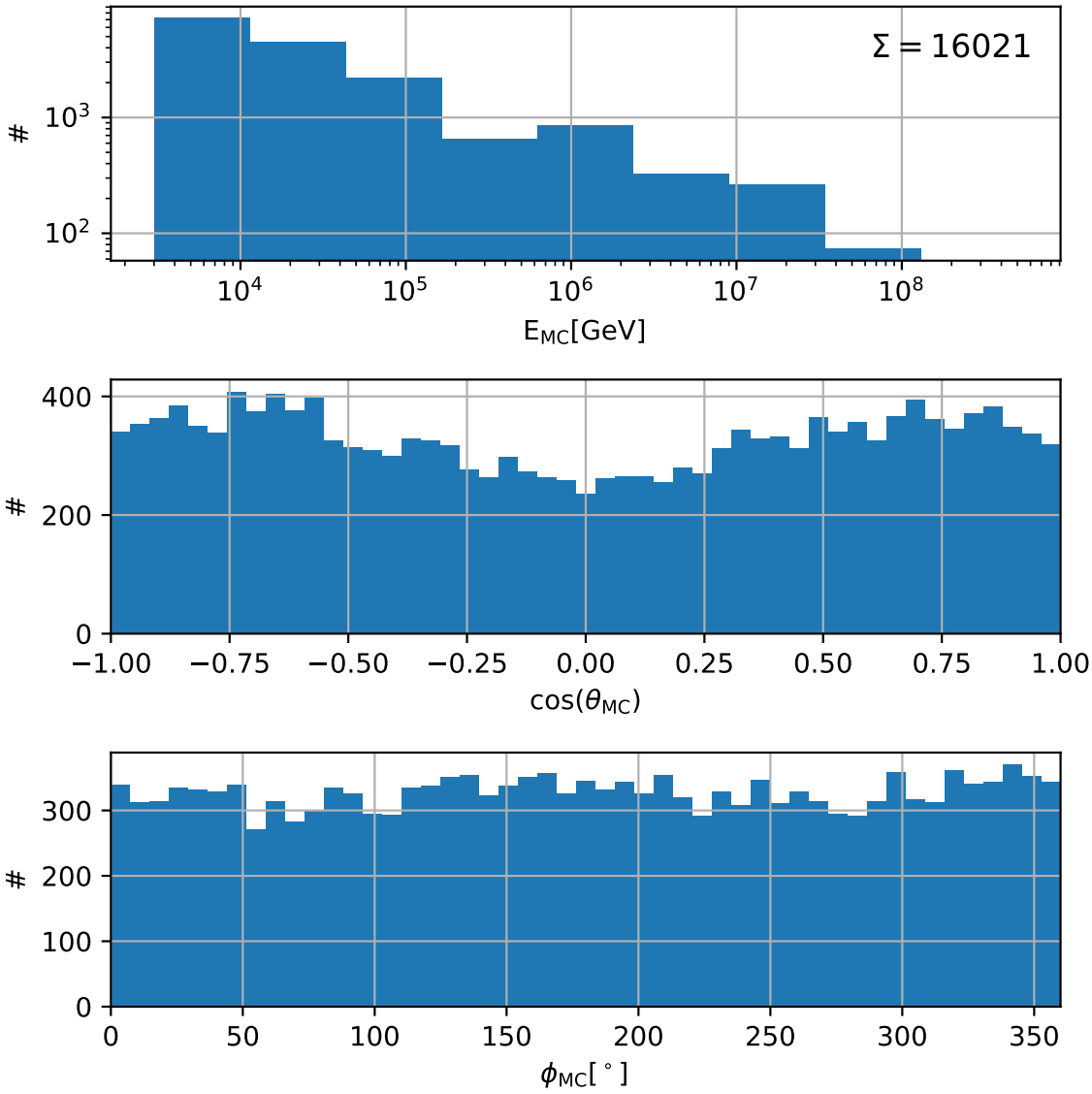

Figure 4.11: Properties of the dataset 20198 for mDOM and PDOM normalized on the mDOM (PDOM upscaled by 2.24). The number in the upper right corner is the total amount of triggered events (SMT8 adapted for Gen2). *Top*: Total amount of triggered events versus true initial muon energy. *Center*: Total amount of triggered events versus cosine of the true zenith angle (θ_{MC}) of the simulated muon. *Bottom*: Total amount of triggered events versus the true azimuth angle of the simulated muon.

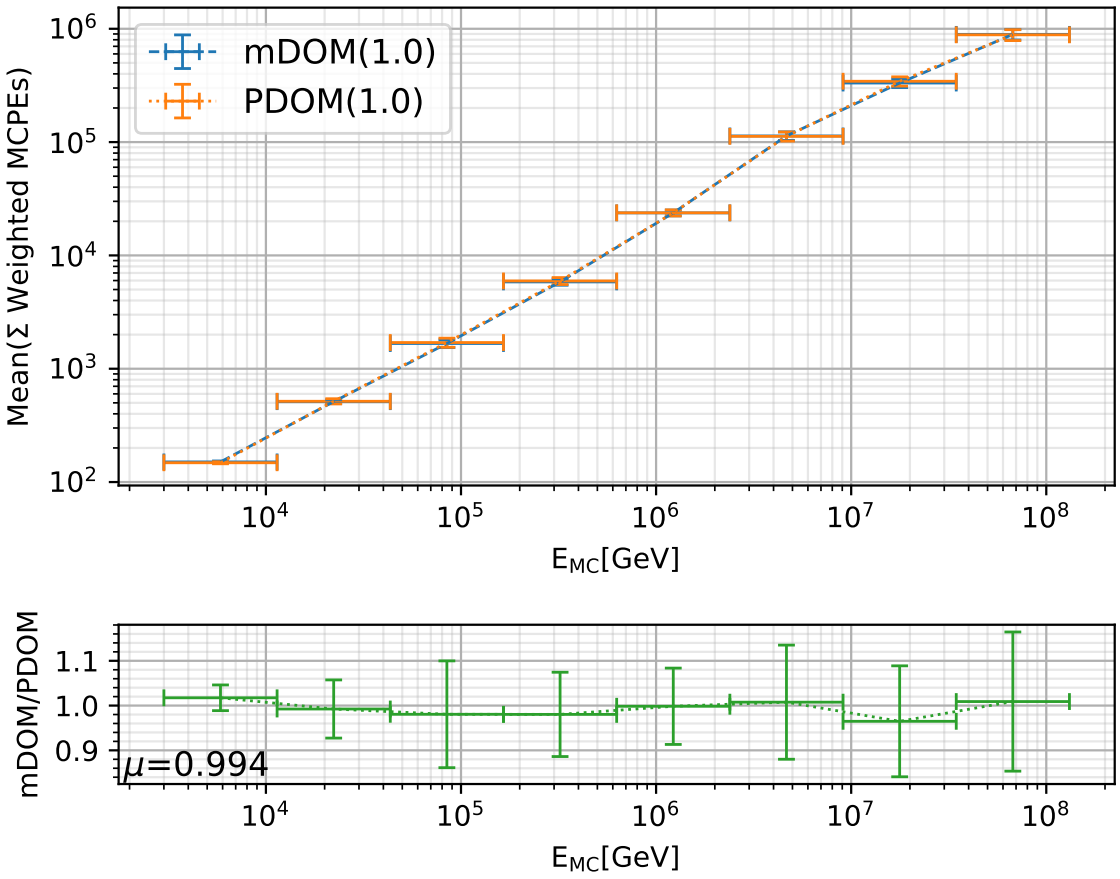

Figure 4.12: Comparison of the mean amount of detected photons (MCPEs) per energy bin for two versions (nominal PDOM and downscaled mDOM) of dataset 20198. The horizontal bars indicate the width of the energy bin, while the vertical error bars mark the standard error of the mean value. *Top*: Muon energy versus mean amount of MCPEs per bin. *Bottom*: Ratio of the mean values within the respective energy bin. The parameter μ denotes the mean of all ratios.

dataset with equalized effective photocathode area should be equal within statistical fluctuations. The sanity check of dataset 20198 concerning the amount of detected photons is shown in figure 4.12 and 4.13. It can be seen that the amount of detected photons per energy bin is within the boundaries of statistical fluctuations. Additionally, a clear linear correlation between E_{MC} (initial energy of the injected muon) and the amount of detected photons is present, as one would expect. At this point, there is no obvious reason to distrust any of the processes that led to these numbers, meaning that MuonGun, PROPOSAL, CLSim as well as the up- and downscaling of the effective photocathode area can be assumed to work as intended.

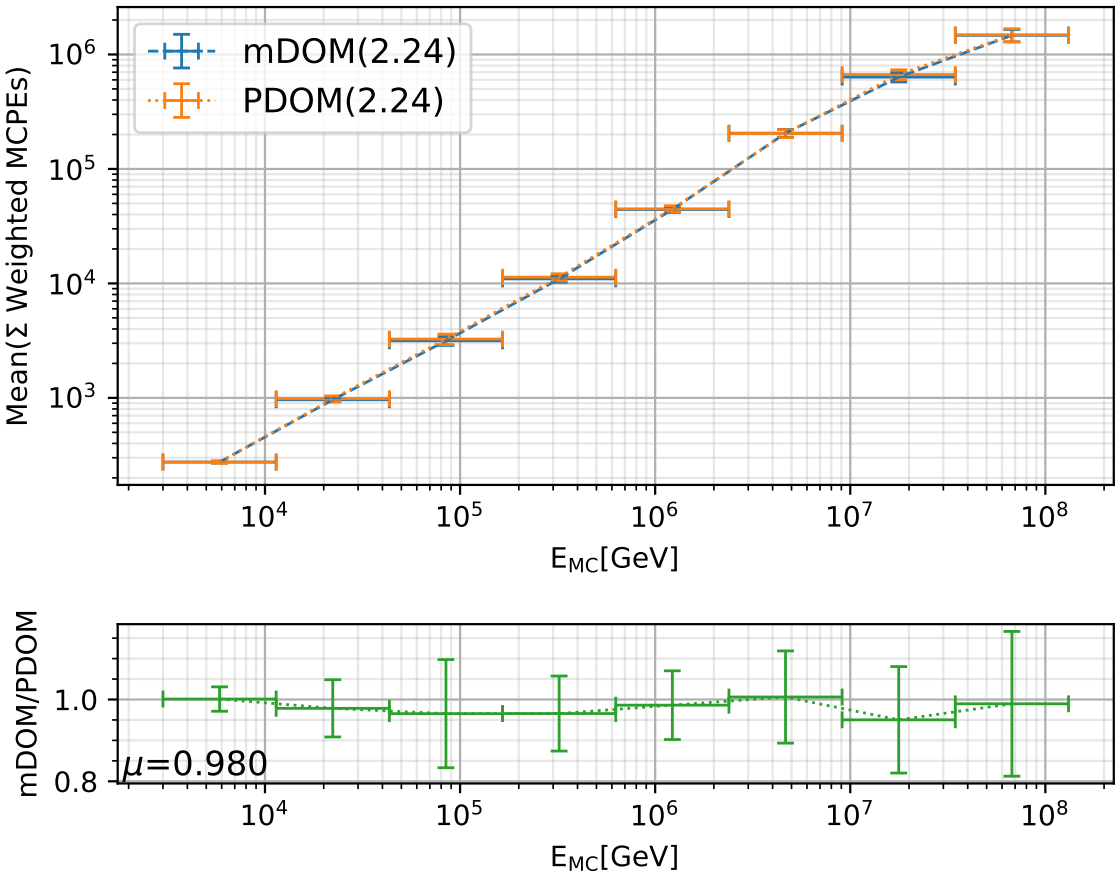

Figure 4.13: Comparison of the mean amount of detected photons (MCPEs) per energy bin for two versions (upscaled PDOM and nominal mDOM) of dataset 20198. The horizontal bars indicate the width of the energy bin, while the vertical error bars mark the standard error of the mean value. *Top*: Muon energy versus mean amount of MCPEs per bin. *Bottom*: Ratio of the mean values within the respective energy bin. The parameter μ denotes the mean of all ratios.

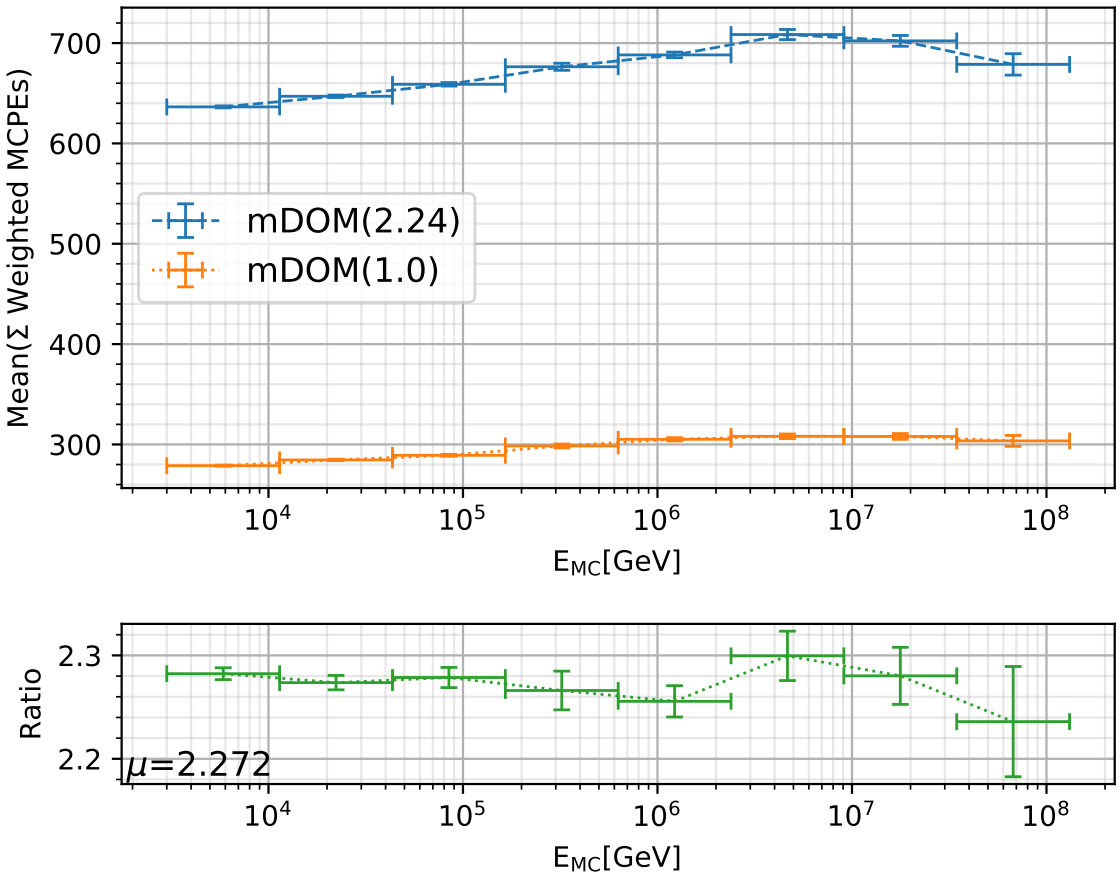

Figure 4.14: Comparison of the mean amount of MCPEs on Gen2 DOMs due to noise per energy bin for two versions (downscaled mDOM and the nominal mDOM) of dataset 20198. The horizontal bars indicate the width of the energy bin, while the vertical error bars mark the standard error of the mean value. *Top*: Energy versus mean amount of MCPEs per bin. *Bottom*: Ratio of the mean values within the respective energy bin. The parameter μ denotes the mean of all ratios.

4.3.2 Noise Simulation

The next process, which is affected by up- or downscaling is the simulation of noise. This is handled by multiplying the thermal rate and the decay rate (see section 4.1.3.1) with the scaling factor ϵ. Assuming that this is implemented correctly, a comparison of the amount of MCPEs due to noise on Gen2 DOMs between two versions of a dataset equipped with the same sensor type should yield a constant ratio equal to the scaling factor. This comparison as a function of energy can be seen in figure 4.14 for the mDOM and in figure 4.15 for the PDOM. In both cases the mean of the ratios, labeled μ, is slightly above the scaling factor $\epsilon = 2.24$. This is assumed to be a consequence of the extended event duration of events simulated in detectors with larger total

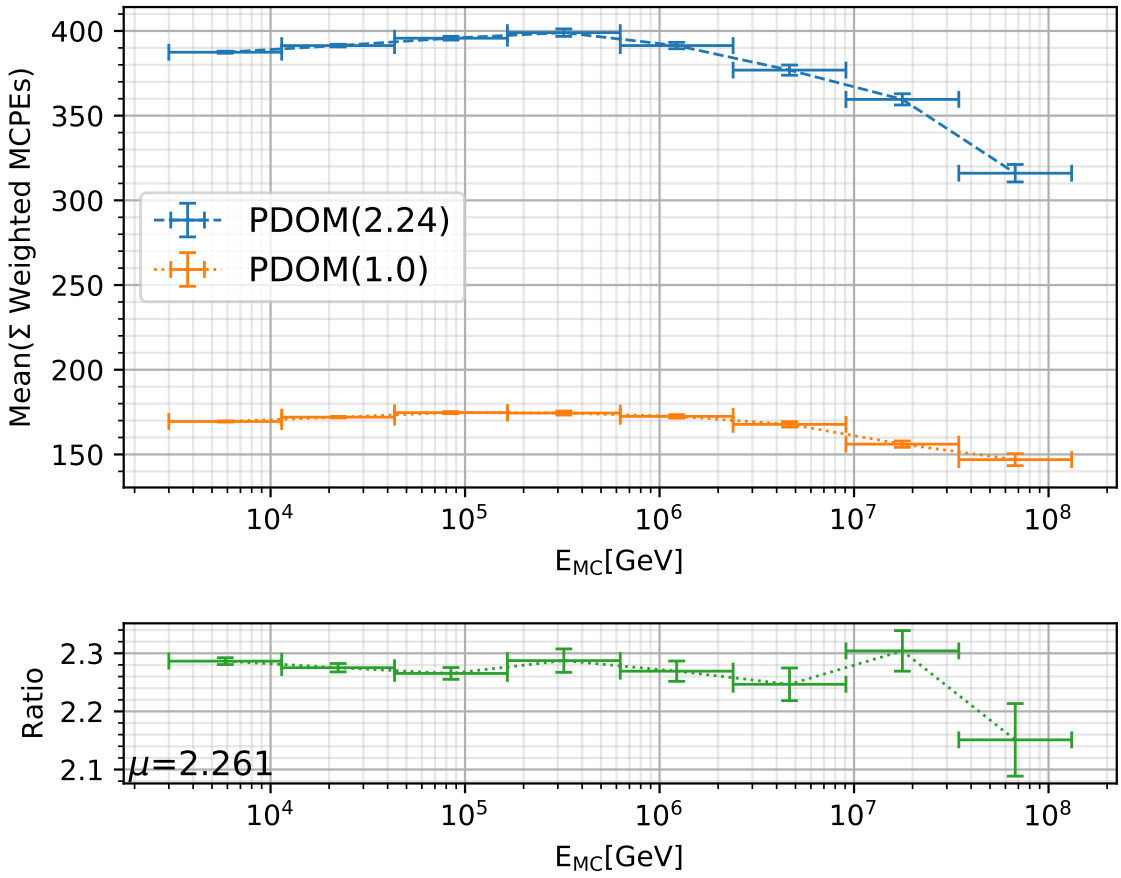

Figure 4.15: Comparison of the mean amount of MCPEs on Gen2 DOMs due to noise per energy bin for two versions (nominal PDOM and upscaled PDOM) of dataset 20198. The horizontal bars indicate the width of the energy bin, while the vertical error bars mark the standard error of the mean value. *Top*: Energy versus mean amount of MCPEs per bin. *Bottom*: Ratio of the mean values within the respective energy bin. The parameter μ denotes the mean of all ratios.

photocathode area, whereas event duration means the time difference between time of the first non-noise MCPE and the last non-noise MCPE. The increase of event duration with photocathode area is caused by the increased probability of detecting a very early photon and/or late photon. This prolonged event duration is approximately 5 % for both sensor types.
Another feature present in both figures, more visible in the PDOM figure though, is a decrease of simulated noise for very high-energy events. At the time of this writing, this is assumed to be a bug without any physical meaning. Given that this feature is present in all four versions of the dataset without changing the ratio in the affected energy bins too much, and the relatively low contribution of MCPEs from noise ($< 2\,\%$ above 1 PeV before any hit cleaning), this error is assumed to have no noticeable effect on the obtained results and is therefore ignored for the rest of this thesis.

4.3.3 PMT Saturation

Another important phenomenon to check is PMT saturation. Along with the up- and downscaling of the effective photocathode area it is necessary to up- and downscale the saturation threshold. The necessity of this becomes clear if one keeps in mind that in a real detector increasing the effective photocathode area means deploying more modules. Upscaling of the effective photocathode area of a module by a factor of two within the simulation translates into the deployment of twice as many modules. And while in the simulation twice the amount of photons would be detected by the upscaled module, the same amount of photons, in reality, would be distributed on two modules. If an adequate scaling of the saturation threshold would not be applied, the simulated modules would experience saturation too soon, in the case of an upscaled module, or not soon enough, in the case of a downscaled module. Therefore the saturation threshold, so the ideal current at which saturation starts to have an effect, is scaled with the same factor ϵ as the effective photocathode area. This is the reason why the PMT response simulations had to be done in two different modules respectively for IC86 DOMs, for which no scaling is applied, and for Gen2 DOMs. If a PMT saturates, the PMTResponseSimulator adds an entry to a specific dictionary within the event frame including the PMT number as well as the time window in which this PMT is saturated. In order to check if the simulation of the up- and downscaling of saturation effects is done correctly, a total saturation time T_{sat} is calculated per event, as

$$T_{\text{sat}} = \sum_i t_{\text{sat},i} \quad , \tag{4.6}$$

with i being the PMT identification and $t_{\text{sat},i}$ is the total saturation time of the respective PMT during the event. If the simulation works as expected, then the mean of T_{sat} within an energy bin should not change for a sensor if up- or downscaling is applied. The comparison of this mean is displayed in figure 4.16 for the mDOM and in figure 4.17 for the PDOM. It can be seen in these plots, that up- or downscaling of both sensor types does not affect the saturation time.

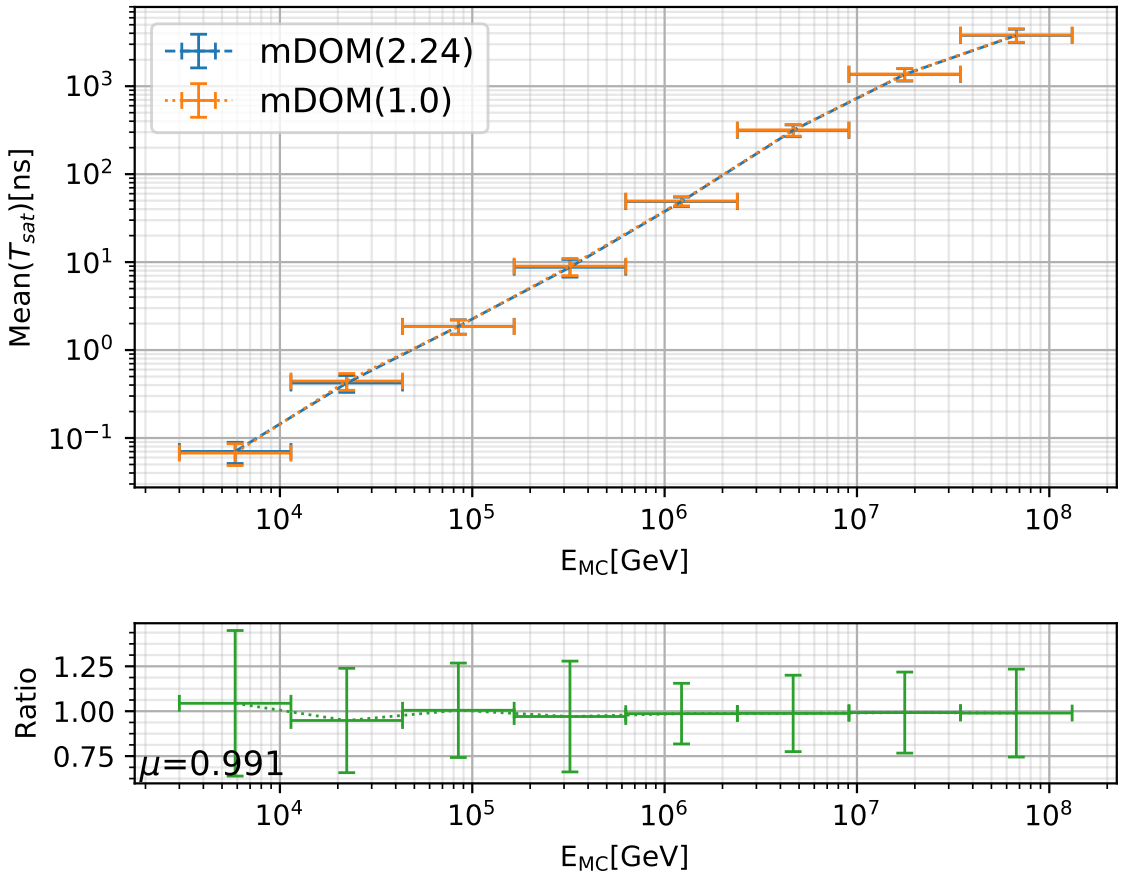

Figure 4.16: Sanity check for the correct up- and downscaling of the saturation threshold with dataset 20198. The horizontal bars indicate the width of the energy bin, while the vertical error bars mark the standard error of the mean value. *Top*: E_{MC} versus the mean total saturation time per event for the downscaled mDOM and the nominal mDOM. *Bottom*: Ratio of the mean of the nominal mDOM (2.24) over the mean obtained with the downscaled mDOM (1.0). The parameter μ denotes the mean of all ratios.

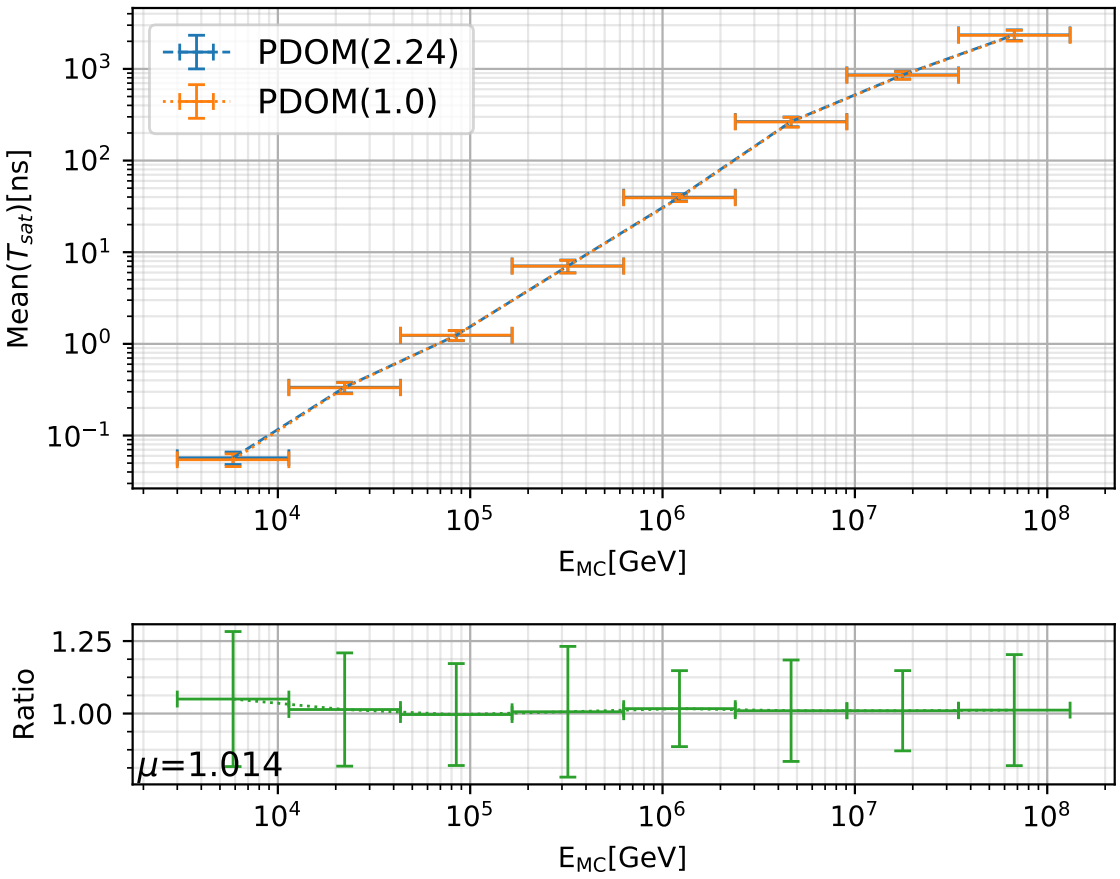

Figure 4.17: Sanity check for the correct up- and downscaling of the saturation threshold with dataset 20198. The horizontal bars indicate the width of the energy bin, while the vertical error bars mark the standard error of the mean value. *Top*: E_{MC} versus the mean total saturation time per event for the upscaled PDOM and the nominal PDOM. *Bottom*: Ratio of the mean of the upscaled PDOM (2.24) over the mean obtained with the nominal PDOM (1.0). The parameter μ denotes the mean of all ratios.

Thus, it can be assumed that the up- and downscaling of the saturation behavior of a PMT is implemented correctly, and does not induce any unwanted bias into the simulations.

4.3.4 Trigger

The next sanity check was conducted to ensure the correct behavior of the trigger algorithms. Although the trigger simulation is nothing new and the algorithms themselves did not need any adjustment to be able to handle multi PMT sensors, they do depend on the correct flagging of HLC hits, which had to be adjusted. In order to determine if this causes problems, the length of the mean of the readout window, which is determined by the trigger, has been compared for effective photocathode area equalized versions of the same dataset per energy bin. The comparison of these quantities is displayed in figure 4.18 and figure 4.19. A slightly longer readout window can be seen for the mDOM in both plots, but this can be expected due to the higher probability of a hit being flagged as a HLC hit on a multi PMT module. This, in turn, increases the probability of a hit still meeting the trigger condition and in consequence a longer trigger and readout window. Similar to the other sanity checks, this behavior does not give reason to distrust the simulations up to this point. Therefore, there are no significant biases remaining at this point.

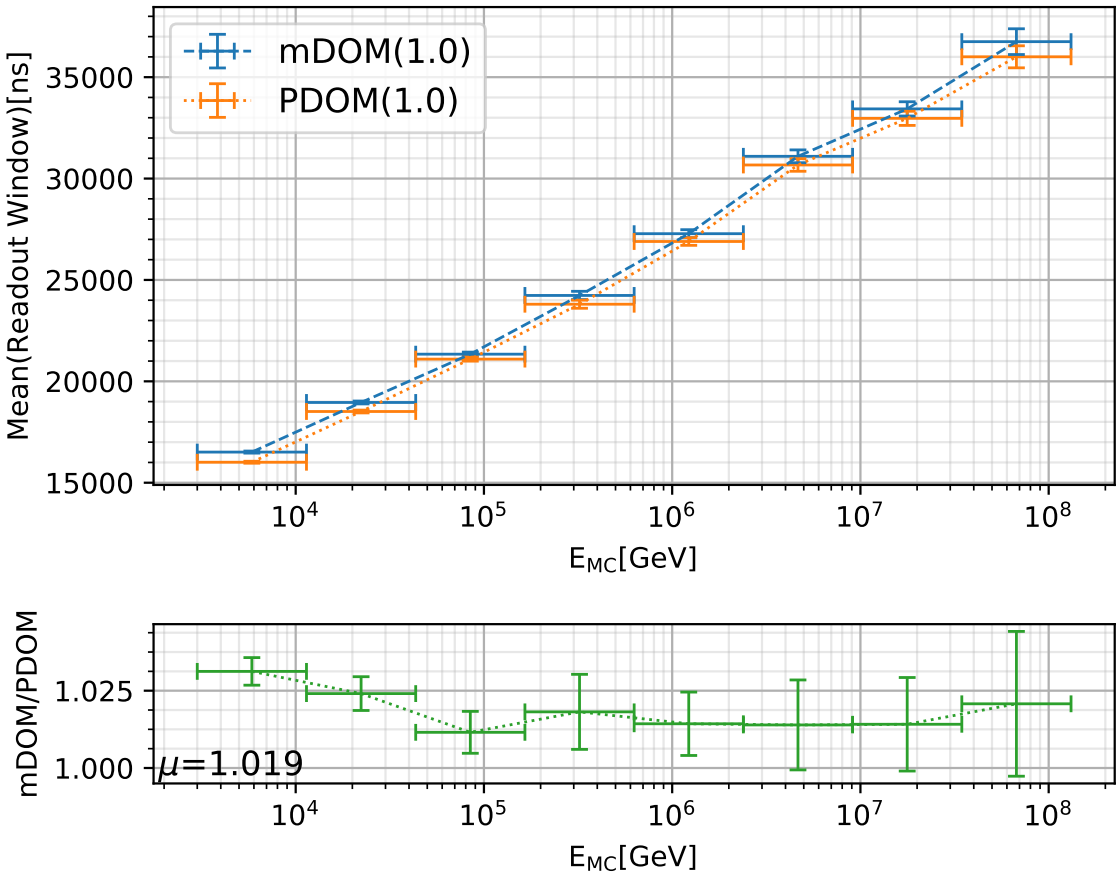

Figure 4.18: Sanity check of the readout window for dataset 20198. The horizontal bars indicate the width of the energy bin, while the vertical error bars mark the standard error of the mean value. *Top*: E_{MC} versus the mean readout window length per event. Compared are simulations obtained with the nominal PDOM and the downscaled mDOM. *Bottom*: Ratio of the respective values from the top plot. The parameter μ denotes the mean of all ratios.

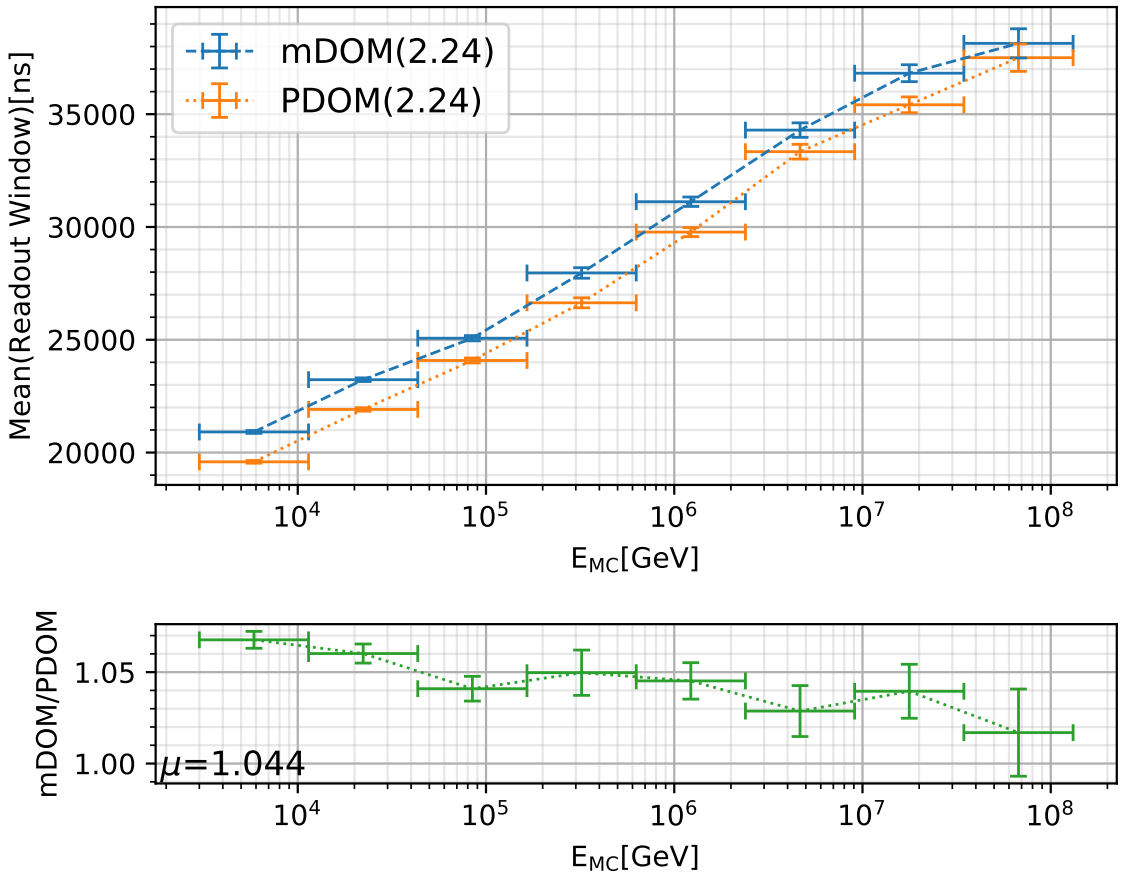

Figure 4.19: Sanity check of the readout window for dataset 20198. The horizontal bars indicate the width of the energy bin, while the vertical error bars mark the standard error of the mean value. *Top*: E_{MC} versus the mean readout window length per event. Compared are simulations obtained with the upscaled PDOM and the nominal mDOM. *Bottom*: Ratio of the respective values from the top plot. The parameter μ denotes the mean of all ratios.

CHAPTER 5

MUON TRACK RECONSTRUCTION STUDIES

While the previous chapter outlines how a through-going muon event inside the IceCube-Gen2 high-energy array is simulated, so how a concrete muon with a concrete position, direction, time and energy translates into collected charge per time and PMT, the content of this chapter is the reverse process, namely the reconstruction of such a through-going muon. Reconstruction in this context means the translation of the electronic signals acquired by the detector into the original properties of the muon.

5.1 Muon Track Reconstruction Methods

There are numerous reconstruction algorithms in IceCube, most of them tailored to a specific event topology, energy regime and performance. For this thesis, two of these existing algorithms, utilizing different approaches, have been used, namely MuEx and SplineMPE. Before the details of these approaches will be discussed, some key similarities are presented.

5.1.1 Maximum Likelihood Method

One of the key techniques commonly utilized for reconstruction algorithms is a maximum likelihood method. The principle of this method is to estimate a free parameter (or a set of free parameters), denoted as θ, of a model, given N observations $X = \{x_0, ..., x_N\}$[11]. As the name suggests, it revolves around the likelihood function, which is defined as

$$L(X, \theta) = \prod_{i=0}^{N} P(x_i|\theta), \tag{5.1}$$

where $P(x_i|\theta)$ is a probability density function (PDF), which, in turn, is defined by the applied model.

The key concept of the maximum likelihood method is to find $\hat{\theta}$ such that

$$L(X,\hat{\theta}) = \max_{\theta} L(X,\theta). \tag{5.2}$$

$\hat{\theta}$ is the parameter estimate, that makes the observed data X most likely given the hypothesis or model.
The data X in this context are all reconstructed pulses that are contained within the time window defined by the trigger and are not removed by the hit cleaning algorithm. A reconstructed pulse contains the reconstructed time of the detected photon, the integrated charge and the respective PMT identification number (ID). The PMT ID allows to determine the exact position, orientation and sensor type, which is necessary for the reconstruction.
In terms of reconstructing track-like events detected with the IceCube-Gen2 high-energy array θ mostly consists of up to six parameters, namely muon energy, two directional parameters, two positional parameters and time. Not all reconstruction algorithms are designed to find the best solution for all seven parameters, instead they are usually tailored to either reconstruct a subset of these, like just the muon energy or the muon direction.
Furthermore, reconstruction strategies differ in the used PDFs, which heavily depend on the assumed model. The definitions and implementations of these PDFs mark the main difference between the algorithms used for reconstruction in this thesis, thus are described in more detail in the following sections.

5.1.2 MuEx

MuEx, successor of MuE[52], is an in-ice event energy reconstruction algorithm, which is also capable of reconstructing a muon track if none is provided as a first guess or seed to the algorithm. This enables its use as a first guess algorithm used in order to produce a seed for more complex approaches further down the processing chain.
MuEx itself is a strictly analytical algorithm utilizing the maximum likelihood method in order to estimate the track parameters, assuming a smooth energy loss profile of an infinite muon. This approximation starts to deviate considerably from the actual energy loss profile of muons with energies above 1 TeV (see figure 3.3). The likelihood used in MuEx utilizes a Poisson distribution convolved with a function G and is defined as

$$L = \prod_{i=1}^{N_{\text{PMTs}}} \int_0^{\text{inf}} G(\lambda_i,\lambda) \cdot \frac{e^{-\lambda} \cdot \lambda^{k_i}}{k_i!} d\lambda. \tag{5.3}$$

N_{PMTs} is the total number of PMTs, $\lambda_i = \lambda_i(\theta)$ denotes the expected total charge, given θ, (formulas given in [66]) and k_i the observed charge of the "i"th PMT [98].
The kernel G has been introduced to handle systematic uncertainties, unwanted effects due to the analytic modeling of the light yield and to reduce the effects of large stochastic energy losses

of the muon. G is implemented as ([66]):

$$G(\lambda_i, \lambda) = \frac{\text{const.}}{\lambda} \cdot \left(e^{-\omega \cdot \ln(\lambda/\lambda_i)} + \left(\frac{\ln(\lambda/\lambda_i)}{\sigma} \right)^2 \right) \tag{5.4}$$

The additional parameter ω ("skewness" parameter) has been introduced to handle large over-fluctuations of the light yield.

5.1.3 SplineMPE

SplineMPE pursues a different approach. The first significant difference compared to MuEx is the used likelihood. While MuEx makes use of a Poisson distribution, so only comparing the observed charge to the expected charge without using any time information, SplineMPE utilizes the so-called multi photoelectron (MPE) PDF, which incorporates the time of the first observed hit on each PMT wighted with the total detected charge (of each respective PMT). The MPE likelihood is a binned multinomial likelihood, see definitions in [98], which introduces three time bins per PMT. The first bin is chosen such that it does not contain any hits, the second bin contains exactly the first hit on a PMT and the last bin contains all remaining hits. The explicit form of the MPE likelihood can be written as (from [98]):

$$L = \prod_{i=1}^{N_{\text{PMTs}}} \frac{N_{\text{hits},i}}{0!1!(N_{\text{hits},i}-1)!} \cdot w_0^0 \cdot w_1^1 \cdot w_2^{N_{\text{hits},i}-1} \tag{5.5}$$

$$L = \prod_{i=1}^{N_{\text{PMTs}}} N_{\text{hits},i} \cdot \left(\int_{t_{1,i}-\Delta t}^{t_{1,i}+\Delta t} p_i(t)dt \right) \left(\int_{t_{1,i}+\Delta t}^{\infty} p_i(t)dt \right)^{(N_{\text{hits},i}-1)} \tag{5.6}$$

$$L \underset{\Delta t \to 0}{=} \prod_{i=1}^{N_{\text{PMTs}}} \underbrace{N_{\text{hits},i} \cdot p_i(t_{1,i}) \cdot (1 - P_i(t_{1,i}))^{N_{\text{hits},i}-1}}_{\text{MPE PDF}} \tag{5.7}$$

N_{PMTs} is hereby the total number of hit PMTs, $N_{\text{hits},i}$ the total number of hits observed on the "i"th PMT, $w_{\{0,1,2\},i}$ is the probability of a hit being in bin 0, 1 or 2 respectively, $t_{1,i}$ is the time of the first hit, p_i is the time residual probability density function (PDF) and P_i the cumulative density function (CDF). Implicitly, p_i and P_i are both functions of θ. The time residual t_{res}, or residual time, is defined as

$$t_{\text{res}} = t_{\text{det}} - t_{\text{prompt}} - t_{\text{emit}}, \tag{5.8}$$

where t_{det} denotes the absolute detection time, t_{prompt} is the time a photon would need from (assumed) point of emission to PMT if it propagates in a straight line, so without any scattering, while t_{emit} is the (assumend) time of emission.
A more intuitive way of thinking about the MPE likelihood, is to see the MPE probability density function as the probability of observing the first hit on a PMT at time t_1 given a total of N_{hits} observed hits. This means, that the only information used in this formulation of the likelihood is the time of the first hit and the amount of hits per PMT, dismissing the arrival times of all other

hits. The information that a certain PMT has not detected any photons within the event time window (no-hit information) is also not included.
The reason for this and the success of the MPE likelihood, compared a single photoelectron (SPE) likelihood, which utilizes the arrival time of all detected photons, is based on systematic uncertainties (e.g. of the ice properties) and discrepancies between the hypothesis and the actual event topology. The first detected photon on a PMT is the least scattered photon, therefore the deviation between modeled and observed arrival time due to systematic uncertainties of the ice are smaller compared to late hits. Since within this thesis only simulations are reconstructed there are no uncertainties of the ice, but there are differences between the applied model and the actual event topology.
SplineMPE assumes an infinite muon track with a smooth energy loss profile, neglecting stochastic losses due to bremsstrahlung, pair production or photonuclear processes, similar to MuEx. This means that SplineMPE assumes that every photon has been emitted from the muon track itself instead of somewhere within an electromagnetic or hadronic cascade along the muon track. Such stochastic processes would cause the emission of photon bunches, rather than a smooth, continuous emission of photons. Neglecting the time distribution of the detected photons and only including the time of the first photon makes the MPE likelihood more robust against a wrong hypothesis compared to a likelihood that includes the full time information.
The last difference of SplineMPE compared to MuEx is the usage of so-called lookup tables instead of an analytical approach for the formulation of the likelihood function. These tables are used in order to calculate the time residual probability density function p_i and its respective cumulative density function P_i.

5.1.4 Photon Lookup Tables

Photon lookup tables, as used in this thesis, are an approach to quantify the dynamic photon field created by the emission of Cherenkov light from certain emitters within the ice of the detector convolved with the angular sensitivity and wavelength acceptance of a PMT within a DOM. In mathematical terms, one can think of a photon lookup table as a function $\mathcal{T}_{\theta,\zeta}$, which takes the position $\vec{X}$ of a PMT as input and returns the time residual PDF as well as the expected amount of detected photons $N_{\text{hits, exp}}$:

$$\mathcal{T}_{\theta,\zeta}(\vec{X}) = (\text{PDF}, N_{\text{hits, exp}}) \tag{5.9}$$

The parameter vector θ incorporates the light emitter type and direction, while ζ is a placeholder for the ice properties.
Originally, photon tables have been produced to be used as a simulation tool, but more computing power as well as new algorithms, like CLSim, have made pre-produced photon tables obsolete for event simulation, while simultaneously improving accuracy and enabling the integration of more complicated medium properties, like anisotropy, and dynamic light emission profiles [43].

In terms of reconstruction on the other hand, photon tables still play a crucial role. One reason for this is that the PDFs obtained with the help of photon tables are much more accurate compared to previously used analytical approaches (e.g. [104]), hence enabling more accurate reconstruction results [55]. It can be argued, that photon tables are still less accurate then direct simulation, but obtaining a time residual PDF through direct simulation for a certain certain realization of θ with high enough statistics is very time consuming. Nevertheless, there are efforts of implementing this approach into the reconstruction algorithms in IceCube, but this is mainly targeted for low-energy neutrino events. On the one hand this is due to fewer relevant PMTs, therefore fewer PDFs per minimization step to produce, and on the other hand inaccuracies of the photon tables are more severe in low-energy events (more on this in section 5.1.4.4).

5.1.4.1 Production of Photon Lookup Tables

Photon tables are produced by simulating the emission of Cherenkov light, emitted by a certain source with properties θ. Since photon tables are always produced for one sensor type only, the wavelength acceptance of the sensor type in question is folded into the spectrum of emitted photons. This prevents the propagation of photons which have zero possibility of being detected, thus increasing computing efficiency. Instead of calculating if a photon is absorbed while propagating from one scattering point to the next, each photon has a unique weight proportional to its survival probability up to its current position times the wavelength acceptance of the sensor. Therefore, photons are propagated in small steps and at each step the angular sensitivity of a PMT within a DOM located at the current position is calculated. This sensitivity times the current weight of the photon, which is equal to the detection probability, is then stored. In favor of reducing the effects of statistical fluctuations, this process is done multiple times for the same source and the results are averaged. The necessity of discretizing the dimensions involved leads to an eight dimensional histogram of a photoelectron yield, two directional dimensions of the source $\theta_{\text{src}}, \phi_{\text{src}}$, three spatial and two directional dimensions for the position and orientation of the PMT, $\vec{X}, \theta_{\text{PMT}}$ and ϕ_{PMT} and one dimension for time, t. Including horizontal ice layers would add one extra dimension and tilted ice layers also one more.
The production of such a histogram with enough entries in each bin would required a tremendous amount of computing power and, at the same time, would be very hard to cross check. Therefore some steps have been taken in order to reduce the dimensionality. One measure undertaken is to assume horizontal ice layers, reducing the dimensionality by one. Since the IceCube DOM has only one PMT facing downwards, the directional dimensions of the PMT can be omitted as well, reducing dimensionality by another two dimensions. Ignoring the ice anisotropy enables ignoring the azimuthal direction of the source, which also reduces the dimensionality by one. Usage of horizontal ice layers enables taking advantage of the symmetry of the remaining situation. Only one half-sphere of the potential positions of the PMT, with the source at the center of the reference frame, needs to be stored. These steps reduce the dimensions of the remaining histogram from

ten to six.
To be able to reuse most of the already existing methods for the production of photon tables also for the mDOM, which has multiple PMTs looking in different directions, the inclusion of horizontal ice layers had to be dropped as well, thus reducing the amount of dimensions to five. Doing this, enables a reconstruction algorithm to simply rotate the reference frame such that the PMT for which the PDF needs to be evaluated is looking downwards. The photon tables, which then are used to obtain the PDF, are produced in a similar way to IceCube DOM photon tables. In practice, the source zenith angle θ_{src} has been decoupled from the other dimensions, which means that for each simulated source zenith angle a four dimensional histogram has been produced.
For this thesis, photon tables for two different source types have been produced: infinite tracks with a smooth continues light emission profile and point like sources with a cascade like emission profile. Since the acceptance functions of a PDOM PMT and a mDOM PMT are different, one set of photon tables per DOM type is required. For IceCube DOMs and PDOMs the same photon tables have been used, since these sensor types are, apart from a constant scaling factor of the quantum efficiency, essentially the same in terms of angular acceptance and wavelength dependence.

5.1.4.2 Integration of the Flat Disk Approach

In order to integrate the characteristics of a PMT inside an mDOM the code responsible for the production of photon tables for the PDOM had to be adjusted accordingly. To achieve a high agreement between simulation and photon tables, thus enabling better reconstruction results, the flat disk approach, as implemented in the normal simulation chain of CLSim, has been used here as well.
For each photon during the photon table production an interaction with an mDOM is enforced after each propagation step. At first, the center of the mDOM interacting with the photon in question is randomly chosen from a half sphere with radius $r_{\mathrm{mDOM}} = 17.8\,\mathrm{cm}$ centered at the current position of the photon (see figure 5.1). During the next step, the intersection of the prolonged photon path with a down-facing PMT, implemented as a flat disk, is checked (see figure 5.2). If the photon path hits the flat disk from ahead, the current photon weight is multiplied by $A(\theta)/\cos(\theta)$, to correct for the flat disks geometrical factor, and the corrected weight is added to the respective bin in a four dimensional histogram (three spatial dimensions and oen time dimension). The angle θ is the angle between the symmetry axis of the PMT and the incident direction of a photon (see figure 5.2). If the photon path missed the flat disk, no entry in the histogram is made. Afterwards, the photon is propagated by another step with its weight, position, direction and time updated accordingly. This process is repeated either, until all photons have reached a certain distance form their source, or until the photons weight has dropped below a certain threshold, similar to the table production for IceCube DOMs/PDOMs.

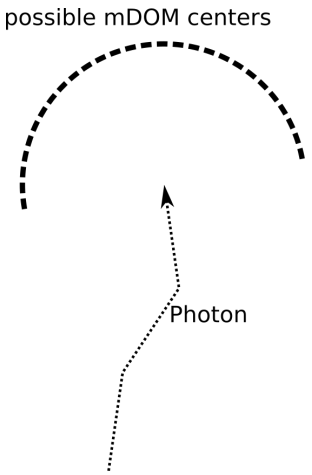

Figure 5.1: A possible mDOM center position is randomly chosen from a half sphere with radius $r_{\mathrm{mDOM}} = 17.8\,\mathrm{cm}$, dashed line, centered at the position of the photon, dotted line.

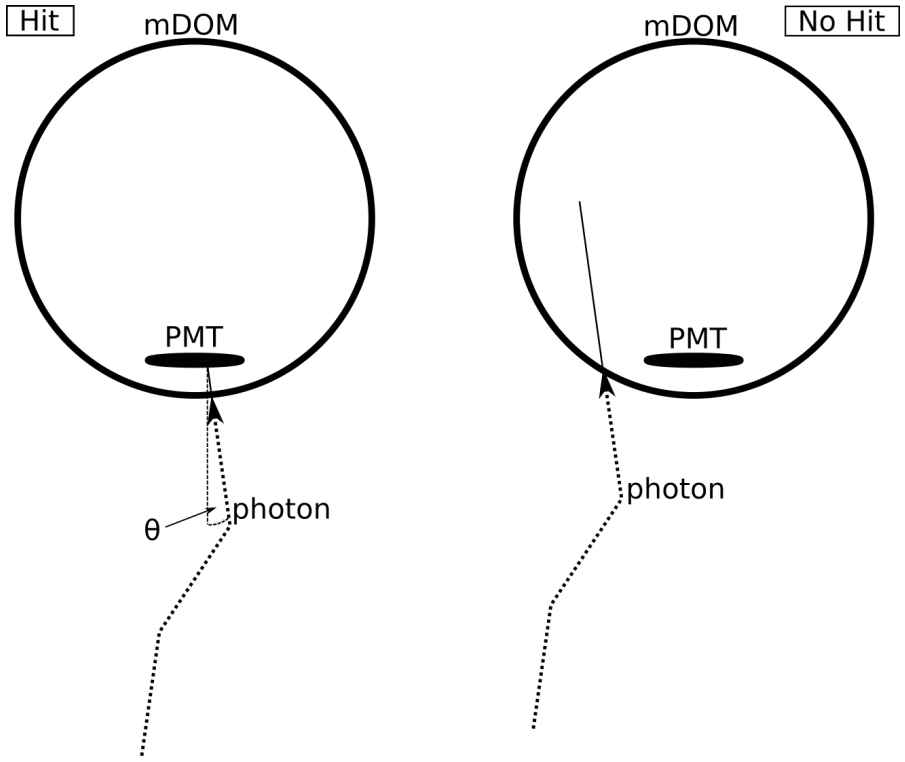

Figure 5.2: Visualization of the decision process whether a PMT is hit (left) or missed (right) during photon table production for mDOMs. The angle θ is the angle between the symmetry axis of the PMT and the incident direction of a photon.

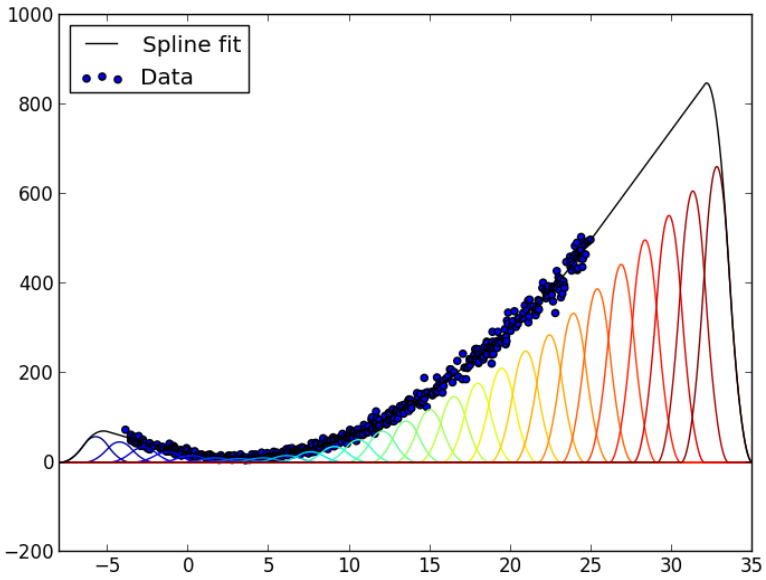

Figure 5.3: Spline fit (solid black line) with B-splines (colored lines) of order two to one dimensional data points (blue dots). Taken from [44].

5.1.4.3 Spline Fits of Photon Tables

The usage of these histograms as photon tables, as has been done in the past, does cause various numerical artifacts, like empty bins, bins with only a few entries or large statistical fluctuations [79]. Increasing the dimensionality, to incorporate more features of the ice for example, worsens these problems even further. In combination with the discretized nature of the histograms convergence problems of minimizers during reconstruction as a result of bumpy likelihoods have appeared.

A successful approach to remove all of these shortcomings is the use of penalized spline fits [25] instead of bare histograms. The basic idea behind this approach is to use a linear combination of Basis-splines, also called B-splines, to fit onto data points. In figure 5.3 this has been done with one dimensional data. Each of the colored curves represents one B-Spline of order two multiplied with a specific coefficient α_i, which is determined during the fitting process. The black line is the linear combination of all B-Splines. The fit curve can be written as:

$$S_{\vec{t},k}(x) = \sum_{i=1}^{I} \alpha_i B_{i,k}(x), \tag{5.10}$$

where $\vec{t}$ is the knot vector, which, roughly said defines the amount of B-splines used and the position of each B-spline, k is the order of the splines used, α_i represents the coefficient of each B-Spline and I is the total amount of B-splines used (depending on the knot vector). The B-Splines

can be expressed as [24]:

$$B_{i,1}(x) := \begin{cases} 1, & \text{if } t_i \leq x < t_{i+1} \\ 0, & \text{otherwise} \end{cases} \tag{5.11}$$

$$B_{i,k+1}(x) := \frac{x - t_i}{t_{i+k} - t_i} B_{i,k}(x) + \frac{t_{i+k+1} - x}{t_{i+k+1} - t_{i+1}} B_{i+i,k}(x). \tag{5.12}$$

The knot vector $\vec{t}$ and the order k are constants, whereas the coefficients α_i are determined during the fitting process. Only the knot vector, the order and the coefficients are needed to reproduce a spline curve, which makes it very efficient to store such a function. Furthermore, a spline curve of order $k \geq 1$ is smooth and $k-1$ times differentiable, which can be very useful for minimizers taking advantage of the first or second derivative of a function. A B-spline $B_{i,k}(x)$ is only non-zero for $t_i \leq x < t_{i+k+1}$, which makes the evaluation of a spline curve very fast and independent of the amount of B-splines used for the whole curve.
Extending this to n dimensions transforms equation 5.10 to

$$S(\vec{x}) = \sum_{i_1}^{I_1} \cdots \sum_{i_n}^{I_n} \alpha_{i_1 \cdots i_n} B_{m_i}^{i_1}(x_1) \cdots B_{m_n}^{i_n}(x_n), \tag{5.13}$$

while the knot vector $\vec{t}$ transforms to a n-dimensional knot grid and for each additional dimension the amount of coefficients increases as well.
The coefficients $\vec{\alpha}$ from equation 5.10 can be obtained with the least square approach:

$$M^\top M \vec{\alpha} = M^\top \vec{y}, \tag{5.14}$$

where M is a matrix with one column for each B-spline and one row for each data point: $M_{ij} = B_{j,k}(x_i)$. This procedure, however, can lead to severe overfitting, which, in turn, can cause problems when used by minimizers. To compensate for this, a regularization term can be introduced [25] turning equation 5.14 into:

$$(M^\top M + \lambda P^\top P)\vec{\alpha} = M^\top \vec{y}. \tag{5.15}$$

λ is hereby the strength of the regularization, also called smoothing parameter since larger values of λ enforce the spline fit to follow the general trend of the data instead of local features [79], thus substantially reducing ringing effects. For further details on the regularization of spline fits, also called penalized splines, and how P is defined, see [25].
For an efficient evaluation of the integrated time residual PDF, the cumulative distribution function (CDF) is fitted. To be able to derive the PDF, the CDF needs to be monotonically increasing, otherwise negative, unphysical values for the residual PDF might occur. Enforcing monotonicity in spline fits can be done by changing from a B-spline basis to a T-spline ("Trapezoidal" spline) basis [33], whereas a T-spline is defined by

$$T_j^k(x) = \sum_{m=j}^{N} B_m^k(x). \tag{5.16}$$

It can be shown, that a spline curve

$$S_{\vec{t},k+1}(x) = \sum_{j=-k}^{N} b_j T_j^{k+1}(x) \tag{5.17}$$

is monotonically increasing if all coefficients $b_j \geq 0$ [33].
An implementation of multi dimensional penalized spline fits with the possibility of enforcing monotonicity in certain dimensions has been realized within the "photospline" project [46] as part of the IceTray software framework of IceCube. This implementation has been used for all spline fits needed for this work.

5.1.4.4 Photon Table Sanity Checks

In order to ensure that the spline fitting process of the photon tables does yield good results and to avoid introducing a bias of the later comparison of results obtained with mDOMs and PDOMs, sanity checks of the spline fits have been conducted during this work. These checks have been executed in two stages.

Overall Sanity Checks Within the first stage, overall quality checks of each table have been performed to check for unexpected or obviously unphysical behavior and convergence of the integrated time residual PDFs. To accomplish this, the test procedure loads the produced spline tables and generates plots of the time residual function and the amplitude for different source orientations with respect to sensor positions. Due to the simplifications and symmetries described in section 5.1.4.1, this is a four-dimensional problem for the amplitude and a five-dimensional problem for the time residual functions. To produce two-dimensional plots, amplitude versus distance for example, the radius is varied while the other dimension have been fixed to certain values.
Since photon tables for two source and two sensor types have been produced in this context, even a step size of 10° would produce a large amount of plots. Two of these plots are presented here, while more plots have been moved to appendix A.

Figure 5.4 shows one of these plots obtained with the mDOM cascade spline table with $\theta_{\text{source}} = 120°$. On the left hand side the amplitude is plotted versus azimuth ϕ_{PMT}, zenith θ_{PMT} and distance between source and sensor (denoted as radius in this context), while on the right hand side the time residual PDF for three specific values of the respective coordinate is shown. For cascade spline tables a spherical coordinate system is used with the light source at the center. Each parameter, that is neither on one of the axis nor explicitly mentioned in the respective legend of a plot is fixed to a reasonable but arbitrary value.
The upper left plot shows the amplitude versus the azimuth coordinate of the sensor for three different radii (θ_{PMT} is fixed to 45°). Three things can be checked with this plot: first, the amplitude decreases with increasing distance from the source. Second, the amplitude is symmetrical with respect to ϕ_{PMT}. And third, the visibility of the Cherenkov angle, which causes the two

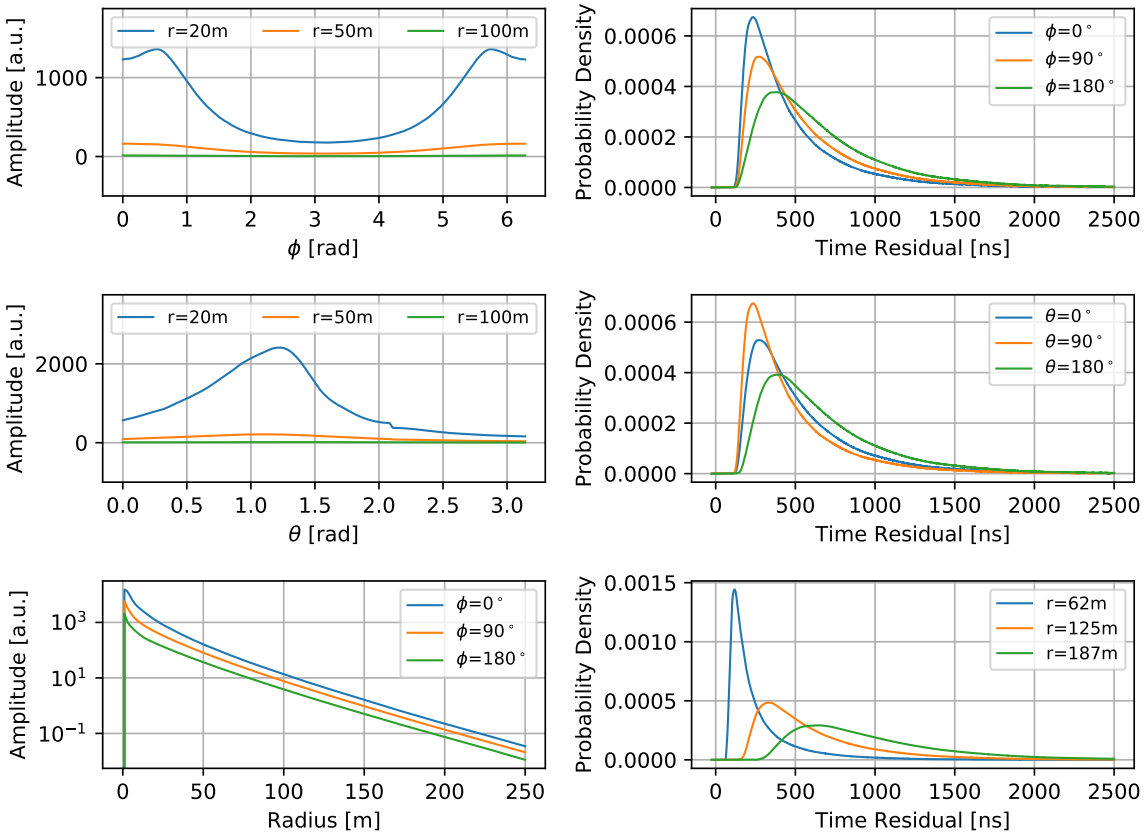

Figure 5.4: Fitted mDOM cascade photon table spline curves for $\theta_{\text{src}} = 120°$. *Top left:* Amplitude versus ϕ_{PMT} for three different radii with a fixed value of $\theta_{\text{PMT}} = 45°$. *Center left:* Amplitude versus θ_{PMT} for three different radii with a fixed value of $\phi_{\text{PMT}} = 0°$. *Bottom left:* Amplitude versus radius for three different PMT azimuth angles with a fixed value of $\theta_{\text{PMT}} = 45°$. *Top right:* Probability density versus time residual for three different PMT azimuth angles with a fixed radius r=100 m and a fixed value of $\theta_{\text{PMT}} = 45°$. *Center right:* Probability density versus time residual for three different PMT zenith angles with fixed a radius r=100 m and a fixed value of $\phi_{\text{PMT}} = 0°$. *Bottom right:* Probability density versus time residual for three different PMT radii with a fixed value of $\theta_{\text{PMT}} = 90°$ and fixed value of $\phi_{\text{PMT}} = 0°$. The color code is different for each plot.

peaks at the right and left hand side of the plot. The upper right plot shows the time residual distribution for three distinct values of ϕ_{PMT} (the color code is different for each plot!), with $\theta_{\mathrm{PMT}} = 45^\circ$ and radius= 100 m. The first aspect to notice is the changing shape of the curve with varying values of ϕ_{PMT}. With increasing values of ϕ_{PMT}, up to 180°, the detection probability of a sensor decreases, causing the curve to get broader and more shallow. Since the distance is the same for all three curves, the earliest possible detection time is approximately the same for all three curves and at the same time all curves converge to zero with increasing time. The last aspect can be summarized to the convergence of the integrated time residual functions, so the CDFs, to unity. This has been explicitly checked every time values from a spline table are read without any differences larger then 0.01 being found.
The center left plot shows the amplitude versus θ_{PMT}, again for three different radii ($\phi_{\mathrm{PMT}} = 0^\circ$), while the center right plot displays the time residual function for three distinct values of θ_{PMT}. Apart from the more distinct peak caused by the characteristic emission profile of Cherenkov light sources a small kink is visible in the blue curve of the center left plot. Although penalized splines were chosen to explicitly reduce the effect of statistical fluctuations and possible binning effects, it cannot be excluded with complete certainty that at some positions within the parameter space of the spline fits unphysical characteristics like this kink are still present. However, it is assumed that such small artifacts do not have large effects on reconstruction results, while, at the same time, are extremely hard to detect due to the large parameter space. The center right plot does not show any unintended behavior, but, similar to the upper right plot, correctly reflects a change of shape of the time residual PDF when the sensor orientation with respect to the source becomes more unfavorable.
The bottom two plots are produced in a similar fashion, but now with the radius as the parameter of interest. The bottom right plot correctly displays the expected decrease of the amplitude with an increase of distance between light source and sensor. Similar to the other time residual plots, the shape of the PDF changes towards a broader and more shallow characteristic with less advantageous sensor positions. An additional feature visible in this plot is the shift of the rising edge towards later times with increasing distance. This is caused by the fact that the photons have to cover a larger distance before reaching the sensor, which also increases the chance of being scattered or absorbed.
A similar figure was made with a PDOM infinite track spline table (see figure 5.5). For an infinite track as a light source, it makes more sense to use a cylindrical coordinate system with the track as longitudinal axis. Consequently, there is no θ_{PMT} coordinate, but a $\mathrm{Z}_{\mathrm{PMT}}$ coordinate instead. Since a homogeneous ice model has been used to produce these tables, the expected amplitude while varying the sensor position along the longitudinal axis (center left plot) should be constant, but a small change is visible. This is, similar to the kink in the center left plot of figure 5.4, believed to be a deficiency of how these tables were produced, so most likely statistical fluctuations within the histograms that have not been flattened entirely by the penalized spline

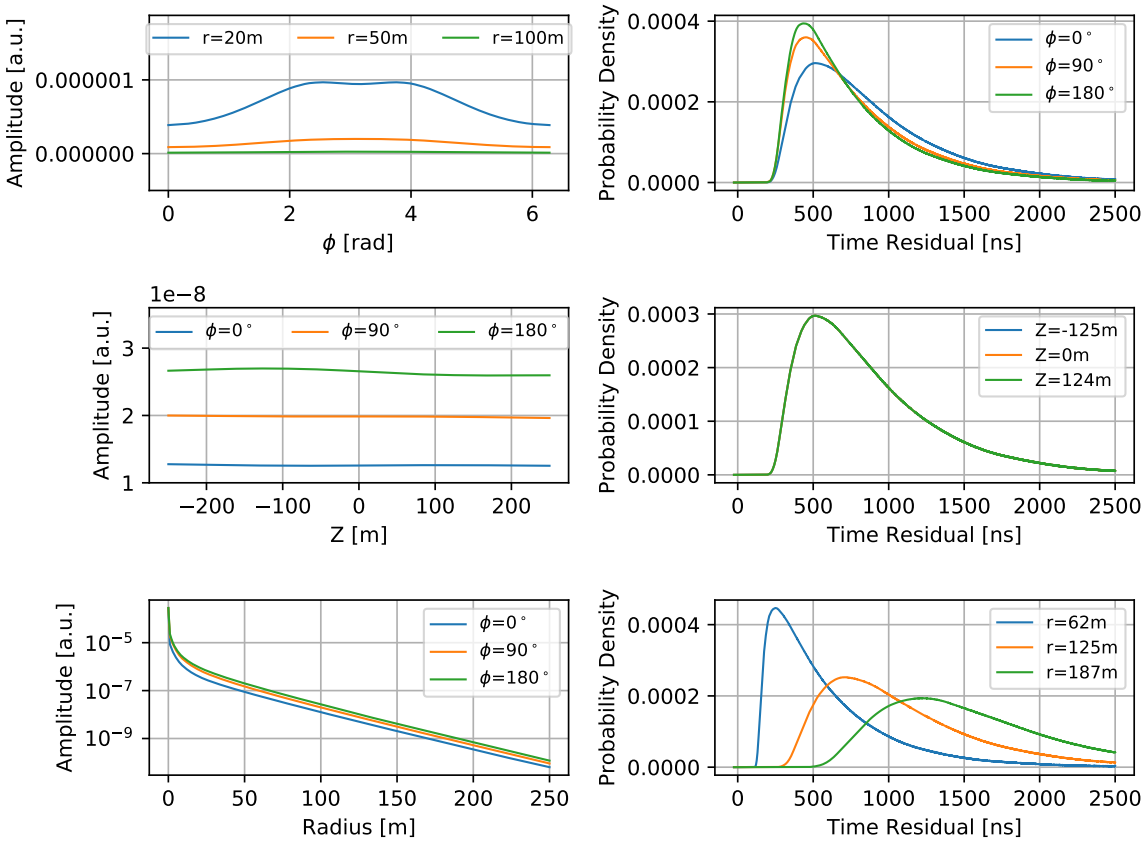

Figure 5.5: Fitted PDOM infinite track photon table spline curves for $\theta_{\text{src}} = 70°$. *Top left:* Amplitude versus ϕ_{PMT} for three different radii with a fixed value of $Z_{\text{PMT}} = 1.6\,\text{m}$. *Center left:* Amplitude versus Z_{PMT} for three different PMT azimuth angles and fixed a radius of r=100 m. *Bottom left:* Amplitude versus radius for three different PMT azimuth angles with a fixed value of $Z_{\text{PMT}} = 1.6\,\text{m}$. *Top right:* Probability density versus time residual for three different PMT azimuth angles with a fixed radius r=100 m and a fixed value of $Z_{\text{PMT}} = 1.6\,\text{m}$. *Center right:* Probability density versus time residual for three different values of Z_{PMT} with a fixed radius r=100 m and a fixed value of $\phi_{\text{PMT}} = 0°$. *Bottom right:* Probability density versus time residual for three different PMT radii with a fixed value of $Z_{\text{PMT}} = 1.6\,\text{m}$ and a fixed value of $\phi_{\text{PMT}} = 0°$. The color code is different for each plot.

fitting procedure.

In summary, the quality check of the produced photon tables and spline tables did not expose any critical errors or behavior.

Quantitative Sanity Checks During the second stage a Kolmogorov-Smirnov test (KS test) was applied to compare the CDF from the spline fit tables to the empirical cumulative distribution function (ECDF) obtained from simulated events. The KS test allows quantifying the

statistical goodness of fit, while the usage of simulated events enables to test in multiple regions of the parameter space of the spline tables without the need of producing time consuming new simulations.
The test statistic of a KS test, D, is the maximum deviation of the observed distribution, the ECDF from the simulated events, denoted as $S_N(t)$, from the expected distribution, the spline table CDF, denoted as $F(t)$ [28]:

$$D_N = \max|S_N(t) - F(t)| \quad \text{for all } t \tag{5.18}$$

Hereby is N the number of data points. When

$$D_N > \frac{K_\alpha}{\sqrt{N}} \tag{5.19}$$

the hypothesis, in this case $F(t)$ describes the distribution of the data, is rejected with a significance level of α. For $N > 35$, K_α can be approximated by $\sqrt{-0.5\ln(\alpha/2)}$, while for smaller samples tabulated values are used [57].
The ECDF can be defined as

$$S(t) = \frac{1}{N}\sum_{i=1}^{N} H(t - t_i) \quad \text{, with} \tag{5.20}$$

$$H(x) = \begin{cases} 0, & x < 0, \\ 1, & x \geq 0. \end{cases} \tag{5.21}$$

Within this context, $N = N_{\text{PMT}}$ is the total amount of detected photons on one PMT and t_i is the individual arrival time.
The whole test procedure can be summarized in two steps per PMT. The first step is to create a "spline service object", which is basically the function $\mathcal{T}_{\theta,\zeta}$ from equation 5.9. The ice properties ζ are already included in the produced spline tables, but the characteristics of the light emitters differ from event to event (different muon, different stochastic losses), which has to be taken into account. To accomplish this the algorithm iterates over all simulated light sources, which have been produced by the PROPOSAL package, and calculates the CDF as well as the expected amount of photons for each light emitter per PMT. The CDFs are weighted with the expected amount of photons, summed up and renormalized. This yields the total CDF for a PMT given a certain combination of light sources, $F(t)$. Next, the ECDF, $S(t)$ is calculated for the PMT in question. For this step only the arrival times of detected photons without any noise, PMT or electronic effects are considered, since these effects are not part of the photon table production chain. With the total CDF from the spline tables and the ECDF from the event itself, the test statistic D can be obtained according to equation 5.18.
An example of the so obtained distributions is shown in figure 5.6 for a PMT within an mDOM. The PMT displayed in this figure detected a total of 193 photons at a distance (closest distance between muon track and the PMT in question) of 60 m. Three distinct peaks are visible within

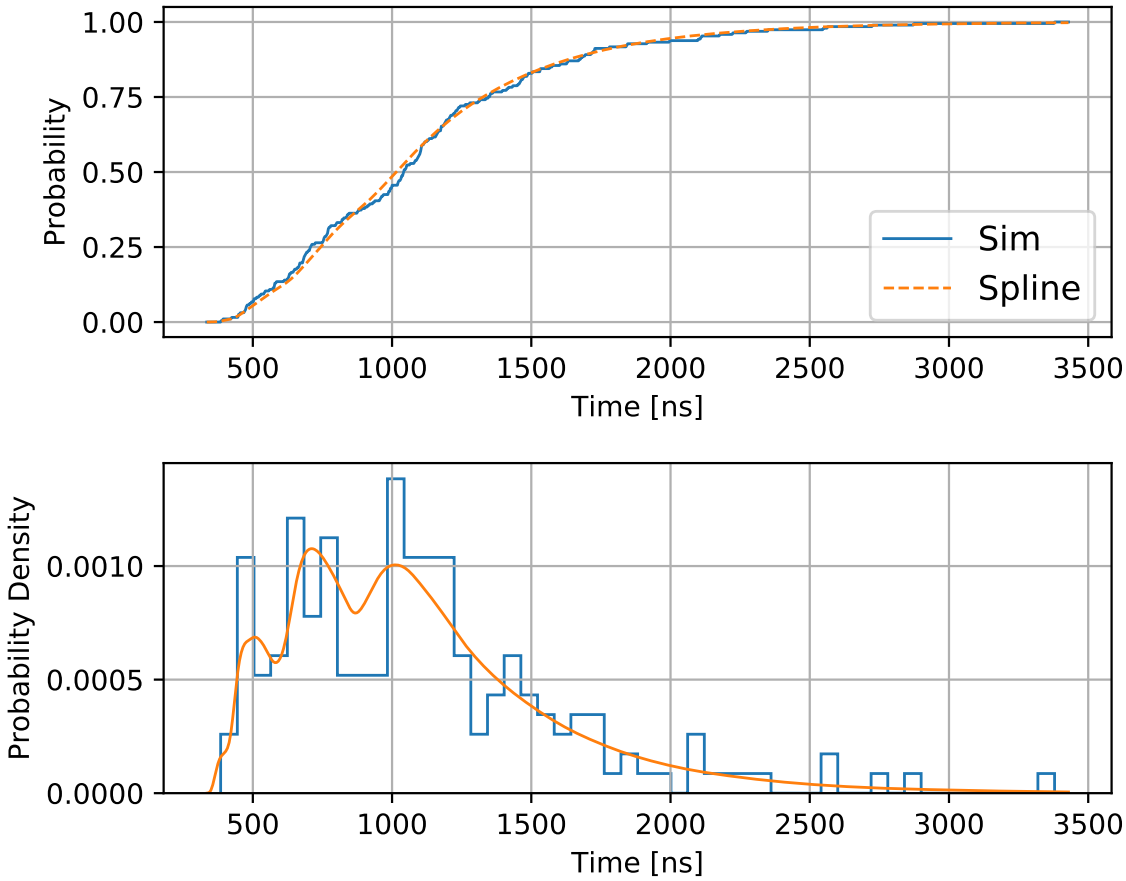

Figure 5.6: Comparison of the mDOM spline tables to the normal simulation of a 76 PeV through-going muon event with a minimal distance between track and PMT of 60 m. *Top:* ECDF (blue solid line) obtained from the normal simulation compared to the CDF (dashed orange line) from the spline tables for a PMT within a mDOM. *Bottom:* Normalized histogram of the binned arrival times from the simulation (blue) compared to the PDF from the spline tables (orange).

the bottom plot of this figure both, in the orange curve and the blue histogram. This is most likely caused by three stochastic losses, leading to three distinct cascades, along the muon path. Each of these cascades produced light which arrived at the PMT at different times creating the observed distribution. The positioning of these peaks in the two curves as well as their hight seems to be in good agreement. Comparing the ECDF (blue solid line, top plot) from the simulation to the CDF (orange dashed line, top plot) to each other suggests conformity as well. With the test statistic $D = 0.044$, $N = 193$ and a significance level of $\alpha = 0.01$ ($K_\alpha = 1.63$) the hypothesis, that the data (blue curves) is distributed according to the distribution form the spline tables (orange curves) cannot be rejected and is therefore accepted.
A similar figure (figure 5.7) has been produced for the PMT within a PDOM. In this case 2911 photons have been detected by this particular PMT at a distance of 110 m to the track. The shape in this example is dominated by one large distinct peak, probably caused by one high energetic cascade on the track within the vicinity of the DOM. As well as in the previous example, a good agreement between the orange and the blue curves is visible. With $D = 0.014$, $N = 2911$ and $\alpha = 0.01$ ($K_\alpha = 1.63$) the hypothesis, the data is distributed according to the curves from the spline tables, cannot be rejected hence, is also accepted.
In order to obtain a quantity describing the overall agreement between spline tables and normal simulations, denoted by Δ in this context, the KS-test has been applied to ≈ 14000 PMTs of multiple events in the low-, mid- and high-energy range of the dataset 20198, for both, the nominal mDOM and the upscaled PDOM. The parameter Δ is defined as the ratio of tests passed over tests conducted and can now be used to compare the quality of the spline tables of the two sensor types to each other. The obtained values including the estimated standard error intervals are $\Delta_{\text{mDOM}} = 0.8440 \pm 0.0031$ and $\Delta_{\text{PDOM}} = 0.8116 \pm 0.0033$, which indicate a slightly better conformity for the mDOM then for the PDOM.

5.2 Quality Cuts

Before an unbiased comparison of the angular resolutions obtained with the two different sensor types can be conducted, quality cuts for the event selection have to be applied. The original motivation of quality cuts is to reduce the amount of background and badly reconstructed events within a data sample before an analysis is carried out. At this point of the thesis background does not play any role, but a reduction of badly reconstructed events is desirable on the one hand, to work out more clearly the improvement on angular resolution due to the segmented sensor, and on the other hand to be able to compare the performance on a level which is relevant for possible future analyses.
However, the parameters which are normally used for quality cuts are sensor-dependent and there is the risk of introducing a bias by applying standard quality cuts. To be able to achieve an

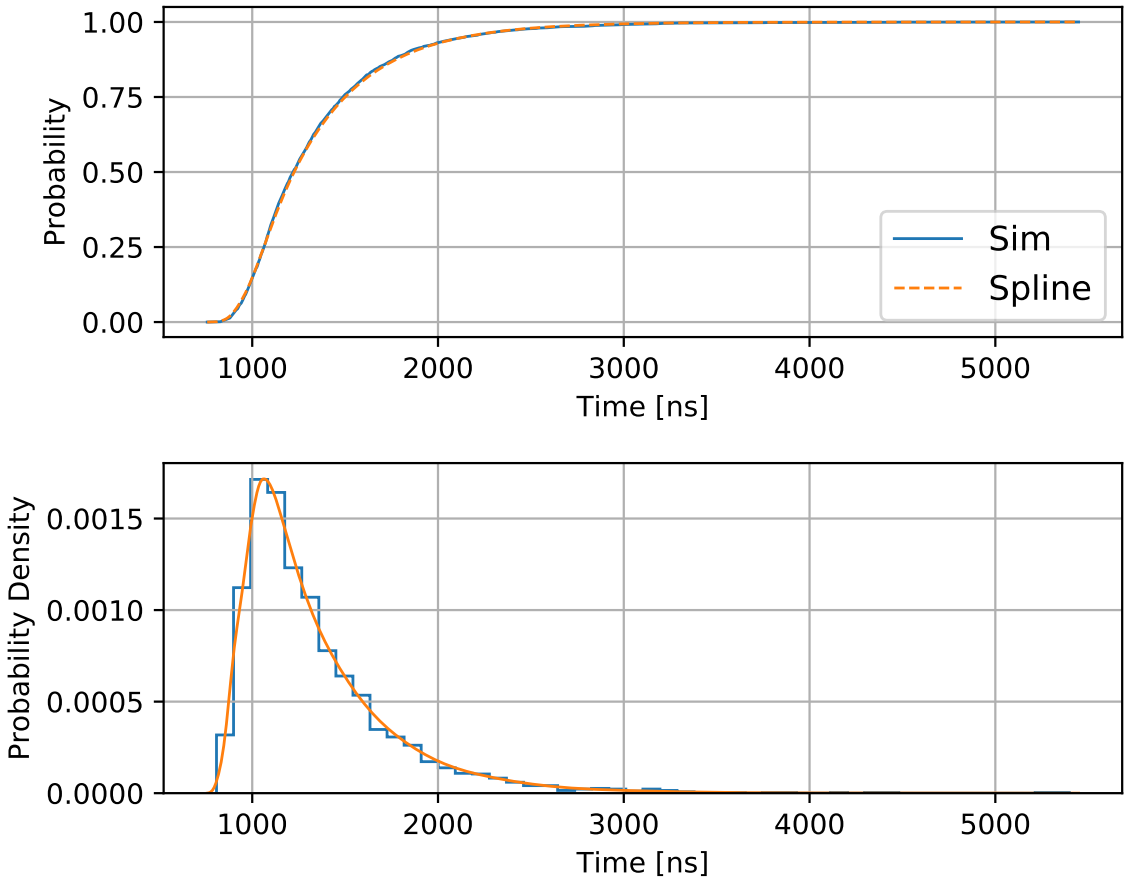

Figure 5.7: Comparison of the PDOM spline tables to the normal simulation of a 95 PeV through-going muon event with a minimal distance between track and PMT of 110 m. *Top:* ECDF (blue solid line) obtained from the normal simulation compared to the CDF (dashed orange line) from the spline tables for the PMT within a PDOM. *Bottom:* Normalized histogram of the binned arrival times from the simulation (blue) compared to the PDF from the spline tables (orange).

unbiased comparison of the performance of the two sensor types, sensor-independent quality cuts have been defined and applied.

5.2.1 Sensor-Dependent Quality Cut Parameters

Two of the most used parameters utilized as quality cuts for the event selection are the parameters called "NDir" and "LDir". In order to calculate these two quantities for an event, a reconstructed track hypothesis is needed, as well as the information which PMT has seen how much light. Both of these informations obviously depend on the simulated sensor.

5.2.1.1 Number of Direct Hits

Number of direct hits, abbreviated as "NDir" is the amount of "direct hits" which have been identified for a specific event. A "direct hit" is supposed to be a detected, unscattered photon which propagated directly from the hypothetic source to the PMT. If the exact trajectory of the muon, the exact optical properties of the ice as well as the wavelength of the photon in question is known one can calculate the exact arrival time of a potential direct photon at the PMT. Since all of these properties are only know to a certain limit, a time window of $\pm 15\,\text{ns}$ around the expected arrival time is defined. If a photon is detected within this time window, it is labeled as a direct hit. To make this parameter more stringent "NDir" is not equal to the actual amount of detected hits that meet the direct hit criterion, but set equal to the number of DOMs that have detected at least one hit labeled as direct hit.
The main intention of using "NDir" as a parameter for a quality cut is to have a proxy on the quality of the reconstructed track. A better agreement between the reconstructed and the actual muon trajectory increases the probability of labeling a detected photon as direct hit. Consequently, more direct hits should mean a better reconstruction result. Figure 5.8 shows the two dimensional histogram of dataset 20198 (simulated with the downscaled mDOM) binned in "NDir" and the opening angle (=angular difference between true muon direction and reconstructed muon direction). It can be seen, that all events with a large opening angle, hence a badly reconstruction result, tend to have a lower value of "NDir". The orange vertical line within these two plots marks a threshold of "NDir"=6. Using this threshold would dismiss every event left of that line, thus removing almost all events with an opening angle of $\geq 20°$, but also lots of events with an opening angle of $\leq 1°$, as can be seen in the zoomed in plot.

5.2.1.2 Projected Distance Between Direct Hits

The second sensor-dependent parameter used for a quality cut in this work is the largest projected distance between direct hits, called "LDir". This parameter is obtained by projecting every direct hit back to the assumed point of emission on the reconstructed muon trajectory and then calculating the larges distance between two assumed emission points. The definition of "LDir"

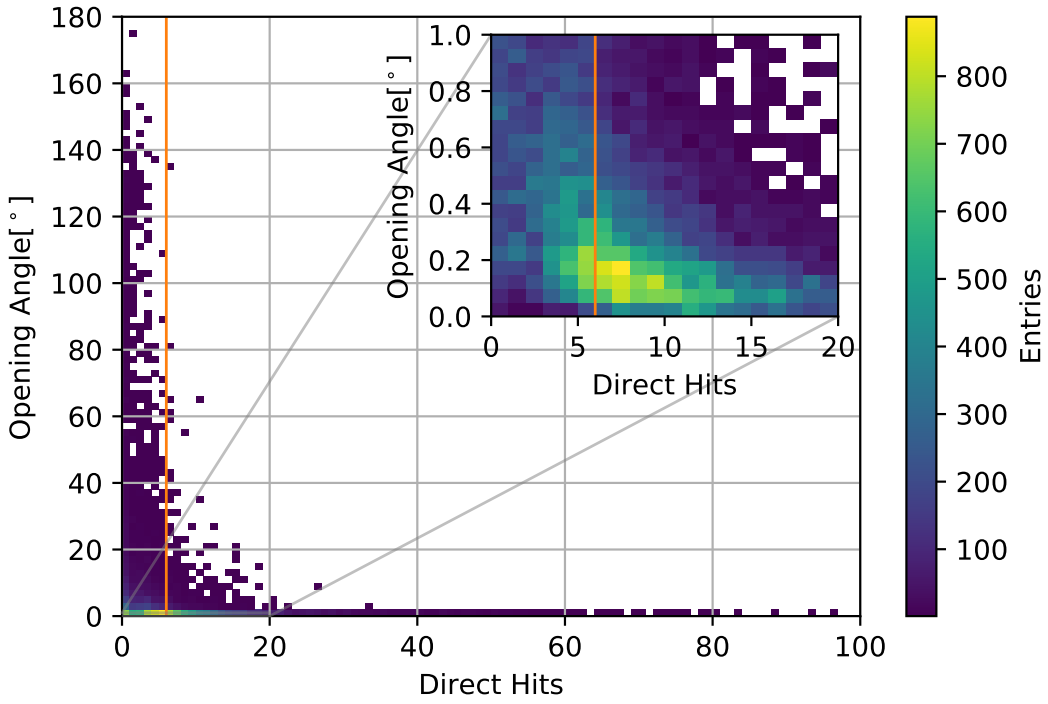

Figure 5.8: Two dimensional histogram of dataset 20198 of the downscaled mDOM binned in NDir and opening angle. The vertical orange line marks the threshold of NDir = 6. The scale on the color bar is only valid for the full size plot. For the zoomed in figure the scale is about 1/10 of the full size plot.

is motivated by two concepts. First, a larger value of "LDir" should remove so-called "corner-clippers" from the final sample, so events where the muon penetrates the instrumented volume only at the edge of the detector, thus emitting only a limited amount of photons that can be detected. And second, large values of "LDir" mean that two modules with a large distance have detected hits, that are labeled as direct hits. The larger the value of "LDir", the larger the distance between these two modules, which translates into a larger lever arm and therefore into more stringent constrains for the direction of the muon, leading to a better reconstruction result.
Figure 5.9 shows the two-dimensional histogram of dataset 20198 (downscaled mDOM), binned in "LDir" and opening angle. Similar to "NDir", a negative correlation between the opening angle and the value of "LDir" is visible. A threshold of "LDir"$\geq 120\,\mathrm{m}$ was used within this work (indicated as the orange line in the plots).

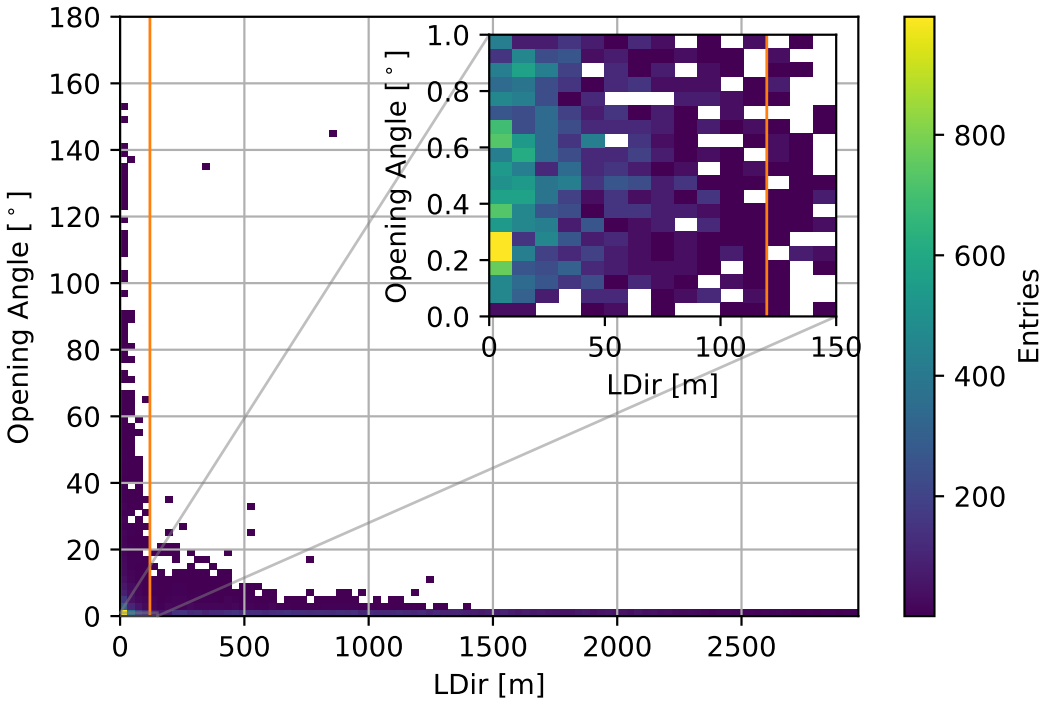

Figure 5.9: Two dimensional histogram of dataset 20198 of the downscaled mDOM binned in LDir and opening angle. The vertical orange line marks the threshold of LDir = 120. The scale on the color bar is only valid for the full size plot. For the zoomed in figure the scale is about 1/10 of the full size plot.

5.2.2 A Sensor-Independent Quality Cut Parameter

To be able to compare the angular resolution of a data set achieved with different sensor types without introducing a bias and still remove badly reconstructed events it is useful to define sensor-independent, MC-based cuts. For this purpose the length of the muon within the vicinity of the detector is used. The longer a muon propagates through the detector, the more light can be detected, while more detected hits provide more information and more information consequently lead to better reconstruction results. Furthermore, a longer lever arm means more stringent constrains on the possible muon directions, which should also consequently translate into a better reconstruction.

In order to obtain this value, a convex hull surrounding all modules of the detector is computed. Afterwards, the intersection points of the muon with the convex hull are calculated with the usage of the Monte Carlo information. The distance between these two points is then defined as the "MCLength".

In figure 5.10 two two-dimensional histograms are shown of dataset 20198 (downscaled mDOM)

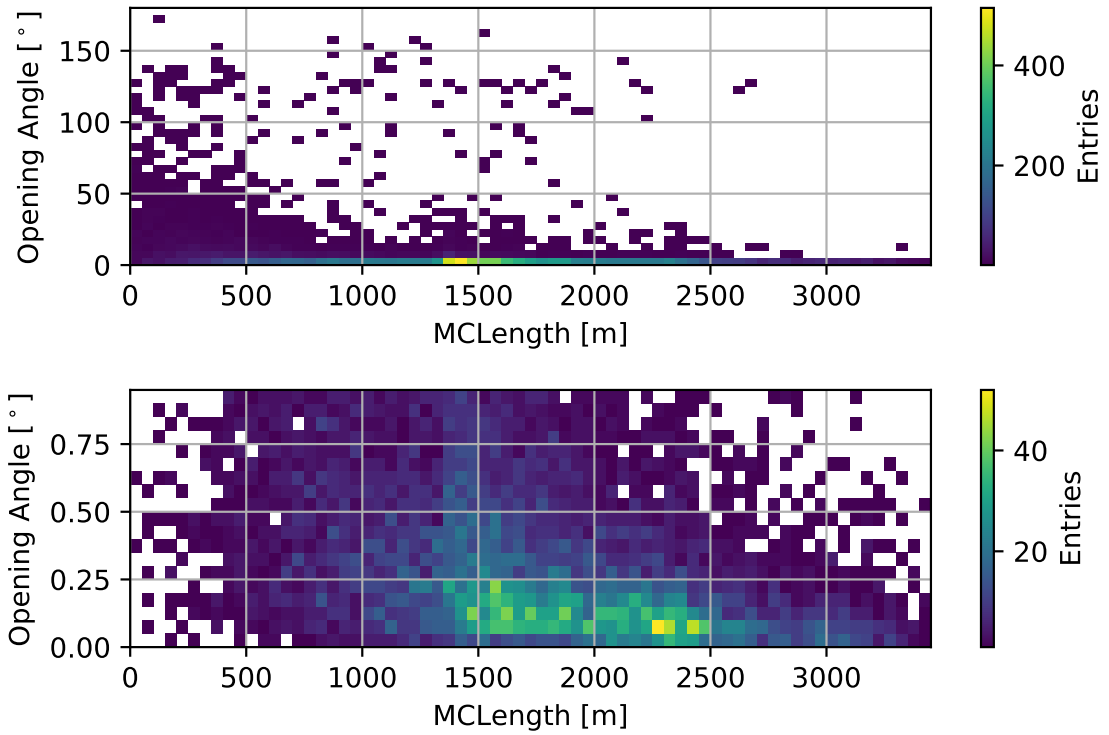

Figure 5.10: Two dimensional histogram of dataset 20198 of the downscaled mDOM binned in MCLength and opening angle.

binned in MCLength and opening angle. A negative correlation between MCLength and opening angle is visible, but the overall behavior of the MCLength as a quality cut parameter differs compared to NDir or LDir. It differs on the one hand, that events with a large opening angle are more spread out throughout the parameter space, which makes it impossible to remove these completely. On the other hand, events with a good reconstruction result tend to have a larger MCLength, thus, a cut on this parameter does not remove as many "good" events as a cut on LDir for example.

5.3 Muon Track Reconstruction with SplineMPE

At the time of this writing, SplineMPE was the standard track reconstruction algorithm in IceCube. Therefore, the main goal of this thesis was to compare the angular resolution obtained with SplineMPE of the Gen2 high-energy array equipped with mDOMs to the angular resolution of the Gen2 high-energy array equipped with PDOMs, also obtained with SplineMPE. These results will be presented in this section. All obtained results only compare sensors with equalized effective photocathode areas (see section 4.2.1).

5.3.1 Preprocessing and the Application of Quality Cuts

Before the obtained angular resolutions of two datasets are compared to each other, a few preprocessing steps are applied. One of them is to ensure, that the two datasets, which are compared, contain exactly the same events. Unless explicitly mentioned, all datasets, which were used to produce a plot, have been prepared in this manner.
The next step, before any resolutions are compared, is the application of quality cuts (see section 5.2). Two different sets of quality cuts have been used independently. The first set of cuts, denoted here as "standard cuts", only contains cuts on sensor-dependent parameters, namely "NDir" and "LDir", which are calculated without the usage of any Monte Carlo information. The exact cut values, for events to be kept within the dataset, are

- NDir ≥ 6 , and
- LDir $\geq 120\,\mathrm{m}$.

All events, that do not satisfy all of these conditions will be removed. Since these two parameters are sensor-dependent, a cut on these values removes a different amount of events from the dataset depending on what sensor type was used during the simulation of the set in question. This effects the obtained angular resolution and the obtainable sensitivity (see chapter 6).
The second set of cuts, actually it is just one cut at a time, denoted as "Monte Carlo Cuts (MC Cuts)", use the sensor-independent parameter "MCLength". Comparisons have been made after the application of different thresholds for "MCLengths". Each plot or result explicitly contains the applied value. Contrary to the standard cuts, a cut on a Monte Carlo parameter is sensor-independent, given the fact that the datasets contain the exact same events before the cut is applied. Therefore, the remaining amount of events after the application of the Monte Carlo Cut stays equal for the two datasets being compared. The usage of these cuts enables the exact comparison of the achievable angular resolution of two datasets, but, since Monte Carlo information is being used, this cut cannot be used in the calculation of a detector point source sensitivity.

5.3.2 Combination of Datasets 20016 and 20198

The best angular resolution can be obtained from a muon originating near the horizon, so muons with a zenith angle between 85° and 95°. These particles produce the longest track within the instrumented volume of the detector and have the longest lever arm for reconstruction. In combination with the suppressed atmospheric muon background the highest sensitivity of the IceCube-Gen2 high-energy array for point sources is expected to be at the horizon. Since the amount of events within a zenith band of $85^\circ < \theta_\mu < 95^\circ$ of dataset 20198 is rather low, dataset 20016, which contains only horizontal events but is equal in any other aspect, has been included

into the analysis of the angular resolution. The corresponding sanity checks have been moved to appendix B.

5.3.3 Reconstruction Chain

Most reconstruction strategies used nowadays are successive processes. This usually means, that a faster, but less advanced, algorithm is the first step of the reconstruction chain, followed by increasingly complex and mostly slower algorithms. One common reason for this approach is to reduce the processing time. This is achieved by providing the complex reconstruction algorithm with the result of the faster algorithm as seed. The faster algorithm starts its minimization process already close to the optimal solution meaning that the total amount of minimization cycles is reduced and fewer evaluations of the likelihood function are needed.
Within this work the successive reconstruction with different algorithms has been used in order to reconstruct muon tracks. The MuEx reconstruction is used as a first guess algorithm, hence providing a seed for the more complex SplineMPE reconstruction. SplineMPE is applied at first in a so-called "default" mode, producing a more accurate seed, which is then used by SplineMPE in "recommended" mode. The difference between these two modes boils down to the inclusion of the jitter (see section 4.1.3.1) in the likelihood function and a hit cleaning strategy, both only utilized by SplineMPE while in the "recommended" setting.
The inclusion of the jitter is implemented by convolving the MPE PDF (see eq. 5.7) with a guassian with $\sigma = 2\,\text{ns}$:

$$\text{PDF}_{\text{MPE,rec}}(t) = \text{PDF}_{\text{MPE}}(t) * \mathcal{N}(t, \sigma^2) = \int \text{PDF}_{\text{MPE}}(\tau) \cdot \mathcal{N}(t - \tau, \sigma^2) d\tau \tag{5.22}$$

The hit cleaning process compares the ECDF of the arrival times of photons on a PMT with the CDF obtained from the spline tables, using the provided seed as the hypothesis. This is an iterative process, utilizing a Kolmogorov-Smirnov test. The last detected photon is successively removed until either the obtained test statistic is under the desired threshold (requiring a significance level of 80 %) or until only one photon is left. Keeping in mind, that the hit cleaning is only done at the very first iteration of the reconstruction process (of SplineMPE in "recommended" mode), it is obvious why this hit cleaning strategy is only applied during the last step of the reconstruction chain. Using a hit cleaning like this with a bad seed would remove too many photons, thus increasing the risk of a suboptimal reconstruction result.

5.3.4 Angular Resolution

Within this section the angular resolution as a function of the true muon energy (MCEnergy) obtained by the IceCube-Gen2 high-energy array equipped with either nominal mDOMs (2.24)[1] or

[1] For the rest of this thesis an abbreviation, especially in figures, is used: <sensor type>(effective area in units of the nominal PDOM). mDOM (2.24) stands for the nominal mDOM, mDOM (1.0) for the downscaled mDOM, PDOM (2.24) is short for the upscaled PDOM and PDOM (1.0) is an abbreviation for the nominal PDOM.

upscaled PDOMs (2.24) will be presented and compared to each other. Apart from a dependence on the energy, the angular resolution also depends on the zenith angle of the muon, therefore the results are also split into three different zenith bands: muons with a zenith angle near the horizon, up-going and down-going muons. Different results for up- and down-going muons are expected since the acceptance of the PDOM is more sensitive to up-going light, while the acceptance of a mDOM (the whole module) is almost uniform over the whole solid angle (see figure 3.22). In the following, the opening angle between the reconstructed muon direction and the true muon direction is denoted as Ψ. The vertical error bars in the following figures indicate the standard error while the horizontal error bars show the width of the respective energy bin.

5.3.4.1 Horizontal Muons

The horizontal zenith band contains all muons with $85° \leq \theta_\mu \leq 95°$.

Cut: MCLength > 1000 m Figure 5.11 shows the angular resolution for muons in the horizontal band binned in energy for the nominal mDOM (2.24) and the upscaled PDOM (2.24). As cut value the parameter MCLength was used with a threshold of 1000 m in order to remove a large portion of badly reconstructed events. After the cut, 15416 out of 18934 events remain in the data sample, which is equal to an overall efficiency of 81.4%.
Throughout the whole energy range, a significant improvement of the angular resolution achieved with the nominal mDOM (2.24) is visible when compared to the respective values obtained with the upscaled PDOM (2.24). Below a muon energy of 100 TeV, the improvement is in the area of 10 % – 15 %, increasing to more then 20 % – 40 % for higher energies. A shift of the minimum opening angle can be seen when the two curves are compared. While the best angular resolution with the upscaled PDOM (2.24) is obtained at an energy around 1 PeV, the opening angle achieved with the nominal mDOM (2.24) continuously decreases until a muon energy around 10 PeV before it starts to increase again. Similar results are obtained by comparing the angular resolution of the downscaled mDOM (1.0) with the nominal PDOM (1.0) (see figure C.1 in the appendix).

Cut: Standard Cuts The angular resolutions obtained after the application of the standard cuts (NDir≥ 6 and LDir≥ 120 m) is presented in figure 5.12. Since these cuts are sensor-dependent, different efficiencies for the two sensor types are obtained. With the nominal mDOM (2.24) 12689 out of 18934 events remain in the sample, yielding an overall efficiency of 67.0 %. A detector equipped with upscaled PDOMs (2.24) achieves a smaller efficiency of 63.7 % with 12066 out of 18934 events remaining in the data sample, although the efficiencies become similar at energies of ≈ 300 TeV and above.
In regards of the angular resolution, the application of the standard cuts yields a slightly reduced improvement of the angular resolution compared to the results obtained with the Monte Carlo cut, however, with an increased efficiency of the mDOM at lower energies. Below 3 PeV the angular

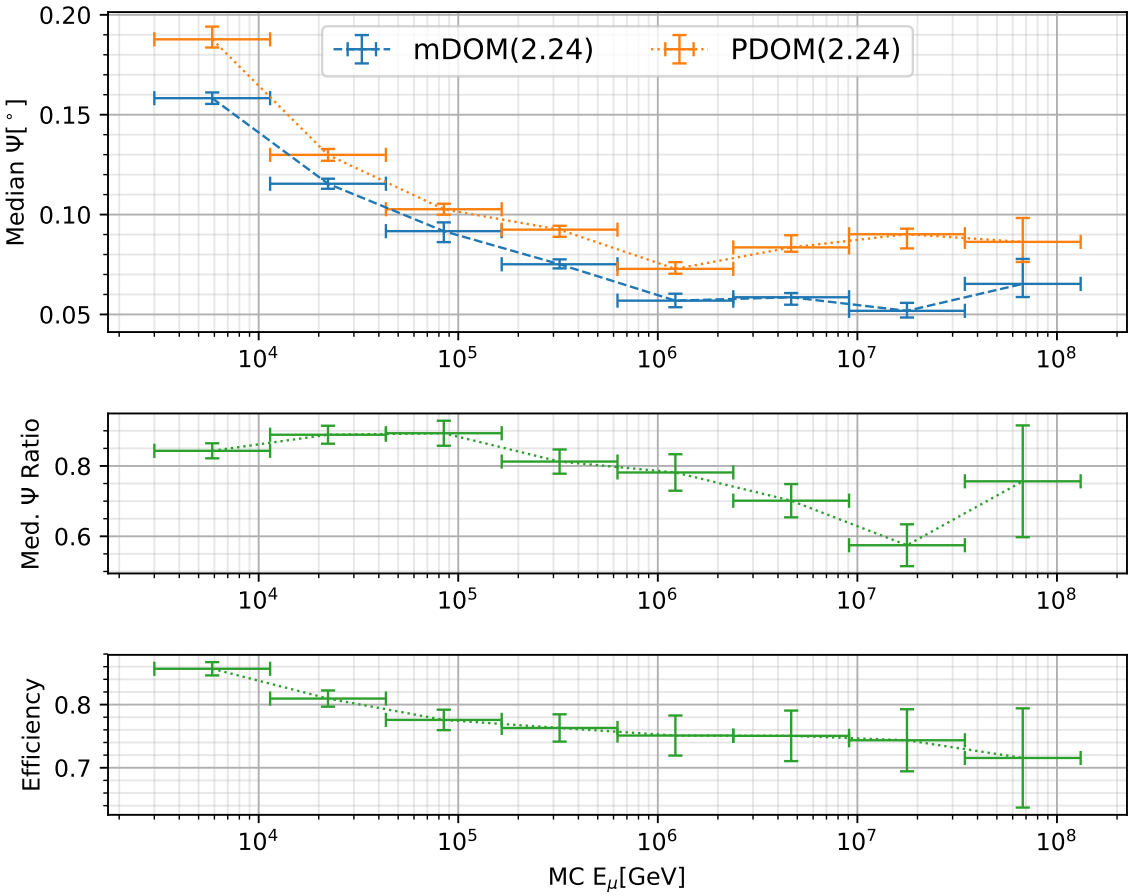

Figure 5.11: Horiztontal muons with MCLength > 1000 m. The vertical error bars indicate the standard error and the horizontal bars show the width of the respective energy bin. *Top:* Comparison of the median angular resolution per energy bin of the nominal mDOM (2.24) and the upscaled PDOM (2.24). *Center:* Ratio of the median angular resolution (mDOM / PDOM) per energy bin. *Bottom:* Selection efficiency versus muon energy in the respective zenith range after the cut on MCLength (equal for both sensor types).

error achieved by a detector equipped with nominal mDOMs (2.24) is between 10 % – 15 % better compared to the same results obtained with a detector equipped with upscaled PDOMs (2.24). At higher energies this improvement gets as large as 30 % – 40 %. The improvement is slightly lower when comparing the downscaled mDOM (1.0) to the nominal PDOM (1.0) in this manner (see figure C.2 in the appendix).
Similar to the resolutions obtained with the cut on MCLength, different positions of the minimum of each curve can be seen. The smallest opening angle obtained with the upscaled PDOM (2.24) is located around 1 PeV, while the best resolution achieved with the nominal mDOM (2.24) can be found at a muon energy around 10 PeV. An increase of the median opening angle above the respective minima is visible for both sensor types and both cut sets. It is assumed, that this is an effect of the discrepancy between the hypothesis used in SplineMPE, all light is emitted by a smooth infinite track, and the actual simulated event, which includes stochastic losses along the muon track. With increasing muon energy this discrepancy becomes larger until it eventually causes the reconstruction results to worsen.

5.3.4.2 Down-going Muons

Down-going muons are muons with a zenith angle in the range of $0° \leq \theta_\mu < 85°$.

Cut: MCLength > 500 m Due to the smaller amount of events in this zenith range the threshold for the cut on MCLength has been reduced to 500 m. The result of the comparison of the nominal mDOM (2.24) and the upscaled PDOM (2.24) is displayed in figure 5.13. In contrast to the horizontal zenith range an improvement of the angular resolution between 10 % – 20 % can be seen in all but two energy bins with no distinct energy dependency. However, the error bars overlay in all but the lowest two energy bins. It can be argued that a larger data sample might increase the significance in gain of the angular resolution due to the segmentation of the mDOM at higher energies. With the available datasets this statement cannot be made with statistical certainty.
After the cut, 6004 out of 7188 events remain in the data sample, which yields an overall efficiency of 83.5 %. The analog comparison of the angular resolution obtained with the downscaled mDOM (1.0) and the upscaled PDOM (1.0) yields a slightly more distinct improvement due to the sensor segmentation (see figure C.3 in the appendix). However, a larger data sample for down-going muons is needed in both cases in order to increase the significance of the improvement.

Cut: Standard Cuts The comparison of the opening angle for down-going muons after standard cuts have been applied is shown in figure 5.14. Apart from the energy bin of the highest energies, which seems to be dominated by badly reconstructed events, the medians of the opening angles of both sensor types appear to be fairly equal with a small tendency indicating better

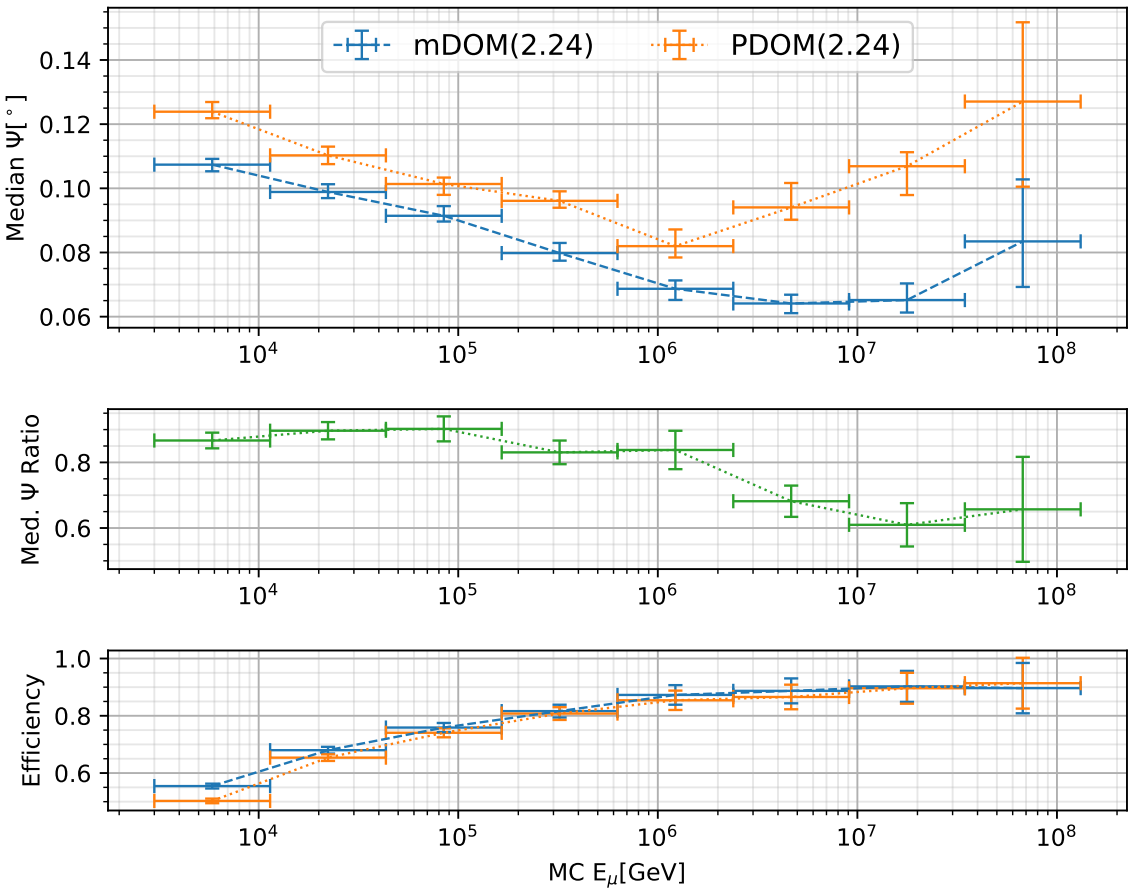

Figure 5.12: Horizontal muons after the standard cuts have been applied. The vertical error bars indicate the standard error and the horizontal bars show the width of the respective energy bin. *Top:* Comparison of the median angular resolution per energy bin of the nominal mDOM (2.24) and the upscaled PDOM (2.24). *Center:* Ratio of the median angular resolution (mDOM / PDOM) per energy bin. *Bottom:* Selection efficiency versus muon energy in the respective zenith range after the standard cuts.

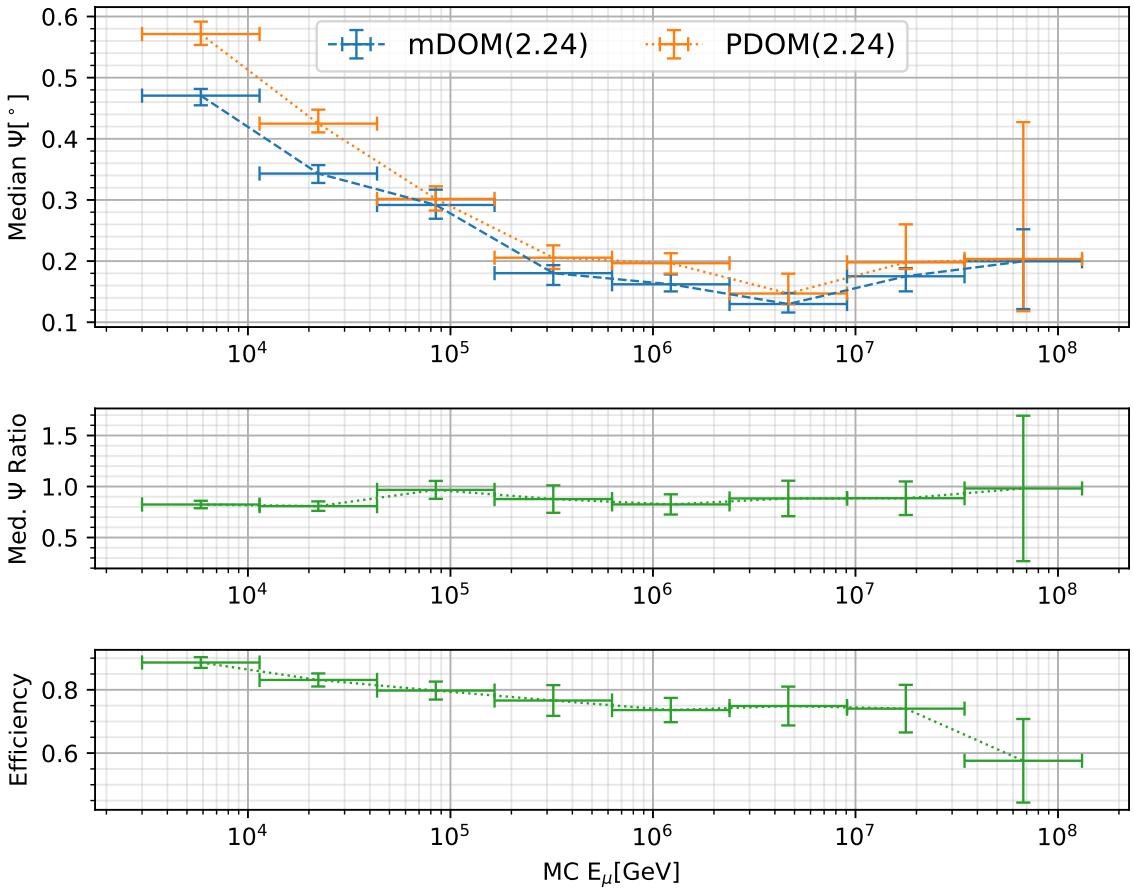

Figure 5.13: Down-going muons with MCLength > 500 m. The vertical error bars indicate the standard error and the horizontal bars show the width of the respective energy bin. *Top:* Comparison of the median angular resolution per energy bin of the nominal mDOM (2.24) and the upscaled PDOM (2.24). *Center:* Ratio of the median angular resolution (mDOM / PDOM) per energy bin. *Bottom:* Selection efficiency versus muon energy in the respective zenith range after the cut on MCLength (equal for both sensor types).

results achieved by the nominal mDOM (2.24).
The major effect of the sensor segmentation for this comparison lies in the different efficiencies. With 3382 out of 7188 events passing, an efficiency of 47.1 %, a detector equipped with nominal mDOMs (2.24) instead of upscaled PDOMs (2.24) has around 24 % more events in the final data sample. In the case of the PDOM (2.24), 2735 events out of 7188 remain after the cuts have been applied, which yields an efficiency of 38.0 %. Especially in the energy range of 1 PeV and below, the efficiency of an detector equipped with mDOMs (2.24) is much higher when the standard cuts are applied. The median opening angle for both sensor types seems to decrease only slightly with increasing energy in contrast to the results obtained after the cut on MCLength. This is mainly a consequence of the different selection efficiencies which show a strong energy dependency for both sensor designs.
The results obtained in a similar comparison of the downscaled mDOM (1.0) and the nominal PDOM (1.0) are comparable (see figure C.4 in the appendix).

5.3.4.3 Up-going Muons

Up-going muons are required to have a zenith angle in the range of $95° < \theta_\mu \leq 180°$.

Cut: MCLength > 500 m Similar to down-going muons, the threshold for the cut on MCLength has been reduced to 500 m in order to increase the amount of events left in the data sample. Figure 5.15 shows the median opening angle for up-going muons obtained with a detector equipped with the nominal mDOM (2.24) in comparison to the median opening angle obtained with the upscaled PDOM (2.24). In this scenario, the PDOM (2.24) leads to better results than the mDOM (2.24) for energies below 100 TeV with a decreased angular error in between 7 % – 13 %. For energies above 1 PeV a detector equipped with nominal mDOMs (2.24) yields an improved angular resolution of 5 % – 25 %.
The efficiency is 83.5 % for both sensor types with 6082 out of 7188 events remaining after the cut. The comparison of respective results obtained with the downscaled mDOM (1.0) and the nominal PDOM (1.0) do not show a significant difference for the angular resolution for both sensor types in all but two energy bins (see figure C.5 in the appendix). In order to make a more comprehensive statement for this case, a larger data sample would be needed.

Cut: Standard Cuts The opening angle after the application of the standard cuts to the sample of up-going muons is shown for both sensor types in figure 5.16. After these cuts, the nominal mDOM (2.24) slightly outperforms the upscaled PDOM (2.24) over the whole energy range in all but two energy bins. For energies below 1 PeV the nominal mDOM (2.24) yields a reduced angular error up to 10 %, except in the range of 100 TeV where the upscaled PDOM (2.24) leads to a slightly reduced median opening angle. At higher energies the improvement of the nominal mDOM (2.24) gets as large as 25 %. The median angular resolutions of the energy bin of the

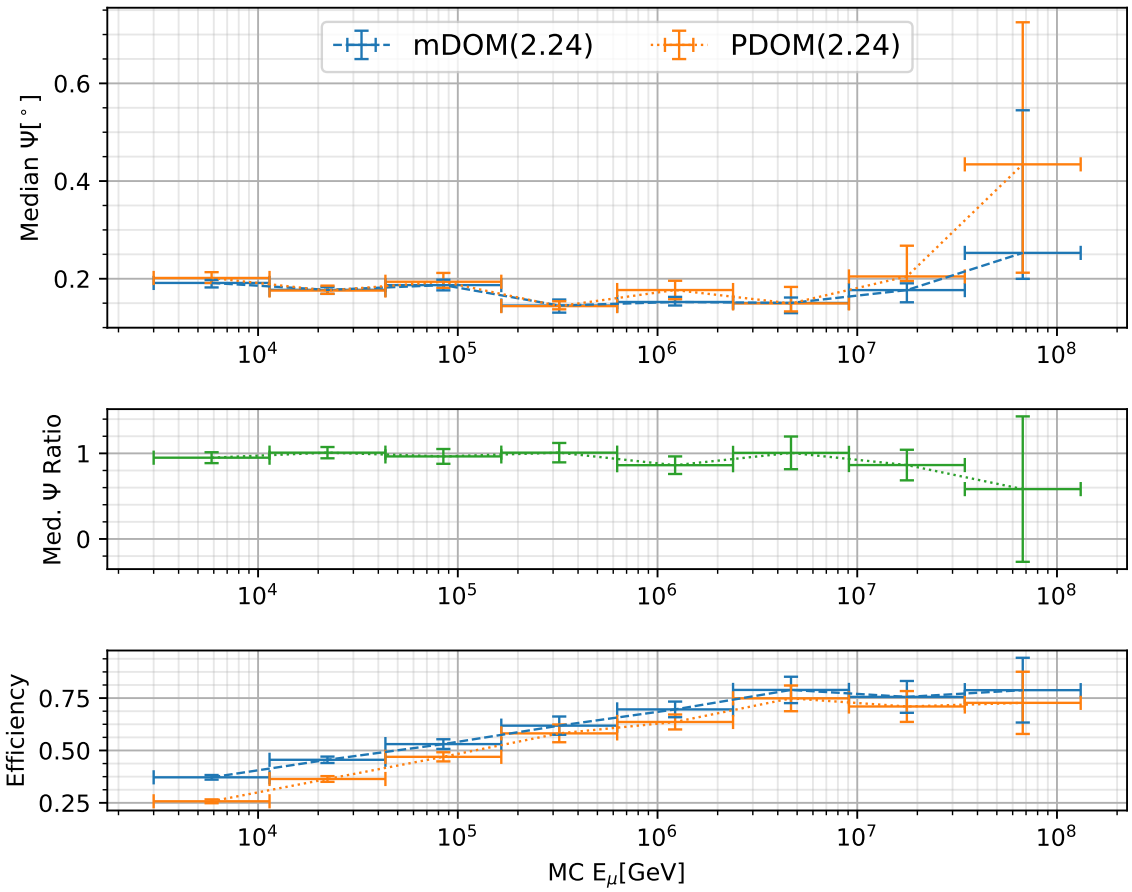

Figure 5.14: Down-going muons after the standard cuts have been applied. The vertical error bars indicate the standard error and the horizontal bars show the width of the respective energy bin. *Top:* Comparison of the median angular resolution per energy bin of the nominal mDOM (2.24) and the upscaled PDOM (2.24). *Center:* Ratio of the median angular resolution (mDOM / PDOM) per energy bin. *Bottom:* Selection efficiency versus muon energy in the respective zenith range after the standard cuts.

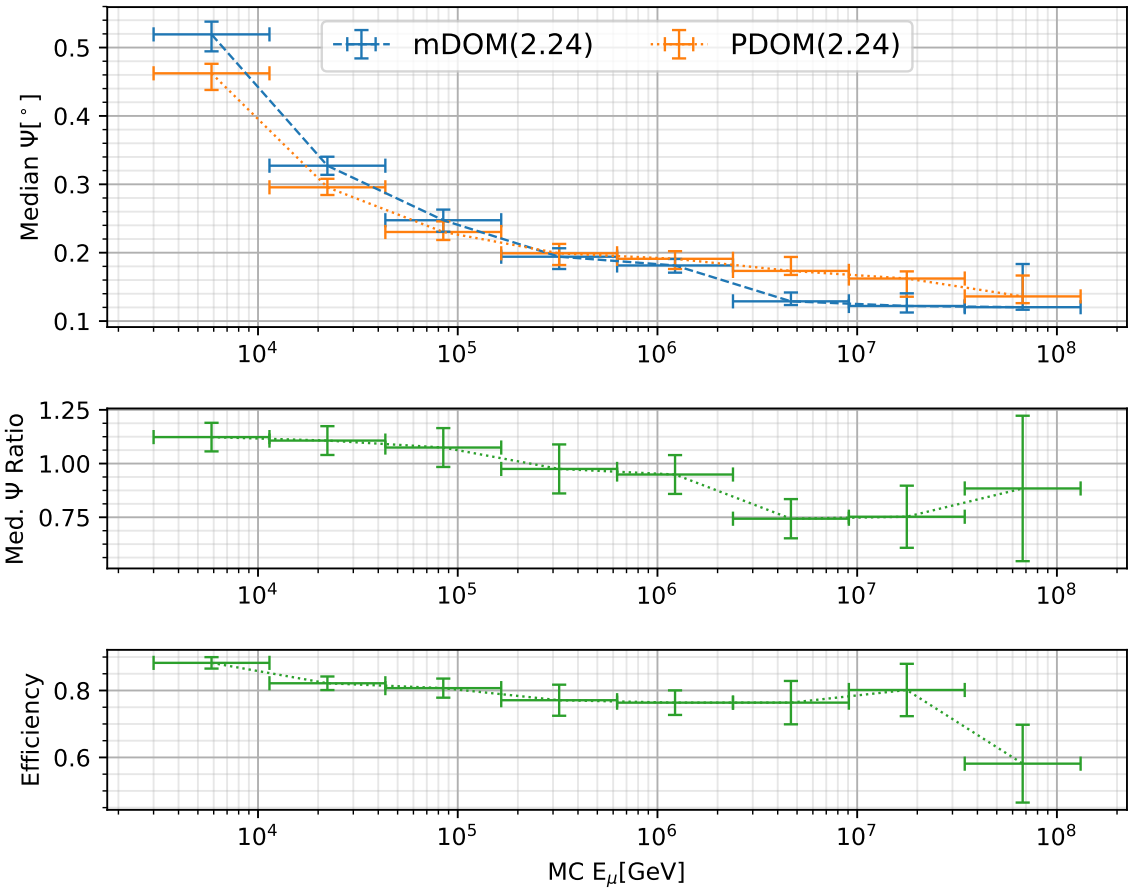

Figure 5.15: Up-going muons with MCLength > 500 m. The vertical error bars indicate the standard error and the horizontal bars show the width of the respective energy bin. *Top:* Comparison of the median angular resolution per energy bin of the nominal mDOM (2.24) and the upscaled PDOM (2.24). *Center:* Ratio of the median angular resolution (mDOM / PDOM) per energy bin. *Bottom:* Selection efficiency versus muon energy in the respective zenith range after the cut on MCLength (equal for both sensor types).

highest energies seem to be dominated by relatively large statistical fluctuations for both sensor types, which is indicated by the large error bars on the median opening angle and the respective ratio.
With 3556 out of 7287, equal to an overall efficiency of 48.8 % for the nominal mDOM (2.24), the selection efficiency of the upscaled PDOM (2.24) is slightly higher with 3706 out of 7287 events remaining after the cuts (=50.9 %). Contrary to the scenario with down-going muons, the efficiency of the upscaled PDOM (2.24) is now higher, especially below 100 TeV. This can be explained by the single downwards oriented PMT of the PDOM. Comparable to the down-going case, the difference of the two sensor designs is now shifted to the efficiency. Similar results can be seen when comparing the angular resolution of the downscaled mDOM (1.0) to the nominal PDOM (1.0) (see figure C.6 in the appendix).

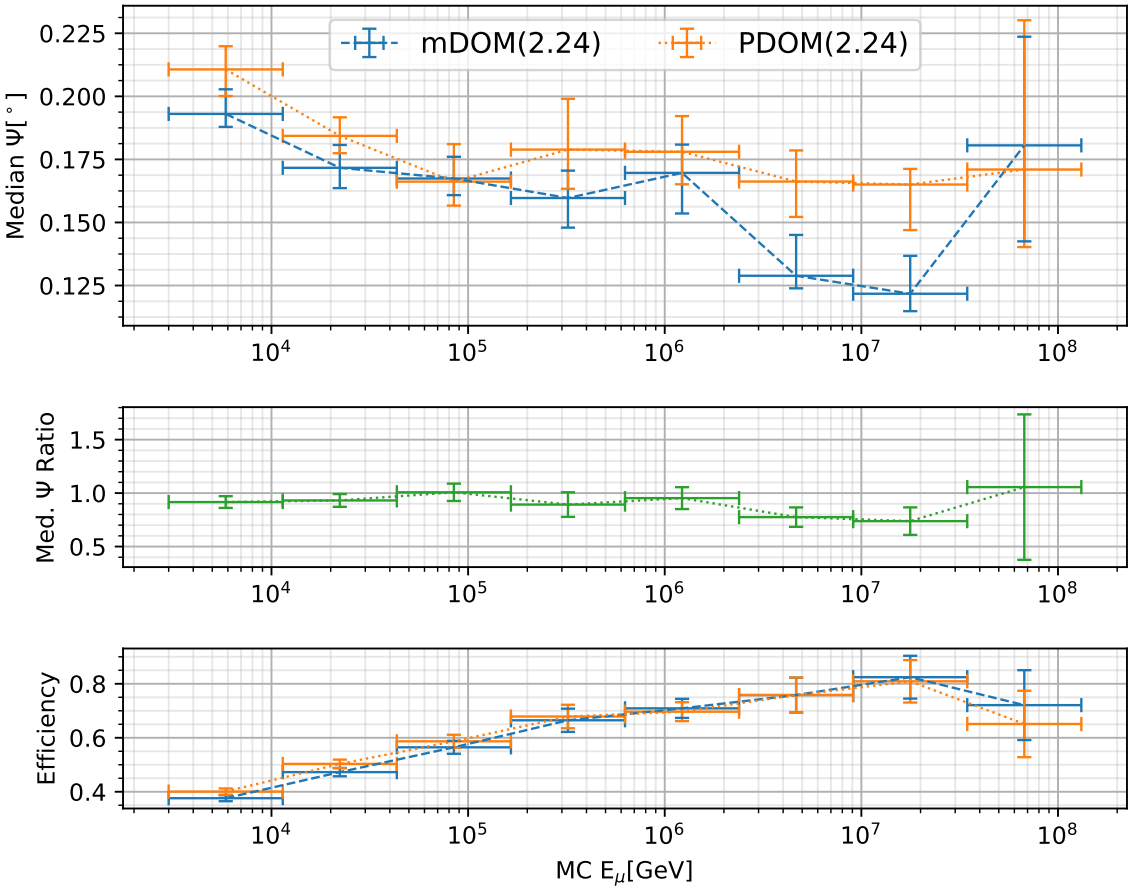

Figure 5.16: Up-going muons after the standard cuts have been applied. The vertical error bars indicate the standard error and the horizontal bars show the width of the respective energy bin. *Top:* Comparison of the median angular resolution per energy bin of the nominal mDOM (2.24) and the upscaled PDOM (2.24). *Center:* Ratio of the median angular resolution (mDOM / PDOM) per energy bin. *Bottom:* Selection efficiency versus muon energy in the respective zenith range after the standard cuts.

CHAPTER 6

SENSITIVITY STUDIES

While the last chapter showed that a segmentation of the basic detection unit of the Gen2 high-energy array does lead to an improvement of the angular resolution of through-going muon induced track-like events for down-going and horizontal muons, it remains unclear how this translates into a potential of identifying neutrino point sources or setting upper limits on their fluxes. The goal of the following chapter is to answer these questions. The chapter is split in three parts. The first part describes briefly the statistical formulae, assumptions and simplifications used in order to estimate upper limits and fluxes necessary for a discovery, while the second part outlines the relevant sources of background and their respective parametrizations. The last part presents the Gen2-analysis framework, how the angular resolution and the selection efficiency of the two sensor designs is integrated and finally presents the estimated upper limits and fluxes necessary for a discovery as a function of the declination of potential neutrino point sources.

6.1 Theoretical Framework

This section outlines the statistical formulae, assumptions and simplifications used to estimate upper limits and discovery fluxes.

6.1.1 Basics of a Binned Likelihood Analysis

Most analyses of IceCube as well as in many other particle physics experiments utilize a likelihood based approach to test various hypotheses, such as the presence of a signal. There are two families of likelihood based analyses, applying either a binned or an unbinned likelihood function. While the basic idea of both approaches is similar, the unbinned likelihood usually yields lower exclusion

and discovery fluxes in point source analyses [12]. For practical reasons, however, the binned method is used within this work. The formalism and naming conventions used for this work follows mainly the procedure described in [21].
For each selected event an observable x can be measured, which is then used to populate a histogram $\mathbf{n} = [n_1, ..., n_N]$. The expectation value for each bin can be written as

$$E[n_i] = \mu s_i + b_i, \tag{6.1}$$

where s_i corresponds to the expected amount of signal events in the "i"th bin and b_i corresponds to the expected amount of background events in the respective bin. The parameter μ denotes the signal strength in this context, therefore $\mu = 1$ corresponds to the nominal signal strength from the model, whereas $\mu = 0$ corresponds to a background-only scenario. The expectation values s_i and b_i can be written as

$$s_i = s_{\text{tot}} \int_{\text{bin}\,i} f_s(x;\boldsymbol{\theta}_s)\mathrm{d}x \quad \text{and} \tag{6.2}$$

$$b_i = b_{\text{tot}} \int_{\text{bin}\,i} f_b(x;\boldsymbol{\theta}_b)\mathrm{d}x \quad , \tag{6.3}$$

where s_{tot} and b_{tot} denote the mean total amount of signal and background events, $f_s(x;\boldsymbol{\theta}_s)$ and $f_b(x;\boldsymbol{\theta}_b)$ are the signal and background probability density functions (PDFs) of x and $\boldsymbol{\theta}_s$ and $\boldsymbol{\theta}_b$ represent all parameters the respective PDFs depend on. All parameters that are not of immediate interest but need to be taken into account, called nuisance parameters, are combined in $\boldsymbol{\theta} = (b_{\text{tot}}, \boldsymbol{\theta}_b, \boldsymbol{\theta}_s)$. The parameter s_{tot} is not a nuisance parameter but rather is dictated by the used signal model and therefore fixed.
The likelihood function can then be defined as a product of Poisson probabilities, one for each bin:

$$L = \prod_{i=1}^{N} \frac{(\mu s_i + b_i)^{n_i}}{n_i!} e^{-(\mu s_i + b_i)}. \tag{6.4}$$

In order to perform a statistical test on a hypothesized value of μ, one defines a likelihood ratio

$$\lambda(\mu) = \frac{L(\mu, \hat{\hat{\boldsymbol{\theta}}})}{L(\hat{\mu}, \hat{\boldsymbol{\theta}})} = \frac{\max_{\boldsymbol{\theta}} L(\mu, \boldsymbol{\theta})}{\max_{\mu', \boldsymbol{\theta}'} L(\mu', \boldsymbol{\theta}')}. \tag{6.5}$$

$\hat{\hat{\boldsymbol{\theta}}}$ is hereby the maximum likelihood estimator for a fixed value of μ while $\hat{\mu}$ and $\hat{\boldsymbol{\theta}}$ are the unconditional maximum likelihood estimators. It can be seen that $0 \leq \lambda(\mu) \leq 1$, while values near 0 mean a bad agreement between the hypothesized value of μ and the data and values near 1 imply a good agreement.
For mathematical reasons one defines a test statistic

$$t = -2 \ln \lambda(\mu) = -2 \cdot \left[\ln \left(\max_{\boldsymbol{\theta}} L(\mu, \boldsymbol{\theta}) \right) - \ln \left(\max_{\mu', \boldsymbol{\theta}'} L(\mu', \boldsymbol{\theta}') \right) \right]. \tag{6.6}$$

Higher values of the test statistic t mean an increasing incompatibility between the specified value of μ and the data. For a statistical test of a hypothesized value of μ one can use t as a

measurement of the disagreement between the hypothesis and the data. It is common practice to quantify this discrepancy with the p-value,

$$p_\mu = \int_{t_{\text{obs}}}^{\infty} \text{f}(t|\mu)\text{d}t, \tag{6.7}$$

with t_{obs} being the observed value of t given the data under the assumption of signal strength μ. The function $\text{f}(t|\mu)$ denotes the corresponding PDF of t. To be able to calculate a p-value, the distribution $\text{f}(t|\mu)$ needs to be determined. With large data samples and in the case of nested models, meaning that the free parameters of the null hypothesis are a subset of the free parameters of the alternative hypothesis, the distribution of t can be approximated by a χ^2 distribution with $N_{\text{d.o.f.}} = \text{df}_{\text{alt}} - \text{df}_{\text{null}}$ degrees of freedom, with "df" being the number of free parameters of the alternative and null hypothesis [93].

6.1.2 Sensitivity & Discovery Potential

The two figures of merit used within this work to quantify the performance of the future Gen2 high-energy array is the sensitivity and the discovery potential.
Given there is no signal in the data, the sensitivity is defined as the signal strength $\mu_{\text{u.l.}}$ which can be excluded with a confidence level of 90% in half of the cases. Translated into the formalism of the previous section, including the approximation of $\text{f}(t|\mu)$ as a χ^2 distribution with one degree of freedom, this means

$$p = 0.1 = \int_{t_{\mu_{\text{u.l.}}}}^{\infty} \text{f}(t|\mu_{\text{u.l.}})dt \tag{6.8}$$

$$\approx \int_{t_{\mu_{\text{u.l.}}}}^{\infty} \chi^2(t|\mu_{\text{u.l.}})dt. \tag{6.9}$$

With the cumulative distribution of χ^2 the value of $t_{\mu_{\text{u.l.}}}$ and subsequently $\mu_{\text{u.l.}}$ can be derived.
The discovery potential is defined as the signal strength $\mu_{\text{d.p.}}$ at which a background only hypothesis can be excluded with 5σ, which corresponds to a p-value of $5.7 \cdot 10^{-7}$, in half of the cases, given that there is a signal with signal strength $\mu_{\text{d.p.}}$. With a similar approach as above, this yields

$$p = 5.7 \cdot 10^{-7} = \int_{t_{\mu=0}}^{\infty} f(t|\mu = 0)dt \tag{6.10}$$

$$= \int_{t_{\mu=0}}^{\infty} \chi^2(t|\mu = 0)dt. \tag{6.11}$$

6.1.3 The Asimov Data Set

In general one would now sample realizations of different hypotheses, derive the test statistic t for each realization and find the desired medians. There is, however, a tremendous short cut possible in finding these quantities by utilizing a special, artificial data set called the "Asimov

data set" [21]. Instead of evaluating the test statistic for each realization anew, each bin of the histogram **n** is filled with its expectation value:

$$n_i = E[n_i] = \mu' s_i(\boldsymbol{\theta}') + b_i(\boldsymbol{\theta}'). \tag{6.12}$$

With the Asimov data set the Asimov likelihood L_A and subsequently the Asimov likelihood ratio

$$\lambda_A(\mu) = \frac{\max_{\boldsymbol{\theta}} L_A(\mu, \boldsymbol{\theta})}{\max_{\mu'', \boldsymbol{\theta}''} L_A(\mu'', \boldsymbol{\theta}'')} = \frac{\max_{\boldsymbol{\theta}} L_A(\mu, \boldsymbol{\theta})}{L_A(\mu', \boldsymbol{\theta}')} \tag{6.13}$$

can be defined. It has been shown in [21] that the test statistic t_A derived from the Asimov likelihood ratio is equal to the median of the test statistic t as defined in equation 6.6, which enables a very convenient way of estimating the sensitivity and discovery potential of an experiment. For the sensitivity this leads to

$$t_A(\mu_{\text{u.l.}}) = -2 \cdot \ln \left[\frac{\max_{\boldsymbol{\theta}} L_A(\mu_{\text{u.l.}}, \boldsymbol{\theta})}{L_A(\mu' = 0, \boldsymbol{\theta}')} \right], \tag{6.14}$$

and for the discovery potential one finds

$$t_A(\mu = 0) = -2 \cdot \ln \left[\frac{\max_{\boldsymbol{\theta}} L_A(\mu = 0, \boldsymbol{\theta})}{L_A(\mu' = \mu_{\text{d.p.}}, \boldsymbol{\theta}')} \right]. \tag{6.15}$$

6.2 Background

This section outlines all sources of background relevant within the context of neutrino point source searches, while mainly focusing on the most commonly used parameterizations of these. The background components can be split into three parts, namely atmospheric muons, atmospheric neutrinos and diffuse astrophysical neutrinos.

6.2.1 Atmospheric Muons

Muons produced by cosmic rays interacting with molecules of the atmosphere are one of the largest sources of background. Muons with an energy above the threshold of roughly 500 GeV are able to penetrate the instrumented volume of the IceCube in-ice array leading to a trigger rate of about 2.15 kHz [96]. With increasing zenith angles, atmospheric muons have to propagate through more and more material until they reach the detector, which leads to a decrease of penetrating atmospheric muons up to a zenith angle of approximately 85° above which no atmospheric muons reach the detector any more.
The dominant muon production channels in the atmosphere are

$$\pi^{\pm} \rightarrow \mu^{\pm} + \nu_{\mu}(\bar{\nu}_{\mu}) \quad (\text{BR:} \approx 100\%) \quad \text{and} \tag{6.16}$$

$$K^{\pm} \rightarrow \mu^{\pm} + \nu_{\mu}(\bar{\nu}_{\mu}) \quad (\text{BR:} \approx 63.5\%). \tag{6.17}$$

During a cosmic ray induced air shower, muon bundles are rather produced then single muons, each muon with a different energy following an energy distribution depending on the properties

of the cosmic ray primary. IceCube, however, typically is not capable of distinguishing between the single muons within a muon bundle. Therefore, a muon bundle is often approximated as a single muon with an energy equal to the sum of all muons within the bundle [94].
The energy of a muon bundle at the detector has been parameterized in [94] as a function of the energy of the primary, the mass number of the primary and the zenith angle. In combination with a parametrization of the cosmic ray flux it is possible to derive an energy and zenith angle dependent flux of atmospheric muons, or muon bundles, at the detector. A common parameterization of the cosmic ray flux from [99], called H3a, has been used. The implemented differential flux as a function of bundle energy (at the detector) and zenith angle is displayed in figure 6.1 for an energy range of 500 GeV to 1 EeV.

6.2.2 Atmospheric Neutrinos

Besides atmospheric muons reaching the vicinity of the instrumented volume, neutrinos created in interactions of cosmic rays in the atmosphere depict the second major background contribution in the context of neutrino point source searches.
Up to energies of $E_\nu \approx 500\,\text{TeV}$ the dominant production channel of atmospheric neutrinos is via decaying $\pi^\pm$ and $K^\pm$ (see equation 6.16) [83]. Atmospheric neutrinos originated in such a process are also called conventional neutrinos. Pions with energies above 100 GeV start to interact with nuclei in the atmosphere producing more pions with lower energy, which causes a steepening of the neutrino energy spectrum ($\frac{d\Phi}{dE} \propto E^{-3.7}$ [38]) compared to the initial cosmic ray flux (see figure 6.2) [105]. Since pions and kaons have a relatively long lifetime ($\tau \approx 10^{-8}\,\text{s}$ [53]), these particles loose some of their energy while propagating through the atmosphere before decaying [65]. The comparatively long lifetime of these mesons causes a zenith dependency of the atmospheric neutrino flux. At horizontal zenith angles the distance between the interaction of the primary cosmic ray particle and the surface is much larger, which increases the probability of the pions and kaons to decay before loosing energy in interactions [30]. This leads to a higher flux of atmospheric neutrinos for more horizontal zenith angles [65]. In order to implement the effect of conventional atmospheric neutrinos, the model from M. Honda et. al. [39] with a reweighing of the initial cosmic ray flux from T. Gaisser et. al. [32] has been used.
With neutrino energies above 500 TeV, another production channel of atmospheric neutrinos becomes important, namely the production of neutrinos by decaying charmed mesons. The very short lifetimes of charmed mesons ($\tau \approx 10^{-12}\,\text{s}$ [53]) cause a harder spectrum of prompt neutrinos since these particles decay before they can interact with the surrounding material. Thus, the prompt neutrino flux is believed to be isotropic with a shape close to primary cosmic ray spectrum, i.e. $E^{-2.7}$ [83]. One of the most common parameterization of the prompt neutrinos flux is the so-called Enberg parameterization (see figure 6.3). This parameterization has been used in this study to estimate the prompt neutrino flux. Due to large uncertainties and low statistics at the energy range where prompt neutrinos start to dominate over conventional neutrinos, analysis

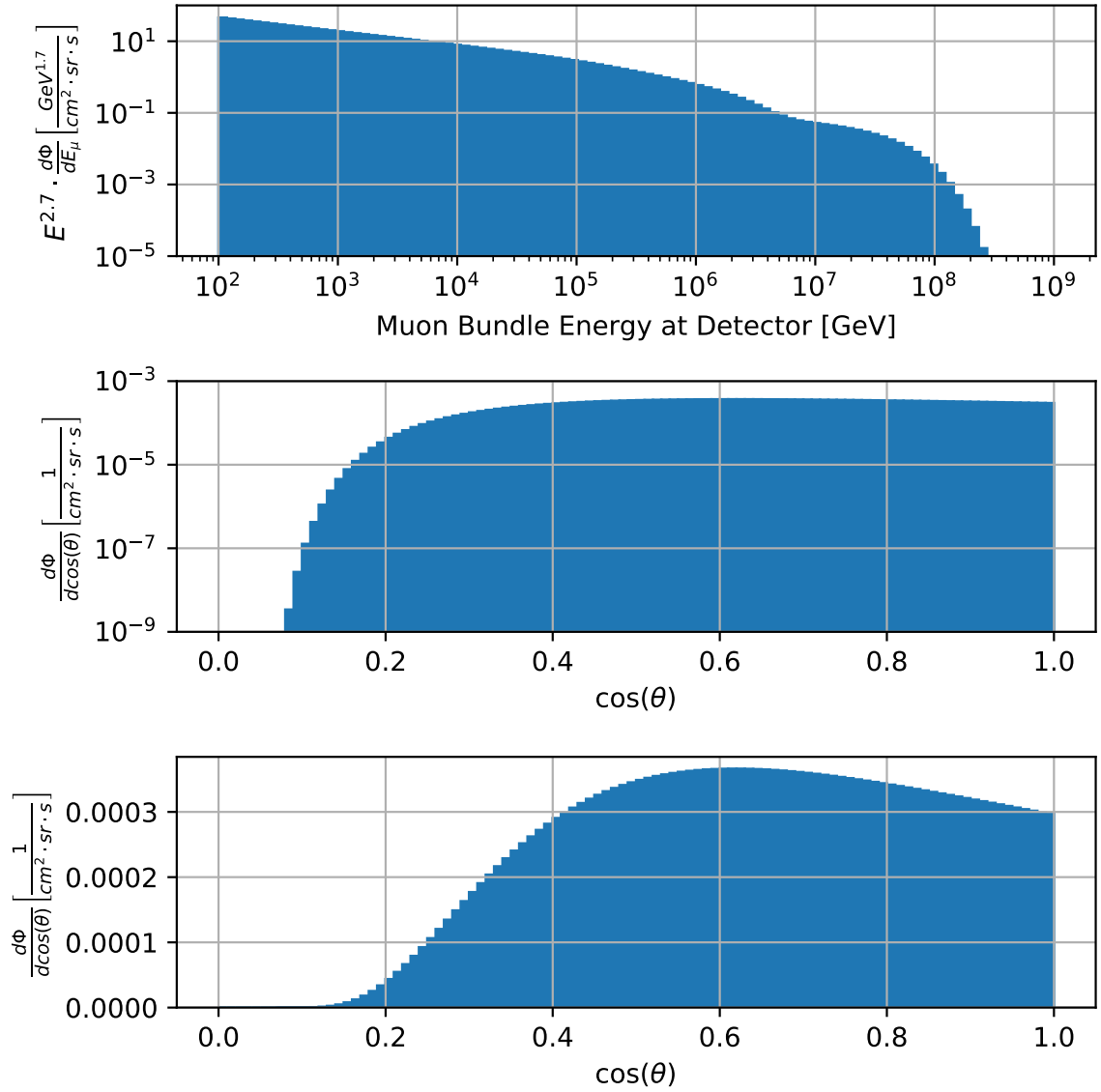

Figure 6.1: Differential atmospheric muon flux at the detector as implemented in the Gen2-analysis framework. *Top*: Muon flux versus bundle energy evaluated at $\cos(\theta) = 0.6$. *Center:* Muon flux versus $\cos(\theta)$ integrated over an energy range of 500 GeV to 1 EeV with a logarithmic y-scale. *Bottom:* Muon flux versus $\cos(\theta)$ integrated over an energy range of 500 GeV to 1 EeV with a linear y-scale in order to visualize the zenith dependency of the flux at zenith angles close to zero.

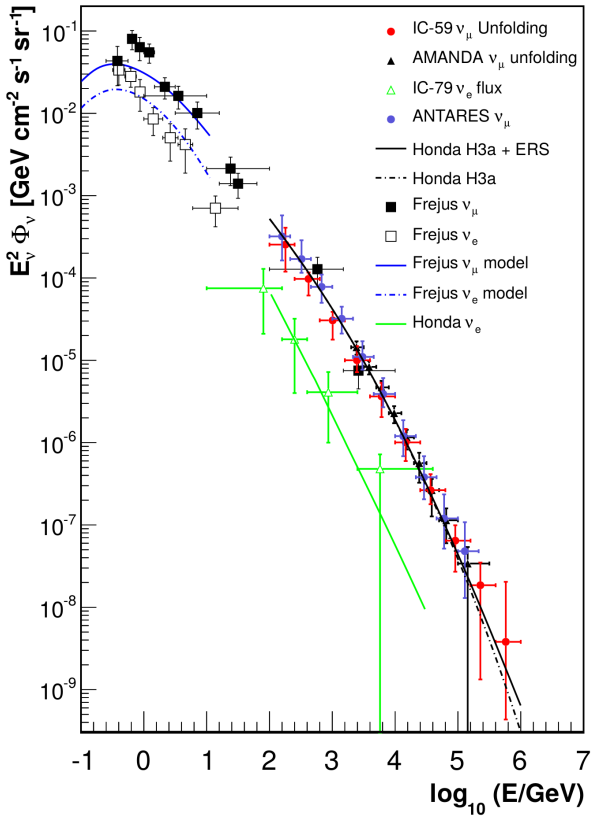

Figure 6.2: Unfolding results of the atmospheric neutrino flux obtained by IceCube and other experiments (markers) including the predictions of several models (lines). Taken from [65].

of the atmospheric neutrino spectrum utilizing IceCube data have not been able to prove the existence of a prompt component yet (e.g. [65]).

6.2.3 Astrophysical Diffuse Neutrinos

The last relevant background component for neutrino point source searches are diffuse neutrinos of astrophysical origin, which have been discovered by IceCube in 2013 [63]. The diffuse astrophysical neutrino flux is simply modeled by an unbroken power-law per neutrino flavor since there is only a limited amount of data available:

$$\frac{d\Phi_{\nu_\mu+\bar{\nu}_\mu}}{dE} = 10^{-18}\left(\frac{E_\nu}{100\,\mathrm{TeV}}\right)^{\gamma}\cdot\frac{1}{\mathrm{GeV}\cdot\mathrm{cm}^2\cdot\mathrm{s}\cdot\mathrm{sr}}. \tag{6.18}$$

6.3 Sensitivity to Point Sources

Within the last section of this chapter the Gen2-analysis framework [50] is described. This framework has been used within this thesis to estimate upper limits and discovery fluxes of a

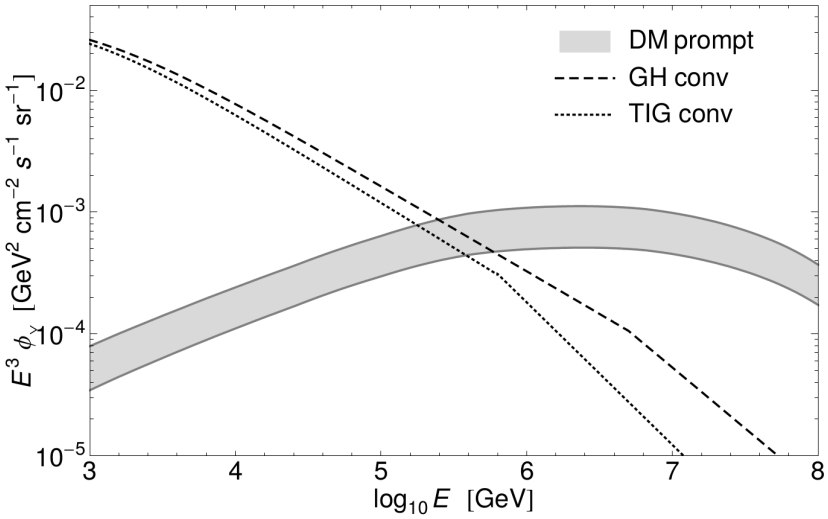

Figure 6.3: Predictions for the prompt and conventional $\nu_\mu + \bar{\nu}_\mu$ flux from vertical direction. The shaded band shows the theoretical uncertainties for the prompt flux calculated in [26] (same model as used in this study). The dashed lines shows the model of the conventional flux from Gaisser and Honda [31]. The dotted line is a different calculation of the conventional neutrino flux from [77]. Taken from [26].

hypothetical Gen2 high-energy array for neutrino point sources. Furthermore, the necessary steps in order to integrate the respective angular resolutions and selection efficiencies of the nominal mDOM (2.24) and the upscaled PDOM (2.24) into the calculations are described in detail. Additionally, this section briefly describes the implementation of a surface veto, which is necessary in order to calculate reasonable point source upper limits and discovery fluxes for point sources with a zenith angle below 90°. Finally, the estimated figures of merit achievable with the Gen2 high-energy array equipped with either mDOMs or PDOMs are presented.

6.3.1 The Gen2-Analysis Framework

One of the core functions of the Gen2-analysis framework is to convert a given flux into event rates in the form of filled bins of one or more observables (e.g. reconstructed direction). Since only the sensitivity for neutrino point sources is of interest within this context, the only observable is the opening angle between the reconstructed direction of a through-going muon and the direction of the hypothetical point source, denoted as Ψ[1].

An event rate within a bin of an observable is a function of the underlying particle flux and the effective area of the detector. The effective area in turn, depends on the detector geometry, a selection efficiency and, in the case of a point source study, an angular resolution (also called

[1]More advanced neutrino point source studies might include other observables, like reconstructed energy, but for simplicity reasons only the opening angle is taken into account within this work.

point spread function in this context). Selection efficiency and angular resolution are (usually) functions of energy (as can be seen in section 5.3.4). For this study, the opening angle Ψ has been divided into 300 bins, from 0° to 3° with a bin width of 0.01°. The event rate within bin Ψ_i can be written as

$$\Psi_i = \mu \cdot s_i + b_i \tag{6.19}$$

similar to the formula in equation 6.12, where s_i and b_i are the respective signal and background components while μ denotes a signal strength parameter. Since the nature of the signal component varies from the nature of the background component, the way how s_i and b_i are calculated is slightly different.

For the calculation of the signal component the kinematic angle, so the angle between the initial muon neutrino and the secondary muon, is neglected. For neutrino energies above 100 TeV, this angular offset can be neglected (see figure 3.9), but for energies below this threshold, the angular resolution of track-like events achieved in this thesis does get close to the kinematic angle (see e.g. fig. 5.12). Since the largest contribution to the point source sensitivity, however, does come from neutrinos with energies of 100 TeV and above (e.g. [98] or [73]), it is assumed, that this approximation does not change the results in a significant way.

Given these simplifications, the signal component in bin Ψ_i from a neutrino point source with zenith angle $\theta_{\text{p.s.}}$ can be written as

$$s_i(\theta_{\text{p.s.}}) = \int_{\Psi_i} \int_{E'_\mu} \Phi_\mu(E_\mu, \theta_{\text{p.s.}}) \cdot A_\mu(E_\mu, \theta_{\text{p.s.}}) \cdot P(\Psi, E_\mu, \theta_{\text{p.s.}}) \mathrm{d}E_\mu \mathrm{d}\Psi, \quad \text{with} \tag{6.20}$$

$$\Phi_\mu(E_\mu, \theta) = \int_{E'_{\nu_\mu}} \Phi_{\nu_\mu}(E_{\nu_\mu}) \cdot \eta(E_{\nu_\mu}, E_\mu, \theta) \mathrm{d}E_{\nu_\mu} \quad \text{and} \tag{6.21}$$

$$A_\mu(E_\mu, \theta) = \text{Eff}_\mu(E_\mu, \theta) \cdot \frac{1}{2\pi} \cdot \int_0^{2\pi} A_{\text{geo}}(\theta, \phi) \mathrm{d}\phi \quad . \tag{6.22}$$

The function $P(\Psi, E, \theta_{\text{p.s.}})$ denotes the point spread function, which incorporates the angular resolution of through-going muon tracks (see section 6.3.3). The function $\Phi_{\nu_\mu}(E)$ is the differential $\nu_\mu + \bar{\nu}_\mu$ flux of the point source, while $\eta(E_{\nu_\mu}, E_\mu, \theta)$ is the production efficiency of a neutrino with energy E_{ν_μ} and zenith angle θ to produce a muon with energy E_μ at the detector, thus, incorporates the neutrino cross section for a charged current interaction as well as a density model of the Earth. The effective area for muons $A_\mu(E_\mu, \theta)$ is a product of the geometrical area of the detector averaged over the azimuth and the muon selection efficiency $\text{Eff}_\mu(E_\mu, \theta)$ (see. section 6.3.2).

For the background components the calculation of the event rate can be written as:

$$b_{i,\text{bkg}}(\theta_{\text{p.s.}}) = \Omega_i \cdot \int_{E'_\mu} \Phi_{\mu,\text{bkg}}(E_\mu, \theta_{\text{p.s.}}) \cdot A_\mu(E_\mu, \theta_{\text{p.s.}}) \cdot (1 - P_{\text{Veto}}(E_\mu, \theta_{\text{p.s.}})) \mathrm{d}E_\mu \quad \text{,with} \tag{6.23}$$

$$\Omega_i = 2\pi \cdot (\cos(\Psi_i) - \cos(\Psi_{i+1})) \quad . \tag{6.24}$$

bin index	1	2	3	4	5	6	7	8	9	10	11
lower edge	0°	35°	50°	63°	74°	85°	95°	106°	117°	130°	145°
center	25°	43°	57°	69°	80°	90°	100°	111°	123°	137°	155°
upper edge	35°	50°	63°	74°	85°	95°	106°	117°	130°	145°	180°

Table 6.1: Zenith angle bins used for the estimation of the sensitivity and the discovery potential.

The parameter Ω_i denotes hereby the solid angle of the Ψ bin between Ψ_i and Ψ_{i+1}. If the background component happens to be a neutrino flux, then the production efficiency $\eta(E_{\nu_\mu}, E_\mu, \theta)$ is used to convert the neutrino flux into a muon flux at the detector, similar to what is done with the signal component. The factor $P_{\text{Veto}}(E_\mu, \theta_{\text{p.s.}})$ is non-zero only for atmospheric background (atmospheric muons and neutrinos) and incorporates the effect of a surface veto on the event rate (see section 6.3.4). The total background b_i is the sum of all relevant background components. There is one approximation used in order to calculate the event rate b_i, namely that the background flux does not change significantly within a zenith range of $\theta_{\text{p.s.}} - \Psi_{\max} < \theta_{\text{p.s.}} < \theta_{\text{p.s.}} + \Psi_{\max}$, with $\Psi_{\max} = 3\,^\circ$.

6.3.2 Muon Selection Efficiency

The first sensor-dependent component that influences the event rate in Ψ_i is the muon selection efficiency $\text{Eff}_\mu(E_\mu, \theta)$, which describes the probability of a muon with energy E_μ (at the detector) and zenith angle θ to end up in the final data sample. Therefore, the selection efficiency is a function of the applied quality cuts, hence, depends on the sensor type (see section 5.3.4).
The effective area of a detector is actually a product of the geometric area, the cut-dependent selection efficiency and a function usually denoted as trigger efficiency. The trigger efficiency, in turn, is nothing else then a function describing the probability of an event to be marked by a certain trigger algorithm, and therefore usually also dependent of energy, direction and sensor type. Since the trigger algorithm integrated in the simulation chain used in this work (see section 4.1.4.1) has a relatively low energy threshold, while at the same time the energy region important for the IceCube Gen2 high-energy array is relatively high, it is assumed, that the trigger efficiency of muons with energies at the detector of 500 GeV and above is approximately equal to one.
The selection efficiency for the nominal mDOM (2.24) and the upscaled PDOM (2.24) is defined as the ratio of selected events after the standard quality cuts have been applied over the total amount of events (from the combined datasets 20016 and 20198) derived for eleven equal area zenith bands (see table 6.1) and eight energy bins (see table 6.2).
The datasets available for this work, however, only cover an energy range from 3 TeV to 70 PeV. Since neither the selection efficiency, nor the flux of all relevant components is close to zero outside this energy range, the selection efficiency function acquired with the simulation had to be extrapolated. In order to avoid any bias concerning the comparison of the achievable point

bin index	1	2	3	4	5	6	7	8
lower edge [GeV]	$3.0 \cdot 10^3$	$1.1 \cdot 10^4$	$4.3 \cdot 10^4$	$1.7 \cdot 10^5$	$6.3 \cdot 10^5$	$2.4 \cdot 10^6$	$9.1 \cdot 10^6$	$3.5 \cdot 10^7$
center [GeV]	$5.9 \cdot 10^3$	$2.2 \cdot 10^4$	$8.5 \cdot 10^4$	$3.2 \cdot 10^5$	$1.2 \cdot 10^6$	$4.7 \cdot 10^6$	$1.8 \cdot 10^7$	$6.7 \cdot 10^7$
upper edge [GeV]	$1.1 \cdot 10^4$	$4.3 \cdot 10^4$	$1.7 \cdot 10^5$	$6.3 \cdot 10^5$	$2.4 \cdot 10^6$	$9.1 \cdot 10^6$	$3.5 \cdot 10^7$	$1.3 \cdot 10^8$

Table 6.2: Energy bins used for the estimation of the sensitivity and the discovery potential

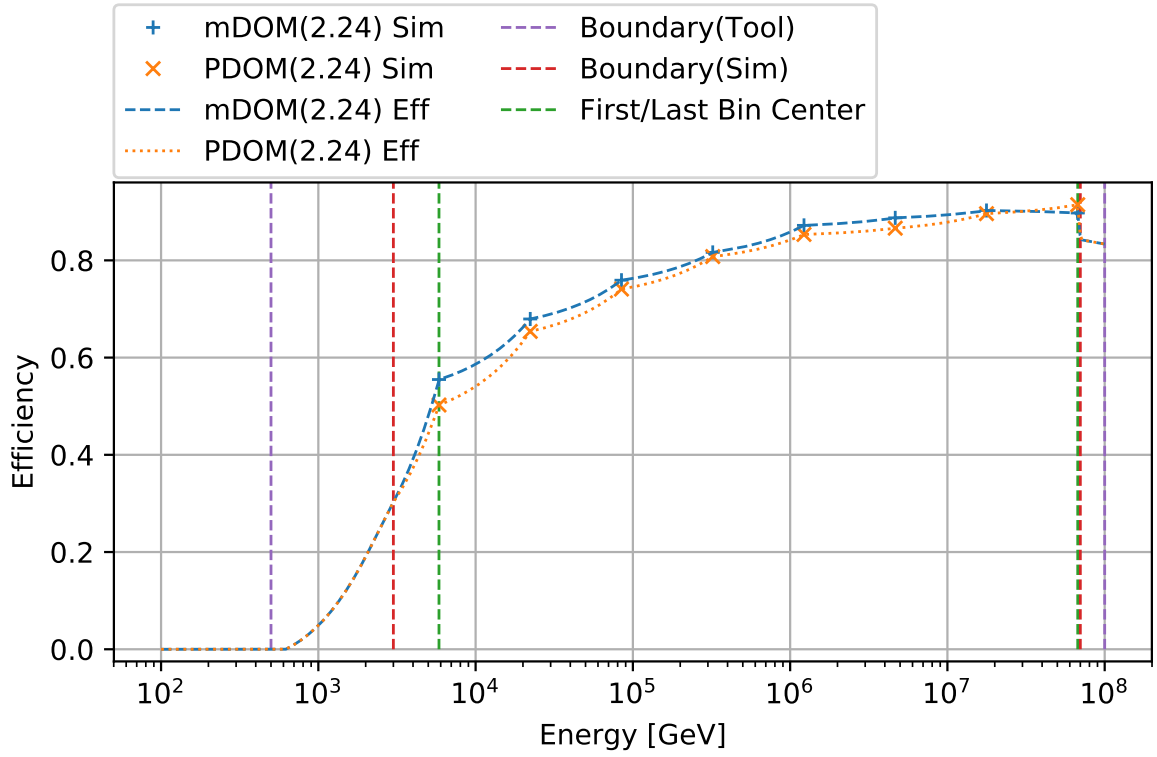

Figure 6.4: Muon selection efficiency versus energy for muons with a zenith angle between 85° and 95° as implemented in the Gen2-analysis framework.

source figures of merit between the two sensor types, outside of the energy range of the available simulations, the exact same function for the extrapolation, namely the default selection efficiency implemented in the Gen2-analysis framework, has been used. Figure 6.4 shows the implemented selection efficiency versus the muon energy at the detector for a muon zenith angle between 85° and 95° (zenith bin 6). The efficiency plots for the other zenith bands can be found in appendix D.3.

The purple vertical lines in this figure mark the hard coded boundaries of the Gen2-analysis framework, the red lines mark the boundaries of the simulations and the green lines mark the first and last center of the used energy bins, so the first and last energy values for which efficiencies from the simulations were available. These six vertical lines define five energy regimes,

two regimes enclosed by the purple and red lines, denoted as extrapolation regime, two regimes enclosed by the red and green lines, denoted as transition regime, and one regime enclosed by the two green lines, which is the energy regime for which values from the simulation are available. The simulated regime reaches from 5.9 TeV to 67 PeV (first to last energy bin center). At each bin center the muon selection efficiency obtained with the simulations is shown for the two different sensor types, while the values between the bin centers have been linearly interpolated. The apparent curvature of the line segments in between two markers is a consequence of the logarithmic visualization of E_μ while the interpolation between two consecutive values is linear in E_μ.
The transition regimes, the first one between 3.0 TeV and 5.9 TeV and the second one between 67 PeV and 70 PeV, mark the transition between efficiencies which are obtained from the simulations to the implemented default efficiencies. The values at the green lines are the first and last efficiencies purely from simulations, the values at the red lines are the first and last efficiencies purely from the functions used for extrapolation. All values in between these lines are obtained via linear interpolation.
The remaining two regimes, the extrapolation regimes between the purple and red lines, only contain values obtained via the functions used for the extrapolation. For both sensor types the exact same extrapolation functions have been used, thus, the values in the extrapolation areas are equal for the mDOM and the PDOM, ensuring an unbiased estimation of the point source figures of merit for both sensor types. A brief study investigating the effect of different extrapolation strategies on the figures of merit has been conducted, showing only minor changes in the absolute values of the sensitivity and the discovery potential, $< 8\,\%$ for both sensor types, and no significant changes concerning the comparison of the two sensor types, $< 1,\%$ (see appendix D.1).

6.3.3 From Median Angular Error to a Point Spread Function

The main advantage of a segmented sensor is the improvement of the angular resolution (shown in chapter 5). In order to integrate the improved direction reconstruction into the Gen2-analysis framework, an energy and zenith angle-dependent continuous point spread function (PSF) $P(E,\theta)$ needs to be derived. The PSF is the probability density function of the opening angle Ψ.
The first intuitive approach would be to use a three dimensional spline surface and fit it on top of the simulation results binned in energy, zenith angle and the opening angle. This has been tried extensively, but due to insufficient statistics, this approach had to be abandoned, because either highly unphysical artifacts appeared in the spline fit, or the spline fit did not describe the results from the simulations well enough.
The approach being used eventually utilizes the so-called "King" function K in order to parameterize the PSF, a procedure also used by XMM [88] with origins in [3] and [40]. The function K is

implemented as

$$K(\Psi,\sigma,\gamma) = \frac{\Psi}{\sigma^2}\cdot\left(1-\frac{1}{\gamma}\right)\cdot\left(1+\frac{1}{2\gamma}\cdot\frac{\Psi^2}{\sigma^2}\right)^{-\gamma}, \tag{6.25}$$

with two free parameters σ and γ, which can now be fit on the simulations to incorporate energy and zenith angle dependent behavior: $\sigma \to \sigma(E,\theta)$ and $\gamma \to \gamma(E,\theta)$.
In order to reduce the effect of the low statistics in the available datasets, the default parameter fits of σ and γ implemented in the Gen2-analysis framework have been used. These default fits have been obtained via a fit on top of a larger simulated muon data set[2]. To integrate the angular resolution presented in section 5.3.4 an energy-dependent scaling function $S_{\mathrm{mDOM/PDOM}}(E,\theta_i)$ for both sensor types and each zenith band, θ_i, has been fitted and was implemented into the Gen2-analysis framework. The functions $S_{\mathrm{mDOM/PDOM}}(E,\theta_i)$ are used to scale the default point spread functions implemented in the Gen2-analysis framework in such a way that the median opening angle of the scaled point spread function is equal to the median opening angle obtained with the simulations for each zenith band and each energy bin center. Linear interpolation was used to generate values for the scaling functions in between the centers of two consecutive energy bins (see the definition of the used zenith bands and energy bins in table 6.1 and 6.2).
Similar to the selection efficiency, the PSF needs to be extrapolated to yield reasonable values outside the simulated energy range. Since no simulations of muons traversing a Gen2 high-energy array like detector covering this energy range are available at the time of this writing, the angular resolution of the IceCube in-ice array (see figure 3.9) is used for the extrapolation from 500 GeV to 3 TeV and an in $\log_{10}(E_\mu)$ linear function is used for the extrapolation from 70 PeV to 100 PeV. The median angular resolution of the integrated PSF used for the sensitivity estimation for muons with a zenith angle between 85° and 95° is shown in figure 6.5 (plots for the other zenith bands can be found in appendix D.3). The steep fall and rise of the median opening angle of the scaled point spread functions (nominal mDOM (2.24) displayed as dashed blue line, upscaled PDOM (2.24) displayed as dotted orange line) are a consequence of the extrapolation. One might argue that the extrapolated values are too high, however, larger values are conservative within this context. Furthermore, the effect of the angular resolution below a muon energy of 6 TeV has very little effect on the absolute point source sensitivity and almost no effect on the improvement potential of the mDOM when compared to the PDOM, which is studied in more detail in appendix D.2. The expected event rate of muons with an energy above 70 PeV is very low, therefore it is assumed that the extrapolation of the PSF to energies above this value has no influence on the obtained figures of merit.

6.3.4 A Simple Surface Veto Simulation

Additionally, the effect of a surface veto on the figures of merit is studied. The basic idea of a surface veto for the IceCube Gen2 high-energy array is to be able to veto atmospheric muons

[2] Conducted by the developer of the Gen2-analysis framework

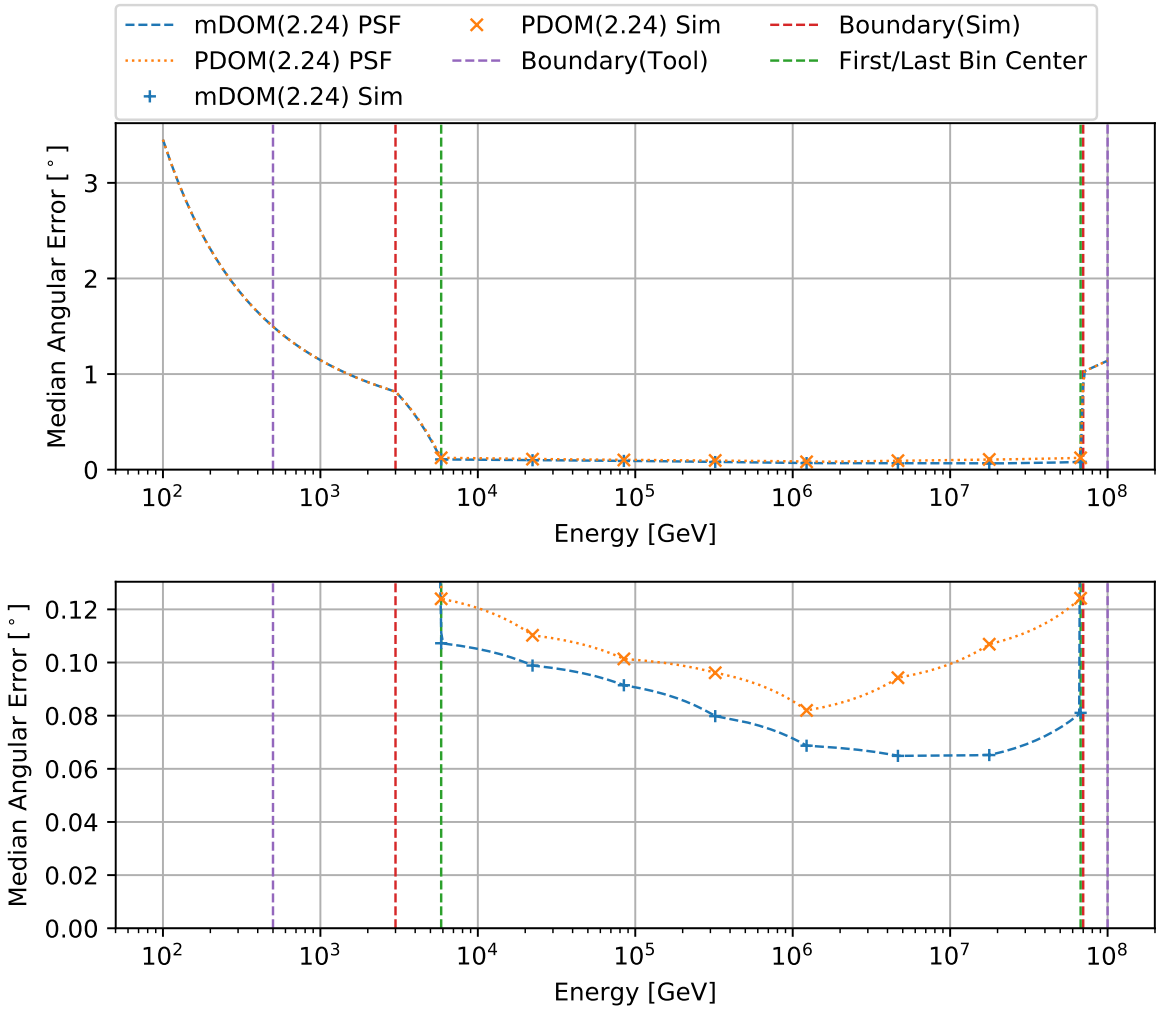

Figure 6.5: Median angular resolution versus energy for muons with a zenith angle between 85° and 95° including extrapolation as implemented in the Gen2-analysis framework. The orange and blue markers show the median opening angle obtained from the available simulations. The dashed blue line and the dotted orange line show the median opening angle of the used point spread function of the nominal mDOM (2.24) and the upscaled PDOM (2.24). The steep fall and rise of these two curves in between the red and green vertical lines are a consequence of the conservative extrapolation of the point spread function to energy regimes for which no simulations were available. The bottom plot is a zoomed in version of the top plot in order to emphasize the differences in angular resolution obtained with the two sensor types.

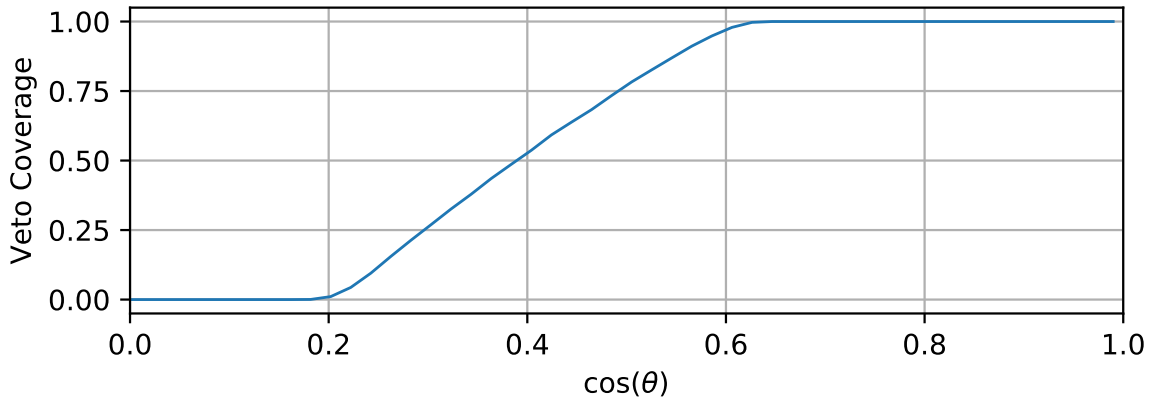

Figure 6.6: Coverage by a $75\,\mathrm{km}^2$ surface veto of the Gen2 high-energy array versus cosine zenith angle.

and atmospheric neutrinos, created in cosmic ray induces showers, by identifying muons created in these showers with the surface veto. All events in the in-ice array which could be correlated with a surface veto event would then be discarded, since they are with a high probability of atmospheric origin, thus reducing the background contamination in the final data sample.
The hypothetical surface veto for Gen2 is implemented to cover an area of $75\,\mathrm{km}^2$ and is located on the ice surface with its center directly above the in-ice array. In order to include this into the sensitivity calculation, the event rates in the respective bins are modified by an additional factor $P_{\mathrm{Veto}}(E_\mu, \theta_{\mathrm{p.s.}})$, which is a product of the coverage of the in-ice array by the surface veto itself (see figure 6.6) and an energy and zenith angle dependent factor. For atmospheric muons, the energy dependence is simply implemented as a step function with a threshold at 100 TeV muon energy at the detector. Above this threshold, the energy factor is one, below it is zero (the threshold is motivated by the veto efficiency of IceTop [82] and [22]). This also means, that, apart from the obviously zenith dependent veto coverage, no further zenith dependence is implemented for atmospheric muons.
For atmospheric neutrinos, however, the situation is much more complicated, since it is not the neutrino itself that triggers the veto, but accompanying muons created in the same atmospheric shower. If there are muons, and how energetic they are also depends on whether the neutrino is a conventional or prompt neutrino and on the primary cosmic ray particle itself. All of these factors are implemented in the veto simulation of the Gen2-analysis framework, but going into too much detail concerning assumptions and respective parameterizations is beyond the scope of this work. Further details on the exact implementation can be found in [50].

6.3.5 Figures of Merit

The final section of this chapter presents the results of the conducted estimation of the figures of merit for neutrino point source searches achieved by the two tested sensor types, assuming an unbroken power law flux for the hypothetical point source of the form:

$$\frac{\mathrm{d}N_{\nu_\mu+\bar{\nu}_\mu}}{\mathrm{d}E_\nu} = \Phi^{\nu_\mu+\bar{\nu}_\mu}_{100\,\mathrm{TeV}} \left(\frac{E_\nu}{100\,\mathrm{TeV}}\right)^{-\gamma} \tag{6.26}$$

A spectral index of $\gamma = 2.0$ was assumed for the point source flux. For both figures of merit, the 90% exclusion limit and the 5σ discovery potential, the corresponding ν_μ and $\bar{\nu}_\mu$ flux normalization at 100 TeV, $\Phi^{\nu_\mu+\bar{\nu}_\mu}_{100\,\mathrm{TeV}}$, multiplied by E^{-2} versus the sinus of the declination, denoted as δ, is presented. In the case of IceCube the relation between zenith angle θ and declination δ is simply: $\sin(\delta) = -1 \cdot \cos(\theta)$ due to its location at the South Pole. At the time of this writing the inclusion of uncertainties on the point spread functions or the selection efficiencies used in the Gen2-analysis framework in order to estimated the figures of merit is not supported. Therefore no uncertainties of the estimated upper limits and discovery potentials have been estimated.

The estimated 5σ discovery potential achieved by the Gen2 high-energy array equipped with nominal mDOMs (2.24) in comparison with upscaled PDOMs (2.24) versus declination is shown in figure 6.7 while the 90% upper limits are presented in figure 6.8. Both figures of merit are shown for a measurement time of 15 years.

The highest performance in both cases is reached for sources at the horizon, which is a result of the better angular resolution, low atmospheric background and a high efficiency of high energetic neutrinos propagating to the instrumented volume. For sources located in the southern sky (negative $\sin(\delta)$) the background contamination due to atmospheric muons is mainly responsible for the increase of the necessary flux normalization for a discovery and the upper limit. For sources located in the northern sky (positive $\sin(\delta)$) the increasing opacity of the Earth for high-energy neutrinos reduces the signal flux at the detector leading to a decreasing performance. Additionally, the angular resolution is worse for sources outside of the horizontal band, which also influences the figures of merit.

The direct comparison of the discovery potentials and upper limits obtained for both sensor types, displayed in the bottom plots of figure 6.7 and 6.8, shows a clear angular dependency. For sources at very low declinations, the discovery flux normalization obtained with the nominal mDOM (2.24) is $\approx 11\%$ lower, compared to the respective values obtained with the upscaled PDOM (2.24) and decreasing to $\approx 8\%$ for horizontal sources. With increasing declinations the discovery fluxes of both sensor types further equalizes, until a turnover at a declination of $\approx 27°$. The upscaled PDOM (2.24) yields lower discovery fluxes for source positions with larger declinations.

A similar result is obtained by comparing the upper limits estimated for both sensor types, however, with a slightly decreased positive effect due to the sensor segmentation of the mDOM. The effect of the presence of a surface veto is shown for both figures of merits and both sensor types (results without surface veto are indicated with the dashed lines). For both sensor types, the

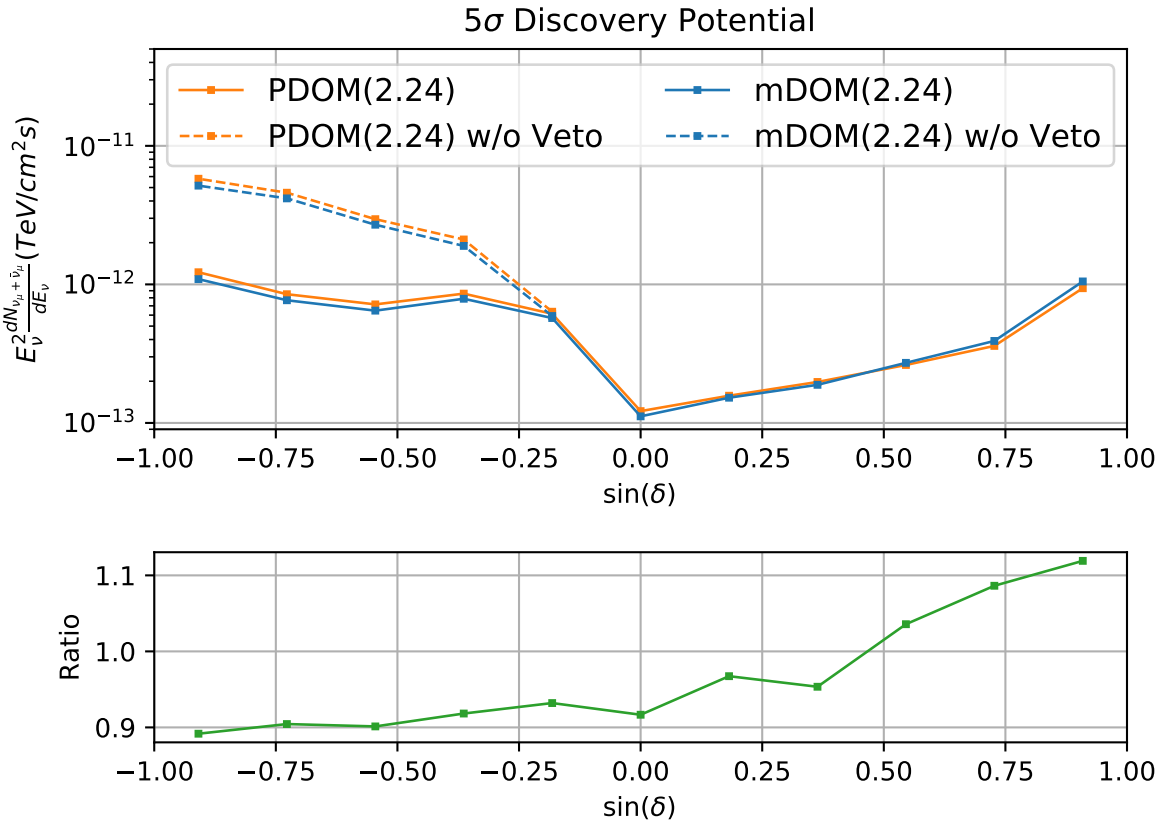

Figure 6.7: Comparison of the estimated 5σ discovery potential with a measurement time of 15 years. *Top*: 5σ discovery potential for neutrino point sources versus sinus declination for the Gen2 high-energy array equipped with the nominal mDOM (2.24) (blue) and the upscaled PDOM (2.24) (orange) calculated for 11 declinations. The dashed lines show the discovery potentials achievable without any surface veto. *Bottom*: Ratio (mDOM (2.24) / PDOM (2.24)) of the achieved discovery potential (with veto) for each declination.

presence of a surface veto decreases the discovery flux up to a factor of five and the upper limits up to a factor of four. The relative difference of the two sensor types does not change significantly if a veto is present or not.

In conclusion, the estimated figures of merit for neutrino point source searches obtained with a binned likelihood and non-optimized quality cuts, indicate that the improved angular resolution for through-going muon induced tracks obtainable by the Gen2 high-energy array when equipped with nominal mDOMs (2.24) instead of upscaled PDOMs (2.24) does improve the discovery potential and the sensitivity for neutrino point sources for most zenith angles. Especially at the horizon, where the Gen2 high-energy array is assumed to be most sensitive, an improvement of up to $\approx 8\%$ was found due to sensor segmentation of the mDOM. Only for potential sources with declinations above $\approx 27^\circ$ the upscaled PDOM (2.24) outperforms the nominal mDOM (2.24).

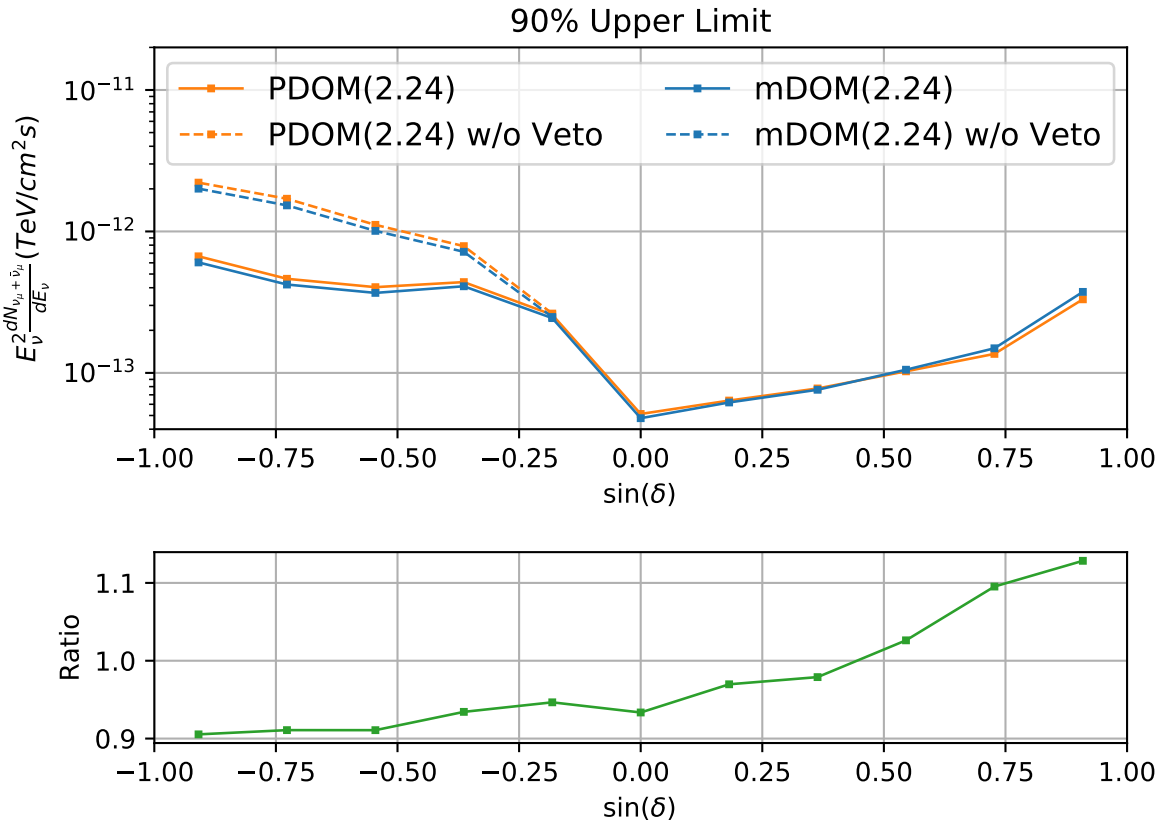

Figure 6.8: Comparison of the estimated 90 % neutrino flux upper limits after a measurement time of 15 years. *Top*: 90% upper limits for neutrino point source fluxes versus sinus declination for the Gen2 high-energy array equipped with the nominal mDOM (2.24) (blue) and the upscaled PDOM (2.24) (orange) calculated for 11 declination bands. The dashed lines show the upper limits achievable without any surface veto. *Bottom*: Ratio mDOM (2.24) / PDOM (2.24) of the achieved upper limit with surface veto for each declination band.

CHAPTER 7

DISCUSSION

This chapter reviews the results regarding the angular resolution and the expected point source figures of merit from the mDOM / PDOM studies described earlier. Various assumptions have been made and their possible impact on the presented results is discussed. Finally, the estimated upper limits and discovery fluxes are put into context of these published by either existing or planed neutrino telescopes.

7.1 Assumptions & Simplifications

The first part of this chapter is going to focus on assumptions and simplifications applied throughout this work.

7.1.1 Unrealistic Ice Model

One simplification is the usage of a homogeneous ice model (see section 4.1.2). While in theory it is possible to use a more realistic ice model, so an ice model with depth-dependent scattering and absorption properties including a tilt and anisotropy, for the reconstruction, in practice this is very time consuming. Integrating horizontal ice layers alone into the spline table production for the mDOM would increase the dimensionality of the photon tables by 3: one additional dimension for the depth, one for the zenith angle and one for the azimuth angle of the PMT in question. The mDOM houses 24 PMTs with different orientations, which yields, in combination with 120 horizontal ice layers, each with a thickness of 10 m, a factor of 2880. This means that the number of bins in the photon tables is multiplied by this factor. The CPU time needed to produce such photon tables, given one uses the same production strategy, would increase by the same factor. While theoretically, this would be possible and, given access to a large enough computing farm,

feasible[1], the existing code used for photon table production, as well as the code for the spline table fitting and the interface to be able to evaluate the so produced spline tables would have to be adjusted significantly. Additionally, the effort for the sanity checks, the evaluation time of the PDFs as well as the required amount of memory needed would increase considerably.
One of the main arguments why a segmented sensor yields better performance on angular reconstruction is the additional directional information provided by the different PMTs, all oriented in different directions. It might be argued that more of the directional information of the photons might be lost before detection when a realistic ice model is used. Figure 7.1 compares the used ice model, denoted as "Homogeneous Ice", with a model where scattering and absorption coefficients of a more realistic ice model, namely "Spice Mie", have been averaged over the instrumented depth of Gen2. One can observe that the scattering coefficient, $\alpha_{\text{scat.}}$, of the homogeneous ice model is about 22 % too low, while the absorption coefficient, $\alpha_{\text{abs.}}$, is about 28 % too low for small wavelengths. Since the ice in a depth between 2000 m and 2100 m is especially contaminated with dust (see section 3.2.4), a comparison with an averaged ice model excluding the so called "dust layer" has been conducted as well, yielding $\alpha_{\text{scat.}}$ being only 9 % too low and $\alpha_{\text{abs.}}$ being 16 % too low (at small wavelengths). It is assumed that the advantages of a segmented sensor are still present when used within a more realistic ice model.

7.1.2 Perfect Knowledge of the Ice

Another aspect to keep in mind is the usage of the exact same ice model for muon simulation and the production of the spline tables used for reconstruction. This, obviously, would not be the case in a real experiment, since the optical properties of the Antarctic ice are still only known with a certain precision and remain being the topic of ongoing research (e.g. [4]). It can be assumed, that a certain deviation between the ice model used for simulation and the ice model used for producing the PDFs utilized by the reconstruction, will result in worse angular resolutions, independent of the sensor type. However, the argument that a segmented sensor would provide additional information, which can be used by a reconstruction algorithm still holds, independent of any ice model discrepancy. Furthermore, previous analyses have shown that uncertainties of the ice properties are sub-dominant with respect to statistical uncertainties (e.g. [9]).

7.1.3 Assumptions & Shortcuts for the Sensitivity Estimation

While the last two sections described simplifications that probably caused the absolute numbers of the estimated neutrino point source figure of merits to be too optimistic, this section outlines two aspects of this work that could have caused these numbers to be not as good as they could be. The first aspect is the consequence of a technical limitation, namely the usage of a binned instead

[1] Assumption of the author

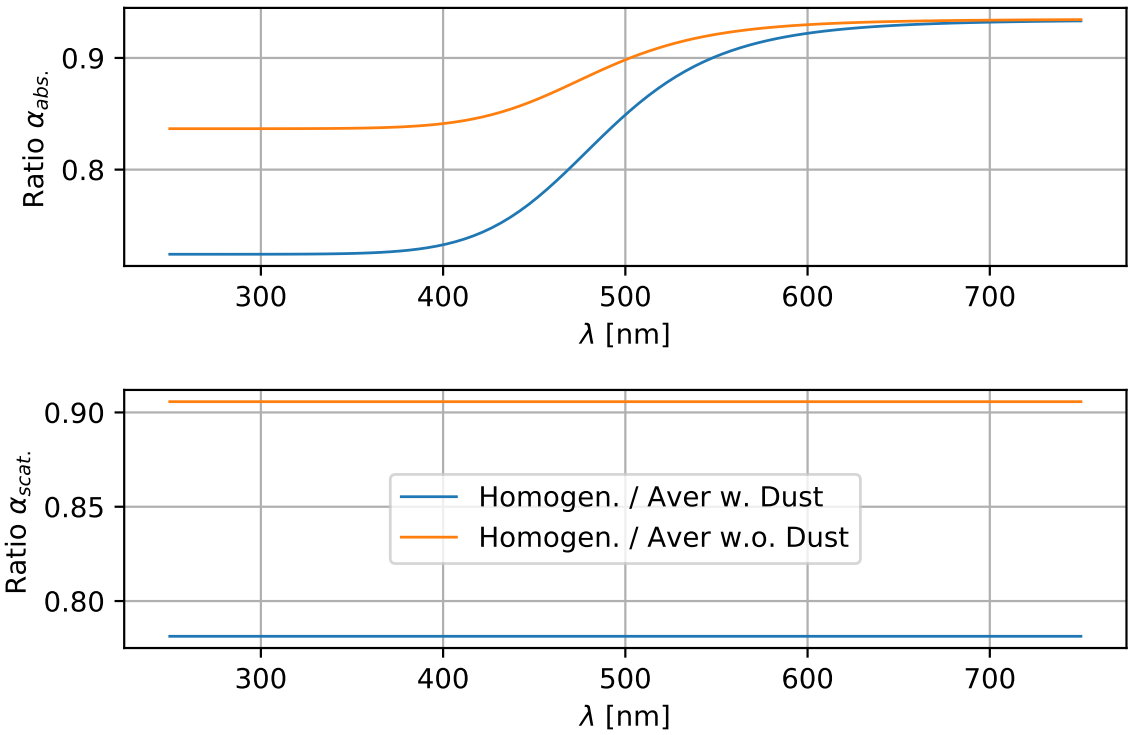

Figure 7.1: Comparison of the homogeneous ice model (used in this work) and the "Spice Mie" ice model. *Top:* Wavelength versus the ratio of the absorption coefficient of the homogeneous ice model over the averaged absorption coefficient of the "Spice Mie" ice model with (blue curve) and without (orange curve) the dust layer. *Bottom:* Wavelength versus the ratio of the scattering coefficient of the homogeneous ice model over the averaged scattering coefficient of the "Spice Mie" model with (blue curve) and without (orange curve) the dust layer.

of an unbinned likelihood for the estimation of the upper limit and the discover flux. The Asimov dataset (see section 6.1.3) is defined as a binned dataset and implemented as such in the Gen2-analysis framework. However, via decreasing the bin size of the observable (opening angle Ψ in this case), one can close the gap to the performance of an unbinned approach. The decision of using 300 equal sized bins from 0° to 3° has been the result of a brief study investigating the impact of the binning to the estimated upper limits and discovery fluxes for both sensor types. A binning with half the bin size did, at least in this case, neither improve the upper limits nor the discovery fluxes significantly for any of the two tested sensor types. Therefore, it is assumed that the relative difference between the two sensor types should be almost unaffected as well by the likelihood choice.

Contrary to the used likelihood method, it can be assumed, that the used quality cuts do have a significant influence on the estimated upper limits and the discovery fluxes. Within a normal

analysis, a significant amount of time is usually spend on optimizing the event selection. A common approach nowadays utilizes machine learning methods for event selection in order to get better results (e.g. [70]). Since a sophisticated selection algorithm is strongly correlated to the used sensor type, the results obtained by using such an approach could not be compared to respective results obtained with another sensor without the risk of introducing a significant bias. Therefore, since the goal of this work is to investigate the effect of the sensor segmentation itself, it has been decided to use very basic but comparable quality cuts, although this means, that the obtained point source figures of merit are probably not be as good as they potentially could be.

7.1.4 Up- and Downscaling of the Effective Photocathode Area

There is one additional grain of salt that needs to be taken into consideration when directly comparing results obtained with a Gen2 high-energy array equipped with mDOMs and the respective results when the array is equipped with PDOMs (after equalizing the respective effective photocathode area). A large part of the work for this thesis has been conducted to ensure that the presented results are a consequence of the segmentation of the sensor itself and not be biased by any other aspects. The most obvious differences of the two sensor types potentially influencing the angular resolution is the effective photocathode area, which directly influences the amount of detected photons. In order to eliminate this bias, the effective areas of the sensor types have been artificially either up- or downscaled, resulting in two unrealistic sensors: an upscaled PDOM and a downscaled mDOM which can then be compared to the respective unscaled counterparts, yielding the presented results which reflect a direct consequence of the segmentation itself. However, a PDOM upscaled with a factor of 2.2 is not equal to 2.2 real PDOMs and 2.2 downscaled mDOMs are not equal to one nominal mDOM. Hence, this thesis did not answer the question, which sensor design should be used for the Gen2 high-energy array with respect to neutrino point source searches, but investigated the effect of a mDOM-like distribution of the photocathode area, including the additional directional information obtained with such a sensor design, compared to the photocathode distribution of the PDOM.

7.2 Comparison to other Experiments

Within the last section of this chapter, the obtained results are compared to point source sensitivities from existing experiments, namely ANTARES [62] and IceCube, and to the estimated sensitivity of KM3NeT/ARCA [6], see figure 7.2. The sensitivities for the Gen2 high-energy array are shown for a version equipped with nominal mDOMs(2.24) including a surface veto (as described in sec 6.3.4) for an exposure time of 6 instead of 15 years, to be comparable to estimated sensitivities of KM3NeT/ARCA.
According to the results obtained in this work the Gen2 high-energy array will be the most sensitive telescope for neutrino point sources with a declination of $\geq -5^\circ$ (zenith angle of $\geq 85^\circ$

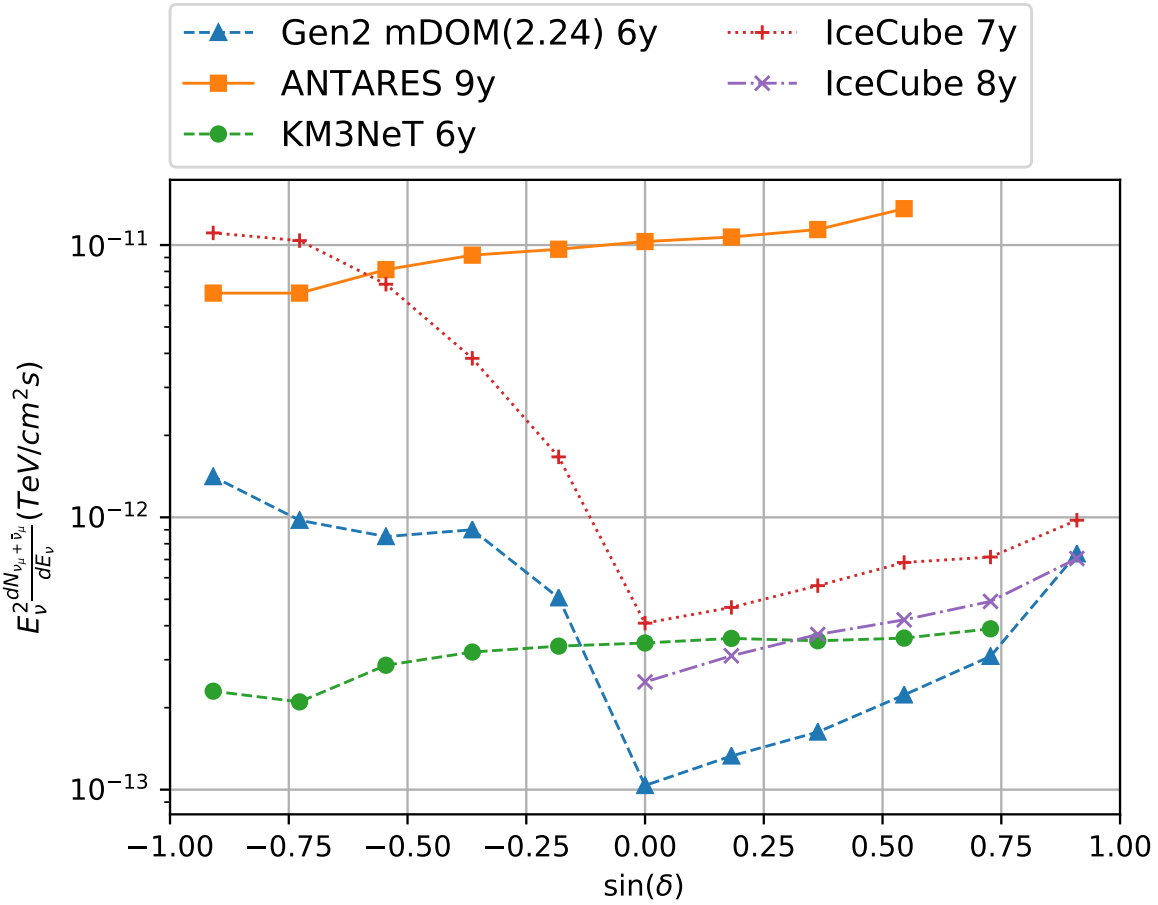

Figure 7.2: 90% exclusion upper limits VS sinus declination for ANTARES [2], KM3NeT/ARCA [90], IceCube with 7 years of data [68], IceCube with 8 years of data [73] and Gen2 high-energy array equipped with nominal mDOMs(2.24) for 6 years of exposure (this work). The flux of the hypothetical neutrino point source has been model in each case with an unbroken power law and a spectral index of −2.0.

in IceCube coordinates). For potential sources with a declination below this angle, the planned KM3NeT/ARCA detector will be more sensitive, since, even with a surface veto, the influence of atmospheric muons significantly reduces the performance of instruments at the South Pole. The most distinct difference between these two next generation neutrino telescopes is obtained for horizontal sources with the Gen2 high-energy array equipped with mDOMs being a factor of ≈ 3.3 more sensitive then Km3NeT/ARCA.

When compared to already existing experiments, one obtains an improved sensitivity of almost two orders of magnitude for horizontal sources with respect to ANTARES and a factor of 2.4 when compared to the current results obtained by IceCube (IceCube with 8 years of data). For point sources with a declination near the south pole ($\delta = -90\,^\circ$), the Gen2 high-energy array is still going to be more sensitive by a factor of 4.7 compared to ANTARES, however, once KM3NeT/ARCA is operational, that is going to be the most sensitive instrument in that region in the sky. For positive declinations, Gen2 will be the most sensitive instrument, including existing and planned experiments.

The fact, that the estimated Gen2 sensitivity for the highest declination is slightly worse, then what has been obtained by the IceCube point source analysis with 8 years of data, indicates that the calculated figures of merit might be too conservative. One of the reasons, why the point source analysis with 8 years of IceCube data is so much better then the 7-year analysis, is a highly refined and optimized data selection strategy. This strengthens the assumption that a more sophisticated event selection strategy optimized for a segmented sensor could improve the performance of the Gen2 high-energy array further.

CHAPTER 8

SUMMARY, CONCLUSION & OUTLOOK

The main objective of this thesis was to investigate the effect of the sensor segmentation of the "multi-PMT Digital Optical Module" (mDOM), as the base detection unit for the planned IceCube Gen2 high-energy array compared to the "PINGU Digital Optical Module" (PDOM), an upgraded version of the standard IceCube digital optical module. The focus lay on the achievable angular resolution of through-going muon tracks and the subsequently estimated exclusion limits and discovery fluxes for potential neutrino point sources. Various sanity checks conducted in this work ensured that only the segmentation and the distribution of the photocathode area of the respective sensor design itself influenced the results.

Apart form the segmentation, the total photocathode area is the most dominant difference between an mDOM and a PDOM. To overcome this difference for the comparison the quantum efficiency of both sensor types was artificially increased or decreased during the simulation to equalize the photon detection efficiency. In order to ensure that no bias is introduced in the simulation of through-going muon track events in a common Gen2 high-energy array layout called "Sunflower 240m", almost every step in the processing pipeline had to be adjusted and checked.

Various steps in the reconstruction algorithm had to be adjusted to be able to reconstruct events detected with mDOMs. The standard algorithm for reconstructing muon track directions in IceCube was SplineMPE, which was also used in this work. SplineMPE utilizes a likelihood approach in order to estimate track event parameters. The likelihood consists of probability density functions (PDFs), one for each photomultiplier (PMT) that detected at least on photon during the estimated event time window. The PDFs depend on the sensor design itself, incorporating the orientation, the angular and the wavelength acceptance of the respective PMT, as well as the optical characteristics of the ice and have to be calculated in advance. The software for the

production of such PDFs was adjusted, such that the resulting shape is as accurate for a PMT inside an mDOM as for a PMT inside a PDOM. For the sake of simplicity a homogeneous model of the Antarctic ice was used instead of the standard, layered ice model. In order to minimize the bias, which could have been introduced during the production of the mDOM PDFs, qualitative and quantitative test procedures utilizing a Kolmogorov-Smirnov test have been developed. These tests ensure that the new mDOM PDFs resemble an mDOM equally well as the conventionally produced PDFs resemble a PDOM.

The definition of parameters used as quality cuts for the event selection had to be reworked as well. Since the parameters used for quality cuts are functions of sensor-dependent observables, a sensor-independent, Monte-Carlo based parameter, the true length of the muon within the instrumented volume, has been defined. With this parameter it was possible to perform an unbiased comparison of the achievable angular resolution of the two sensor designs.

At first horizontal through-going muons have been considered, which yield the best angular resolution with the Gen2 high-energy array, and the sensor-independent parameter was used for the event selection. For the remaining muons the median angle between reconstructed and true muon direction, also called opening angle, is between 10 % to 20 % lower when mDOMs instead of PDOMs with upscaled photocathode areas are used. For muon energies above 1 PeV the improvement is up to 40 %. For down-going muons an improvement between 10 % and 20 % has been found in all but two energy intervals. Reconstruction of up-going muon tracks with energies below 1 PeV with mDOMs lead to larger median opening angles with values in between 7 – 13 % higher compared to the PDOM with increased photocathode area. This behavior changes above 1 PeV for which the mDOM yields up to 25 % better resolution.

Two conventional, sensor-dependent cut parameters, NDir and LDir, have been used for an event selection as well. The median opening angle for horizontal muons was reduced by 10 % to 15 %, and up to 40 % for the highest energies, when mDOMs instead of upscaled PDOMs have been simulated and the conventional cut parameters have been used for an event selection. For up- and down-going muons the median opening angle of the two sensor types becomes more similar after the application of the conventional, sensor-dependent cut parameters. The main differences of the two sensor designs shifts to the event selection efficiency, so the ratio of the amount of events in the selected data set over the total amount of events. Up-going muon events have a higher probability of being in the final data set if the detector is equipped with PDOMs, while down-going muons have a higher probability of being selected when the array is equipped with mDOMs.

In the last part of this thesis, the sensitivity and the discovery potential for neutrino point sources achievable with the Gen2 high-energy array equipped with either the nominal mDOM or the upscaled PDOM was estimated by utilizing an Asimov dataset. For declinations of hypothetical sources below 21°, a Gen2 high-energy array equipped with nominal mDOMs yields better exclusion limits and lower discovery fluxes than the same detector geometry equipped with

upscaled PDOMs. Especially for potential sources with a declination close to zero, the discovery flux achieved with mDOMs is $\approx 8\,\%$ lower compared to the PDOM with equalized photocathode area. With decreasing source declination angle, this ratio gets as large as $11\,\%$.
In comparison to published exclusion limits of existing or planned neutrino telescopes the results obtained in this work indicate that the Gen2 high-energy array equipped with mDOMs is going be the most sensitive instrument for neutrino point sources with a positive declination and a declination close to zero.
It can be assumed that the full potential of the mDOM as the base detection unit of a neutrino telescope has not been reached yet. The work done during this thesis paved the way for further studies with the mDOM. All available software for simulating mDOM events has been checked, including the SplineMPE reconstruction algorithm. Additionally, the functionality of producing mDOM photon PDFs has been implemented and a test procedure to efficiently test these PDFs has been developed.
One of the next steps, is the inclusion of a more realistic ice model into the event reconstruction. Furthermore, it is believed that more advanced reconstruction algorithms incorporating a more realistic event hypothesis will benefit from the additional information available due to the usage of mDOMs, even more than the reconstruction algorithm used in this thesis did. Another aspect with potentially huge impact on point source sensitivity of the Gen2 high-energy array is the event selection. Previous analyses have shown that an optimized event selection can have a large impact on the resulting sensitivity.
More aspects have to be investigated in order to decide which sensor design should be used as a base detection unit for the Gen2 high-energy array. However, the majority of the results obtained in this thesis have shown the potential of improving the event reconstruction when a segmented detection unit, like the mDOM, is used.

Zusammenfassung, Fazit & Ausblick

Das Hauptziel dieser Arbeit war es den Effekt der Sensorsegmentierung des "multi-PMT Digital Optical Modules" (mDOM) als Basisdetektionseinheit für das geplante "IceCube Gen2 high-energy array" verglichen mit dem "PINGU Digital Optical Module" (PDOM), einer verbesserten Version des Standard IceCube Digital Optical Modules, zu untersuchen. Der Fokus wurde hierbei auf die erreichbare Richtungsauflösung von durchgehenden Myonenspuren gelegt und die damit abgeschätzten obere Flussgrenze und das Entdeckungspotential von Neutrinopunktquellen.
Während dieser Arbeit wurden verschiedene Plausibilitätschecks durchgeführt um sicherzustellen, dass lediglich die Segmentierung und die Verteilung der Photokathodenfläche des jeweiligen Sensortyps die Ergebnisse beeinflussen. Neben der Segmentierung ist die absolute Photokathodenfläche der dominanteste Unterschied zwischen einem mDOM und einem PDOM. Um diesen Unterschied für den Vergleich zu beseitigen wurde die Quanteneffizienz beider Sensortypen während der Simulationen jeweils erhöht oder verringert um die Effizienz mit der Photonen detektiert werden anzugleichen. Um sicherzustellen, dass während der Simulation von durchgehenden Myonenspuren in einer für das "Gen2 high-energy array" häufig verwendeten Geometrie, "Sunflower 240 m", keine systematischen Fehler eingeführt wurden, wurde nahezu jeder Schritt in der Prozesskette angepasst und überprüft.
Verschiedene Schritte im Rekonstruktionsalgorithmus mussten angepasst werden um mit mDOMs detektierte Ereignisse rekonstruieren zu können. Der Standardalgorithmus zur Rekonstruktion der Richtung von Myonenspuren in IceCube war SplineMPE, welcher auch für diese Arbeit verwendet wurde. SplineMPE verwendet einen Likelihood Ansatz um die Parameter eines Spurereignisses abzuschätzen. Die Likelihood Funktion besteht aus jeweils einer Wahrscheinlichkeitsdichtefunktion (PDF) für jeden Photomultiplier (PMT), der mindestens ein Photon während des abgeschätzten Zeitfensters eines Ereignisses detektierte. Die PDFs sind abhängig vom Sensortyp und inkludieren die Orientierung, die Winkel- und die Wellenlängenakzeptanz des jeweiligen PMTs sowie die optischen Eigenschaften des Eises und müssen im Vorhinein berechnet werden. Die Software für die Produktion solcher PDFs wurde angepasst, sodass die Form der PDFs eines PMTs in einem mDOM genau so akkurat ist wie die für einen PMT in einem PDOM. Der Einfachheit halber wurde ein homogenes Eismodell des Arktischen Eises verwendet statt dem standardmäßigen, geschichteten Eismodell. Um den Effekt möglicher eingeführter systematischer Fehler bei der Produktion der mDOM PDFs zu minimieren wurden qualitative

und quantitative Tests unter Zuhilfenahme eines Kolmogorov-Smirnov-Tests entwickelt. Diese Tests stellen sicher, dass die neuen mDOM PDFs die einen mDOM genauso gut beschreiben, wie die konventionell produzierten PDFs einen PDOM.
Die Definition der Parameter welche als Qualitätsschnitte für die Ereignisselektion verwendet wurden mussten ebenfalls überarbeitet werden. Da die Parameter, welche für Qualitätsschnitte benutzt wurden Funktionen von sensorabhängigen Messgrößen sind, wurde ein sensorunabhängiger Parameter, die wahre Länge eines Myons innerhalb des instrumentierten Volumens, basierend auf Monte-Carlo Größen, definiert. Mit diesem Parameter war es möglich einen unbeeinflussten Vergleich der mit den beiden Sensortypen erreichbaren Richtungsauflösung zu ziehen.
Zunächst wurden durchgehende Myonen aus horizontaler Richtung, welche die beste Richtungsauflösung im "Gen2 high-energy array" ermöglichen, betrachtet nachdem der sensorunabhängige Schnittparameter für die Ereignisselektion verwendet wurde. Die Mediane der Winkel zwischen rekonstruierter und wahrer Myonenrichtung, auch Öffnungswinkel genannt, ist um 10 % bis 20 % kleiner wenn mDOMs benutzt werden statt PDOMs mit hochskalierter Photokathodenfläche. Für Myonen mit Energien oberhalb von 1 PeV stieg die Verbesserung auf bis zu 40 %. Für von oben kommende Myonen wurde eine Verbesserung zwischen 10 % und 20 % in allen außer zwei Energieintervallen erhalten. Für von unten kommende Myonenspuren mit Energien unterhalb von 1 PeV führte die Verwendung von mDOMs zu 7 % bis 13 % größeren Medianen der Öffnungswinkel verglichen mit dem PDOM mit hochskalierter Photokathodenfläche. Oberhalb von 1 PeV ist die mit dem mDOM erreichbare Auflösung um bis zu 25 % besser.
Zwei konventionelle, sensorabhängige Schnittparameter, NDir und LDir, wurden ebenfalls für eine Ereignisselektion verwendet. Die Mediane der Öffnungswinkel für Myonen aus horizontaler Richtung sind zwischen 10 % bis 15 %, und für die höchsten Energien bis zu 40 %, geringer wenn mDOMs statt hochskalierte PDOMs simuliert und die konventionellen Schnittparameter für eine Ereignisselektion verwendet wurden. Für von oben oder von unten kommende Myonen haben sich die Mediane der Öffnungswinkel der beiden Sensortypen angeglichen nach der Verwendung der konventionellen, sensorabhängigen Schnittparameter. Der Unterschied zwischen den beiden Sensortypen verschiebt sich in die Selektionseffizienz, also dem Verhältnis der Ereignisse im selektierten Datensatz und der Gesamtmenge an Ereignissen. Für von unten kommende Myonen ist die Wahrscheinlichkeit größer selektiert zu werden wenn der Detektor mit PDOMs ausgestattet ist, während für von oben kommende Myonen die Wahrscheinlichkeit größer ist wenn mDOMs verwendet werden.
Im letzten Teil der Arbeit wurde die mit dem "Gen2 high-energy array" erreichbare Sensitivität und das Entdeckungspotenzial bezüglich Neutrinopunktquellen mit Hilfe eines Asimov Datensatzes abgeschätzt. Für hypothetische Quellen mit einer Deklination unterhalb von 21° ergab ein "Gen2 high-energy array" mit mDOMs geringere obere Flussgrenzen und kleinere Flüsse, die notwendig sind für eine Entdeckung als die gleiche Detektorgeometrie ausgestattet

mit hochskalierten PDOMs. Vor allem für Quellpositionen mit einer Deklination nahe null ist der abgeschätzte Entdeckungsfluss mit mDOMs ca. 8 % geringer als mit PDOMs mit angeglichener Photokathodenfläche. Dieses Verhältnis steigt auf 11 % mit abnehmender Deklination der Position der Quellen. Verglichen mit publizierten oberen Flussgrenzen von existierenden oder geplanten Neutrinoteleskopen deuten diese Resultate an, dass das mit mDOMs ausgerüstete "Gen2 high-energy array" das sensitivste Instrument für Neutrinopunktquellen mit positiver Deklination und nahe des Horizonts sein wird.
Es kann vermutet werden, dass das volle Potenzial des mDOMs als Basismodul eines Neutrinoteleskops noch nicht ausgeschöpft wurde. Der Weg für weitere Studien mit dem mDOM wurden während dieser Arbeit geebnet. Die vorhandene Software um Ereignisse mit dem mDOM zu simulieren wurde überprüft genauso wie der SplineMPE Rekonstruktionsalgorithmus. Zusätzlich wurde die Funktionalität für die Produktion von mDOM Photon-PDFs implementiert und ein Testprozedere, um die so erzeugten PDFs effizient testen zu können, entwickelt.
Einer der nächsten Schritte sollte die Inklusion eines realistischeren Eismodells in die Ereignisrekonstruktion sein. Ferner wird vermutet, dass weiterentwickelte Rekonstruktionsalgorithmen, welche realistischere Ereignishypothesen verwenden, noch bessere Ergebnisse erzielen aufgrund der zusätzlichen Information, welche durch die Benutzung von mDOMs verfügbar ist, als der Algorithmus, welcher in dieser Arbeit verwendet wurde. Ein anderer Aspekt mit potenziell großem Einfluss auf die Punktquellensensitivität vom "Gen2 high-energy array" ist die Ereignisselektion. Existierende Analysen haben ergeben, das optimierte Selektionsalgorithmen einen beträchtlichen Effekt auf die resultierende Sensitivität haben können.
Um entscheiden zu können welcher Sensortyp für das "Gen2 high-energy array" verwendet werden sollte müssen noch mehr Aspekte untersucht werden. Allerdings haben die Mehrheit der Ergebnisse aus dieser Arbeit das Verbesserungspotenzial für die Ereignisrekonstruktion aufgezeigt wenn ein segmentierter Sensor, wie das mDOM, verwendet wird.

APPENDIX

ADDITIONAL QUALITATIVE SPLINE TABLE SANITY CHECKS

This chapter contains additional figures similar to those presented in section 5.1.4.4 showing the behavior of the produced spline tables for different parameter configurations. For each sensor and source type three different source angles, 0°, 90° and 180° are displayed. The respective figures have been produced in the exact same way as those shown in chapter 5. Only irregularities similar to those mentioned in section 5.1.4.4, are found in the additional or any other plots made in this manner within the context of this work.

A.1 mDOM Infinite Track Spline Tables

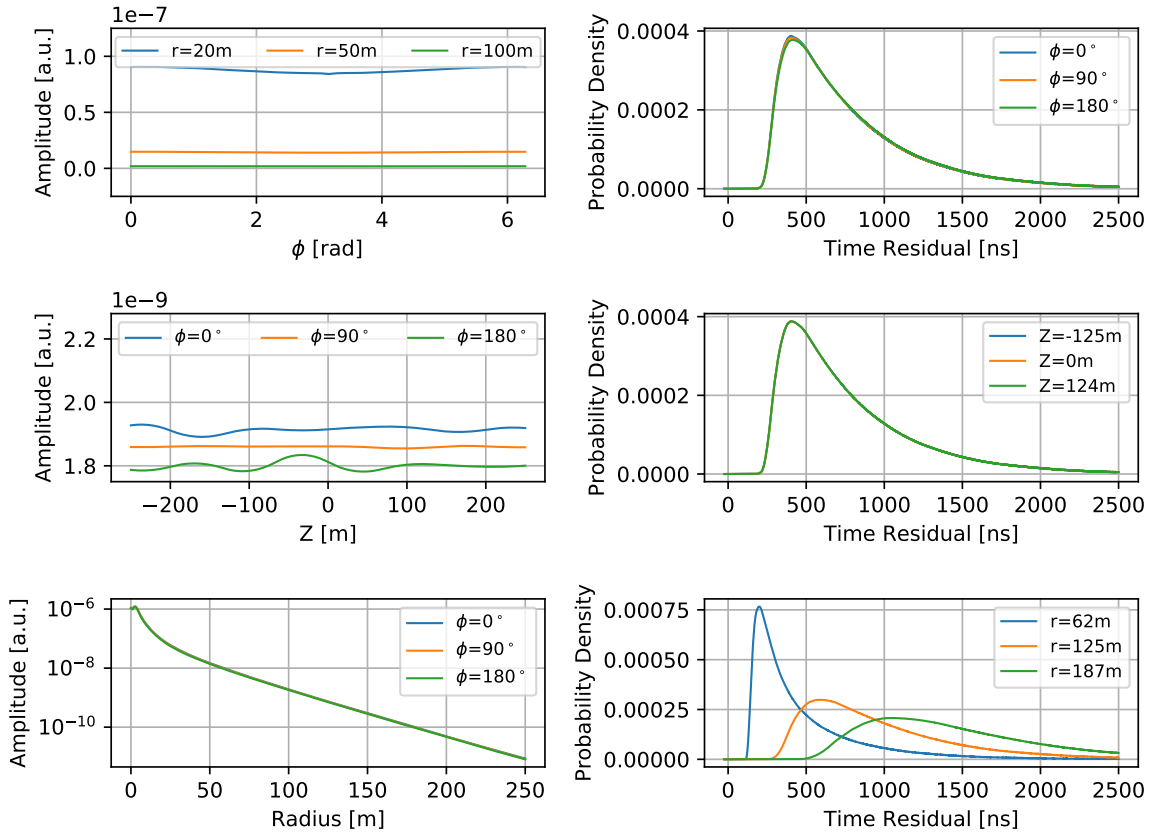

Figure A.1: Fitted mDOM infinite track photon table spline curves for $\theta_{\text{src}} = 0°$. *Top left:* Amplitude versus ϕ_{PMT} for three different radii with a fixed value of $Z_{\text{PMT}} = 1.6\,\text{m}$. *Center left:* Amplitude versus Z_{PMT} for three different PMT azimuth angles and fixed a radius of r=100 m. *Bottom left:* Amplitude versus radius for three different PMT azimuth angles with a fixed value of $Z_{\text{PMT}} = 1.6\,\text{m}$. *Top right:* Probability density versus time residual for three different PMT azimuth angles with a fixed radius r=100 m and a fixed value of $Z_{\text{PMT}} = 1.6\,\text{m}$. *Center right:* Probability density versus time residual for three different values of Z_{PMT} with a fixed radius r=100 m and a fixed value of $\phi_{\text{PMT}} = 0°$. *Bottom right:* Probability density versus time residual for three different PMT radii with a fixed value of $Z_{\text{PMT}} = 1.6\,\text{m}$ and a fixed value of $\phi_{\text{PMT}} = 0°$.

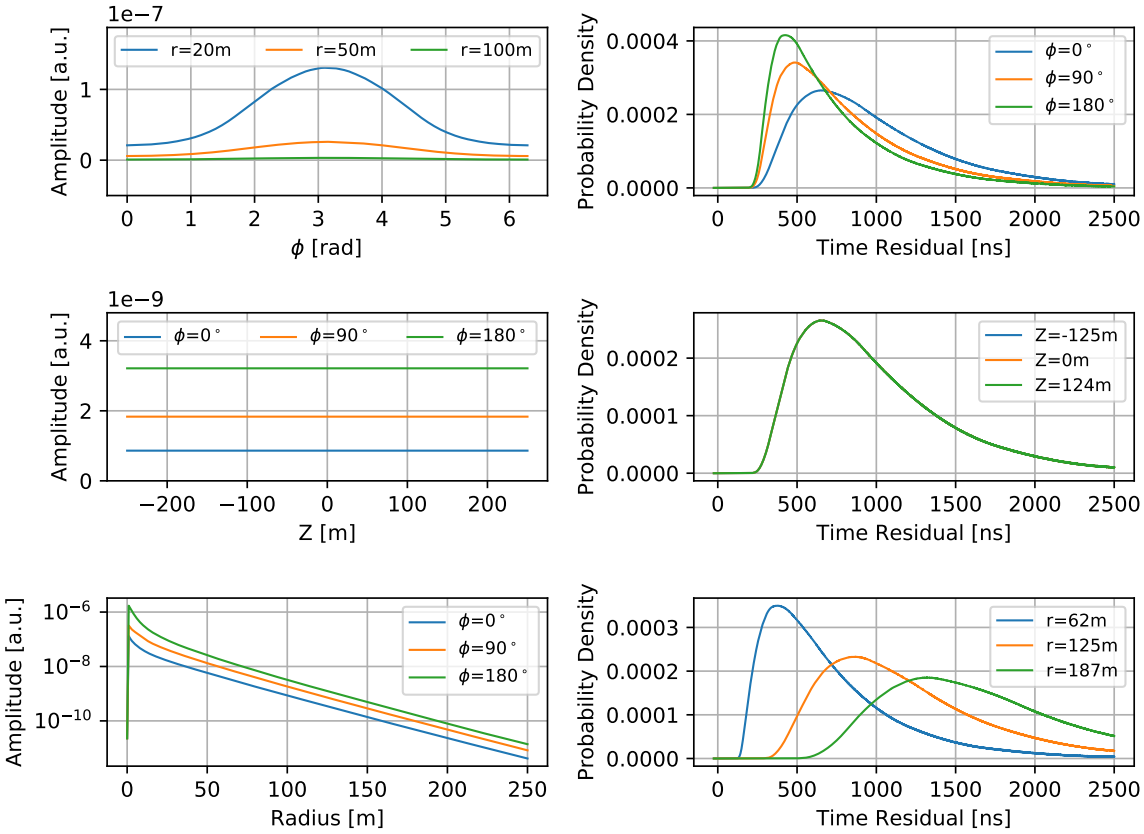

Figure A.2: Fitted mDOM infinite track photon table spline curves for $\theta_{\text{src}} = 90°$. *Top left:* Amplitude versus ϕ_{PMT} for three different radii with a fixed value of $Z_{\text{PMT}} = 1.6\,\text{m}$. *Center left:* Amplitude versus Z_{PMT} for three different PMT azimuth angles and fixed a radius of r=100 m. *Bottom left:* Amplitude versus radius for three different PMT azimuth angles with a fixed value of $Z_{\text{PMT}} = 1.6\,\text{m}$. *Top right:* Probability density versus time residual for three different PMT azimuth angles with a fixed radius r=100 m and a fixed value of $Z_{\text{PMT}} = 1.6\,\text{m}$. *Center right:* Probability density versus time residual for three different values of Z_{PMT} with a fixed radius r=100 m and a fixed value of $\phi_{\text{PMT}} = 0°$. *Bottom right:* Probability density versus time residual for three different PMT radii with a fixed value of $Z_{\text{PMT}} = 1.6\,\text{m}$ and a fixed value of $\phi_{\text{PMT}} = 0°$.

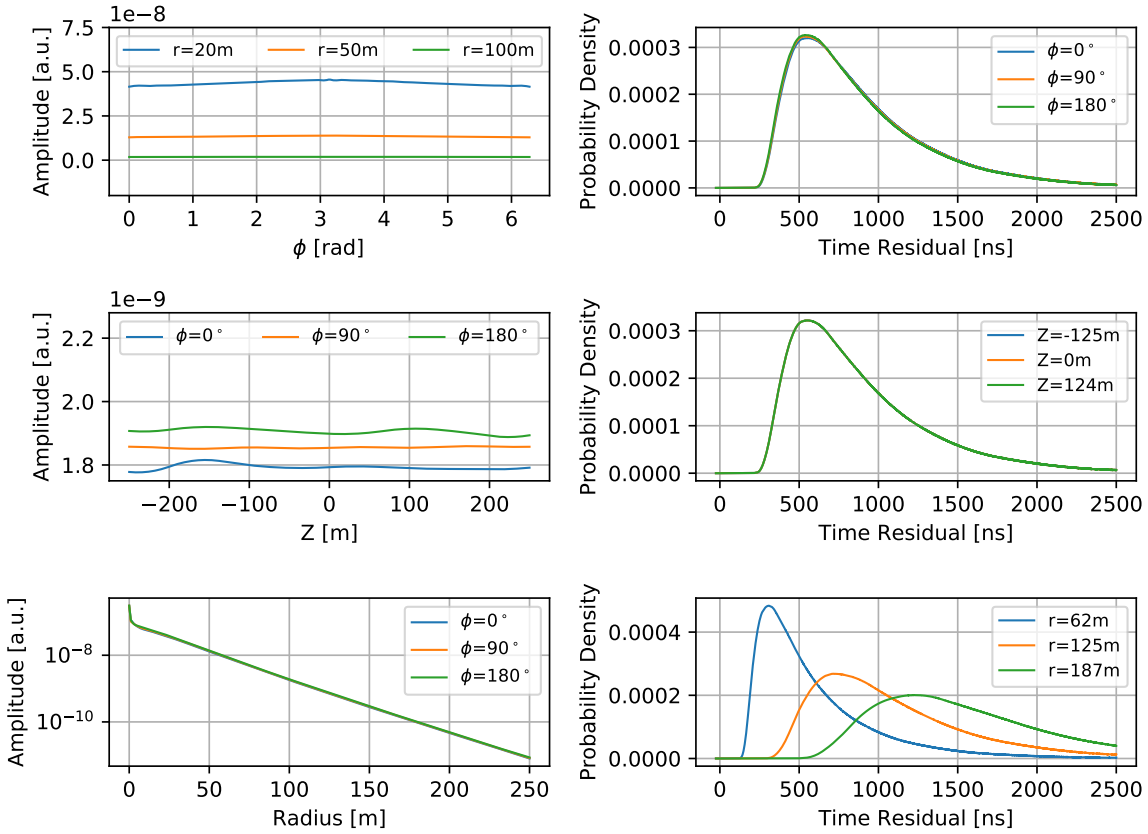

Figure A.3: Fitted mDOM infinite track photon table spline curves for $\theta_{\text{src}} = 180°$. *Top left:* Amplitude versus ϕ_{PMT} for three different radii with a fixed value of $Z_{\text{PMT}} = 1.6\,\text{m}$. *Center left:* Amplitude versus Z_{PMT} for three different PMT azimuth angles and fixed a radius of r=100 m. *Bottom left:* Amplitude versus radius for three different PMT azimuth angles with a fixed value of $Z_{\text{PMT}} = 1.6\,\text{m}$. *Top right:* Probability density versus time residual for three different PMT azimuth angles with a fixed radius r=100 m and a fixed value of $Z_{\text{PMT}} = 1.6\,\text{m}$. *Center right:* Probability density versus time residual for three different values of Z_{PMT} with a fixed radius r=100 m and a fixed value of $\phi_{\text{PMT}} = 0°$. *Bottom right:* Probability density versus time residual for three different PMT radii with a fixed value of $Z_{\text{PMT}} = 1.6\,\text{m}$ and a fixed value of $\phi_{\text{PMT}} = 0°$.

A.2 PDOM Infinite Track Spline Tables

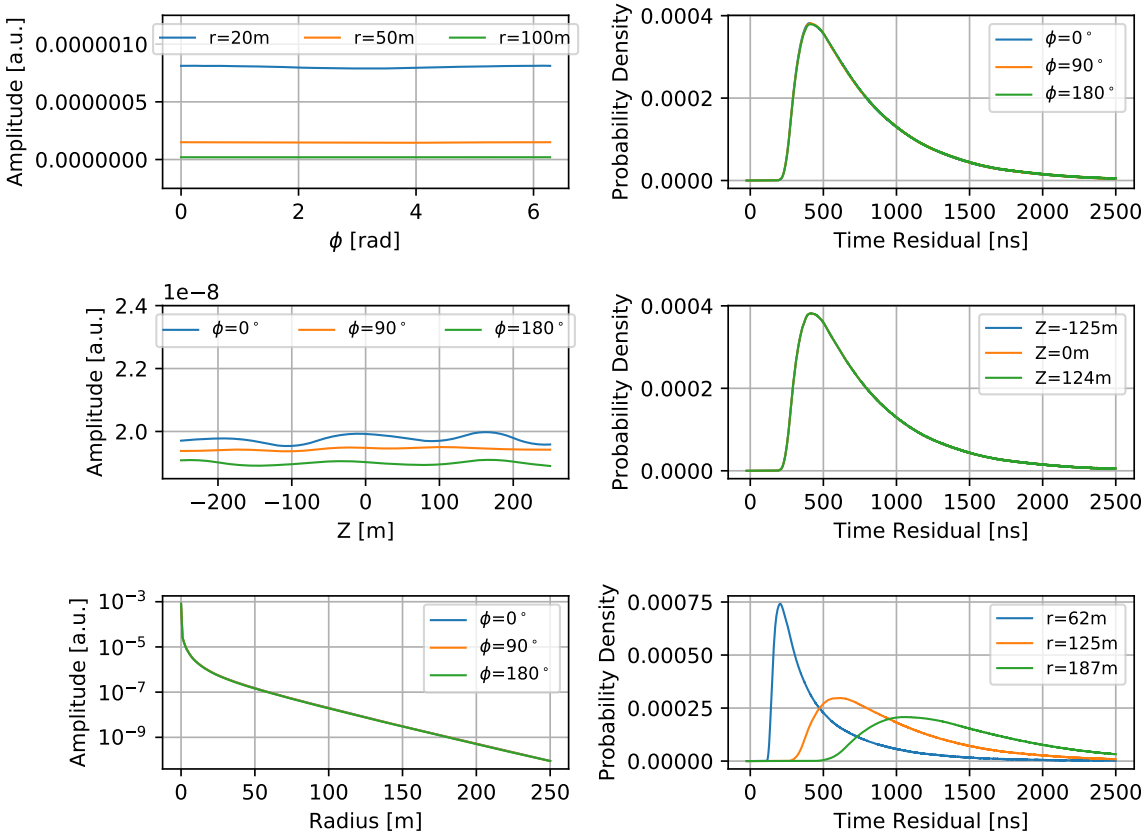

Figure A.4: Fitted PDOM infinite track photon table spline curves for $\theta_{\text{src}} = 0°$. *Top left:* Amplitude versus ϕ_{PMT} for three different radii with a fixed value of $Z_{\text{PMT}} = 1.6\,\text{m}$. *Center left:* Amplitude versus Z_{PMT} for three different PMT azimuth angles and fixed a radius of r=100 m. *Bottom left:* Amplitude versus radius for three different PMT azimuth angles with a fixed value of $Z_{\text{PMT}} = 1.6\,\text{m}$. *Top right:* Probability density versus time residual for three different PMT azimuth angles with a fixed radius r=100 m and a fixed value of $Z_{\text{PMT}} = 1.6\,\text{m}$. *Center right:* Probability density versus time residual for three different values of Z_{PMT} with a fixed radius r=100 m and a fixed value of $\phi_{\text{PMT}} = 0°$. *Bottom right:* Probability density versus time residual for three different PMT radii with a fixed value of $Z_{\text{PMT}} = 1.6\,\text{m}$ and a fixed value of $\phi_{\text{PMT}} = 0°$.

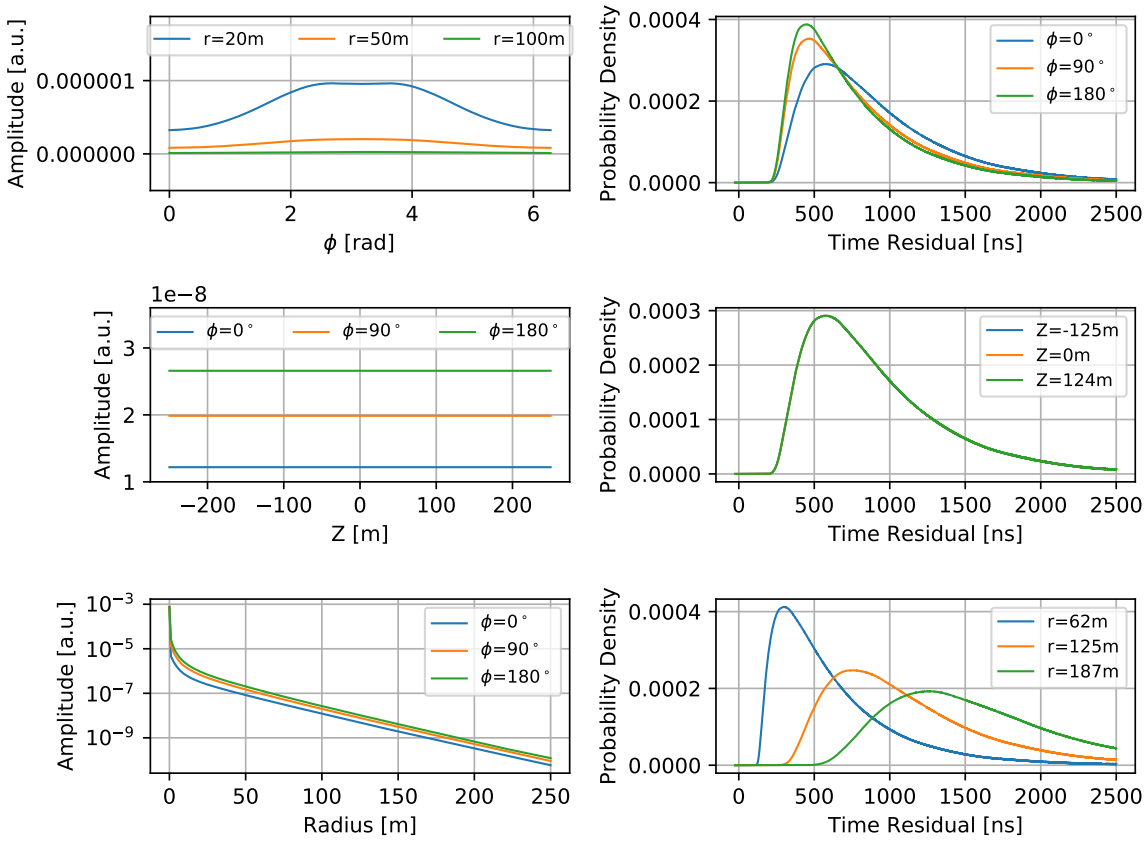

Figure A.5: Fitted PDOM infinite track photon table spline curves for $\theta_{\text{src}} = 90°$. *Top left:* Amplitude versus ϕ_{PMT} for three different radii with a fixed value of $Z_{\text{PMT}} = 1.6\,\text{m}$. *Center left:* Amplitude versus Z_{PMT} for three different PMT azimuth angles and fixed a radius of r=100 m. *Bottom left:* Amplitude versus radius for three different PMT azimuth angles with a fixed value of $Z_{\text{PMT}} = 1.6\,\text{m}$. *Top right:* Probability density versus time residual for three different PMT azimuth angles with a fixed radius r=100 m and a fixed value of $Z_{\text{PMT}} = 1.6\,\text{m}$. *Center right:* Probability density versus time residual for three different values of Z_{PMT} with a fixed radius r=100 m and a fixed value of $\phi_{\text{PMT}} = 0°$. *Bottom right:* Probability density versus time residual for three different PMT radii with a fixed value of $Z_{\text{PMT}} = 1.6\,\text{m}$ and a fixed value of $\phi_{\text{PMT}} = 0°$.

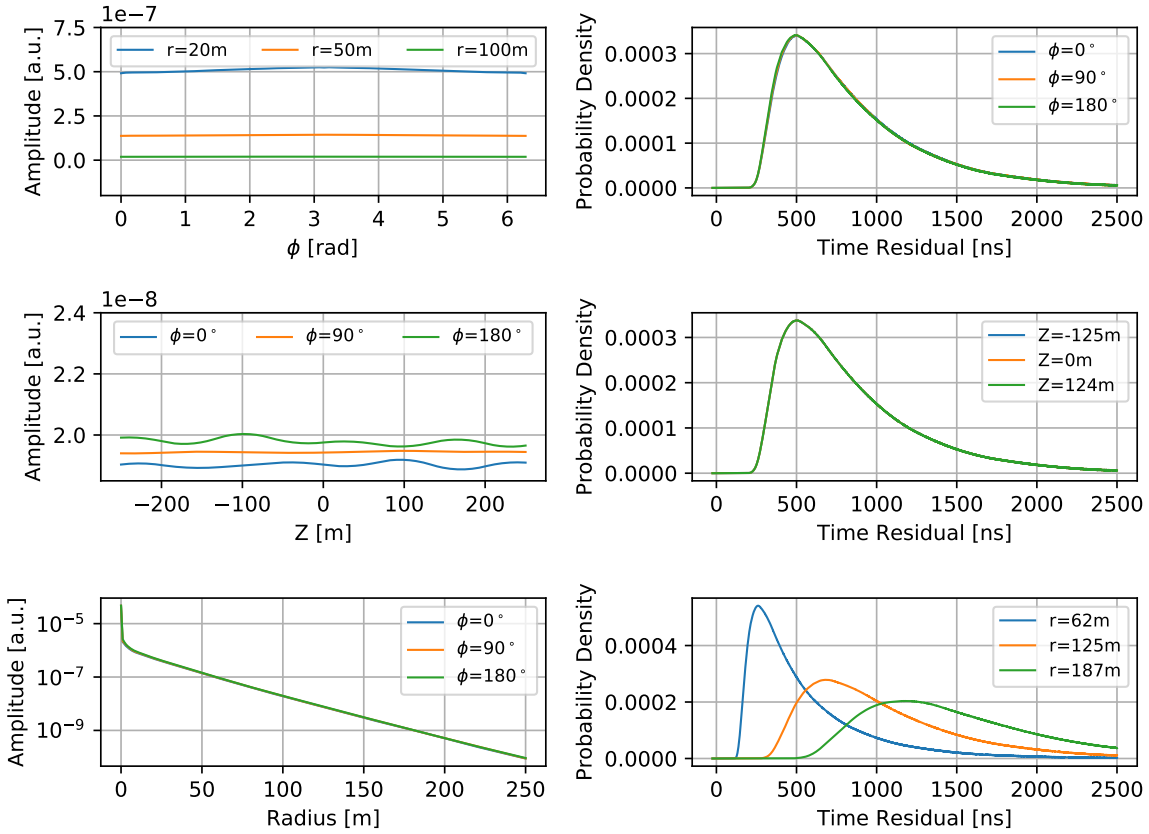

Figure A.6: Fitted PDOM infinite track photon table spline curves for $\theta_{\text{src}} = 180°$. *Top left:* Amplitude versus ϕ_{PMT} for three different radii with a fixed value of $\text{Z}_{\text{PMT}} = 1.6\,\text{m}$. *Center left:* Amplitude versus Z_{PMT} for three different PMT azimuth angles and fixed a radius of r=100 m. *Bottom left:* Amplitude versus radius for three different PMT azimuth angles with a fixed value of $\text{Z}_{\text{PMT}} = 1.6\,\text{m}$. *Top right:* Probability density versus time residual for three different PMT azimuth angles with a fixed radius r=100 m and a fixed value of $\text{Z}_{\text{PMT}} = 1.6\,\text{m}$. *Center right:* Probability density versus time residual for three different values of Z_{PMT} with a fixed radius r=100 m and a fixed value of $\phi_{\text{PMT}} = 0°$. *Bottom right:* Probability density versus time residual for three different PMT radii with a fixed value of $\text{Z}_{\text{PMT}} = 1.6\,\text{m}$ and a fixed value of $\phi_{\text{PMT}} = 0°$.

A.3 mDOM Cascade Spline Tables

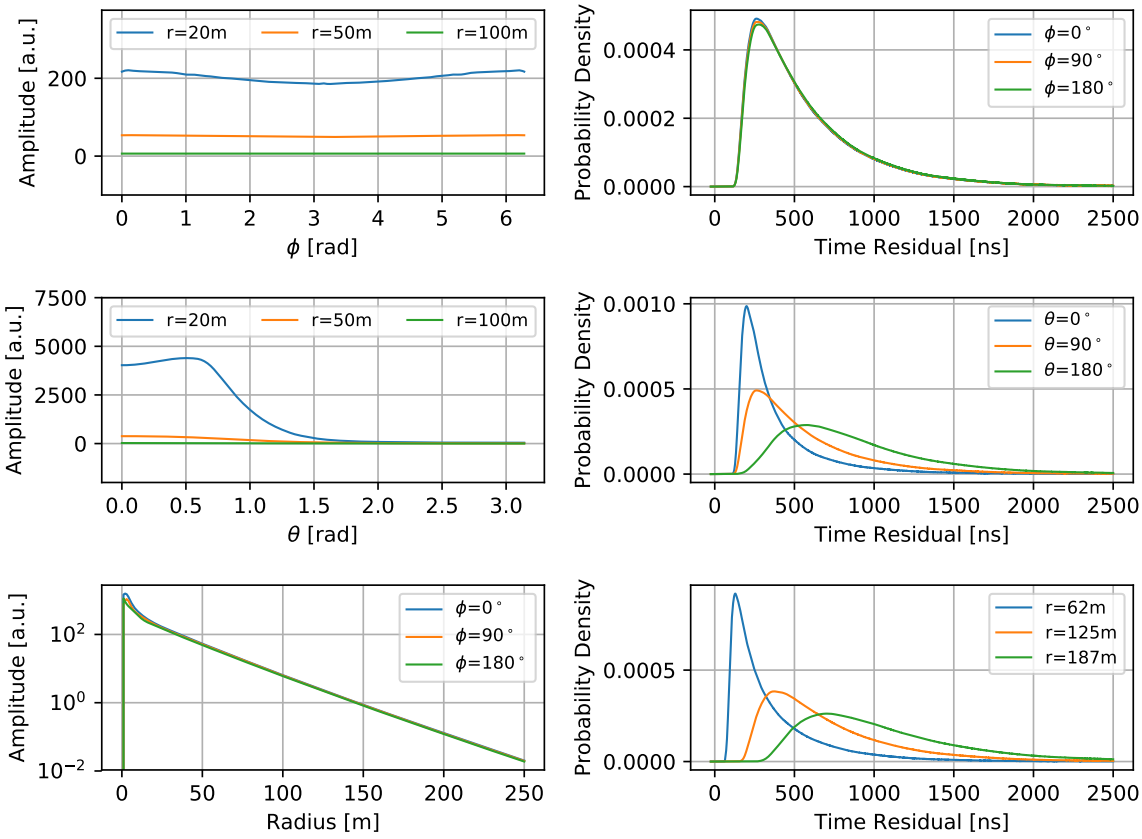

Figure A.7: Fitted mDOM cascade photon table spline curves for $\theta_{\text{src}} = 0°$. *Top left:* Amplitude versus ϕ_{PMT} for three different radii with a fixed value of $\theta_{\text{PMT}} = 45°$. *Center left:* Amplitude versus θ_{PMT} for three different radii with a fixed value of $\phi_{\text{PMT}} = 0°$. *Bottom left:* Amplitude versus radius for three different PMT azimuth angles with a fixed value of $\theta_{\text{PMT}} = 45°$. *Top right:* Probability density versus time residual for three different PMT azimuth angles with a fixed radius r=100 m and a fixed value of $\theta_{\text{PMT}} = 45°$. *Center right:* Probability density versus time residual for three different PMT zenith angles with fixed a radius r=100 m and a fixed value of $\phi_{\text{PMT}} = 0°$. *Bottom right:* Probability density versus time residual for three different PMT radii with a fixed value of $\theta_{\text{PMT}} = 90°$ and fixed value of $\phi_{\text{PMT}} = 0°$.

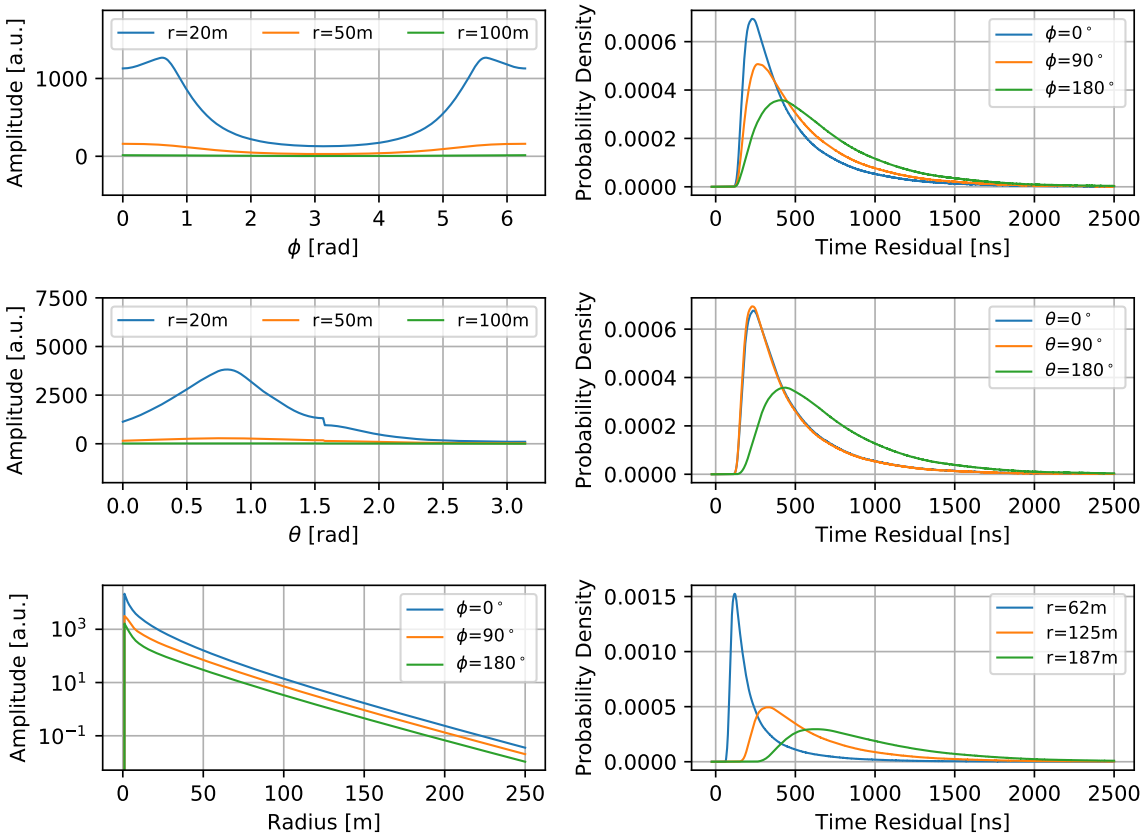

Figure A.8: Fitted mDOM cascade photon table spline curves for $\theta_{\text{src}} = 90°$. *Top left:* Amplitude versus ϕ_{PMT} for three different radii with a fixed value of $\theta_{\text{PMT}} = 45°$. *Center left:* Amplitude versus θ_{PMT} for three different radii with a fixed value of $\phi_{\text{PMT}} = 0°$. *Bottom left:* Amplitude versus radius for three different PMT azimuth angles with a fixed value of $\theta_{\text{PMT}} = 45°$. *Top right:* Probability density versus time residual for three different PMT azimuth angles with a fixed radius r=100 m and a fixed value of $\theta_{\text{PMT}} = 45°$. *Center right:* Probability density versus time residual for three different PMT zenith angles with fixed a radius r=100 m and a fixed value of $\phi_{\text{PMT}} = 0°$. *Bottom right:* Probability density versus time residual for three different PMT radii with a fixed value of $\theta_{\text{PMT}} = 90°$ and fixed value of $\phi_{\text{PMT}} = 0°$.

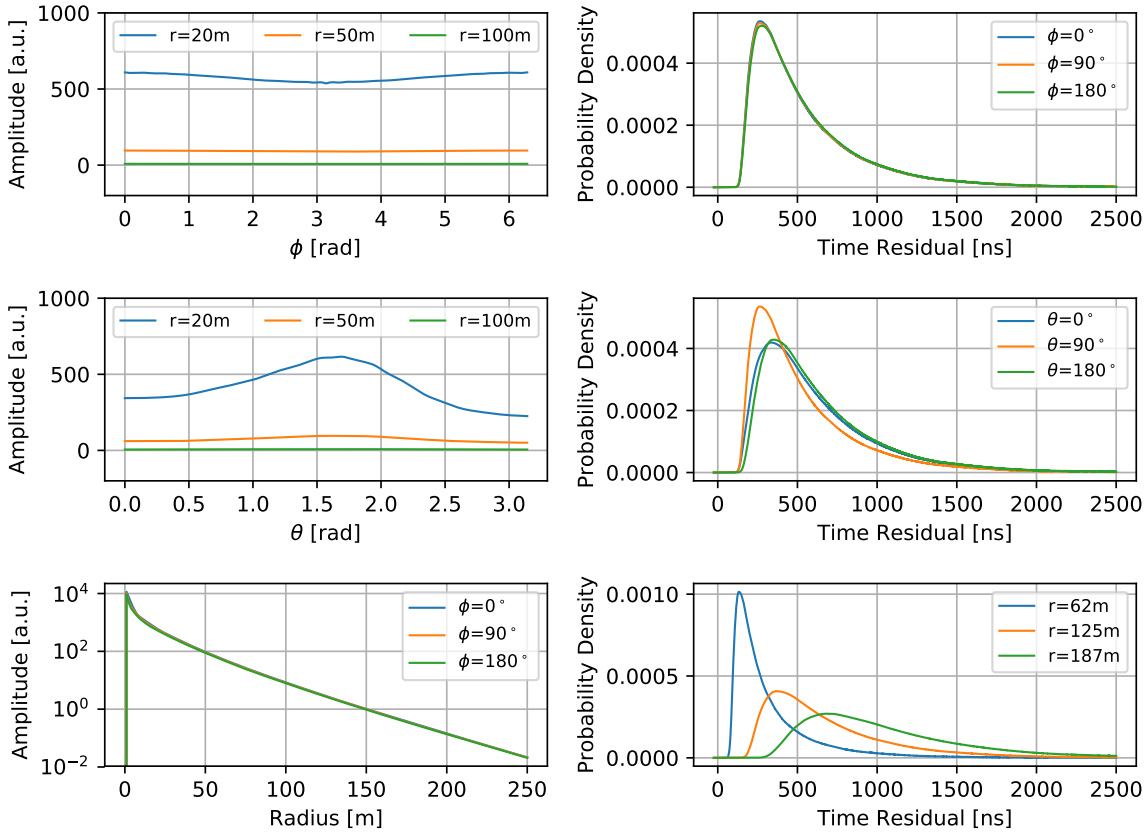

Figure A.9: Fitted mDOM cascade photon table spline curves for $\theta_{\text{src}} = 180°$. *Top left:* Amplitude versus ϕ_{PMT} for three different radii with a fixed value of $\theta_{\text{PMT}} = 45°$. *Center left:* Amplitude versus θ_{PMT} for three different radii with a fixed value of $\phi_{\text{PMT}} = 0°$. *Bottom left:* Amplitude versus radius for three different PMT azimuth angles with a fixed value of $\theta_{\text{PMT}} = 45°$. *Top right:* Probability density versus time residual for three different PMT azimuth angles with a fixed radius r=100 m and a fixed value of $\theta_{\text{PMT}} = 45°$. *Center right:* Probability density versus time residual for three different PMT zenith angles with fixed a radius r=100 m and a fixed value of $\phi_{\text{PMT}} = 0°$. *Bottom right:* Probability density versus time residual for three different PMT radii with a fixed value of $\theta_{\text{PMT}} = 90°$ and fixed value of $\phi_{\text{PMT}} = 0°$.

A.4 PDOM Cascade Spline Tables

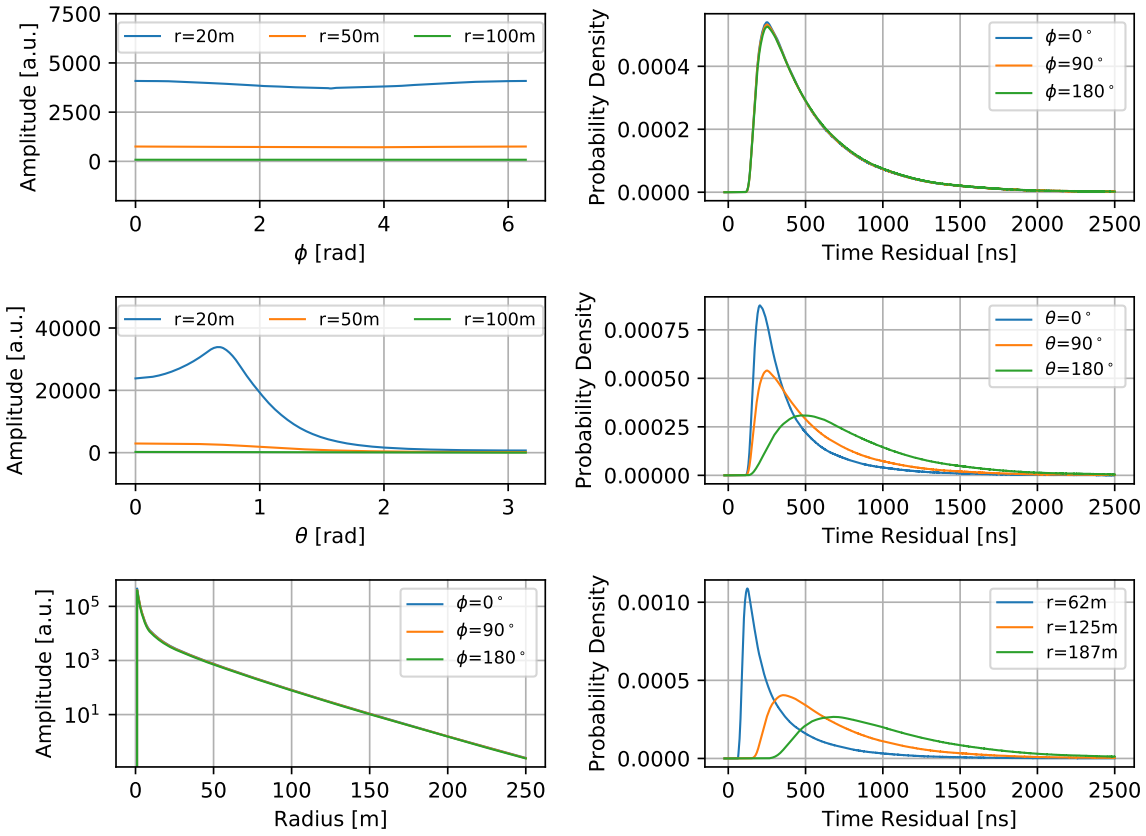

Figure A.10: Fitted PDOM cascade photon table spline curves for $\theta_{\text{src}} = 0°$. *Top left:* Amplitude versus ϕ_{PMT} for three different radii with a fixed value of $\theta_{\text{PMT}} = 45°$. *Center left:* Amplitude versus θ_{PMT} for three different radii with a fixed value of $\phi_{\text{PMT}} = 0°$. *Bottom left:* Amplitude versus radius for three different PMT azimuth angles with a fixed value of $\theta_{\text{PMT}} = 45°$. *Top right:* Probability density versus time residual for three different PMT azimuth angles with a fixed radius r=100 m and a fixed value of $\theta_{\text{PMT}} = 45°$. *Center right:* Probability density versus time residual for three different PMT zenith angles with fixed a radius r=100 m and a fixed value of $\phi_{\text{PMT}} = 0°$. *Bottom right:* Probability density versus time residual for three different PMT radii with a fixed value of $\theta_{\text{PMT}} = 90°$ and fixed value of $\phi_{\text{PMT}} = 0°$.

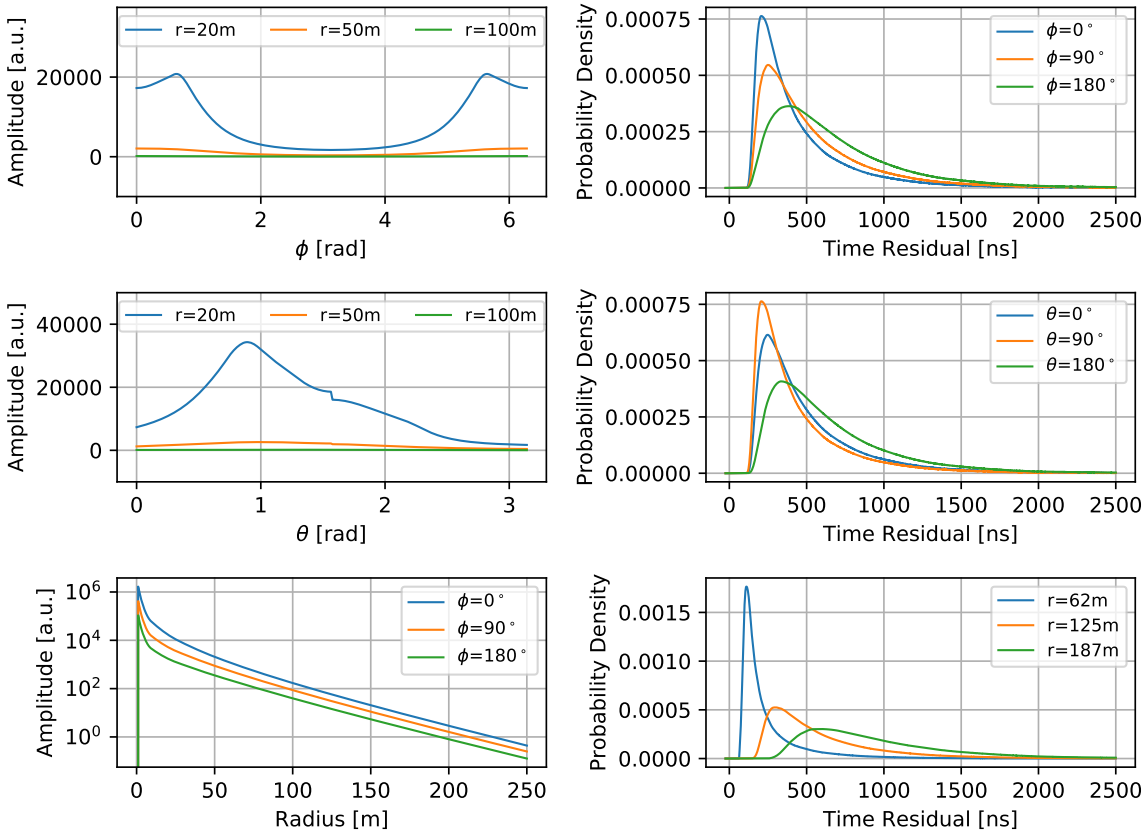

Figure A.11: Fitted PDOM cascade photon table spline curves for $\theta_{\text{src}} = 90°$. *Top left:* Amplitude versus ϕ_{PMT} for three different radii with a fixed value of $\theta_{\text{PMT}} = 45°$. *Center left:* Amplitude versus θ_{PMT} for three different radii with a fixed value of $\phi_{\text{PMT}} = 0°$. *Bottom left:* Amplitude versus radius for three different PMT azimuth angles with a fixed value of $\theta_{\text{PMT}} = 45°$. *Top right:* Probability density versus time residual for three different PMT azimuth angles with a fixed radius r=100 m and a fixed value of $\theta_{\text{PMT}} = 45°$. *Center right:* Probability density versus time residual for three different PMT zenith angles with fixed a radius r=100 m and a fixed value of $\phi_{\text{PMT}} = 0°$. *Bottom right:* Probability density versus time residual for three different PMT radii with a fixed value of $\theta_{\text{PMT}} = 90°$ and fixed value of $\phi_{\text{PMT}} = 0°$.

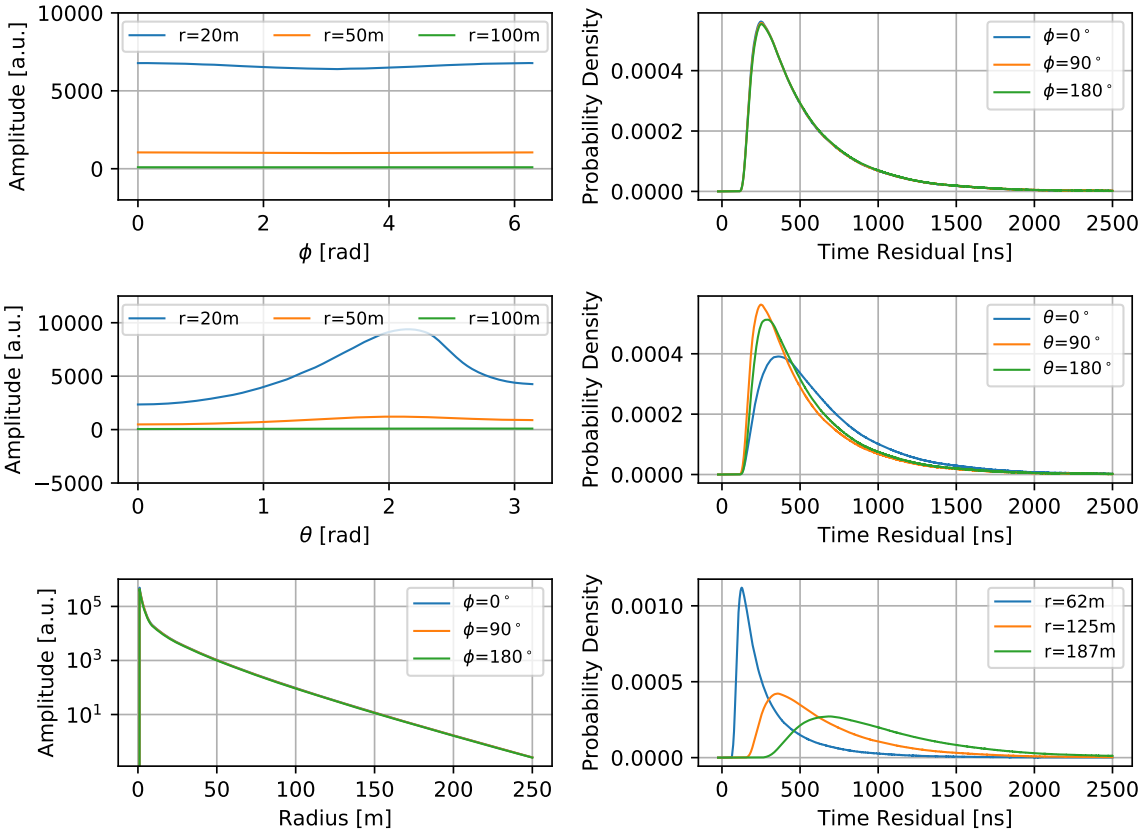

Figure A.12: Fitted PDOM cascade photon table spline curves for $\theta_{\text{src}} = 180°$. *Top left:* Amplitude versus ϕ_{PMT} for three different radii with a fixed value of $\theta_{\text{PMT}} = 45°$. *Center left:* Amplitude versus θ_{PMT} for three different radii with a fixed value of $\phi_{\text{PMT}} = 0°$. *Bottom left:* Amplitude versus radius for three different PMT azimuth angles with a fixed value of $\theta_{\text{PMT}} = 45°$. *Top right:* Probability density versus time residual for three different PMT azimuth angles with a fixed radius r=100 m and a fixed value of $\theta_{\text{PMT}} = 45°$. *Center right:* Probability density versus time residual for three different PMT zenith angles with fixed a radius r=100 m and a fixed value of $\phi_{\text{PMT}} = 0°$. *Bottom right:* Probability density versus time residual for three different PMT radii with a fixed value of $\theta_{\text{PMT}} = 90°$ and fixed value of $\phi_{\text{PMT}} = 0°$.

APPENDIX B

PROPERTIES & SANITY CHECKS OF DATASET 20016

This chapter presents the properties and the results of the sanity checks of dataset 20016. The dataset was simulated with the same tools and the same settings as those used for dataset 20198, which are described in detail in chapter 4. Similar to dataset 20198, four versions of this dataset have been produced, one with all Gen2 strings being equipped with nominal mDOMs (2.24), one with with nominal PDOMs (1.0), one with downscaled mDOMs (1.0) and one with upscaled PDOMs (2.24). The spectral index used for the simulation was -1.4. The only difference to dataset 20198, is that dataset 20016 only contains muons with a zenith angle in between $85°$ and $95°$ (see figures B.1 and B.2). The same sanity checks as described in section 4.3 have been conduced for dataset 20016, which returned comparable results, as can be seen in the figures B.3 through B.10. Thus, similar to the simulation of dataset 20198, no indication of any significant bias between the mDOM and PDOM after equalization of the photocathode area has been found.

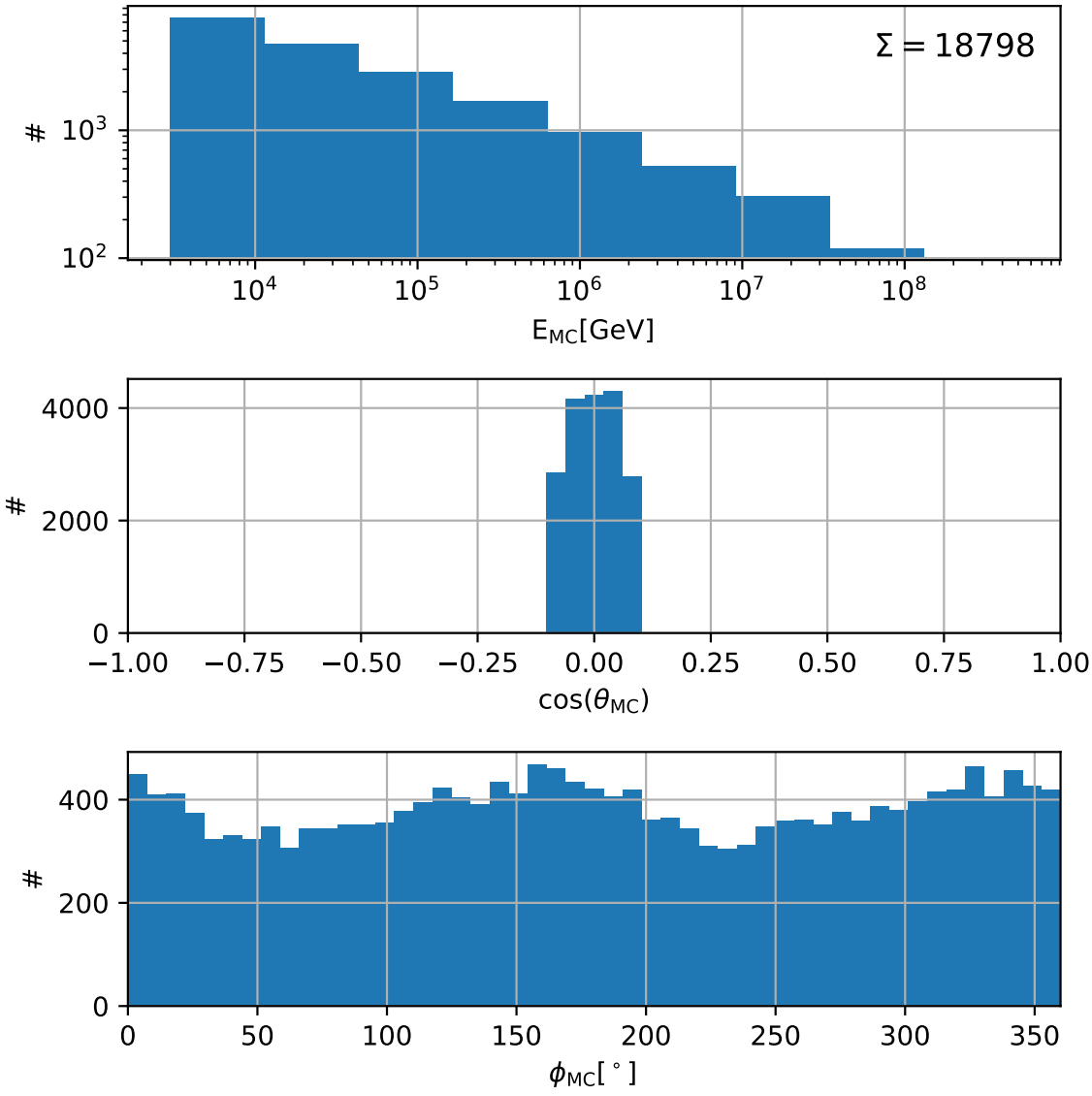

Figure B.1: Properties of the dataset 20016 for mDOM and PDOM normalized on the PDOM (mDOM downscaled by 1/2.24). The number in the upper right corner is the total amount of triggered events (SMT8 adapted for Gen2). *Top*: Total amount of triggered events versus true initial muon energy. *Center*: Total amount of triggered events versus cosine of the true zenith angle (θ_{MC}) of the simulated muon. *Bottom*: Total amount of triggered events versus the true azimuth angle of the simulated muon.

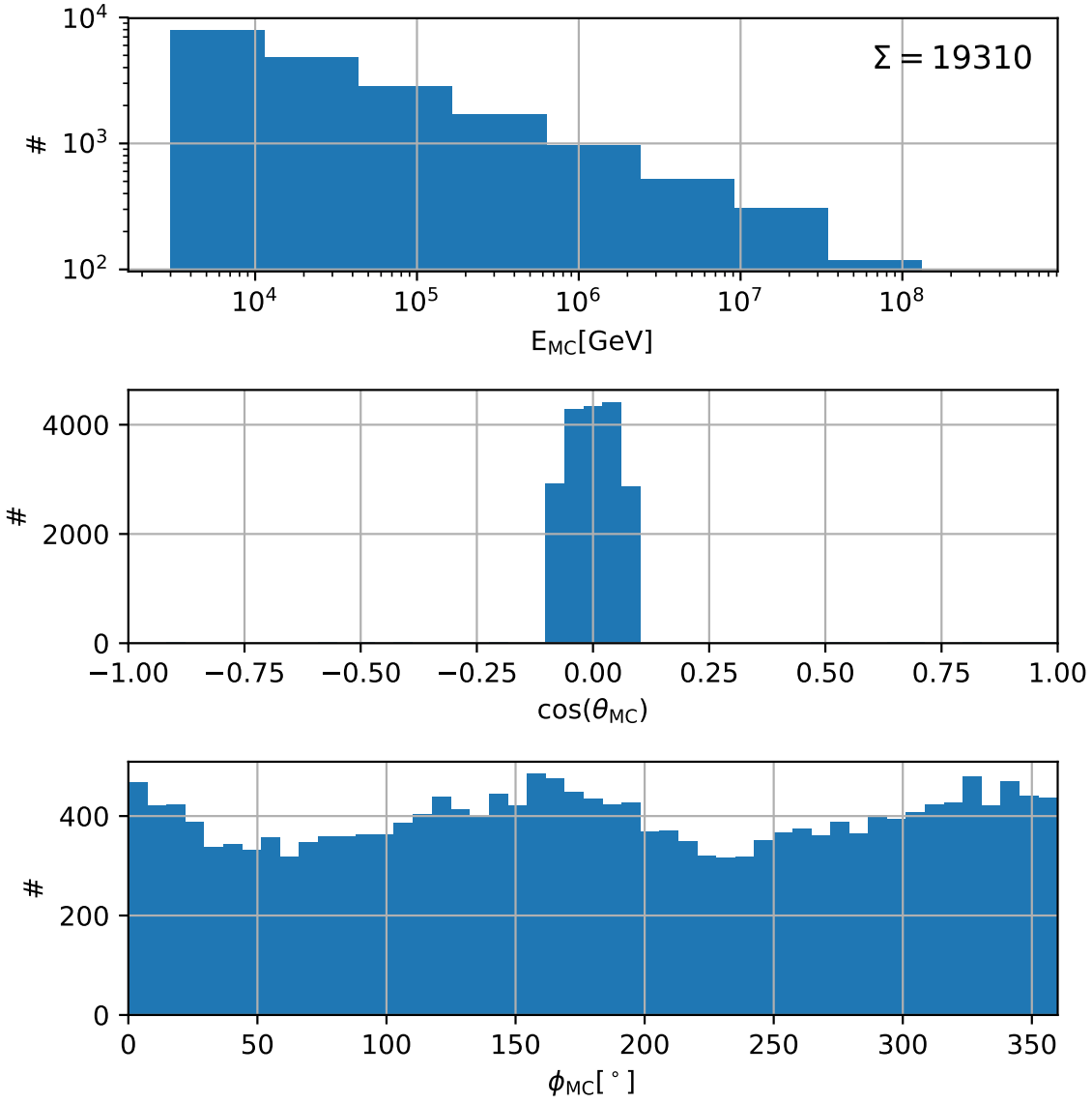

Figure B.2: Properties of the dataset 20016 for mDOM and PDOM normalized on the mDOM (PDOM upscaled by 2.24). The number in the upper right corner is the total amount of triggered events (SMT8 adapted for Gen2). *Top*: Total amount of triggered events versus true initial muon energy. *Center*: Total amount of triggered events versus cosine of the true zenith angle (θ_{MC}) of the simulated muon. *Bottom*: Total amount of triggered events versus the true azimuth angle of the simulated muon.

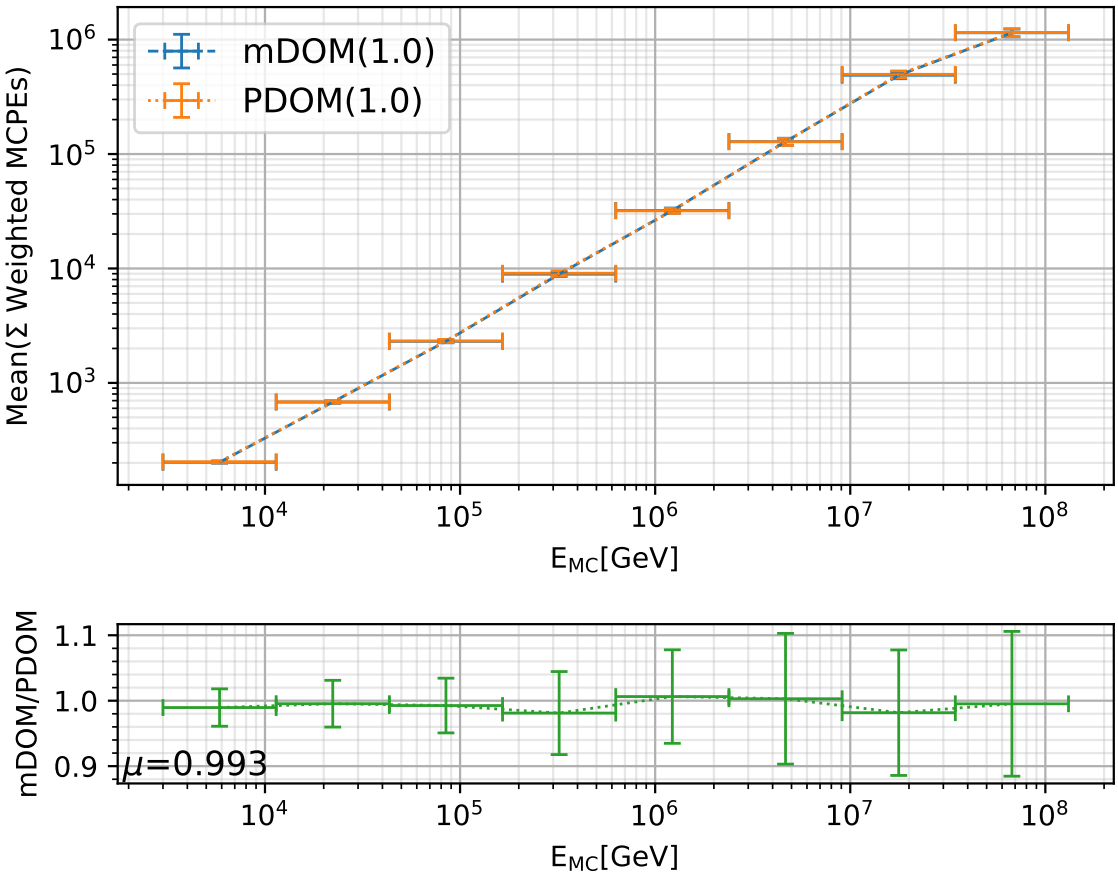

Figure B.3: Comparison of the mean amount of detected photons (MCPEs) per energy bin for two versions (nominal PDOM and downscaled mDOM) of dataset 20016. The horizontal bars indicate the width of the energy bin, while the vertical error bars mark the standard error of the mean value. *Top*: Energy versus mean amount of MCPEs per bin. *Bottom*: Ratio of the mean values within the respective energy bin. The parameter μ denotes the mean of all ratios.

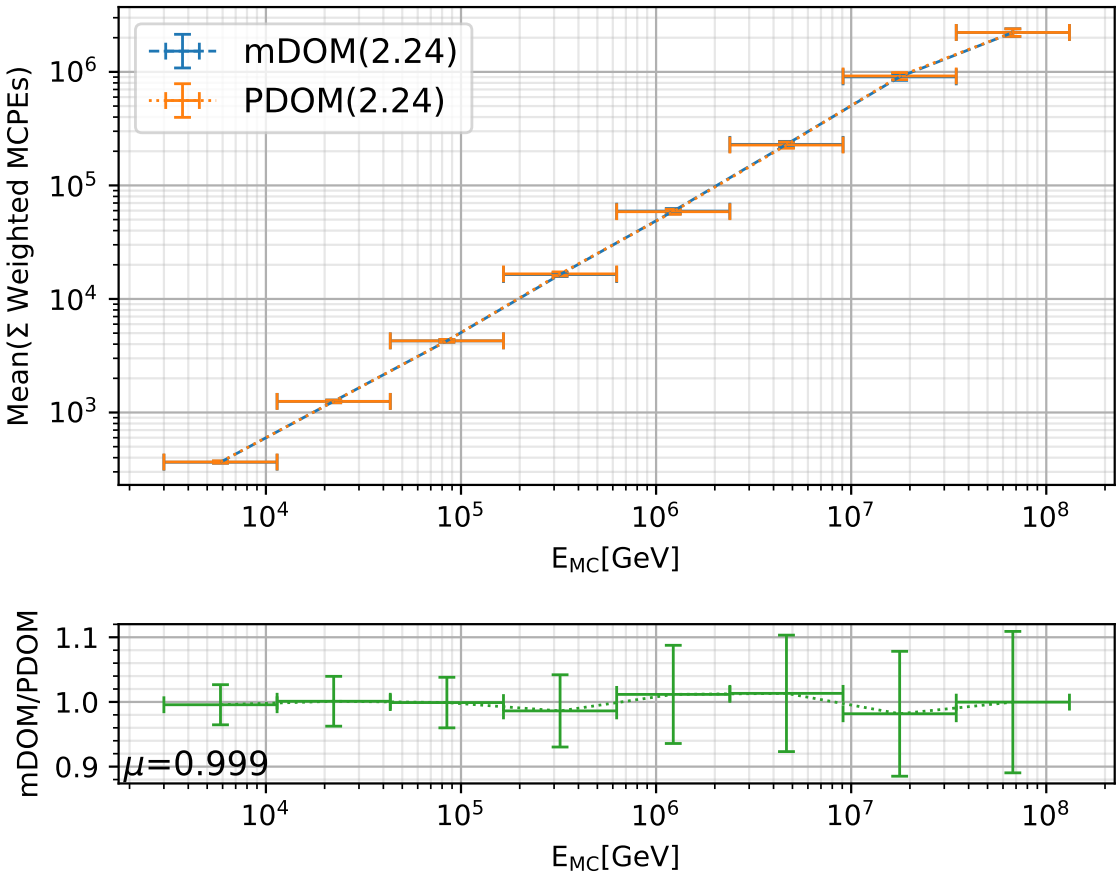

Figure B.4: Comparison of the mean amount of detected photons (MCPEs) per energy bin for two versions (upscaled PDOM and nominal mDOM) of dataset 20016. The horizontal bars indicate the width of the energy bin, while the vertical error bars mark the standard error of the mean value. *Top*: Energy versus mean amount of MCPEs per bin. *Bottom*: Ratio of the mean values within the respective energy bin. The parameter μ denotes the mean of all ratios.

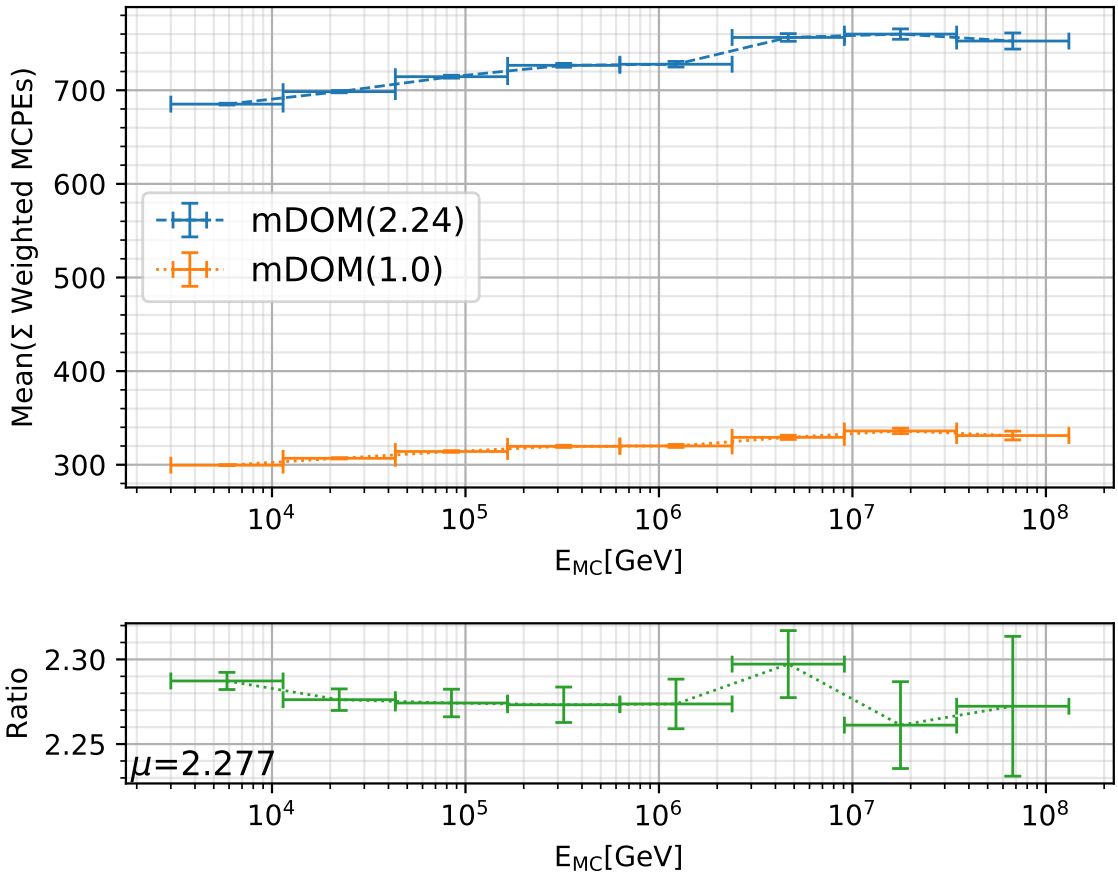

Figure B.5: Comparison of the mean amount of MCPEs on Gen2 DOMs due to noise per energy bin for two versions (downscaled mDOM and the nominal mDOM) of dataset 20016. The horizontal bars indicate the width of the energy bin, while the vertical error bars mark the standard error of the mean value. *Top*: Energy versus mean amount of MCPEs per bin. *Bottom*: Ratio of the mean values within the respective energy bin. The parameter μ denotes the mean of all ratios.

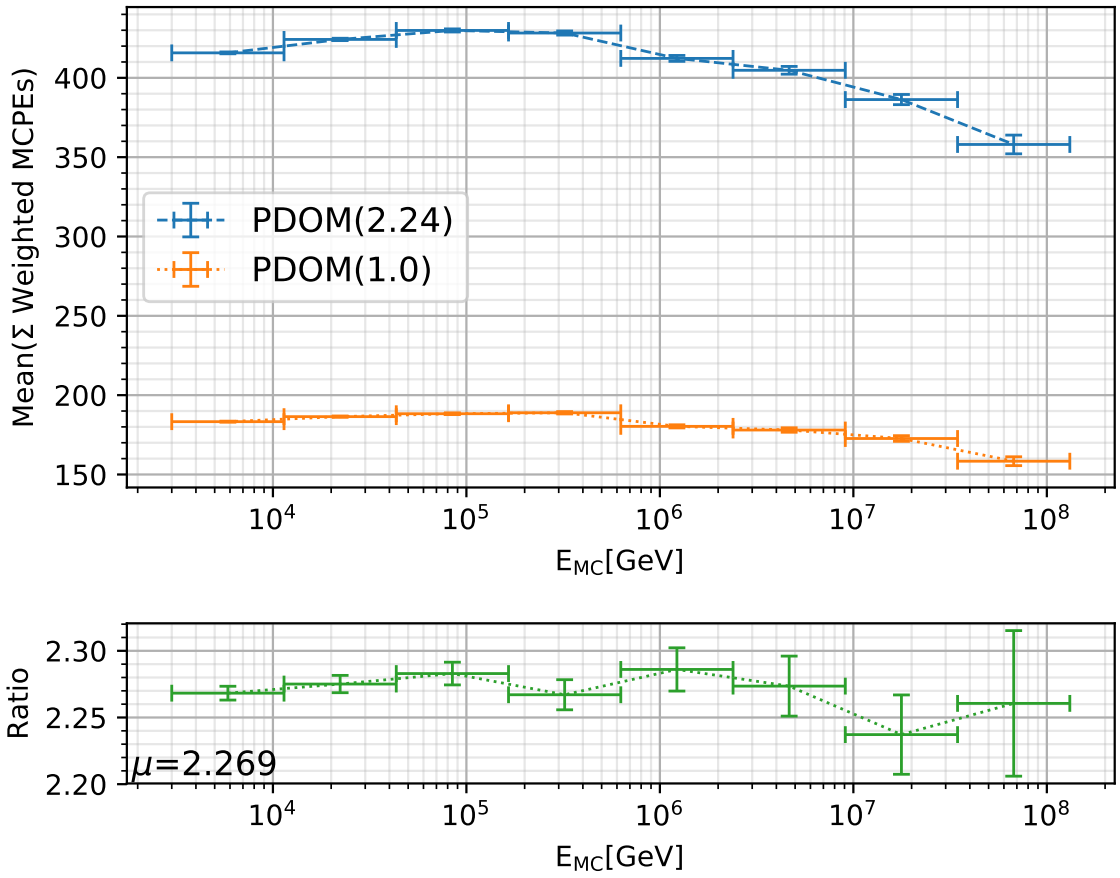

Figure B.6: Comparison of the mean amount of MCPEs on Gen2 DOMs due to noise per energy bin for two versions (nominal PDOM and upscaled PDOM) of dataset 20016. The horizontal bars indicate the width of the energy bin, while the vertical error bars mark the standard error of the mean value. *Top*: Energy versus mean amount of MCPEs per bin. *Bottom*: Ratio of the mean values within the respective energy bin. The parameter μ denotes the mean of all ratios.

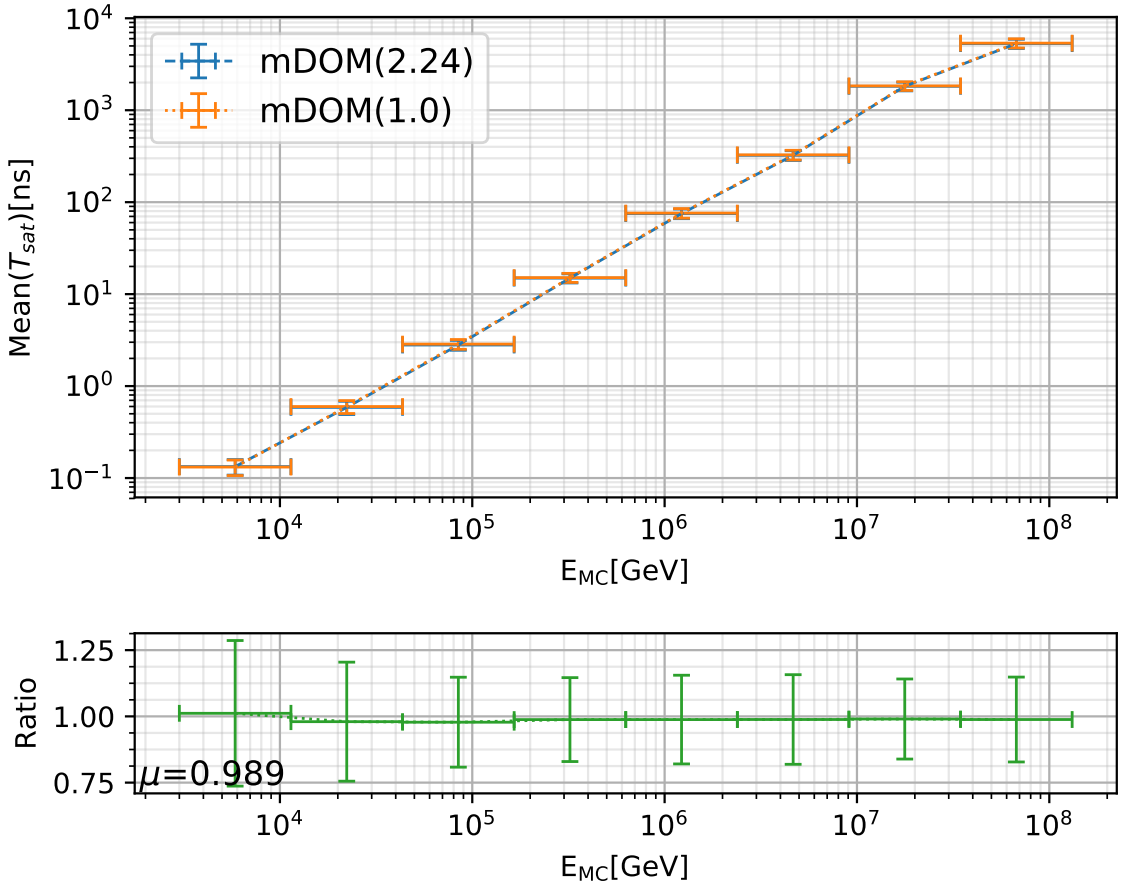

Figure B.7: Sanity check for the correct up- and downscaling of the saturation threshold with dataset 20016. The horizontal bars indicate the width of the energy bin, while the vertical error bars mark the standard error of the mean value. *Top*: E_{MC} versus the mean total saturation time per event for the downscaled mDOM and the nominal mDOM. *Bottom*: Ratio of the mean of the nominal mDOM (2.24) over the mean obtained with the downscaled mDOM (1.0). The parameter μ denotes the mean of all ratios.

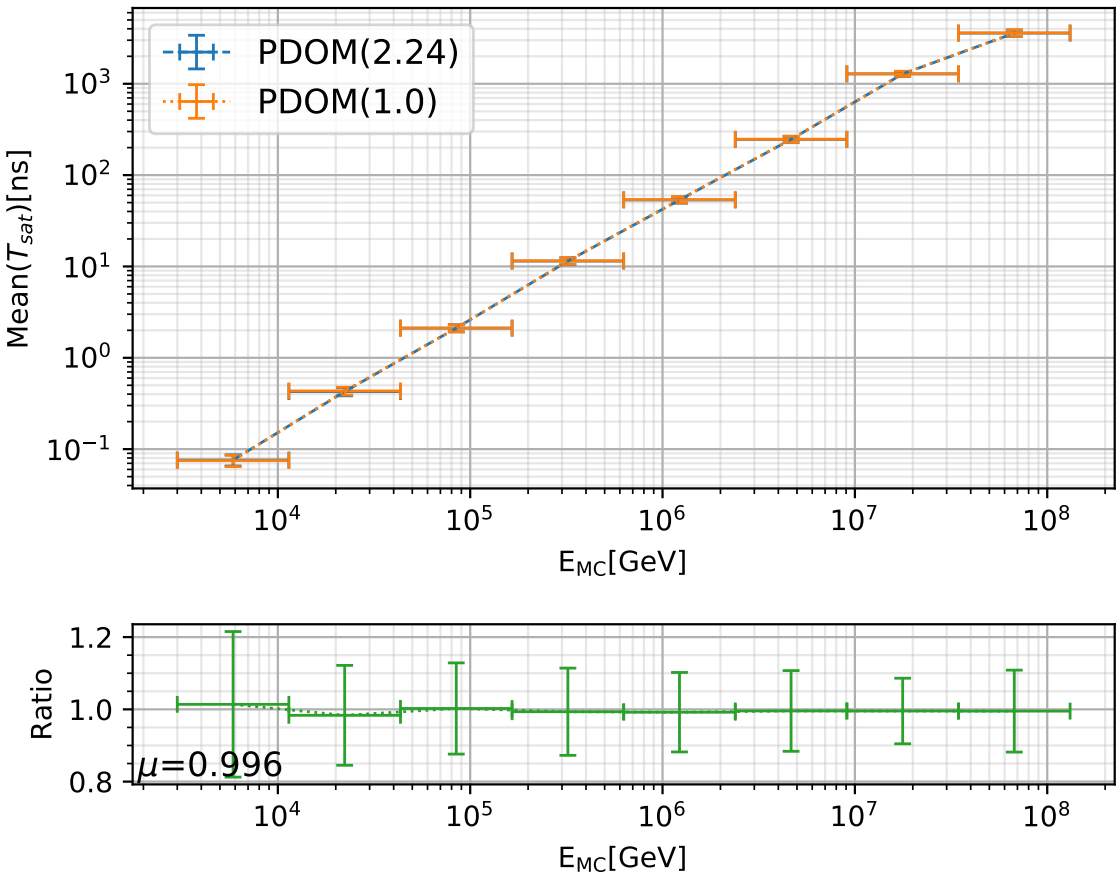

Figure B.8: Sanity check for the correct up- and downscaling of the saturation threshold with dataset 20016. The horizontal bars indicate the width of the energy bin, while the vertical error bars mark the standard error of the mean value. *Top*: E_{MC} versus the mean total saturation time per event for the upscaled PDOM and the nominal PDOM. *Bottom*: Ratio of the mean of the upscaled PDOM (2.24) over the mean obtained with the nominal PDOM (1.0). The parameter μ denotes the mean of all ratios.

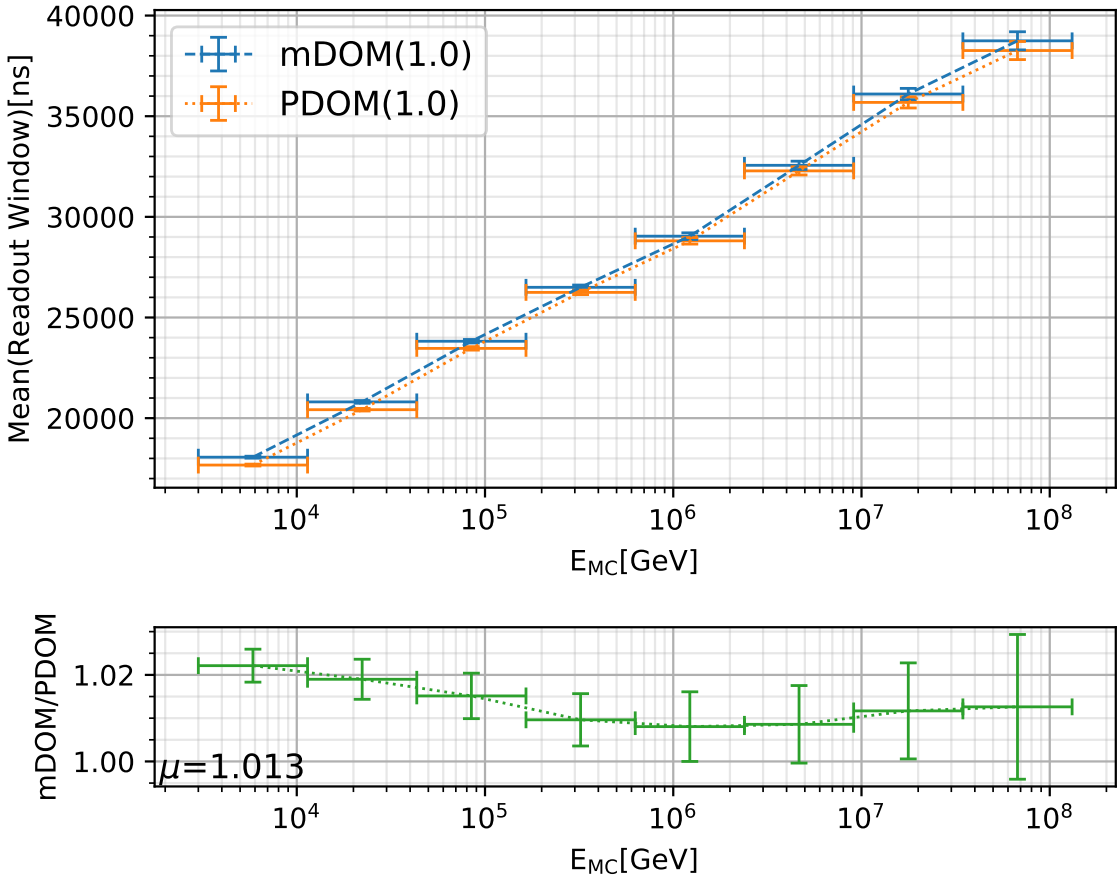

Figure B.9: Sanity check of the readout window for dataset 20016. The horizontal bars indicate the width of the energy bin, while the vertical error bars mark the standard error of the mean value. *Top*: E_{MC} versus the mean readout window length per event. Compared are simulations obtained with the nominal PDOM and the downscaled mDOM. *Bottom*: Ratio of the respective values from the top plot. The parameter μ denotes the mean of all ratios.

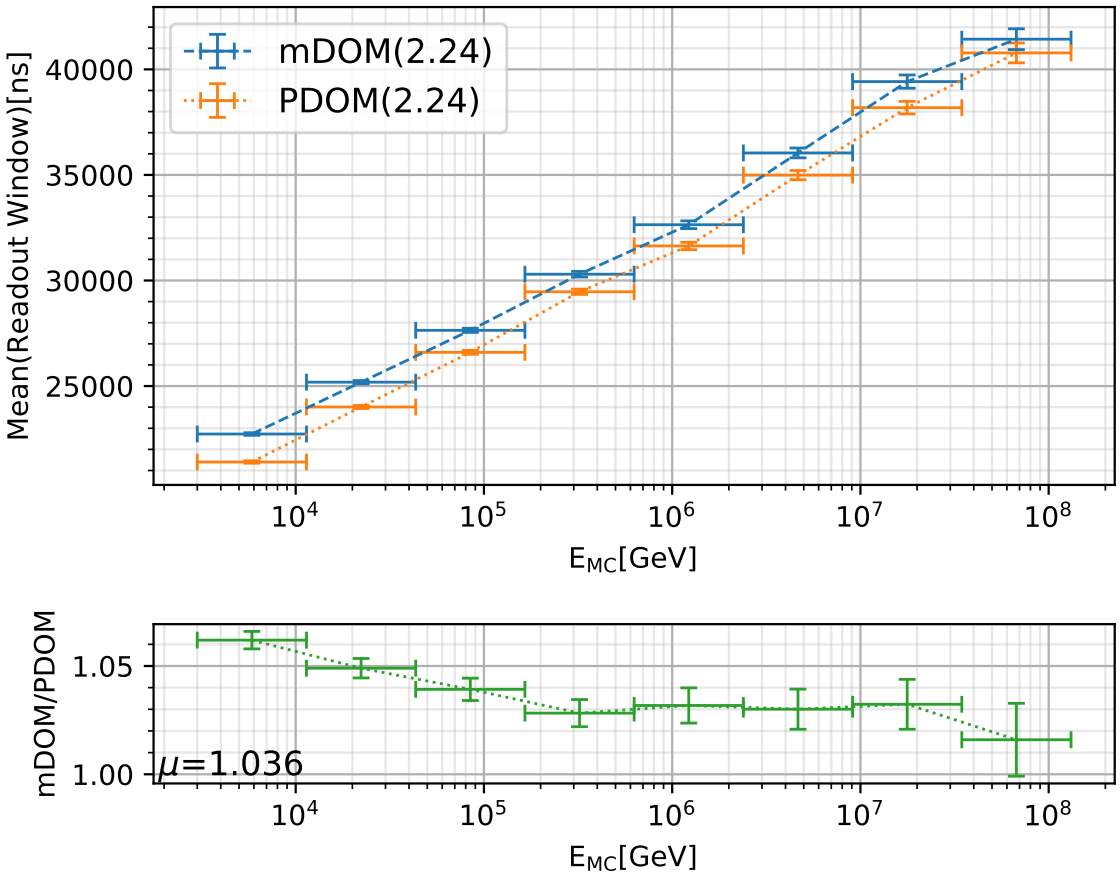

Figure B.10: Sanity check of the readout window for dataset 20016. The horizontal bars indicate the width of the energy bin, while the vertical error bars mark the standard error of the mean value. *Top*: E_{MC} versus the mean readout window length per event. Compared are simulations obtained with the upscaled PDOM and the nominal mDOM. *Bottom*: Ratio of the respective values from the top plot. The parameter μ denotes the mean of all ratios.

APPENDIX C

ADDITIONAL RECONSTRUCTION RESULTS

The following section shows the results of the comparison of the angular resolution obtained with the Gen2 high-energy array either equipped with downscaled mDOMs (1.0) or with nominal PDOMs (1.0). The results are obtained in the same manner as the results presented in section 5.3.4. The applied reconstruction methods, as well as the applied cuts are described in chapter 5.

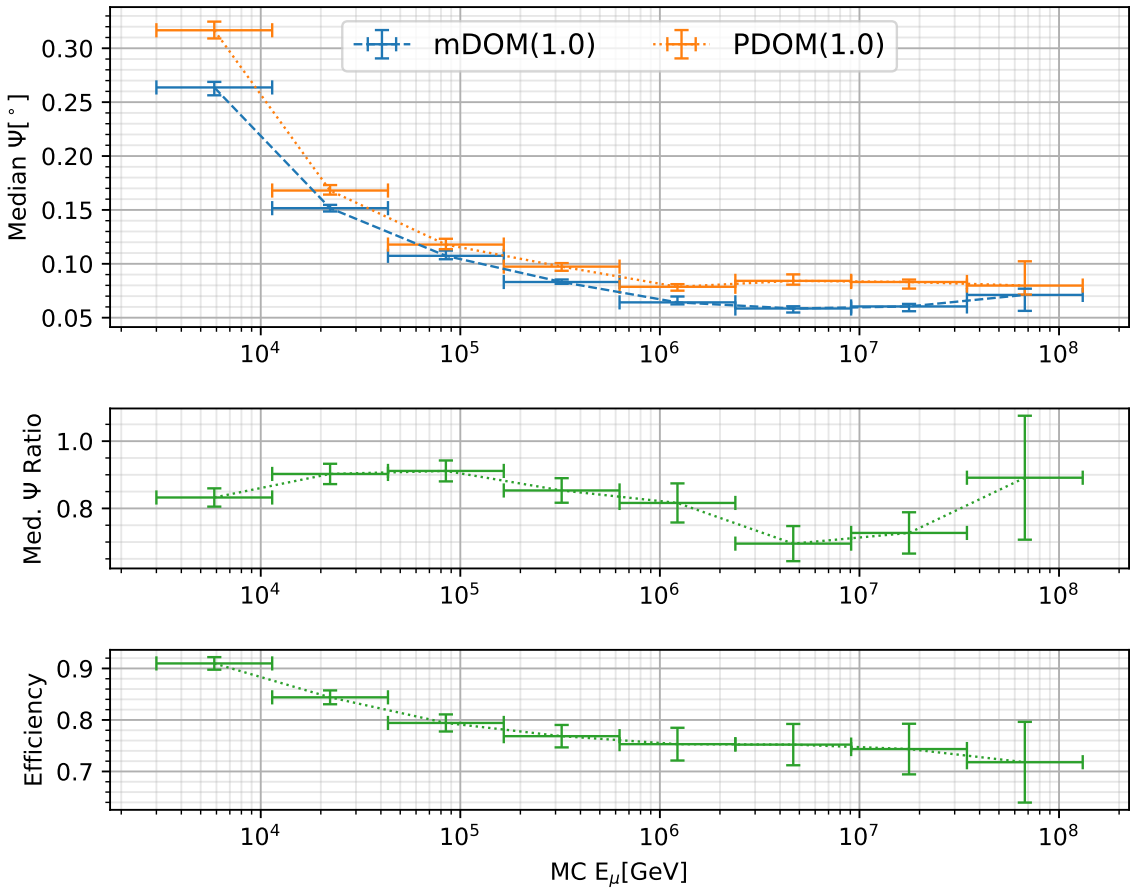

Figure C.1: Horiztontal muons with MCLength > 1000 m. The vertical error bars indicate the standard error and the horizontal bars show the width of the respective energy bin. *Top:* Comparison of the median angular resolution per energy bin of the downscaled mDOM (1.0) and the nominal PDOM (1.0). *Center:* Ratio of the median angular resolution (mDOM / PDOM) per energy bin. *Bottom:* Selection efficiency versus muon energy in the respective zenith range after the cut on MCLength (equal for both sensor types).

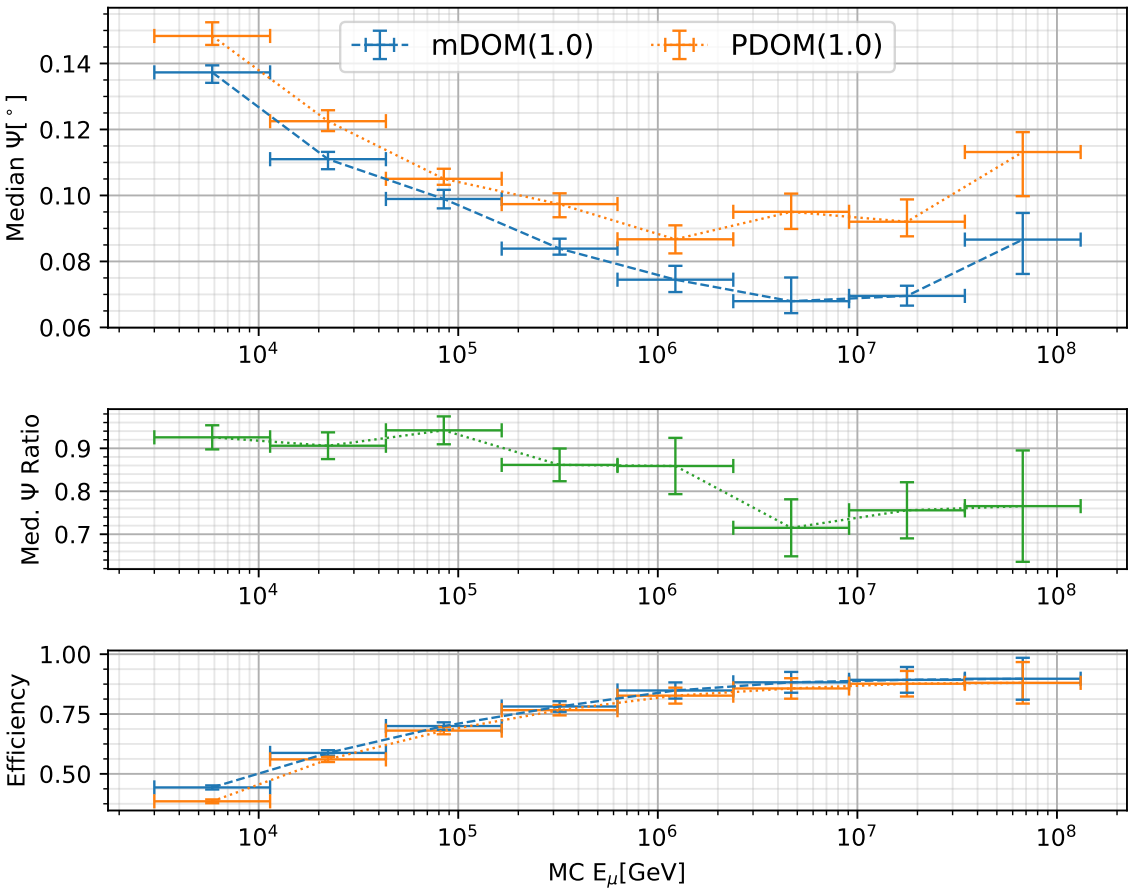

Figure C.2: Horizontal muons after the standard cuts have been applied. The vertical error bars indicate the standard error and the horizontal bars show the width of the respective energy bin. *Top:* Comparison of the median angular resolution per energy bin of the downscaled mDOM (1.0) and the nominal PDOM (1.0). *Center:* Ratio of the median angular resolution (mDOM / PDOM) per energy bin. *Bottom:* Selection efficiency versus muon energy in the respective zenith range after the standard cuts.

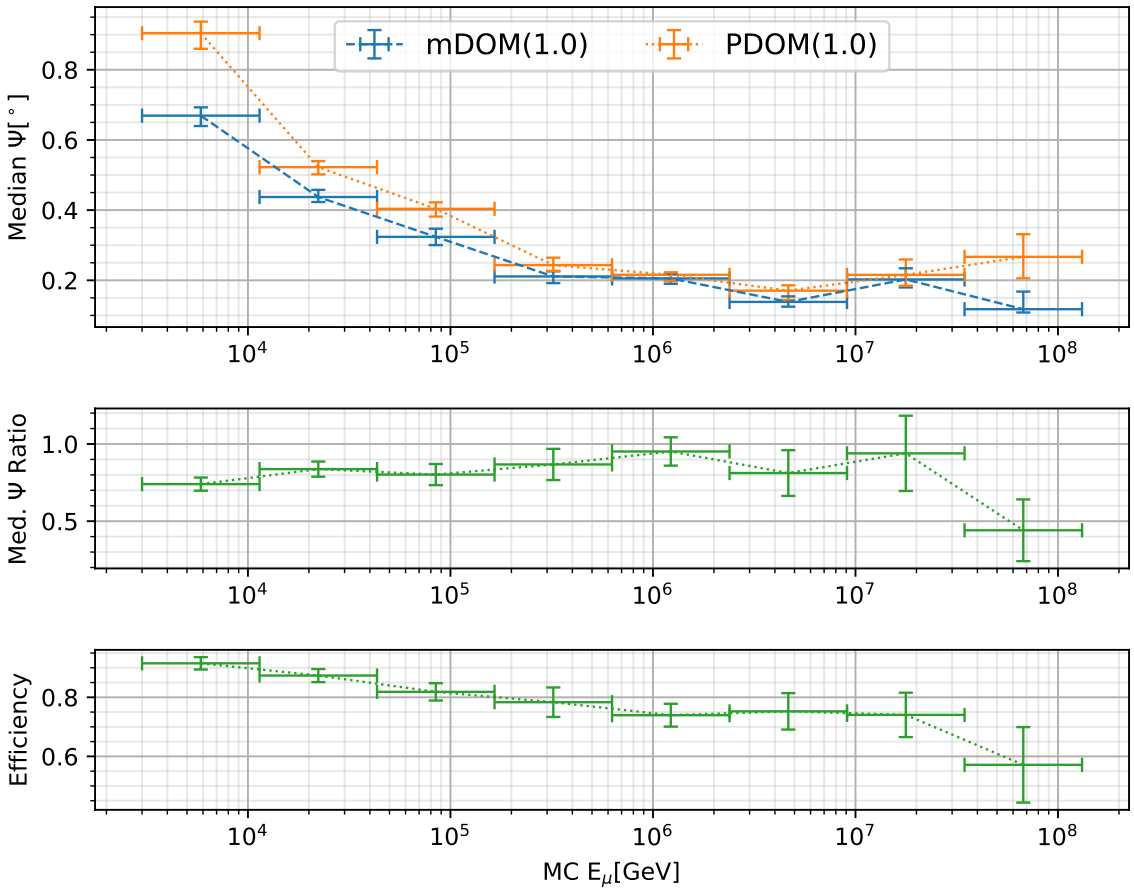

Figure C.3: Down-going muons with MCLength > 500 m. The vertical error bars indicate the standard error and the horizontal bars show the width of the respective energy bin. *Top:* Comparison of the median angular resolution per energy bin of the downscaled mDOM (1.0) and the nominal PDOM (1.0). *Center:* Ratio of the median angular resolution (mDOM / PDOM) per energy bin. *Bottom:* Selection efficiency versus muon energy in the respective zenith range after the cut on MCLength (equal for both sensor types).

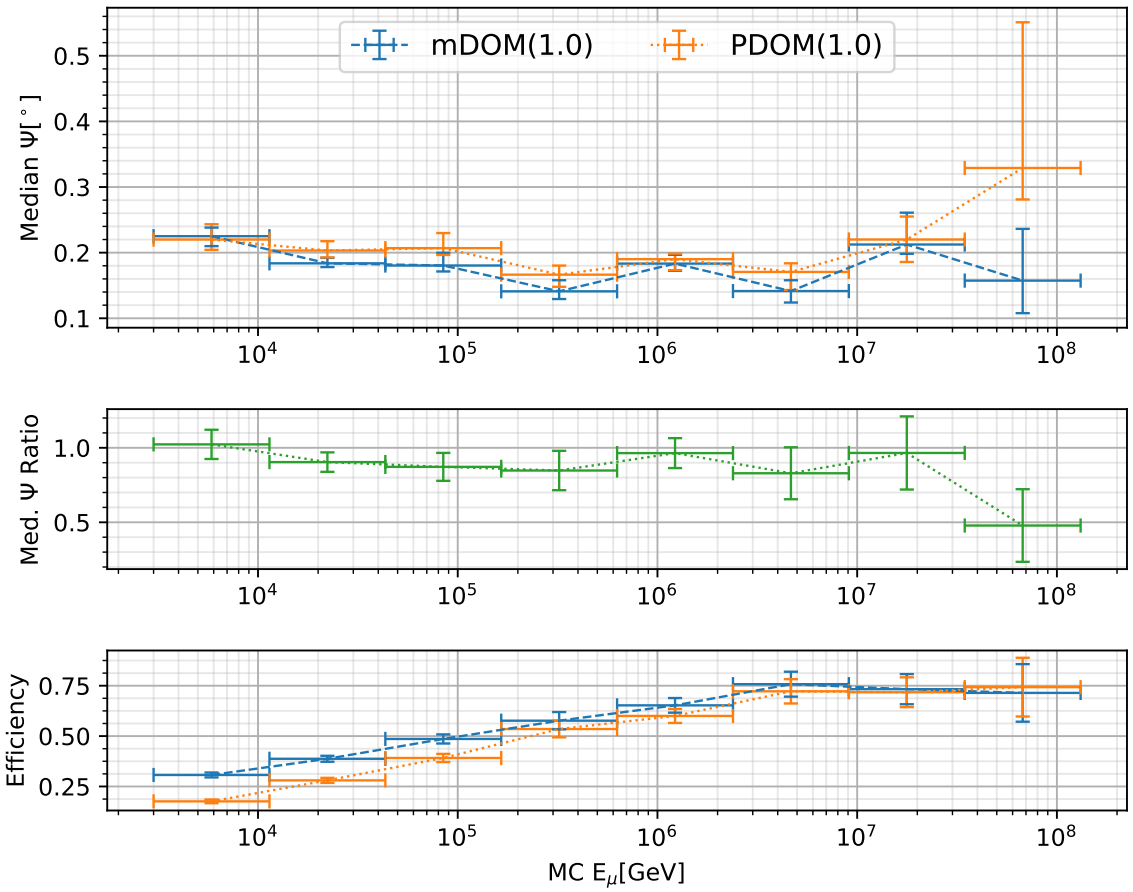

Figure C.4: Down-going muons after the standard cuts have been applied. The vertical error bars indicate the standard error and the horizontal bars show the width of the respective energy bin. *Top:* Comparison of the median angular resolution per energy bin of the downscaled mDOM (1.0) and the nominal PDOM (1.0). *Center:* Ratio of the median angular resolution (mDOM / PDOM) per energy bin. *Bottom:* Selection efficiency versus muon energy in the respective zenith range after the standard cuts.

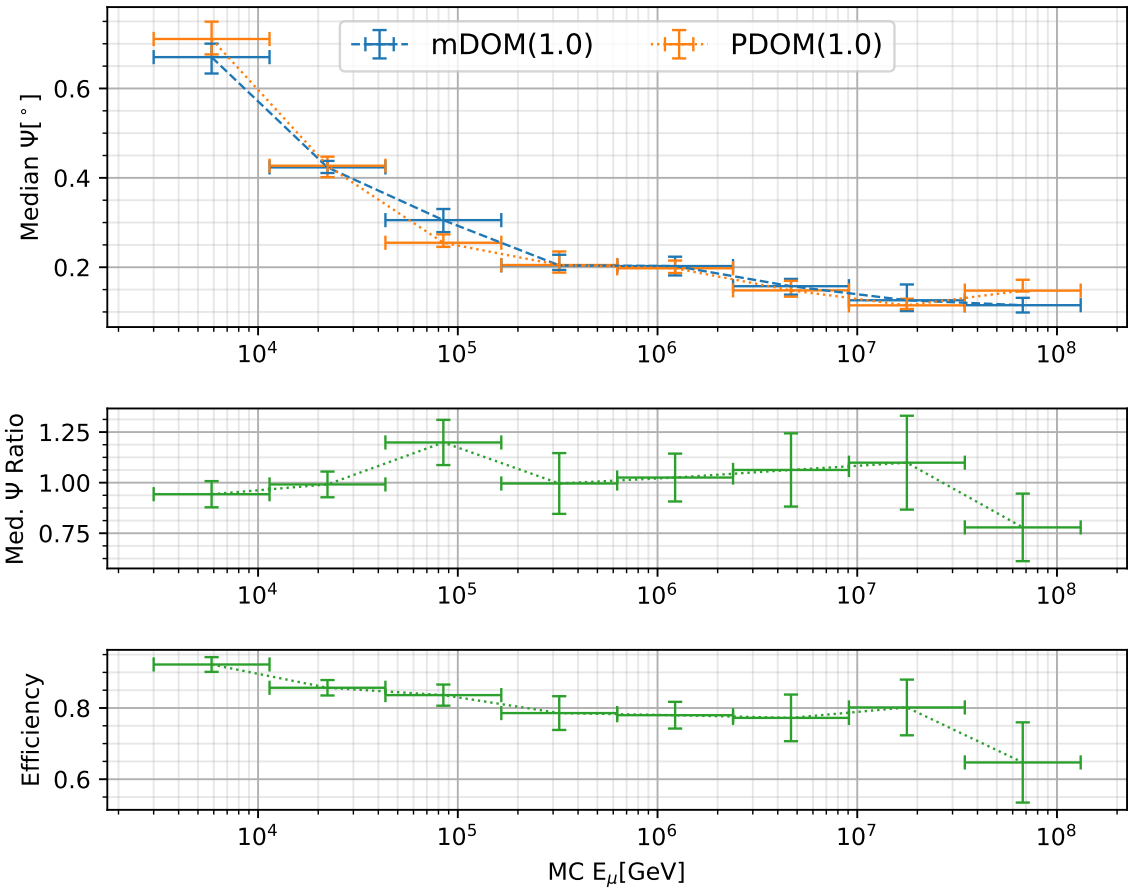

Figure C.5: Up-going muons with MCLength > 500 m. The vertical error bars indicate the standard error and the horizontal bars show the width of the respective energy bin. *Top:* Comparison of the median angular resolution per energy bin of the downscaled mDOM (1.0) and the nominal PDOM (1.0). *Center:* Ratio of the median angular resolution (mDOM / PDOM) per energy bin. *Bottom:* Selection efficiency versus muon energy in the respective zenith range after the cut on MCLength (equal for both sensor types).

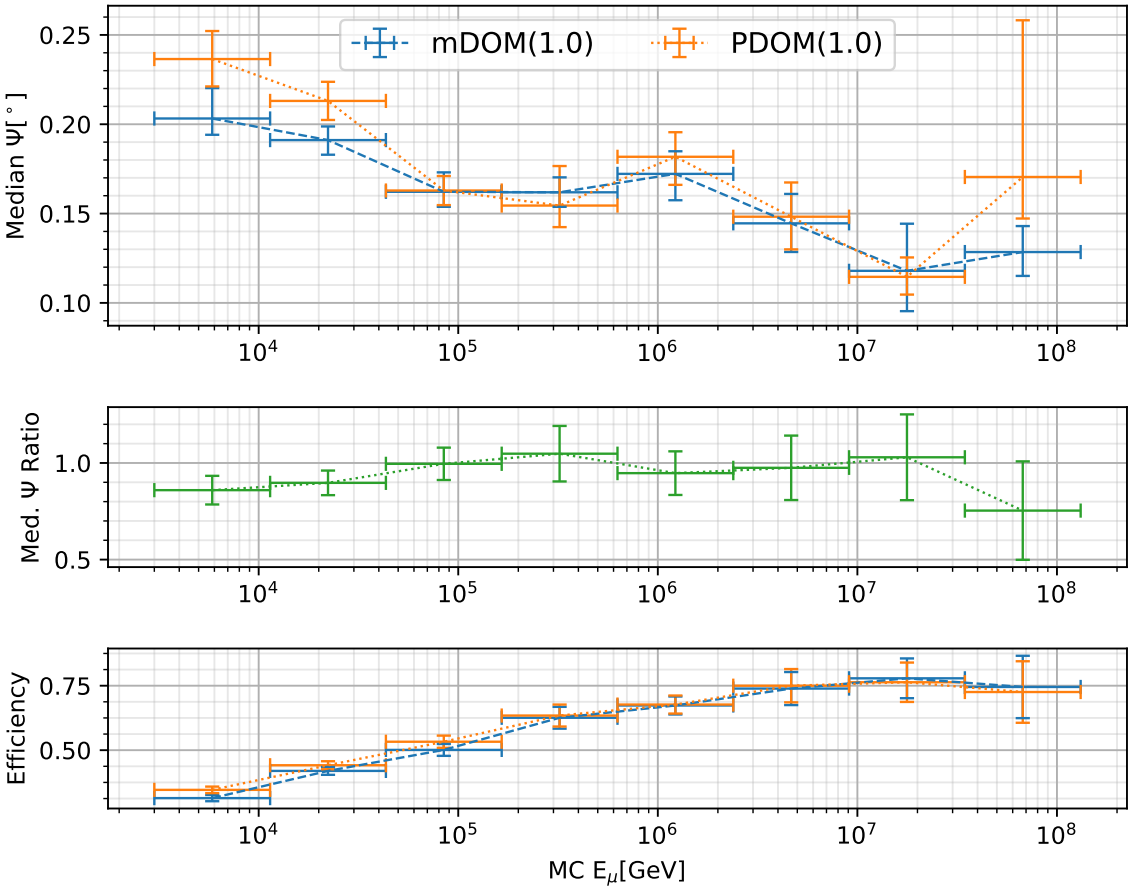

Figure C.6: Up-going muons after the standard cuts have been applied. The vertical error bars indicate the standard error and the horizontal bars show the width of the respective energy bin. *Top:* Comparison of the median angular resolution per energy bin of the downscaled mDOM (1.0) and the nominal PDOM (1.0).. *Center:* Ratio of the median angular resolution (mDOM / PDOM) per energy bin. *Bottom:* Selection efficiency versus muon energy in the respective zenith range after the standard cuts.

APPENDIX D

SELECTION EFFICIENCY & POINT SPREAD FUNCTIONS

This chapter contains additional information about the selection efficiency functions and the point spread functions which have been used in order to estimate the neutrino point source sensitivity and the discovery potential with the Gen2 high-energy array, either equipped with nominal mDOMs (2.24) or upscaled PDOMs (2.24). As described in section 6.3.2 and 6.3.3 the selection efficiency and the angular resolution obtained from the data had to be extended to a larger energy range in order to be usable by the Gen2-analysis framework. Since no information outside of the simulated energy range was available, the respective functions have been extended with reasonable values. In order to make sure that the estimated sensitivities and discovery fluxes are not changed significantly, a brief study has been conducted investigating the effect of the extension on the discovery potential. It is assumed, that the effect of the extension on the discovery potential is similar to the effect on the sensitivity.

D.1 Impact of the Selection Efficiency Extension on the Discovery Potential

In order to test the effect of the extension of the efficiency function on the discovery potential, the obtained efficiencies have been extended with two extreme values, denoted as "min" and "max" (see figure D.1), for both sensors and all zenith bands. As described in section 6.3.2, there is a transition between 3 TeV, the lower energy boundary of the simulations, and 5.9 TeV, the bin center of the first energy bin, so the first value obtained purely from simulations. Within this energy range, the values are obtained by linear interpolation. At 3 TeV the value from the respective extension function is used and at 5.9 TeV the value from the simulation is used. The "min"-method continues the efficiency with zero for energies outside of the simulated energy

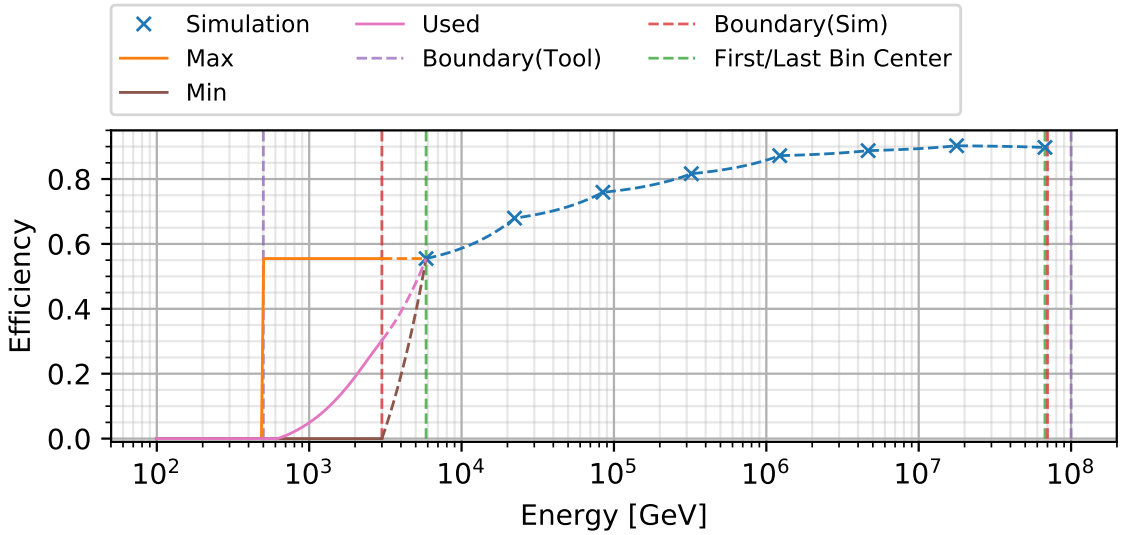

Figure D.1: Efficiency versus energy for different with different efficiency extension methods. The used extensions (pink, denoted "Used") lies between the tested extreme variants, "Min" and "Max".

range, the "max"-methode continues the efficiency with the value obtained from the simulation at 5.9 TeV for energy below the simulated energy range and with the value obtained from the simulation at 67 PeV for values above the simulated energy range. The idea of using these two extreme values for the extension is the assumption that a realistic value, obtained from simulations, for the efficiency in this energy range would lie somewhere in between. If extending the efficiency with these extreme values does not change the ratio of the obtained figures of merit significantly, it can be assumed that a more realistic extension in between these values yields reasonable results without introducing any bias.
The impact of these extension methods on the discovery potential is shown in figure D.2. It can be seen, that for all except one declination the obtained ratios of the discovery potential for the two modules does not change for more then 0.5 % - 1.0 %. Thus, it can be assumed that the usage of the exact same efficiency extension does not have a large impact on the sensitivity and discovery potential ratio comparison of the two modules.

D.2 Impact of the Point Spread Function Extension on the Discovery Potential

Similar to the study of the effect of the extension of the efficiency, the potential impact on the figures of merit through extending the point spread function has been investigated. Contrary

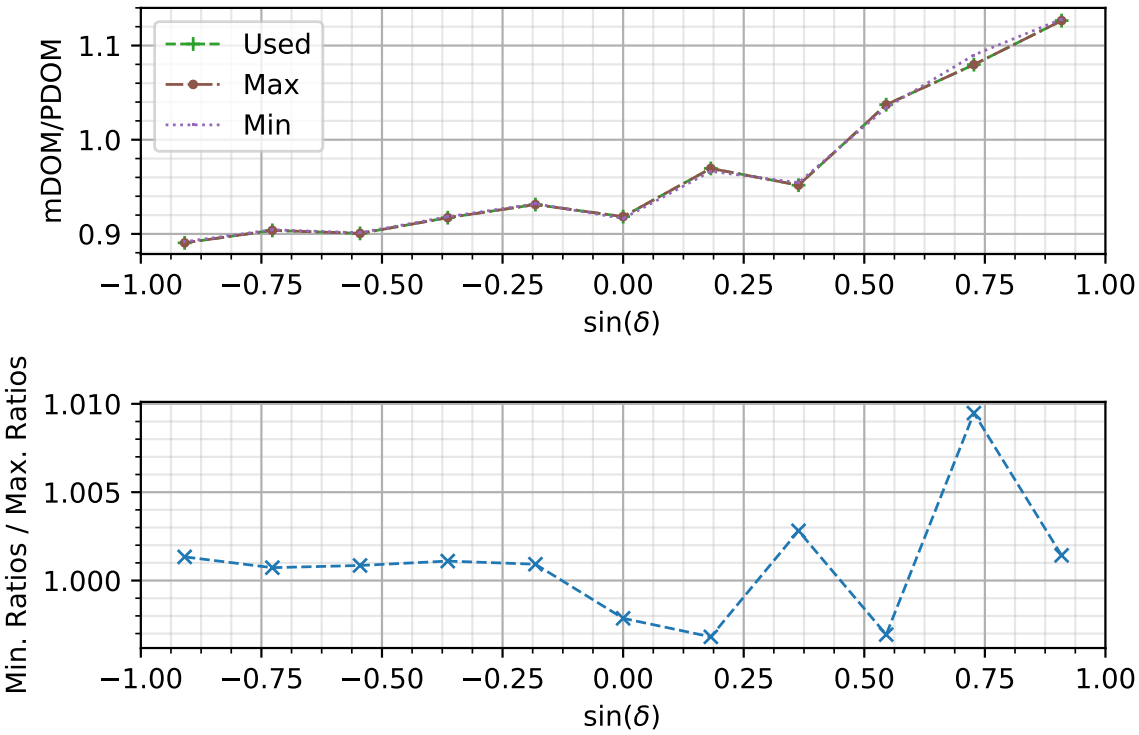

Figure D.2: Impact of the efficiency extension on the discovery potential ratio (mDOM / PDOM). *Top:* Ratios of the 5σ discovery potential (mDOM / PDOM) obtained when different extension methods for the selection efficiency are used. *Bottom:* Relative difference of the ratios obtained with the "Min" extensions compared to "Max" extension.

to the impact study for the efficiency, the point spread functions have been extended with either the values obtained from IceCube, which is a conservative assumption and ended up been the extension used, and a "Max" extension, which artificially sets the median angular resolution outside of the simulated energy range to 90°. The difference on the discovery potential ratio, mDOM over PDOM, obtianed by using either the "Max" extension method or the IceCube extensions method (denoted as "Used") is shown in figure D.3. It can be seen that apart from the highest declination angles, the difference in the rations is less then 0.6% and less then 1.4% at most. Similar to the extension of the selection efficiency, the extension of the used point spread function seems to have very little effect on the performance comparison of the two sensors.

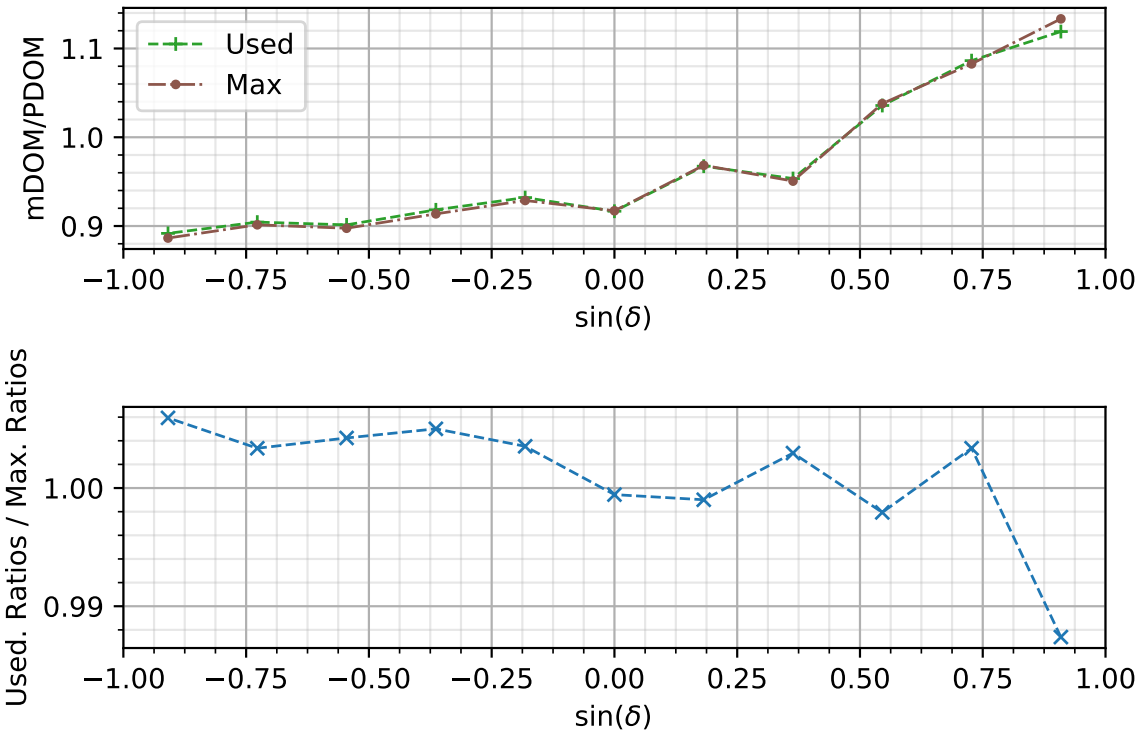

Figure D.3: Impact of the point spread function extension on the discovery potential ratio (mDOM / PDOM). *Top:* Ratios of the 5σ discovery potential (mDOM / PDOM) obtained when different extension methods for the point spread function are used. *Bottom:* Relative difference of the ratios obtained with the "IceCube" (used) extensions compared to "Max" extension.

D.3 Implemented Selection Efficiency & Median Angular Resolution used for Sensitivity and Discovery Flux Estimation for all Zenith Bands

Within the last section of this chapter, the implemented selection efficiency and the median angular opening angle Ψ of the scaled point spread functions used for the estimation of the neutrino point source sensitivities and discovery potentials presented in chapter 6 are shown for all eleven zenith bands (see table 6.1). The following figures do all have the same format. Each figure consists of three plots. The top plot shows the median angular resolution versus the energy for the whole opening angle range, while the center plot shows the same plot, but zoomed in, in order to emphasize the different opening angles obtained from the simulations. The bottom plot shows the selection efficiency versus the energy. The blue dashed line shows the respective functions for the nominal mDOM (2.24), while orange pluses show the exact values obtained from the simulations of the mDOM (2.24). The orange dotted line shows the respective functions

for the upscaled PDOM (2.24), while the respective values obtained from the simulations are marked with a blue "x". The vertical lines in each plot mark different boundaries. The simulation boundaries are marked with the red lines (= energy range of the simulation), while the green lines mark the first and last energy bin center (see table 6.2). The purple lines mark the thresholds of the Gen2-analysis framework.

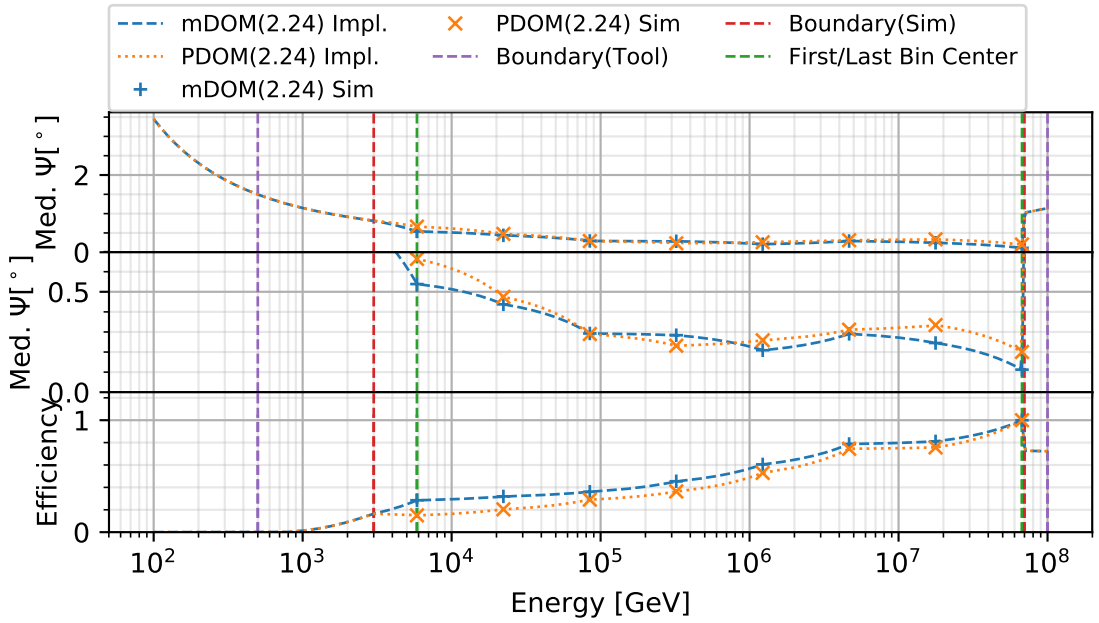

Figure D.4: Zenith band: $0° < \theta < 35°$. *Top:*Median angular resolution versus energy. *Center:* Zoomed in median angular resolution versus energy. *Bottom:* Selection Efficiency versus energy.

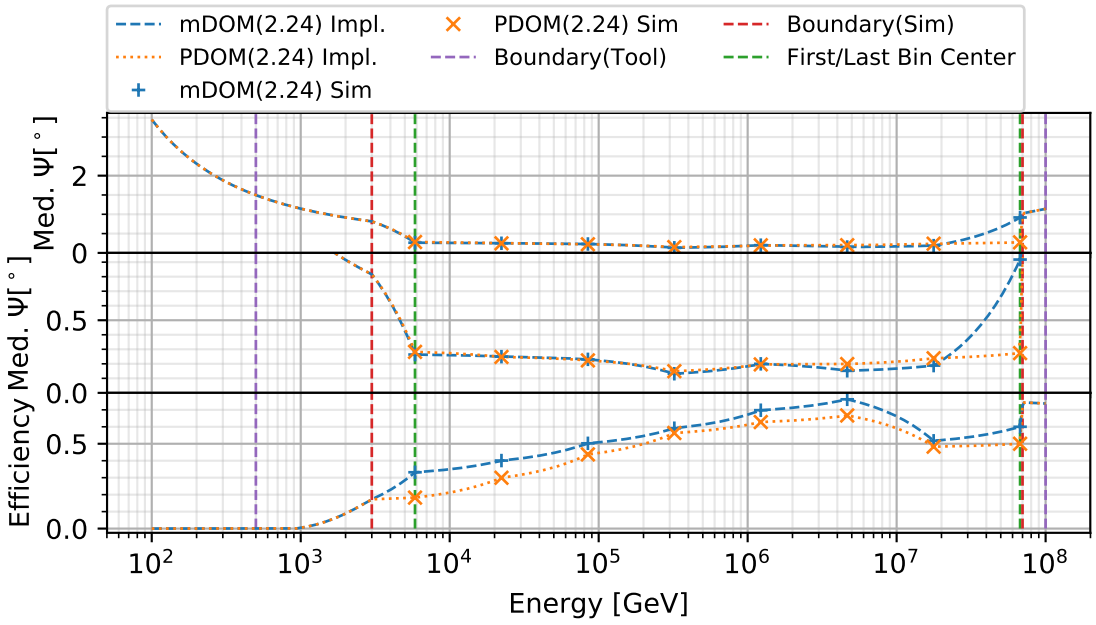

Figure D.5: Zenith band: $35° < \theta < 50°$. *Top:*Median angular resolution versus energy. *Center:* Zoomed in median angular resolution versus energy. *Bottom:* Selection Efficiency versus energy.

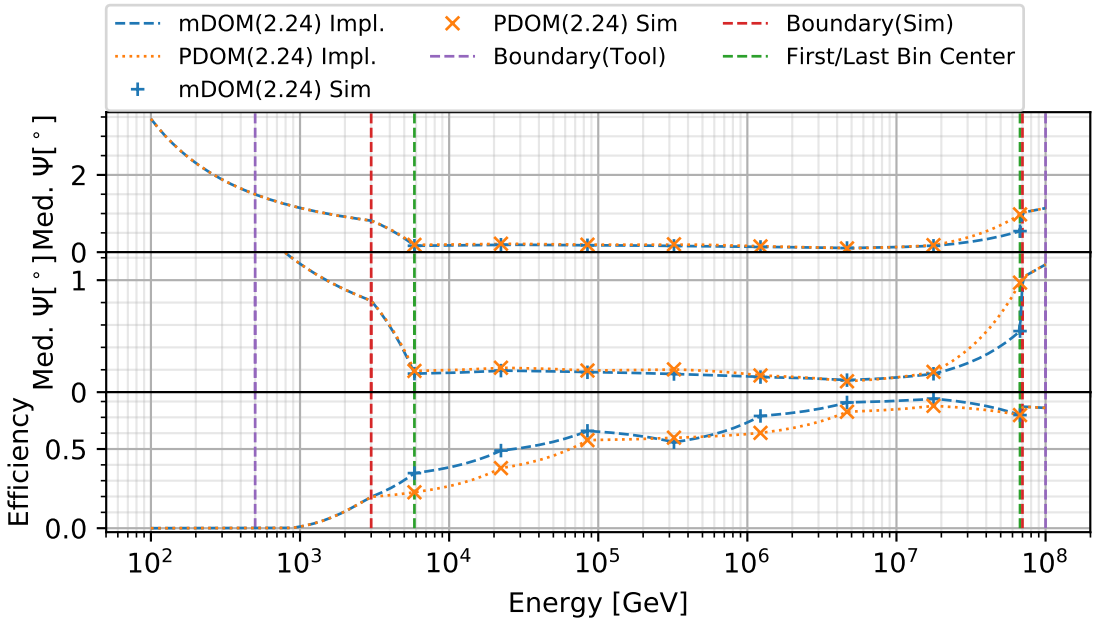

Figure D.6: Zenith band: $50° < \theta < 63°$. *Top:*Median angular resolution versus energy. *Center:* Zoomed in median angular resolution versus energy. *Bottom:* Selection Efficiency versus energy.

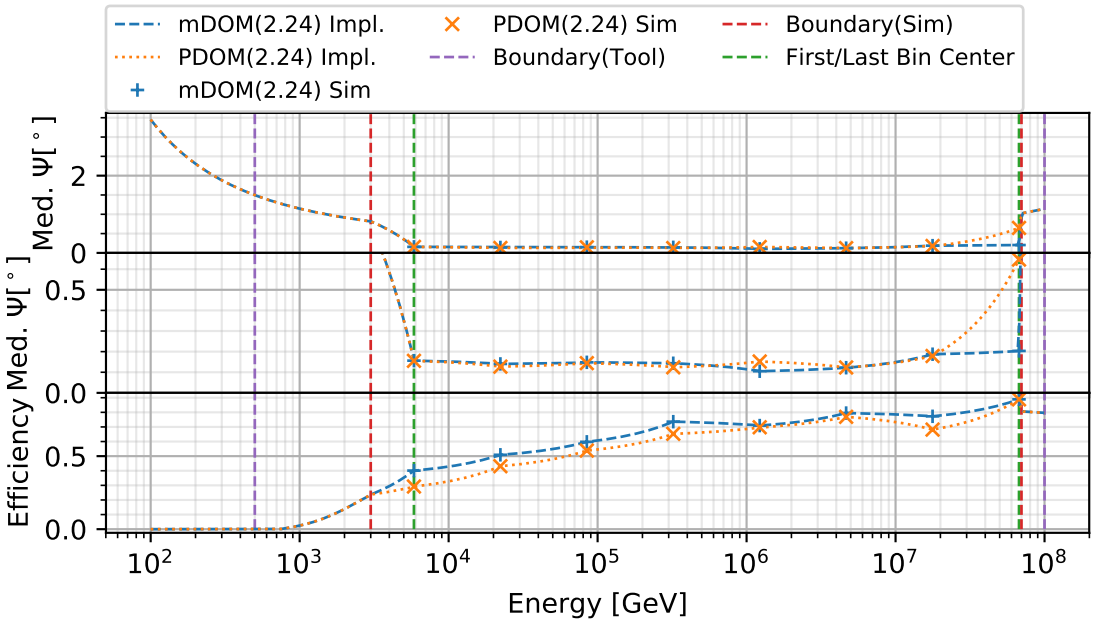

Figure D.7: Zenith band: $63° < \theta < 74°$. *Top:*Median angular resolution versus energy. *Center:* Zoomed in median angular resolution versus energy. *Bottom:* Selection Efficiency versus energy.

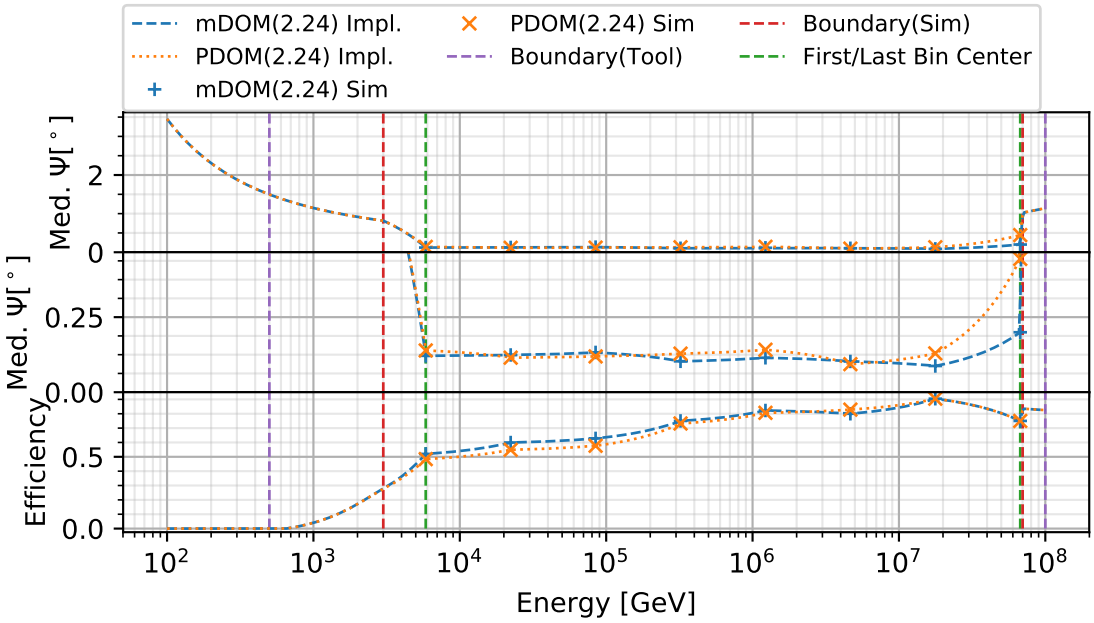

Figure D.8: Zenith band: $74° < \theta < 85°$. *Top:*Median angular resolution versus energy. *Center:* Zoomed in median angular resolution versus energy. *Bottom:* Selection Efficiency versus energy.

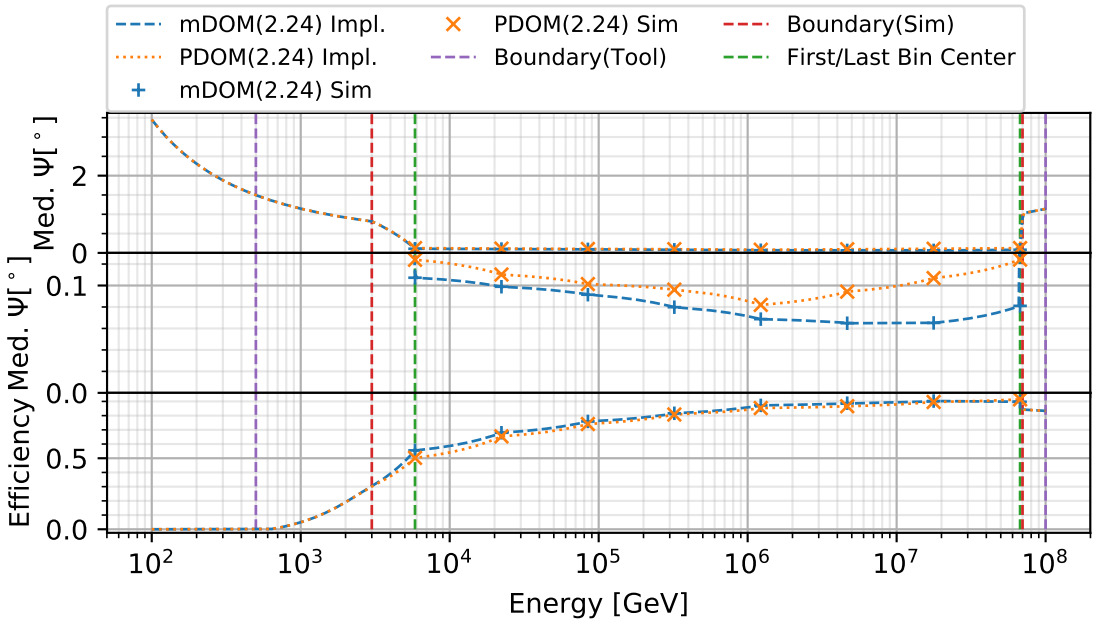

Figure D.9: Zenith band: $85^\circ < \theta < 95^\circ$. *Top:*Median angular resolution versus energy. *Center:* Zoomed in median angular resolution versus energy. *Bottom:* Selection Efficiency versus energy.

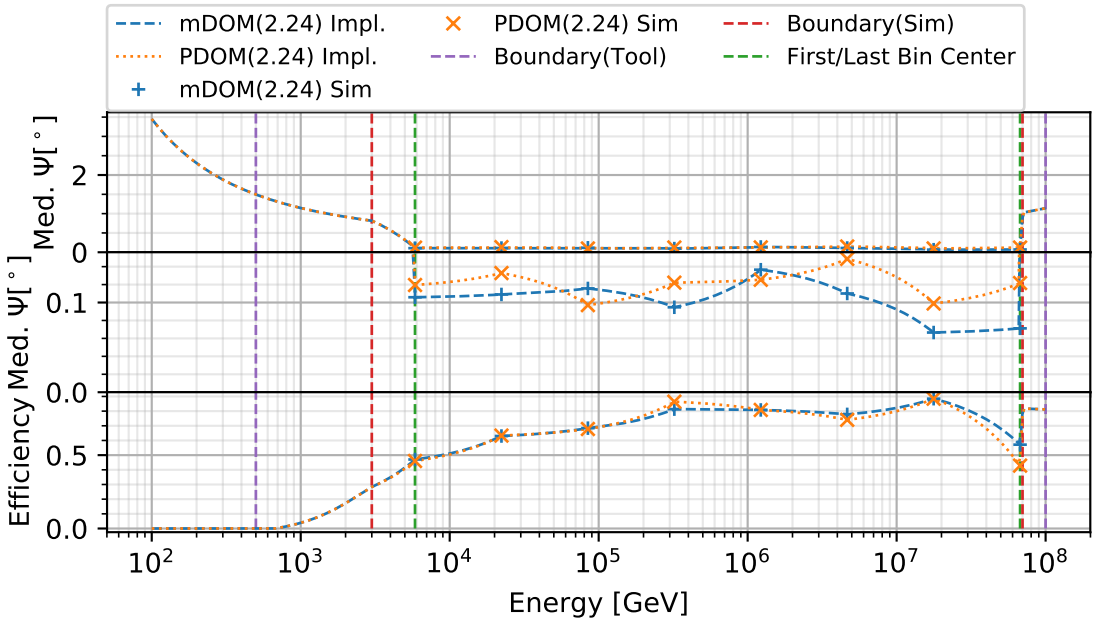

Figure D.10: Zenith band: $95^\circ < \theta < 106^\circ$. *Top:*Median angular resolution versus energy. *Center:* Zoomed in median angular resolution versus energy. *Bottom:* Selection Efficiency versus energy.

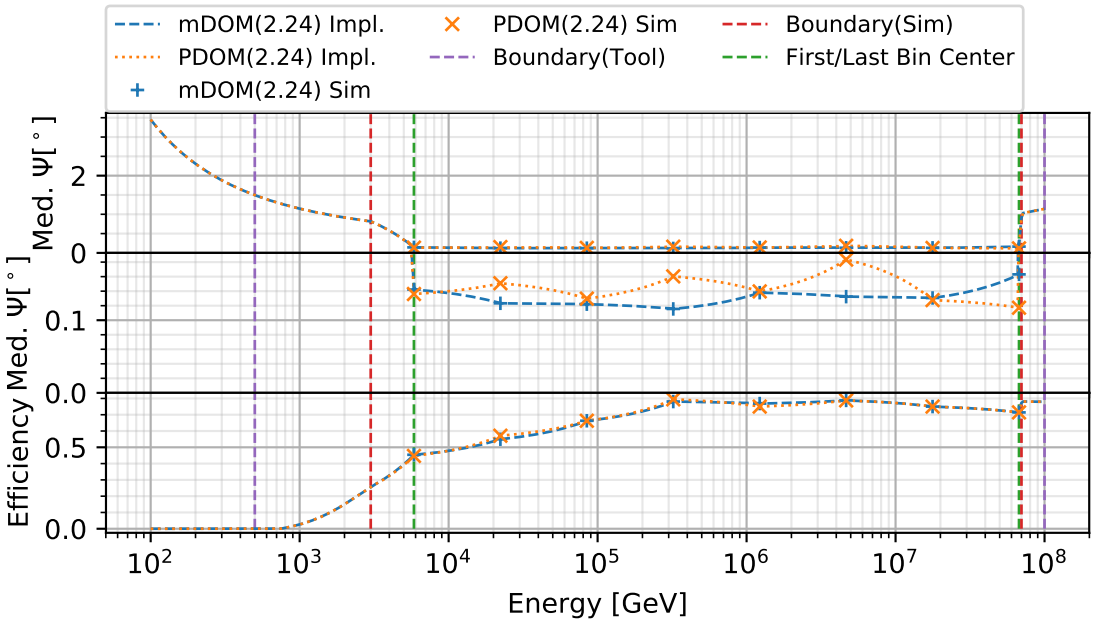

Figure D.11: Zenith band: $106° < \theta < 117°$. *Top:*Median angular resolution versus energy. *Center:* Zoomed in median angular resolution versus energy. *Bottom:* Selection Efficiency versus energy.

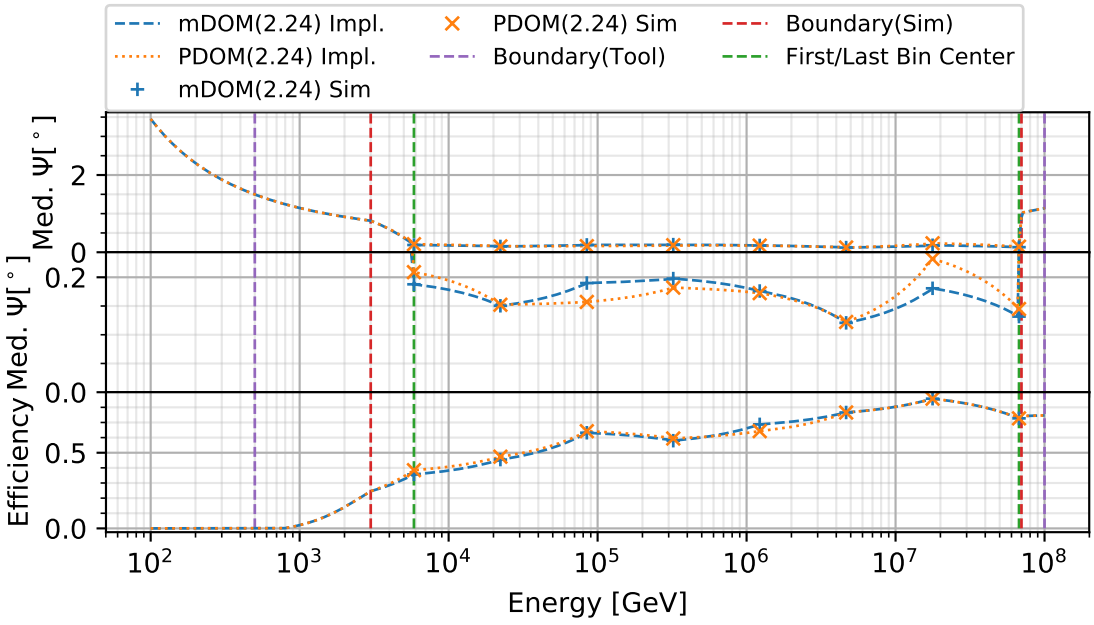

Figure D.12: Zenith band: $117° < \theta < 130°$. *Top:*Median angular resolution versus energy. *Center:* Zoomed in median angular resolution versus energy. *Bottom:* Selection Efficiency versus energy.

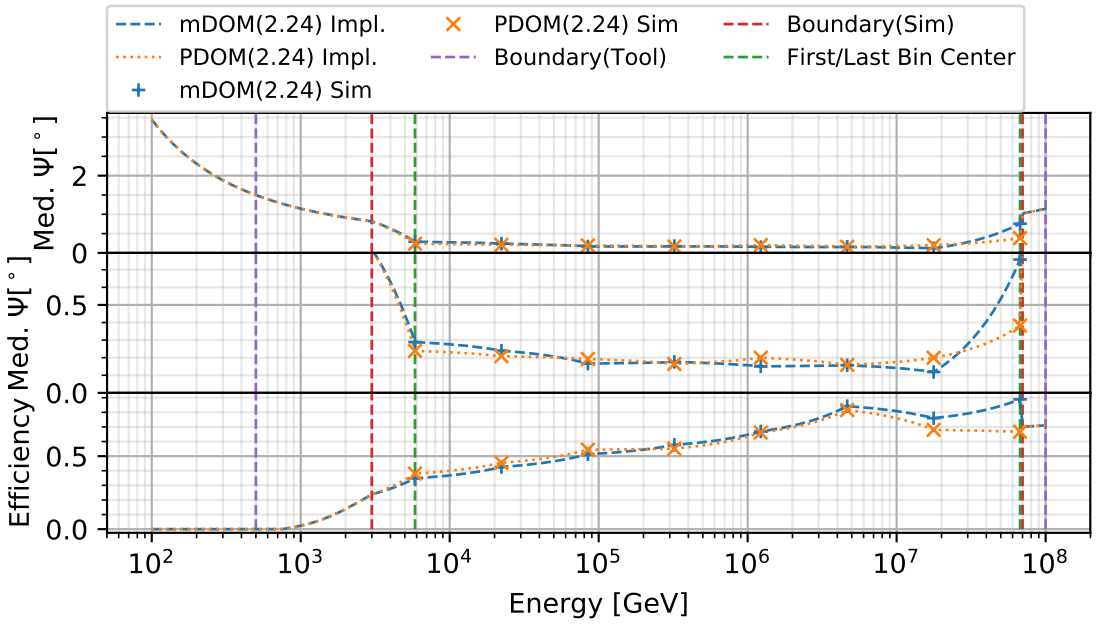

Figure D.13: Zenith band: $130° < \theta < 145°$. *Top:*Median angular resolution versus energy. *Center:* Zoomed in median angular resolution versus energy. *Bottom:* Selection Efficiency versus energy.

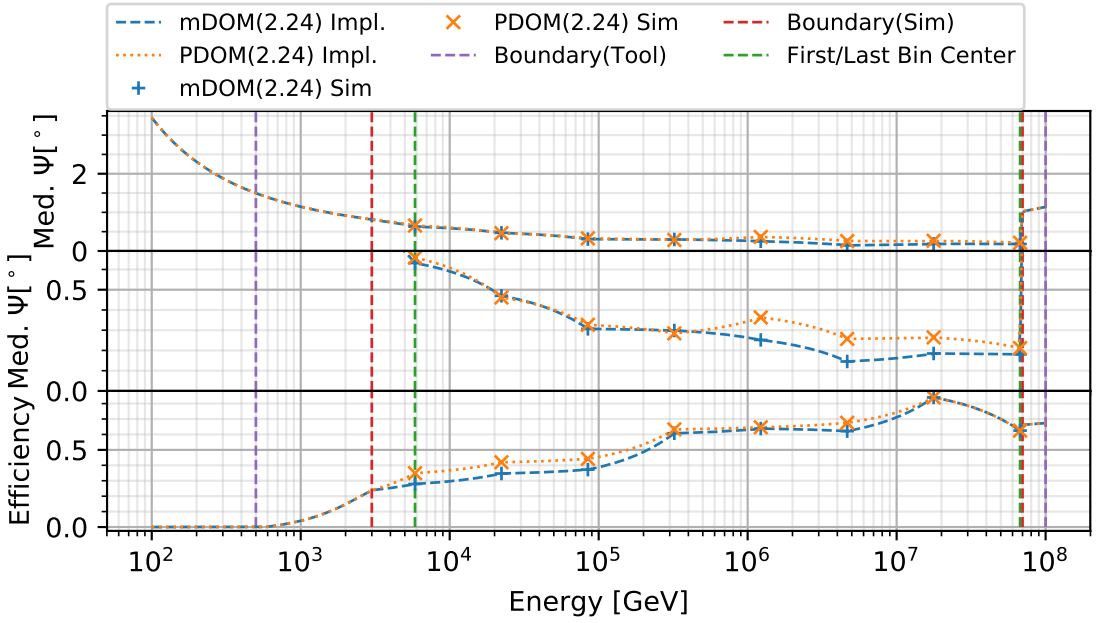

Figure D.14: Zenith band: $145° < \theta < 180°$. *Top:*Median angular resolution versus energy. *Center:* Zoomed in median angular resolution versus energy. *Bottom:* Selection Efficiency versus energy.

BIBLIOGRAPHY

[1] A. ACHTERBERG ET AL. (ICECUBE COLLABORATION), *First year performance of the icecube neutrino telescope*, Astropart.Phys.26:155-173, (2006).

[2] A. ALBERT ET AL. (ANTARES COLLABORATION), *First all-flavor neutrino pointlike source search with the ANTARES neutrino telescope*, Physical Review D, 96 (2017).

[3] A. F. J. MOFFAT, *A theoretical investigation of focal stellar images in the photographic emulsion and application to photographic photometry*, Astronomy and Astrophysics, Vol. 3, p. 455, (1969).

[4] A. ISHIHARA, *The icecube upgrade – design and science goals*, PoS-ICRC2019-1031, (2019).

[5] M. ACKERMANN, *Searches for signals from cosmic point-like sources of high energy neutrinos in 5 years of AMANDA-II data*, PhD thesis, Humboldt-Universität zu Berlin, 2006.

[6] ADRIÁN-MARTÍNEZ ET AL. (KM3NET COLLABORATION), *Letter of intent for KM3net 2.0*, Journal of Physics G: Nuclear and Particle Physics, 43 (2016), p. 084001.

[7] J. ALVAREZ-MUÑIZ AND F. HALZEN, *Possible high-energy neutrinos from the cosmic accelerator RX j1713.7-3946*, The Astrophysical Journal, 576 (2002), pp. L33–L36.

[8] H. ATHAR, C. S. KIM, AND J. LEE, *The intrinsic and oscillated astrophysical neutrino flavor ratios*, Mod.Phys.Lett. A21 (2006) 1049-1066, (2005).

[9] B. J. P. JONES, *Sterile Neutrinos in Cold Climates*, PhD thesis, MIT, sep 2015.

[10] C. BAIXERAS, *The MAGIC telescope*, Nuclear Physics B - Proceedings Supplements, 114 (2003), pp. 247–252.

[11] R. BARLOW, *Statistics*, Wiley John + Sons, 1989.

[12] J. BRAUN, J. DUMM, F. D. PALMA, C. FINLEY, A. KARLE, AND T. MONTARULI, *Methods for point source analysis in high energy neutrino telescopes*, Astroparticle Physics, 29 (2008), pp. 299–305.

[13] C. KOPPER, *Clsim github repository*. `https://github.com/claudiok/clsim`, January 2019.

[14] C. KOPPER FOR THE ICECUBE COLLABORATION, *Observation of astrophysical neutrinos in six years of IceCube data*, in Proceedings of 35th International Cosmic Ray Conference — PoS(ICRC2017), Sissa Medialab, aug 2017.

[15] G. CARMINATI, M. BAZZOTTI, A. MARGIOTTA, AND M. SPURIO, *Atmospheric MUons from PArametric formulas: a fast GEnerator for neutrino telescopes (MUPAGE)*, Computer Physics Communications, 179 (2008), pp. 915–923.

[16] P. A. ČERENKOV, *Visible radiation produced by electrons moving in a medium with velocities exceeding that of light*, Physical Review, 52 (1937), pp. 378–379.

[17] D. CHIRKIN AND W. RHODE, *Propagating leptons through matter with muon monte carlo (mmc)*, [arXiv:hep-ph/0407075v3], (2004).

[18] D. CHIRKIN AND M. RONGEN, *Light diffusion in birefringent polycrystals and the icecube ice anisotropy*, PoS-ICRC2019-854, (2019).

[19] CHRISTIAN HAACK AND CHRISTOPHER WIEBUSCH FOR THE ICECUBE COLLABORATION, *A measurement of the diffuse astrophysical muon neutrino flux using eight years of IceCube data.*, in Proceedings of 35th International Cosmic Ray Conference — PoS(ICRC2017), Sissa Medialab, aug 2017.

[20] A. COOPER-SARKAR, P. MERTSCH, AND S. SARKAR, *The high energy neutrino cross-section in the standard model and its uncertainty*, JHEP 08 (2011) 042, (2011).

[21] G. COWAN, K. CRANMER, E. GROSS, AND O. VITELLS, *Asymptotic formulae for likelihood-based tests of new physics*, The European Physical Journal C, 71 (2011), pp. 1–19.

[22] D. TOSI AND H. PANDYA, *Icetop as veto for icecube: results*, PoS-ICRC2019-445, (2019).

[23] D. XU, *Exploring the universe with neutrinos: Recent results from icecube*, Nucl.Part.Phys.Proc. 287-288, (2017).

[24] C. DE BOOR, *A Practical Guide to Splines*, Springer-Verlag GmbH, 2001.

[25] P. H. C. EILERS AND B. D. MARX, *Flexible smoothing with b -splines and penalties*, Statistical Science, 11 (1996), pp. 89–121.

[26] R. ENBERG, M. H. RENO, AND I. SARCEVIC, *Prompt neutrino fluxes from atmospheric charm*, Physical Review D, 78 (2008).

[27] ESA, NASA, AND F. MIRABEL.
https://www.spacetelescope.org/images/heic0211i/.
Date: 2018-07-11.

[28] F. JAMES, *Statistical Methods in Experimental Physics(2nd Edition)*, World Scientific Pub Co Inc, 2006.

[29] G. T. ZATSEPIN AND V. A. KUZMIN, *Upper Limit of the Spectrum of Cosmic Rays*, Soviet Journal of Experimental and Theoretical Physics Letters, 4 (1966), p. 78.

[30] T. K. GAISSER, R. ENGEL, AND E. RESCONI, *Cosmic Rays and Particle Physics*, Cambridge University Press, 2016.

[31] T. K. GAISSER AND M. HONDA, *FLUX OF ATMOSPHERIC NEUTRINOS*, Annual Review of Nuclear and Particle Science, 52 (2002), pp. 153–199.

[32] T. K. GAISSER, T. STANEV, AND S. TILAV, *Cosmic ray energy spectrum from measurements of air showers*, Frontiers of Physics, 8 (2013), pp. 748–758.

[33] GLEB BELIAKOV, *Shape preserving approximation using least squares splines*, G. Approx. Theory & its Appl., (2000).

[34] R. J. GOULD AND G. P. SCHRÉDER, *Opacity of the universe to high-energy photons*, Physical Review, 155 (1967), pp. 1408–1411.

[35] C. GRUPEN, G. COWAN, S. EIDELMAN, AND T. STROH, *Astroparticle Physics*, Springer-Verlag GmbH, 2005.

[36] D. HECK, J. KNAPP, J. N. CAPDEVIELLE, G. SCHATZ, AND T. THOUW, *Corsika: A monte carlocode to simulate extensive air showers*, tech. rep. FZKA-6019, (1998).

[37] J. HESTER AND A. LOLL.
http://hubblesite.org/image/1823/news/3-nebulae.
Date: 2018-07-11.

[38] M. HONDA, T. KAJITA, K. KASAHARA, AND S. MIDORIKAWA, *Calculation of the flux of atmospheric neutrinos*, Physical Review D, 52 (1995), pp. 4985–5005.

[39] M. HONDA, T. KAJITA, K. KASAHARA, S. MIDORIKAWA, AND T. SANUKI, *Calculation of atmospheric neutrino flux using the interaction model calibrated with atmospheric muon data*, Physical Review D, 75 (2007).

[40] I. KING, *The structure of star clusters. i. an empirical density law*, The Astronomical Journal, 67 (1962), p. 471.

[41] ICECUBE COLLABORATION.
http://software.icecube.wisc.edu/documentation/projects/DOMLauncher/PMTRes.html, January 2019.

[42] ——.
https://wiki.icecube.wisc.edu/index.php/SLC_hit_cleaning, January 2019.

[43] ——.
http://software.icecube.wisc.edu/documentation/projects/clsim/rationale.html, 07 2019.

[44] ——.
http://software.icecube.wisc.edu/documentation/projects/photospline/index.html, May 2019.

[45] ——, *Icecube internal gallery*, January 2019.

[46] ——, *Photospline project*.
http://software.icecube.wisc.edu/documentation/projects/photospline/index.html, January 2019.

[47] J. H. KOEHNE ET AL., *PROPOSAL: A tool for propagation of charged leptons*, Computer Physics Communications, 184 (2013), pp. 2070–2090.

[48] J. REUBELT AND L. CLASSEN, *internal communication*, 2015.

[49] J. VAN SANTEN, *IceCube-gen2: the next-generation neutrino observatory for the south pole*, in Proceedings of 35th International Cosmic Ray Conference — PoS(ICRC2017), Sissa Medialab, aug 2017.

[50] ——, *Gen2-Analysis Framework*.
http://code.icecube.wisc.edu/svn/sandbox/jvansanten/projects/2015/gen2_analysis, 2018.

[51] J. W. ROHLF, *Modern Physics from Alpha to Z0*, PAPERBACKSHOP UK IMPORT, 1994.

[52] J. ZORNOZA AND D. CHIRKIN FOR THE ICECUBE COLLABORATION, *Muon energy reconstruction and atmospheric neutrino spectrum unfolding with the IceCube detector*, International Cosmic Ray Conference 5 (2008), (2008), pp. 1275–1278.

[53] K. A. OLIVE ET AL., *Review of particle physics*, Chinese Physics C, 40 (2016), p. 100001.

[54] K. GREISEN, *End to the cosmic-ray spectrum?*, Physical Review Letters, 16 (1966), pp. 748–750.

[55] K. SCHATTO, *Stacked searches for high-energyneutrinos from blazars with IceCube*, PhD thesis, Johannes Gutenberg-Universität Mainz, 2014.

[56] KOHTA MURASE ET AL., *BLAZARS AS ULTRA-HIGH-ENERGY COSMIC-RAY SOURCES: IMPLICATIONS FOR TeV GAMMA-RAY OBSERVATIONS*, The Astrophysical Journal, 749 (2012), p. 63.

[57] L. SACHS, *Angewandte Statistik*, Springer Verlag, 2013.

[58] J. G. LEARNED AND K. MANNHEIM, *High-energy neutrino astrophysics*, Annual Review of Nuclear and Particle Science, 50 (2000), pp. 679–749.

[59] LEW CLASSEN, *The mDOM – a multi-PMT digital optical module for the IceCube-Gen2 neutrino telescope*, PhD thesis, Friedrich-Alexander Universität Erlangen-Nürnberg, 2017.

[60] E. LONGO AND I. SESTILI, *Monte carlo calculation of photon-initiated electromagnetic showers in lead glass*, Nuclear Instruments and Methods, 128 (1975), pp. 283–307.

[61] M. ACKERMANN ET AL., *Optical properties of deep glacial ice at the south pole*, Journal of Geophysical Research, 111 (2006).

[62] M. AGERON ET AL. (ANTARES COLLABORATION), *ANTARES: The first undersea neutrino telescope*, Nuclear Instruments and Methods in Physics Research Section A: Accelerators, Spectrometers, Detectors and Associated Equipment, 656 (2011), pp. 11–38.

[63] M. G. AARTSEN ET AL. (ICECUBE COLLABORATION), *Evidence for high-energy extraterrestrial neutrinos at the icecube detector*, Science 342, 1242856 (2013), (2013).

[64] ——, *Measurement of south pole ice transparency with the IceCube LED calibration system*, Nuclear Instruments and Methods in Physics Research Section A: Accelerators, Spectrometers, Detectors and Associated Equipment, 711 (2013), pp. 73–89.

[65] ——, *Development of a general analysis and unfolding scheme and its application to measure the energy spectrum of atmospheric neutrinos with icecube*, Eur.Phys.J. C75 (2015) 3, 116, (2014).

[66] ——, *Energy reconstruction methods in the IceCube neutrino telescope*, Journal of Instrumentation, 9 (2014), pp. P03009–P03009.

[67] ——, *Icecube-gen2: A vision for the future of neutrino astronomy in antarctica*, [arXiv:1412.5106v2], (2014).

[68] ——, *All-sky search for time-integrated neutrino emission from astrophysical sources with 7 years of icecube data*, Astrophys. J., 835 (2017) no. 2, 151, (2016).

[69] ——, *The icecube neutrino observatory: Instrumentation and online systems*, JINST 12 P03012 (2017), (2016).

[70] ——, *Observation and characterization of a cosmic muon neutrino flux from the northern hemisphere using six years of icecube data*, The Astrophysical Journal, 833 (2016), p. 3.

[71] ——, *Search for nonstandard neutrino interactions with icecube deepcore*, Phys. Rev. D 97, 072009 (2018), (2017).

[72] ——, *Neutrino emission from the direction of the blazar TXS 0506+056 prior to the IceCube-170922a alert*, Science, (2018), p. eaat2890.

[73] ——, *Search for steady point-like sources in the astrophysical muon neutrino flux with 8 years of IceCube data*, The European Physical Journal C, 79 (2019).

[74] M. J. LARSON, *Simulation and identification of non-paissonian noise triggers in the IceCube neutrino detector*, Master's thesis, The University of Alabama, 2013.

[75] ——, *Vuvuzela icecube wiki page*. `https://wiki.icecube.wisc.edu/index.php/Vuvuzela`, April 2018.

[76] M. TANABASHI ET AL., *Review of particle physics*, Physical Review D, 98 (2018).

[77] M. THUNMAN AND G. INGELMAN AND P. GONDOLO, *Charm production and high energy atmospheric muon and neutrino fluxes*, Astroparticle Physics, 5 (1996), pp. 309–332.

[78] N. KARLSSON FOR THE VERITAS COLLABORATION, *Discovery of vhe gamma-ray emission from the starburst galaxy m82*, [arXiv:0912.3807v2], (2009).

[79] N. WHITEHORN AND JAKOB VAN SANTEN AND SVEN LAFEBRE, *Penalized splines for smooth representation of high-dimensional monte carlo datasets*, Computer Physics Communications, 184 (2013), pp. 2214–2220.

[80] P. B. PRICE AND K. WOSCHNAGG AND D. CHIRKIN, *Agevsdepth of glacial ice at south pole*, Geophysical Research Letters, 27 (2000), pp. 2129–2132.

[81] P. SANDSTROM AND THE ICECUBE-PINGU COLLABORATION, *Digital optical module design for PINGU*, AIP Publishing LLC, 2014.

[82] H. PANDYA AND D. T. AND, *Performance of IceTop as a veto for IceCube*, in Proceedings of 35th International Cosmic Ray Conference — PoS(ICRC2017), Sissa Medialab, aug 2017.

[83] R. ABBASI ET AL., *The energy spectrum of atmospheric neutrinos between 2 and 200tev with the AMANDA-II detector*, Astroparticle Physics, 34 (2010), pp. 48–58.

[84] R. ABBASI ET AL. (ICECUBE COLLABORATION), *The icecube data acquisition system: Signal capture, digitization, and timestamping*, Nucl.Instrum.Meth.A601:294-316,2009, (2008).

[85] ——, *Calibration and characterization of the icecube photomultiplier tube*, Nucl.Instrum.Meth.A618:139-152,2010, (2010).

[86] ——, *The design and performance of icecube deepcore*, Astroparticle Physics, Volume 35, Issue 10, May 2012, Pages 615-624, (2011).

[87] ——, *Icetop: The surface component of icecube*, NIM A700:188,2013, (2012).

[88] A. M. READ, S. R. ROSEN, R. D. SAXTON, AND J. RAMIREZ, *A new comprehensive 2d model of the point spread functions of theXMM-NewtonEPIC telescopes: spurious source suppression and improved positional accuracy*, Astronomy & Astrophysics, 534 (2011), p. A34.

[89] S. AGOSTINELLI ET AL., *Geant4—a simulation toolkit*, Nuclear Instruments and Methods in Physics Research Section A: Accelerators, Spectrometers, Detectors and Associated Equipment, 506 (2003), pp. 250–303.

[90] S. AIELLO ET AL. (KM3NET COLLABORATION), *Sensitivity of the KM3net/ARCA neutrino telescope to point-like neutrino sources*, Astroparticle Physics, 111 (2019), pp. 100–110.

[91] S. ANSOLDI ET AL., *The blazar TXS 0506+056 associated with a high-energy neutrino: insights into extragalactic jets and cosmic ray acceleration*, The Astrophysical Journal Letters, 863 (2018) L10, (2018).

[92] S. L. GLASHOW, *Resonant scattering of antineutrinos*, Physical Review, 118 (1960), pp. 316–317.

[93] S. S. WILKS, *The large-sample distribution of the likelihood ratio for testing composite hypotheses*, The Annals of Mathematical Statistics, 9 (1938), pp. 60–62.

[94] S. YOSHIDA AND A. ISHIHARA AND M. ONO. `http://www.ppl.phys.chiba-u.jp/research/IceCube/EHE/muon_model/atm_muon_model.pdf`, December 2006.

[95] S. SAHU AND B. ZHANG, *On the non-detection of glashow resonance in icecube*, JHEAp 18 (2018) 1-4, (2016).

[96] D. SOLDIN, *Atmospheric muons measured with IceCube*, EPJ Web of Conferences, 208 (2019), p. 08007.

[97] T. DEYOUNG FOR THE ICECUBE COLLABORATION, *Particle physics in ice with icecube deepcore*, Nuclear Instruments and Methods in Physics Research Section A: Accelerators, Spectrometers, Detectors and Associated Equipment, volume 692, p. 180 - 183, (2011).

[98] T. GLUESENKAMP, *Search for a cumulative neutrino flux from 2LAC-blazar populations using 3 years of IceCube data*, PhD thesis, Humboldt-Universität zu Berlin, 2016.

[99] T. K. GAISSER, *Spectrum of cosmic-ray nucleons, kaon production, and the atmospheric muon charge ratio*, Astroparticle Physics, 35 (2012), pp. 801–806.

[100] T. STANEV, *High Energy Cosmic Rays*, Springer Berlin Heidelberg, 2010.

[101] THE HESS COLLABORATION AND F. ACERO, *Detection of gamma rays from a starburst galaxy*, Science 20 Nov 2009: Vol. 326, Issue 5956, pp. 1080-1082, (2009).

[102] U. F. KATZ AND C. SPIERING, *High-energy neutrino astrophysics: Status and perspectives*, Progress in Particle and Nuclear Physics, Volume 67, Issue 3, July 2012, Pages 651-704, (2012).

[103] V. F. HESS, *Über Beobachtungen der durchdringenden Strahlung bei sieben Freiballonfahrten*, Physikalische Zeitschrift, 13 (1912), pp. 1084–1091.

[104] N. VAN EIJNDHOVEN, O. FADIRAN, AND G. JAPARIDZE, *Implementation of a gauss convoluted pandel PDF for track reconstruction in neutrino telescopes*, Astroparticle Physics, 28 (2007), pp. 456–462.

[105] J. VAN SANTEN, *Neutrino Interactions in IceCube above 1 TeV*, PhD thesis, University Of Wisconsin-Madison, 2014.

Danksagung

Zum Abschluss dieser Arbeit möchte ich mich bei verschiedenen Personen bedanken, die mir auf dem Weg zu diesem Punkt geholfen haben.
Zunächst möchte ich Prof. Dr. Gisela Anton und Prof. Dr. Alexander Kappes danken, welche mir die Chance gegeben haben diese Arbeit anzufertigen und mir stets mit Rat, Tat und konstruktiver Kritik zur Seite standen.
Des Weiteren geht ein großes Dankeschön an Dr. Thorsten Glüsenkamp, welcher sich immer viel Zeit genommen hat um mit mir über aktuelle Probleme oder die nächsten Schritte zu sprechen.
Zusätzlich möchte ich mich bei Dr. Jannik Hofestaedt und Dr. Jonas Reubelt für die vielen anregenden Gespräche und vor allem für deren konstruktive Kritik beim Verfassen dieser Arbeit bedanken.
Nicht zuletzt geht ein großes Dankeschön an meine ehemaligen Bürokollegen, Judith Schneider, Gerrit Wrede, Sebastian Fiedlschustern und Johannes Schumann, mit welchen stets ein freundschaftliches Arbeitsklima vorhanden war.
Ein riesiges Dankeschön geht natürlich auch an meine Eltern und an Heike. Ohne deren kontinuielriche und unermüdliche Unterstützung wäre ich nie zu diesem Punkt gekommen.
Zuletzt möchte ich mich bei meiner Frau, Alice, bedanken, welche nicht selten meine Launen und Stimmungen ausbaden musste, wenn ich in einer von vielen frustrierenden Phasen steckte und mich nichts desto trotz bis zum Schluss unterstützt und mir häufig Lösungen für Probleme aufgezeigt hat.
Vielen Dank!